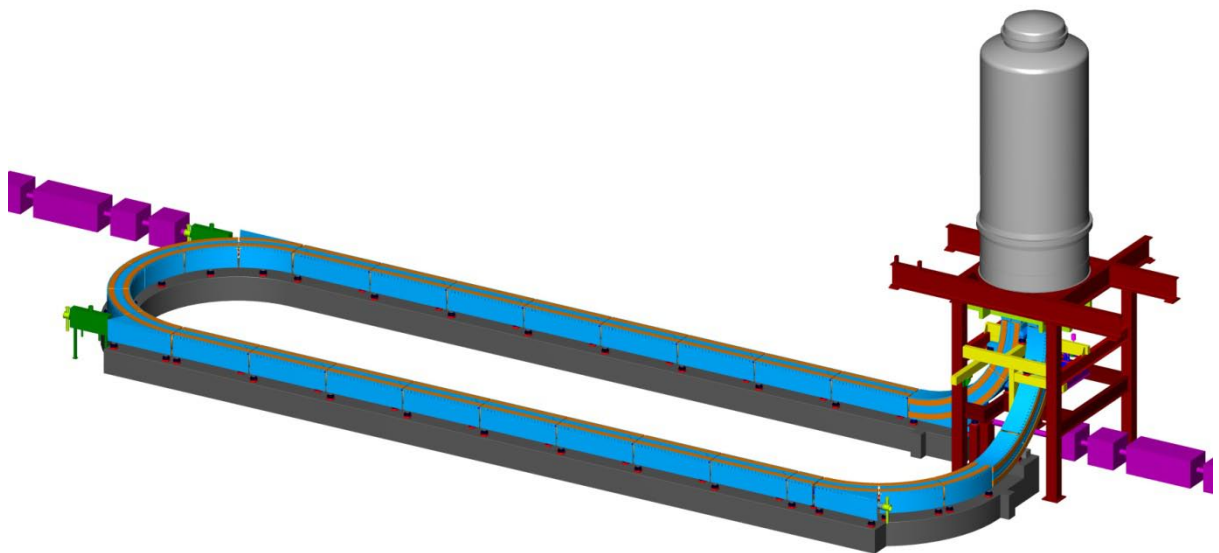


HESR ELECTRON COOLER

Design study

The Svedberg Laboratory
Uppsala University

Uppsala, 2009



CONTENTS

1	INTRODUCTION	7
1.1	Rationale for the present report.....	7
1.2	Motivation for electron cooling at HESR	7
1.3	Background, Previous work	7
2	OVERVIEW.....	8
2.1	Experimental requirements.....	8
2.1.1	Requirements for the electron beam.....	8
2.1.2	Electron energy.....	8
2.1.3	Solenoid field.....	9
2.2	System Overview	10
2.2.1	Layout	10
2.2.2	The high voltage accelerator	11
2.2.3	High voltage precision and stability.....	11
2.2.4	The gun solenoid	12
2.2.5	High voltage column.....	12
2.2.6	Transition.....	12
2.2.7	Bending.....	12
2.2.8	Vacuum system	12
2.2.9	Magnet system design.....	12
2.2.10	Straightness of the solenoid field along the interaction straight.....	13
2.3	Electron beam optimization	13
2.3.1	Alignment between electrons and anti-protons	13
2.3.2	Suppression of dipole oscillations	13
2.3.3	Suppression of beam envelope oscillations	13
3	DESIGN	14
3.1	The high voltage generator	14
3.1.1	Accelerating voltage	14
3.1.2	High voltage tank.....	15

3.1.3	SF6 System.....	16
3.1.4	High voltage column.....	16
3.1.5	Electronics deck.....	17
3.1.6	Generators on high voltage.....	18
3.1.7	Accelerating tubes.....	18
3.1.8	High voltage solenoids and separation boxes.....	18
3.1.9	Generation of power to solenoids on high voltage.....	20
3.1.10	Cooling with SF6 gas.....	20
3.1.11	Conditioning.....	20
3.1.12	Dead section.....	20
3.1.13	Magnet system.....	21
3.1.14	Electron Gun.....	21
3.1.15	The electron collector.....	27
3.1.16	Energy measurement beam line.....	31
3.2	Interaction Straight.....	32
3.2.1	The Solenoid.....	33
3.2.2	Vacuum system.....	36
3.2.3	The Steel Box.....	36
3.2.4	Dipole correctors of modules.....	37
3.2.5	System to align pancake solenoids in straight modules.....	38
3.2.6	System to align modules mechanically.....	38
3.3	Return straight.....	39
3.4	Horizontal bends.....	39
3.4.1	Dipole magnet of bent modules.....	39
3.5	Vertical bends.....	40
3.5.1	Support of coils.....	40
3.5.2	Mounting.....	43
3.6	Merging modules.....	44
3.7	Transition.....	45
3.7.1	Magnet flux return.....	45
3.7.2	Solenoids.....	46

3.7.3	Coils for correction of envelope oscillations	48
3.7.4	Magnetic field in the transition	48
3.7.5	Alignment	49
3.8	Magnetic field measuring system	49
3.8.1	Interaction straight	49
3.8.2	Measurement system bends	54
3.9	Electron beam diagnostics and correction.....	54
3.9.1	Electron beam diagnostics.....	54
3.9.2	Diagnostics of envelope oscillations.....	56
3.9.3	System to detect and quench beam dipole oscillations.....	57
3.9.4	Beam based alignment	57
3.10	Vacuum system	57
3.10.1	Pumping of acceleration/deceleration tubes	57
4	HOW TO ACHIEVE ELECTRON COOLING.....	58
4.1.1	Commissioning of the electron beam and alignment of the electron and proton and antiproton beams	58
5	SERVICES	59
5.1	Control system.....	59
5.2	Water cooling demands	59
5.3	Electricity.....	59
5.4	Temperature stabilization	59
5.5	Compressed air	60
5.6	Radiation protection	60
5.7	Safety system SF6	60
5.8	Building	60
5.8.1	Requirements on the cooler hall:	60
5.8.2	Requirements on the pelletron tower:.....	61
5.8.3	Concrete sockets	62
5.8.4	Tank support.....	62

5.8.5	Space for SF6 handling equipment.....	63
5.8.6	Power supplies room.....	63
6	PROTOTYPE TESTS.....	64
6.1	Magnetic field measuring system	64
6.1.1	The prototype test setup.....	64
6.1.2	Determination of the sensitivity of the measurement system	71
6.1.3	Noise of the measurement system	71
6.1.4	Sensor transport tests	74
6.2	Beam dimension measurement prototype tests.....	75
6.2.1	Motivation and test setup	75
6.2.2	Measurements.....	78
6.2.3	Resolution.....	81
6.2.4	Conclusion	81
6.3	High voltage regulation tests.....	82
6.3.1	Motivation	82
6.3.2	Measurement systems	82
6.3.3	Measurement results	83
6.3.4	Frequency spectra of the measurements.....	85
6.3.5	Conclusions for the HESR Pelletron.....	94
6.4	High-voltage solenoid	95
6.4.1	The solenoid	95
6.4.2	Test set-up.....	96
6.4.3	Transient average coil temperature	96
6.4.4	Azimuthal surface temperature variation	97
6.4.5	Steady state surface temperatures (after 24 hours).....	98
6.4.6	Simulation of coil temperature	98
6.4.7	The conductors.....	99
6.4.8	Steady state coil temperature.....	99
6.4.9	Thermal contact resistance	99
6.4.10	Cooling fins.....	100
6.4.11	Conclusions	100

7	SIMULATIONS	100
7.1	Simulation codes.....	100
7.2	Electron gun	101
7.3	Acceleration column	106
7.4	Transition	108
7.5	Collector	110
7.5.1	Axially symmetric simulation.....	110
7.5.2	Three dimensional simulation	111
7.6	Envelope oscillations.....	113
7.7	Magnetic flux return	113
7.8	The solenoid field	114
7.8.1	The magnetic field of a pancake coil	114
7.8.2	The solenoid field of a pancake-coil array.....	117
7.8.3	The uniformity of the solenoid field.....	119
7.8.4	Distortion due to longitudinal displacement.....	120
7.8.5	Distortions due to deflection of pancake coils.....	124
7.8.6	Distortion due to transverse displacement.....	126
7.8.7	Solenoid correctors	131
7.9	Field errors and dipole oscillations	133
7.9.2	Damping of dipole oscillations.	137
7.10	Vacuum and neutralization	138
7.10.1	Neutralisation.....	138
7.10.2	Expected vacuum level.....	139
7.10.3	Neutralisation with clearing electrodes	139
7.10.4	Conclusion	140
7.11	Simulation of electron cooling.....	140
7.11.1	Target interaction.....	140
7.11.2	Beta-value at the internal target.....	141
7.11.3	Beta-value at the cooling section.....	142
7.11.4	Calculations with BETACOO.....	142

8	DISCUSSION	145
8.1	Generation of high voltage	145
8.2	Magnet system	145
8.2.1	Magnetic field strength	145
8.2.2	Conventional solenoid	146
8.2.3	The pancake coils	146
9	REFERENCES	148

1 INTRODUCTION

1.1 Rationale for the present report

The present report is the Final report of Task 12, HESR 2: Electron Cooling, in the project DIRACsecondary-Beams. The Final report is defined as Deliverable D32 in the Annex I – "Description of Work" of the Contract for a DESIGN STUDY implemented as SPECIFIC SUPPORT ACTION, FP6, Project acronym: DIRACsecondary-Beams (Project full title: Internal Target experiments with highly energetic stored and cooled beams at the International Facility for Antiproton and Ion Research FAIR), Contract no. 515873.

1.2 Motivation for electron cooling at HESR

The purpose of the electron cooling system at HESR is to work together with the stochastic cooling system to prepare the antiproton beam as to provide the required momentum resolution for the experiments. Longitudinal and transverse blow-up of the beam due to the internal target and to intrabeam scattering is to be compensated by either of these systems, or of them working together.

The motivation for the HESR electron cooler can be summarized as follows:

- The PANDA experiment wants a resolution near what corresponds to $\Delta p/p = 10^{-5}$. This cannot be achieved with stochastic cooling alone.
- Electron cooling allows easy cooling also of a bunched beam
- The cooling rate is independent of antiproton intensity, no degradation of cooling at higher intensity.
- The electron cooler gives a possibility for absolute calibration of antiproton energy (by means of H⁻-beam and ⁷Li(*p,n*)-reaction: $E_{\text{threshold}} = 1880.3558 \pm 0.0812$ kV)
- The electron cooler gives a possibility for cooling below 3 GeV, which is difficult with stochastic cooling in HESR due to band overlap.

1.3 Background, Previous work

The existing electron cooler which is closest in energy to the proposed HESR cooler is the cooler at the Fermi National Accelerator Laboratory, FNAL which has demonstrated cooling of 8 GeV antiprotons with a recirculating electron beam of 0.1 A at 4.3 MV.[1]

The HESR electron cooler has to compensate the target effects of the internal PANDA Pellet target. This can only be realised by magnetised cooling using a strong longitudinal magnetic field in the cooling section. In this respect the HESR electron cooler will differ from the one at FNAL. However, the design of the high voltage part is similar and will be based on a Pelletron-type machine [2].

A first study of the electron cooler for HESR was performed by the Budker Institute of Nuclear Physics in Novosibirsk. The results of this study were documented in several reports [3].

2 OVERVIEW

In section 2.1 the most important requirements for the electron cooler are given and in section 2.2 an overview of the design is presented.

2.1 Experimental requirements

The electron cooler presented in this report is designed to fulfil the experimental requirements described in the FAIR Baseline Technical Report [4]. The most challenging task is to cool 8 GeV antiprotons so that these can be used for hadron spectroscopy. This requires a relative momentum resolution better than $4 \cdot 10^{-5}$. Simulations show that the desired momentum resolution can be reached if the requirements of the electron cooler listed below are fulfilled. The simulations are thoroughly described in section 7.11 where other parameters and assumptions, regarding for example internal target and the HESR ring, are given.

2.1.1 Requirements for the electron beam

- *The electron beam current shall be variable from zero up to 1 A.*
- *The electron beam radius shall be 5 mm during electron cooling of 8 GeV antiprotons.*

The electron beam at the interaction straight should have larger radius than the un-cooled antiproton beam. This reduces the effect of resonances induced by the non-linear tune shift caused by the electron beam onto the antiproton beam.

2.1.2 Electron energy

- *The accelerating voltage shall range from 450 kV to 4.5 MV.*

In order to cover the antiproton energy range from 0.83 to 8 GeV, the HESR electron cooler high-voltage charging system is designed for a high-voltage range from 450 kV to 4.5 MV.

- *A future upgrade of the accelerating voltage to 8 MV shall not be excluded.*

This corresponds to antiproton energy of 15 GeV, which is the full energy at HESR.

In a possible future upgrade to a collider mode electron cooling at the full energy is highly required to reach desired luminosity. [5]

- *In the range from 1.6 MV to 4.5 MV the high-voltage stability shall be 99.999 % or better.*

The desired resolution in the experiments with 8 GeV antiprotons is 10^{-5} . Therefore, the relative voltage fluctuations $\Delta U/U$ at 4.5 MV shall be 10^{-5} or smaller.

- *Below 1.6 MV the high voltage fluctuations shall be 16 V or smaller.*

- *The high-voltage ripple shall be small enough that this contributes insignificantly to the effective longitudinal electron temperature.*

According to our calculations, the ripple becomes comparable to other contributions of the longitudinal electron temperature at a level of $2\text{-}3\cdot 10^{-5}$ depending on energy.

2.1.3 Solenoid field

- *The solenoid field strength along the interaction straight shall be variable from 0.07 T to 0.2 T.*

The maximum field strength of 0.2 T is chosen according to the following criteria:

- A strong solenoid field enhances the cooling force. In the magnetized plasma electrons are forced to follow the magnetic field lines which implies that the effective transverse temperature is small and mainly determined by solenoid field errors.
- The solenoid field has to be strong enough to suppress intra-beam scattering since otherwise temperature from the transverse to the longitudinal dimension will be transferred.
- The electron beam size at interaction straight should be of the same size as the antiproton beam. This puts an upper limit on the solenoid field strength to 0.2 T.
- One technical challenge associated with electron beam transport is generation of cyclotron oscillations, especially at high energy and low solenoid field. To suppress these oscillations all the bending should take place at highest possible field strength and with a large bending radius.
- The solenoid field has to be strong enough to suppress beam rotation caused by space charge of electrons and ionized rest gas molecules.

For experiments to be performed at the injection energy of 3 GeV, or below, there is a desire to lower the integrated magnetic field strength in the HERS ring to allow for compensation of the tune-shift. This also implies that the electron beam becomes wider, which is beneficial.

A discussion of the solenoid field strength is given in section 8.2

- *The coherent oscillations of the electron beam as a whole shall not be more than what corresponds to about 10 eV, corresponding to a cyclotron radius of 50 μm at 0.2 T.*
- *The solenoid field shall be continuous enough so that an electron beam with 5 mm radius and energy anywhere in the range from 450 keV to 8 MeV must not be "heated" by any variation of the magnetic field. The envelope and dipole oscillations created by the total effect of all such transitions in the system shall be no more than 0.1 mm amplitude.*

Simulations of the beam envelope oscillations are given in section 7.4.

- *The magnetic field along the interaction straight shall be straight within $1\cdot 10^{-5}$ radians rms per degree of freedom.*
- *The effective length of the region where electrons and antiprotons interact shall be 22 meter.*
- *The electron beam shall be made parallel or accurately deflected with respect to the direction of the anti-proton beam within $2\cdot 10^{-6}$ radians.*

- The vacuum at the interaction straight shall be better than 10^{-9} mbar.

Ionized molecules of rest gas inside the electron beam in combination with the solenoid field causes rotation of the electron beam. The contribution to the average transverse velocity should be negligible. A detailed analysis is given in section 7.10.

2.2 System Overview

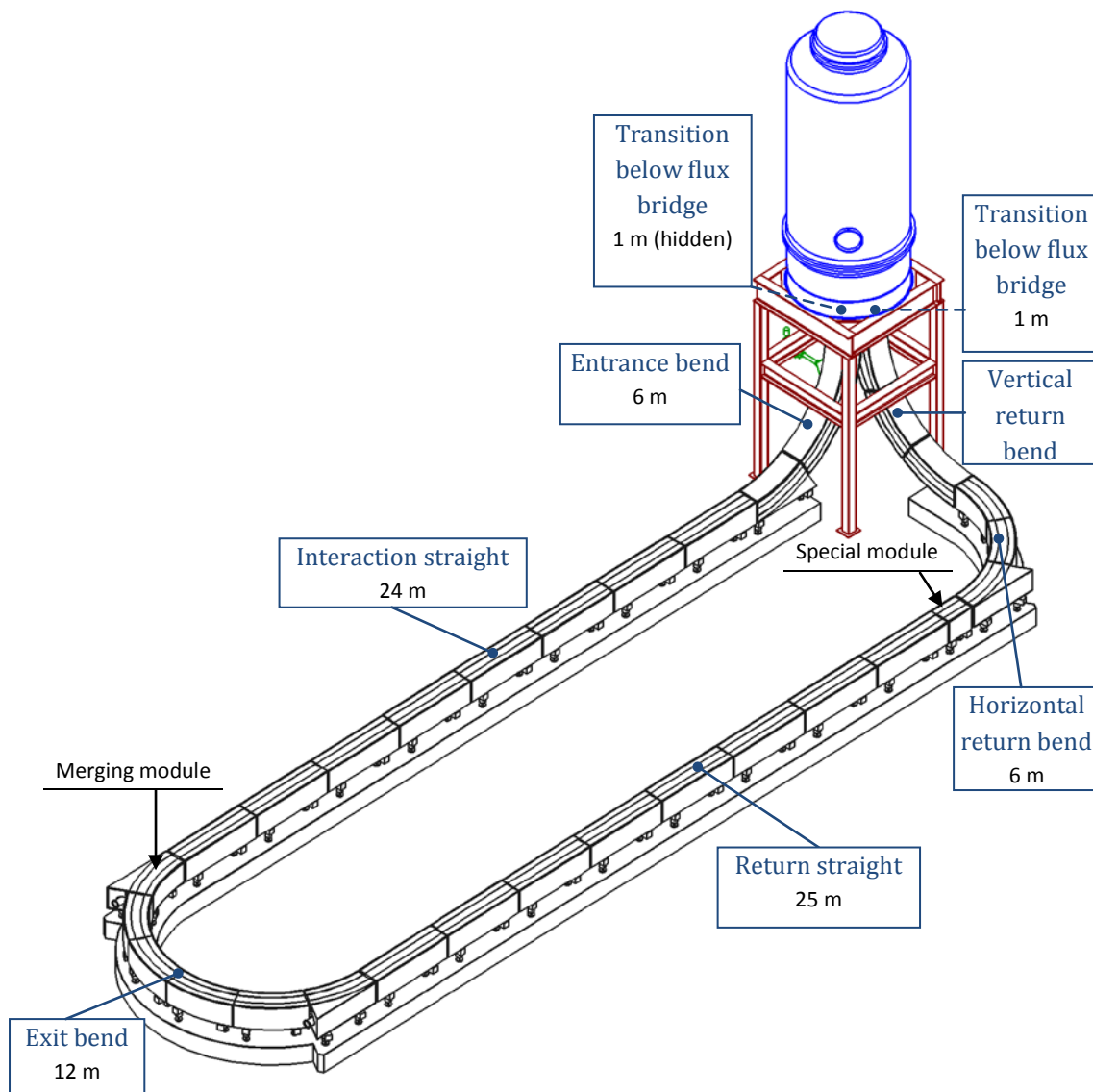


Figure 2-1: Layout of the HESR Electron Cooler

2.2.1 Layout

The layout of the HESR electron cooler is shown in Figure 2-1. The design is based on a Pelletron, an electrostatic accelerator of Van de Graaf type, which charges the high-voltage terminal with pellet chains. The electron beam is created by an electron gun placed at the high-voltage terminal and then accelerated in the acceleration column. All around the system the electrons are guided by a longitudinal magnetic field, created by solenoid coils, directed along the motion of the electrons.

After passing the interaction straight section the electron beam is deflected and transported back to the high voltage column where it is decelerated and deposited in the collector in order to restore energy.

The high-voltage tank containing the Pelletron is filled with SF₆ gas at a pressure of 5.5 bar.

To support the weight of the solenoid coils that are placed on different levels of high voltage, the high-voltage tank has to be vertical. The tank is located above the HESR beam line so that the electrons interact with antiprotons as soon as possible after acceleration, i.e. with smallest possible temperature.

The electron beam transport system is 94 meter in total and has been divided into 12 sections, which are listed in Table 2-1.

Table 2-1

Section	Field strength [T]	Length [m]	Bending angle [deg]
Acceleration column	0.07	5.00	
Transition	0.07- 0.2	2.00	
Entrance bend	0.2	6.28	90
Interaction straight	0.2	23.92	
Exit bend	0.2	12.57	180
Return straight	0.2	24.95	
Horizontal return bend	0.2	6.28	90
Vertical return bend	0.2	6.28	90
Transition	0.07- 0.2	2.00	
Deceleration column	0.07	5.00	
Total		94.28	450

2.2.2 The high voltage accelerator

The Pelletron is commercially available from National Electrostatics Corporation (NEC) [2]. Other solutions have been investigated (section 8.1) but were dismissed due to the following:

- At FNAL a Pelletron has been used for electron cooling at 4.3 MV.
- A Pelletron is constructed in a modular way, which facilitates future increase of the high voltage to at least 8 MV.
- A continuous longitudinal field of 0.07 T, with opposite directions in the accelerating and decelerating tubes, can be created in the Pelletron using solenoid coils placed at different levels of high voltage.
- There is no organic material in the acceleration tubes, which allows baking temperatures of 120° C and a possibility of achieving good vacuum. A vacuum of 10⁻⁹ mbar is important for avoiding high-voltage problems in the presence of the electron beam.

2.2.3 High voltage precision and stability

A separate acceleration tube that is attached to an H⁻ ion source on high voltage and to a spectrometer in the other end is invoked into the acceleration system. This H⁻ beam line, which has a very rigid construction is used for absolute calibration of the energy in the experiments. The outcome is also used as input for the high-voltage regulation system. The design of the H⁻ beam line for energy measurements is shown in section 3.1.16.

2.2.4 The gun solenoid

The electron gun, which is designed to produce an electron beam of 1 Ampere with 5 mm radius, is placed inside a so-called gun lens, i.e. a solenoid coil with an iron shield that focuses the magnetic flux. The magnetic field at the cathode is 0.2 T, and since the solenoid field along the interaction straight is up to 0.2 T, the required beam radius of 5 mm can be achieved.

2.2.5 High voltage column

Inside the high-voltage tank there are limitations in both generating and cooling away of power (section 3.1.9. and 3.1.10). The average solenoid field in the acceleration and deceleration columns is therefore limited to 0.07 T.

2.2.6 Transition

The transition between 0.07 T and 0.2 T, which is the desired field strength along the interaction straight for the highest energies, takes place over a two meter long section which reside half inside and half outside of the tank. The solenoids of this region are connected to individual power supplies, which are adjustable to make the field transition adiabatic. This is to avoid generation of large beam envelop oscillations.

Excess flux from the system below the transition region, where the solenoid field is stronger than in the high voltage column, is guided between the acceleration and deceleration beam lines through a bridge located close to the high voltage tank. (see section 3.7.1) Therefore, no large amount of magnetic flux needs to be returned in magnetic yokes.

2.2.7 Bending

The overall bending radius is 4 meter to reduce generation of cyclotron oscillations, especially at the highest energies.

2.2.8 Vacuum system

To reach the vacuum requirement of 10^{-9} bar, a bake-out temperature of 150 °C is required. Vacuum pumps will be located at both ends of the interaction and return straights, outside of the solenoid field. With no pumping along the 24-meter interaction straight the nominal inner diameter of the vacuum chamber has to be 200 mm.

2.2.9 Magnet system design

2.2.9.1 Modules

The electron-beam transport system outside of the high-voltage tank is divided into a number of manageable modules. These modules are about 3 meters in the straights and 2 meters in the arcs, corresponding to a bending angle of 30 degrees.

The modules are constructed so that floor instabilities or other mechanical shifts might move, but not deform modules. Windings of the same length as the modules will be used to correct the direction of the magnetic field.

During construction or after services the modules will be placed in the beam line fully equipped with the confined solenoids pre-aligned. Thereafter the bolts on the vacuum chamber flanges will be fastened and the module will be aligned mechanically relative to the HESR ring.

2.2.9.2 Dipole windings

Coils that have the full length of a module will correct the electron beam path. These are designed to produce dipole fields of 5×10^{-4} T, with a variation below 1 ‰ across the electron beam.

The corrector windings are used to compensate for the centrifugal drift in bending sections.

Therefore, the corrector windings of bent modules are designed to generate dipole fields of 7.1×10^{-3} T, corresponding to electron energy of 8 MeV.

2.2.9.3 Pancake solenoids

The solenoid of each module is made out of short pancake coils mounted in a rigid iron stand. These pancake solenoids can be adjusted individually to a high precision.

Pancake solenoids of the merging modules are racetrack shaped with variable length.

2.2.10 Straightness of the solenoid field along the interaction straight

The magnetic field on the interaction straight needs to be straight within 1×10^{-5} radians rms.

To diagnose field errors along the interaction straight a magnetic field measuring system will be used. It is integrated with the electron cooler and operates under vacuum. The process of measuring field deviations and manually adjusting the pancake solenoids is expected to be tedious. It should be avoided during normal operation.

2.3 Electron beam optimization

2.3.1 Alignment between electrons and anti-protons

The anti-proton beam needs to be made parallel or accurately tilted with respect to the direction of the straight magnetic field within 2×10^{-6} radians. This is because the transverse cooling rate will be controlled with the angle between the electron and anti-proton beams. See section 7.11.

To minimize deviations of the electrons relative to the anti-protons, beam based alignment will be applied, see section 3.9.4. Then the offset of the electron beam relative to the anti-proton beam is measured and corrected for using the corrector windings. This requires pick-up electrodes in each module with a resolution of 1×10^{-5} m.

2.3.2 Suppression of dipole oscillations

Coherent dipole oscillation will be kept to a minimum by applying field matching of high accuracy. The corrector windings of bent modules will be used to generate the bending field. The angles of the pancake solenoids are adjusted so that the solenoid field matches a reference path determined by the bending field.

Field matching will be carried out during pre-alignment of the pancake solenoids. A special system, described in section 3.9.3, will be used to detect and quench remaining oscillations.

2.3.3 Suppression of beam envelope oscillations

Beam Envelope oscillations will be kept to a minimum by maintaining a uniform solenoid field.

The solenoid of merging modules is made out of ordinary and racetrack shaped pancakes. To make the solenoid field uniform along the electron reference path, extra current will be added to the ordinary power supply. The extra current will be determined off-line during the pre-alignment and matching process.

A special system, described in sections 3.7.3 and 3.9.2, will be used to detect and quench envelope oscillations that are generated during acceleration and in the transition sections.

3 DESIGN

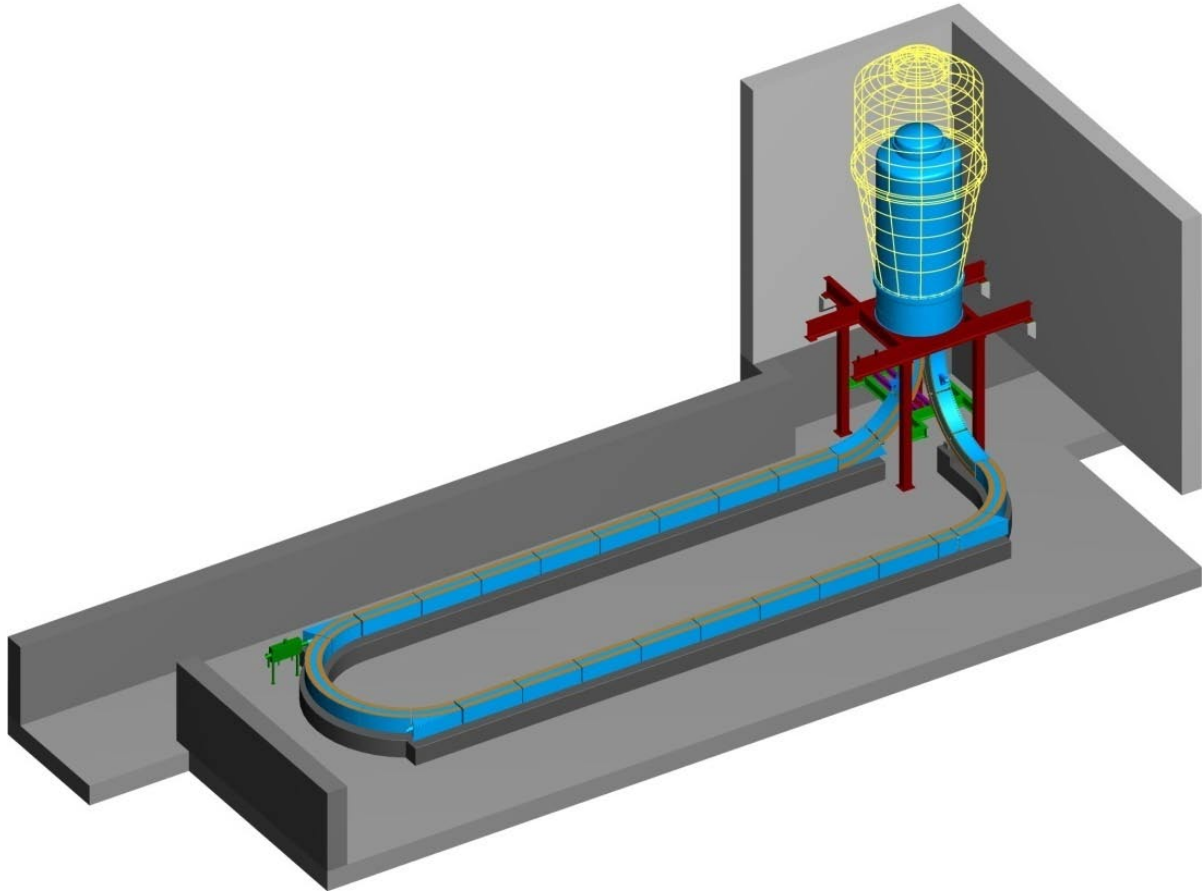


Figure 3-1: Layout of the 4.5 MeV electron cooler based on a Pelletron including high voltage tank and solenoid transport lines. In the case of a future upgrade to 8 MeV a larger high voltage tank is needed, as indicated in the figure.

3.1 The high voltage generator

3.1.1 Accelerating voltage

The experience at FNAL [8], [9], [10], [11], [12] is that the average voltage gradient in the acceleration tubes shall be limited to 12 kV/cm to avoid high voltage break-down in the presence of an electron beam. This means that the length of the acceleration tube needs to be 3.6 m at 4.5 MV.

A design of the high voltage generator based on a NEC's Pelletron 6-URE-2 [2] is shown in Figure 3-1.

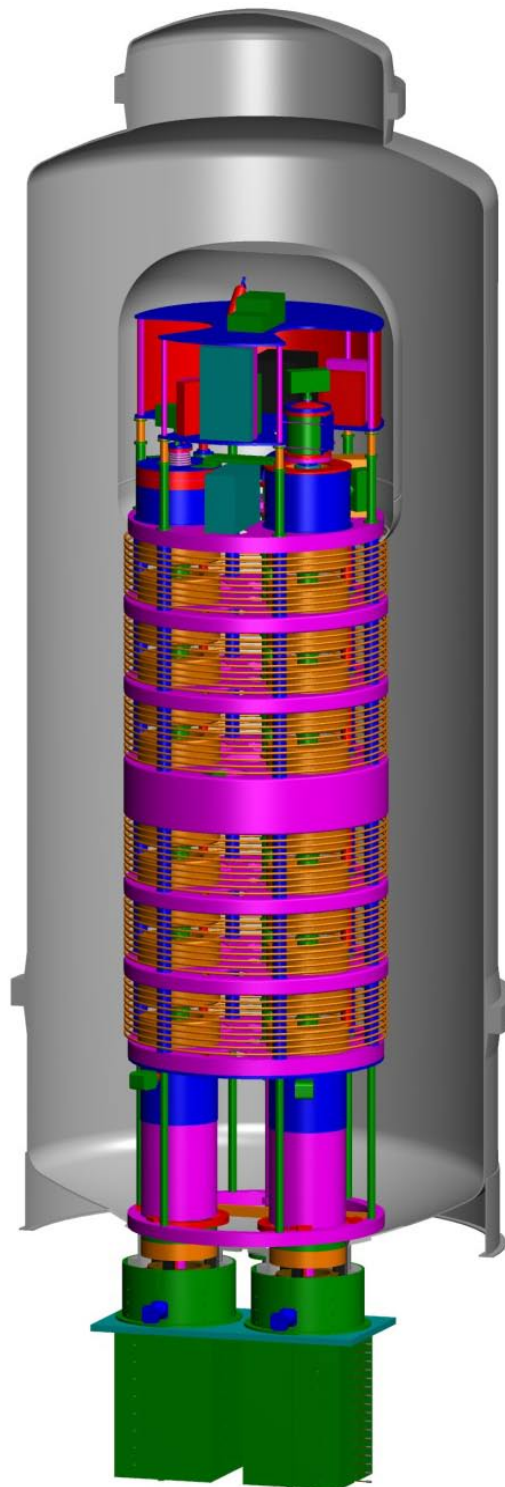


Figure 3-2: High voltage tank and column based on a 6 MV NEC Pelletron.

3.1.2 High voltage tank

The high voltage tank has a diameter of 3.9 m, a height of 10 m and a volume of 95 m³, which is sufficient for operation up to 4.5 MeV. The tank is designed with a flange to enable a prolongation if the maximum voltage is to be increased in a future upgrade. In the case of 8 MeV operation the tank diameter in the upper part must be 5.5 m and the tank height 13 m. The tank is filled with SF₆ gas at a pressure of 5.5 bar above atmospheric pressure (6.5 bar absolute).

3.1.2.1 Mounting and alignment of high voltage tank

Several ways of mounting the tank are possible. The method suggested by NEC is that the tank is transported and lifted as one piece into the building. The advantage of this method is that it will simplify alignment of the tank. This method assumes that it is possible to find a mobile lifting crane capable of lifting the tank as one piece.

It must be possible to remove the roof of the building or, if possible, one wall and roof.

The acceleration tubes must be positioned above a line through the interaction straight with a precision of +/- 1 mm. The alignment of the tank is done with the tank assembled, top access door and bottom flanges removed. The tank is adjusted to vertical by shimming and is bolted to the support.

3.1.3 SF6 System

3.1.3.1 SF6 recirculation system

A SF6 recirculation system is included in the pelletron 6URE-2. The recirculation system has a heat exchanger to cool the SF6 gas, a blower and a gas purification filter.

3.1.3.2 SF6 gas handling system

An additional gas handling plant is needed to evacuate air from the tank, fill the tank with SF6 gas, evacuate SF6 gas from the accelerator tank and transfer the gas to a separate storage tank. The gas handling plant for a 95 m³ accelerator tank has the specifications:

- Evacuation of air from atmospheric pressure to 1 mbar: 12 hours
- Filling of SF6 gas from 1 mbar to 6.5 bar absolute: 7 hours
- Suctioning of SF6 gas from 6.5 bar absolute to 10 mbar: 14 hours
- Dimensions of gas handling plant: length 3 m, width 2 m, height 2 m
- Storage tank: 2500 l /50 bar, length 3.5 m, width 1.3 m, height 1.3 m

3.1.3.3 SF6 safety system

A SF6 safety system is needed to protect personnel and vacuum systems in the case of a leak between the accelerator tank and the vacuum system. The SF6 safety system should include

- Bursting discs to protect the vacuum system from overpressure
- Fast closing valves
- Forced ventilation in critical areas
- Personal oxygen meters with alarm

Design of the SF6 safety system is not included in this study.

3.1.4 High voltage column

The high voltage column has six sections of 0.6 m each holding 750 kV to reach the full energy of 4.5 MeV. The structure is built in a modular way by hollow aluminium disks, so called separation boxes, with a diameter of 2 m and insulation posts.

On top of the high voltage column is the high voltage terminal with electron gun, electron collector and a negative ion source. It is surrounded by a cylindrical shell.

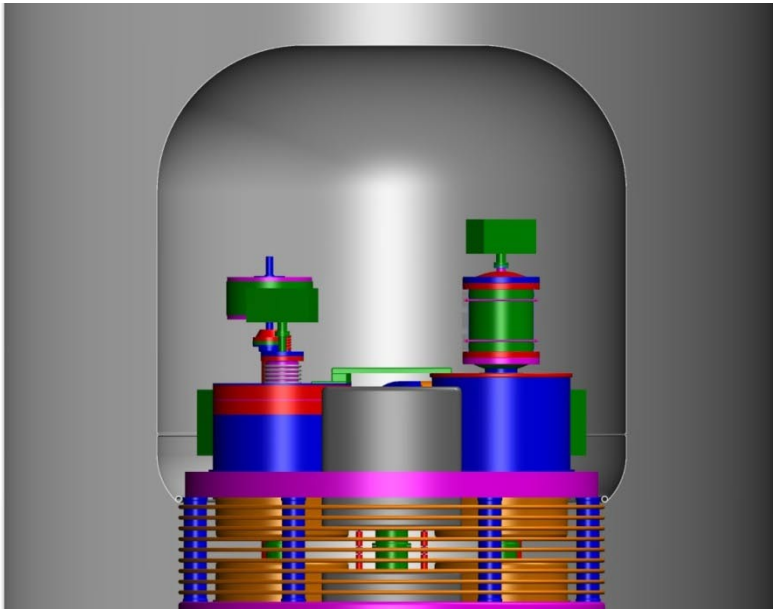


Figure 3-3: High voltage terminal. Accelerating column with gun to the left and decelerating column with collector to the right. An iron bridge is closing the magnetic flux between the two columns.

Charging of the high voltage terminal is done with two charging chains. The chains consist of metal pellets and insulating nylon links. The terminal voltage is stabilized by a corona current flowing from needles located in the terminal shell.

3.1.5 Electronics deck

The “electronics deck” is mounted on top of the high voltage terminal. This deck is at gun cathode potential and contains power supplies for collector, gun control electrode, gun filament and ion pumps and electronics to rapidly turn off the gun in the case of a high voltage break down.

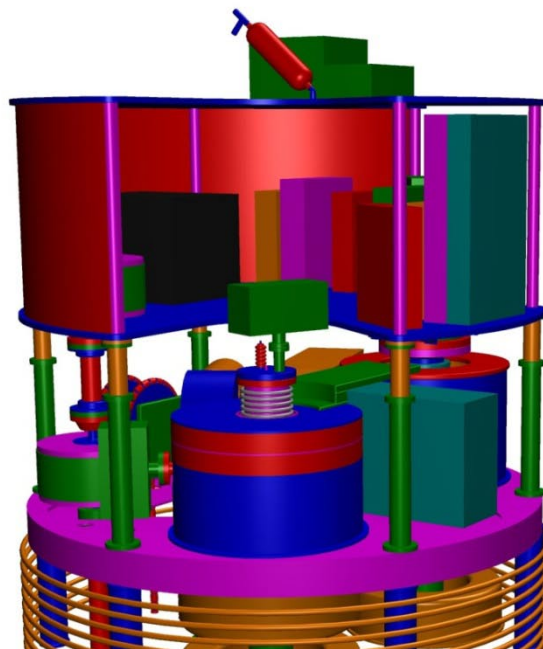


Figure 3-4: Electronics deck mounted on top of high voltage terminal with insulating posts. The electron gun is in the centre of the picture.

3.1.6 Generators on high voltage

Power to the high voltage sections is provided by two rotating shafts driving generators in the different sections:

- 2 x 2 kW generators in the separation boxes at the nominal 1 MV, 2 MV, 4 MV and 5 MV levels,
- 2 x 5 kW generators in the middle large separation box (the so called dead section) at the nominal 3 MV level,
- 10 kW generator at the high voltage terminal,
- 10 kW generator at the electronics deck.

3.1.7 Accelerating tubes

Three accelerating tubes are installed in the high voltage column, one for electron acceleration, one for electron deceleration and one for the negative ion beam, which is used for precision energy measurement. The acceleration tubes are composed of 305 mm long modules, which consist of a bonded set of ceramic cylinders and titanium disks. The minimum aperture is 25.4 mm. The standard module has 21 insulating gaps. The voltage is distributed along the module by a string of resistors connected over the insulating gaps. If service of the resistors is needed the solenoids can be removed from the separation box and moved vertically by 110 mm.

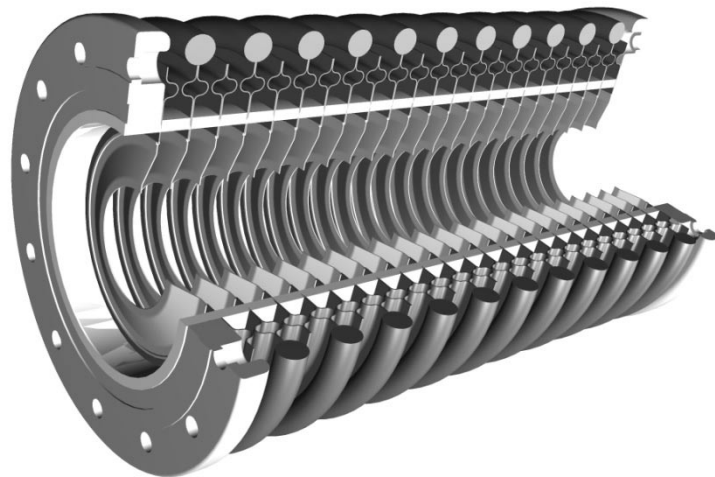


Figure 3-5: One acceleration tube module.

Simulation of electron optics in the accelerating tubes is described in section 7.3.

3.1.8 High voltage solenoids and separation boxes

The electron beam will be transported in a continuous longitudinal magnetic field in the accelerating columns. The magnetic field is generated by solenoids mounted above and below the separation boxes, see Figure 3-6.

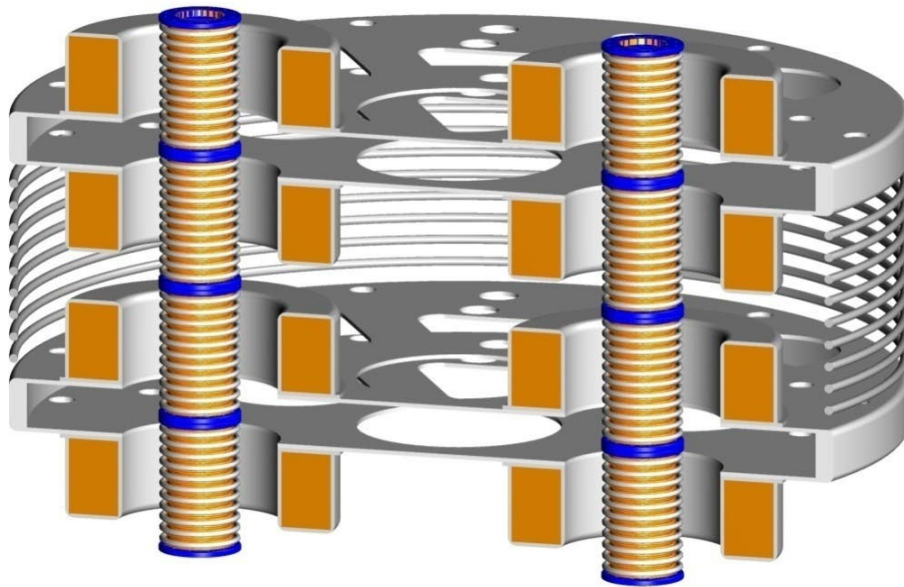


Figure 3-6: Solenoids attached to the separation boxes.

The solenoids attached to the separations boxes will from now on be referred to as the HV-solenoids.

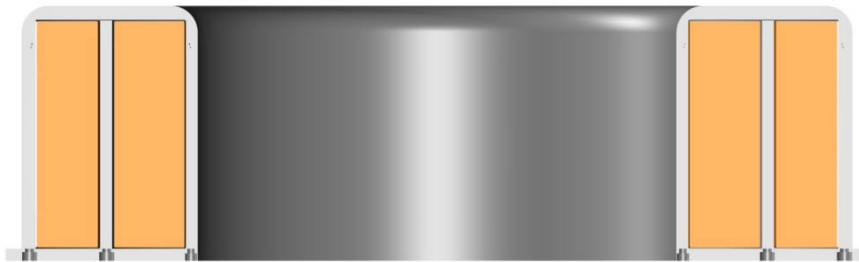


Figure 3-7: Cross section of a HV-solenoid.

The HV-solenoids are wound of enamelled copper wire. Each HV-solenoid has two concentric windings separated by an aluminium ring. The purpose of the ring is to transport heat generated in the windings to the aluminium base which is in thermal contact with the separation box. The coil is surrounded by an aluminium cover.

Winding and manufacturing of the HV-solenoids needs to be done with high precision to meet the requirement of a field straightness better than $1 \cdot 10^{-4}$ radians in the accelerating column. Since the HV-solenoids need to be in good thermal contact with the separation boxes it is not possible to adjust the tilt of the solenoids.

The centre to centre distance between two successive HV-solenoids is 0.305 m.

3.1.9 Generation of power to solenoids on high voltage

Each solenoid needs approximately 750 W to generate the desired field of 0.07 T. The power is provided by two 2 kVA generators in each separation box (not shown in Figure 3-6). The generators are driven by two rotating shafts. Space for the power supplies of the solenoids is provided inside “piece-of-cake” shaped boxes mounted on both sides of the separation boxes. The solenoids are mounted on the separation boxes, one above and one below each box.

3.1.10 Cooling with SF₆ gas

Cooling of the solenoids is provided by heat conduction to the separation boxes. A good thermal contact between the solenoids and the separation boxes is needed to ensure cooling of the solenoids. The separation boxes are cooled by forced circulation of the SF₆ gas. The SF₆ gas is cooled outside the tank by a heat exchanger included in the SF₆ recirculation system. The solenoid cooling principle has been verified by tests using a prototype solenoid and a prototype separation box at The Svedberg Laboratory (see 6.4)

3.1.11 Conditioning

For 4.5 MV terminal voltage the voltage over each section is 750 kV. Electric field simulation for 750 kV/section shows a maximum electric field strength of 99 kV/cm, well below 180 kV/cm which can be regarded as a safe electric field strength in SF₆ at an absolute pressure of 6 bar. Hence, conditioning of an individual section can be done up to 1.4 MV (individual sections can be conditioned by the use of shorting rods).

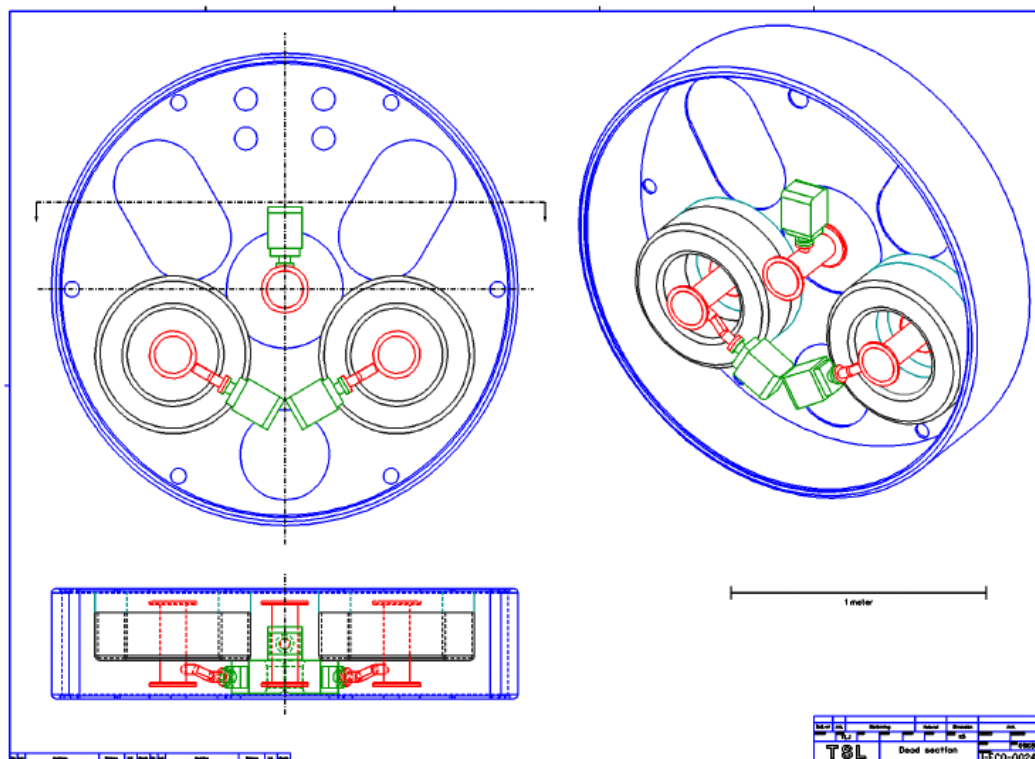


Figure 3-8: Big separation box.

3.1.12 Dead section

There are almost equidistant solenoid positions in the regular sections. These do not give space for installing of ion pumping. Therefore a so-called big separation box is included. Inside this box an extra solenoid is mounted to maintain the equidistance of the solenoid positions. It cannot be

mounted exactly halfway between the surrounding solenoids but has to be shifted 20 mm downwards to allow space for the pumping.

3.1.13 Magnet system

A summary of the data for the solenoids in the acceleration column is given in Table 3-1, where solenoids 2 – 15 are the HV-solenoids and solenoid 1 is the so called gun lens. A similar set of solenoids generate the magnetic field in the decelerating column.

Table 3-1: Solenoids in the acceleration column

Sol. no	z distance from cathode	Δz Coil length	R_{inner}	ΔR	NI ampere-turns	P power	Weight
1	-0.051 m	0.138	0.110 m	0.185 m	22000	0.7 kW	275 kg
2	0.172	0.175	0.190	0.105	16990	0.7	275
3	0.482	0.175	0.190	0.105	16990	0.7	275
4	0.782	0.175	0.190	0.105	16990	0.7	275
5	1.092	0.175	0.190	0.105	16990	0.7	275
6	1.392	0.175	0.190	0.105	16990	0.7	275
7	1.702	0.175	0.190	0.105	16990	0.7	275
8	2.002	0.175	0.190	0.105	16990	0.7	275
9	2.332	0.175	0.190	0.105	16990	0.7	275
10	2.612	0.175	0.190	0.105	16990	0.7	275
11	2.912	0.175	0.190	0.105	16990	0.7	275
12	3.222	0.175	0.190	0.105	16990	0.7	275
13	3.522	0.175	0.190	0.105	16990	0.7	275
14	3.832	0.175	0.190	0.105	16990	0.7	275
15	4.132	0.175	0.190	0.105	16990	0.7	275

The magnetic fields in the accelerating and decelerating columns have opposite directions. A magnetic flux bridge on the high voltage terminal closes the flux between the accelerating and decelerating columns.

Simulation of electron optics in the acceleration column is described in section 7.3.

3.1.14 Electron Gun

3.1.14.1 Requirements on the gun

The gun design is based on a flux in the beam corresponding to a magnetic field $B = 0.2$ T and a beam radius $R_{cs} = 5$ mm in the cooling section. This value of the flux is considered to be a maximum. The gun parameters are

Table 3-2: Electron cooler gun parameters

Parameter	Unit	Nominal
Anode voltage	kV	26
Beam current	A	1
Cathode diameter	mm	10
Cathode field	T	0.2
Bakeable to	°C	150

3.1.14.2 Design

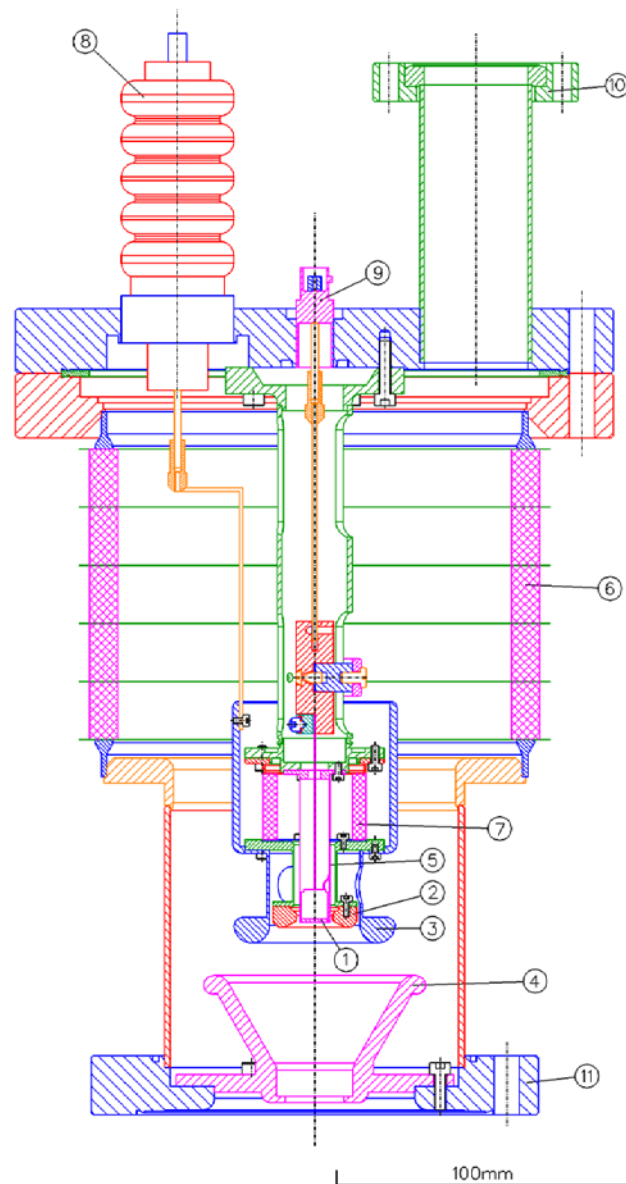


Figure 3-9: Gun assembly drawing. 1 = Dispenser cathode, 2 = control electrode, inner part, 3 = control electrode, outer part, 4 = anode, 5 = cathode skirt, 6 = anode insulator, 7 = control electrode insulator, 8 = control electrode feed through, 9 = cathode filament feed through, 10 = pumping port, 11 = CF 150 flange

The gun is based on the FNAL design [13] and has three electrodes. A negatively biased control electrode is used for

- regulation of the DC beam current
- production a pulsed beam
- current modulation for BPMs
- production of a pencil beam for commissioning purposes
- fast closing of the gun (if a partial discharge occurs it is necessary to close the gun fast. In this way a full discharge can be avoided).

The control electrode consists of two parts, with the inner one fulfilling a function of a thermal shield for the cathode.

The gun employs a dispenser cathode, STD400 from HeatWave Labs Inc, with the diameter of the flat emitting surface of 0.4" (10.16 mm) as compared to 0.3" in the FNAL design. The cathode is mounted on a 0.05 mm thick Mo/Re sleeve and has Molybdenum base flange.

The anode insulator is a 5-gap general purpose acceleration tube from NEC. It allows high voltage testing in air up to 40 kV.

The cathode insulator is custom made and consists of an alumina cylinder with titanium flanges.

Two ion pumps provide separate pumping of the gun chamber and the acceleration tube. This scheme will improve vacuum in the gun during full discharges in the acceleration tube. The gun is separated from the tube by a 15 mm diameter opening in the gun anode.

To avoid large variation of the magnetic field, a standard separation box solenoid is placed between the pumping port and the first acceleration tube. The additional pumping port in combination with the first separation box solenoid results in a drift distance of 0.36 m between the anode (Figure 3-10).

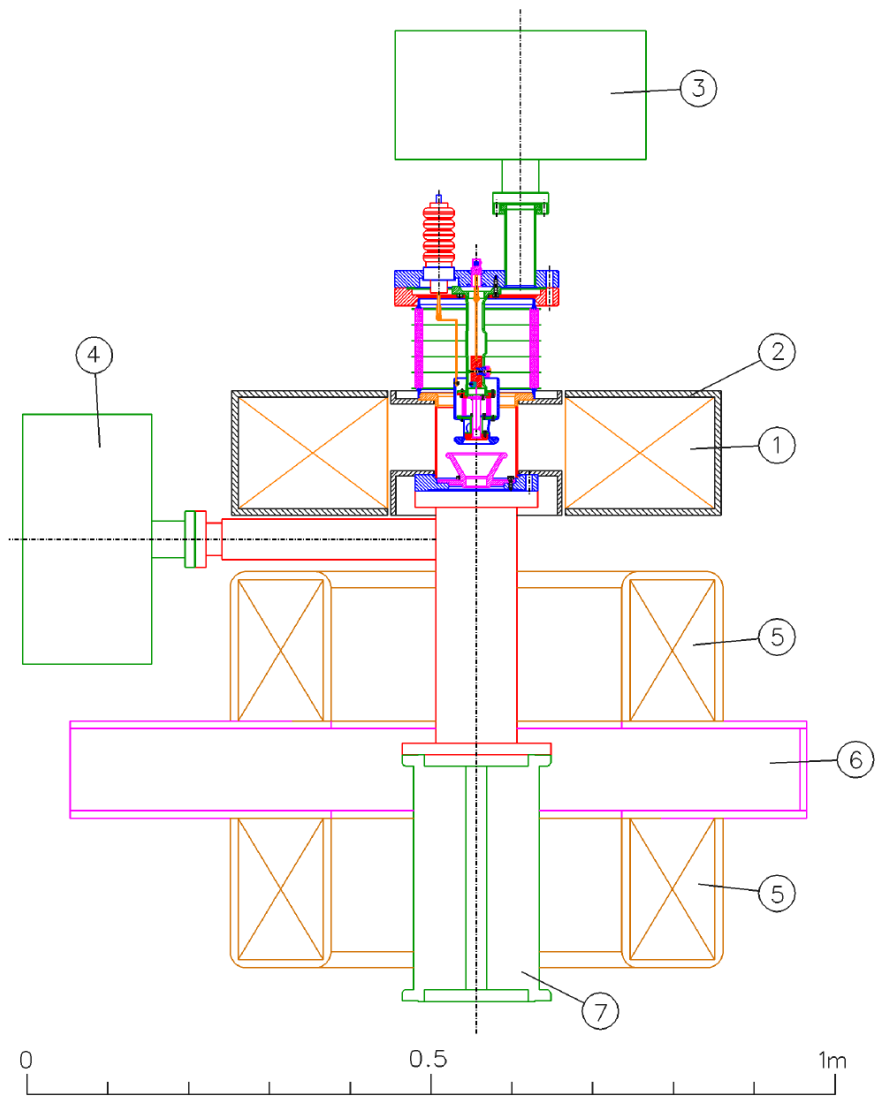


Figure 3-10: Gun and gun lens mounted on the acceleration column. 1 = gun lens, 2 = flux return, 3 = ion pump, 4 = ion pump, 5 = separation box solenoid, 6 = separation box, 7 = acceleration tube.

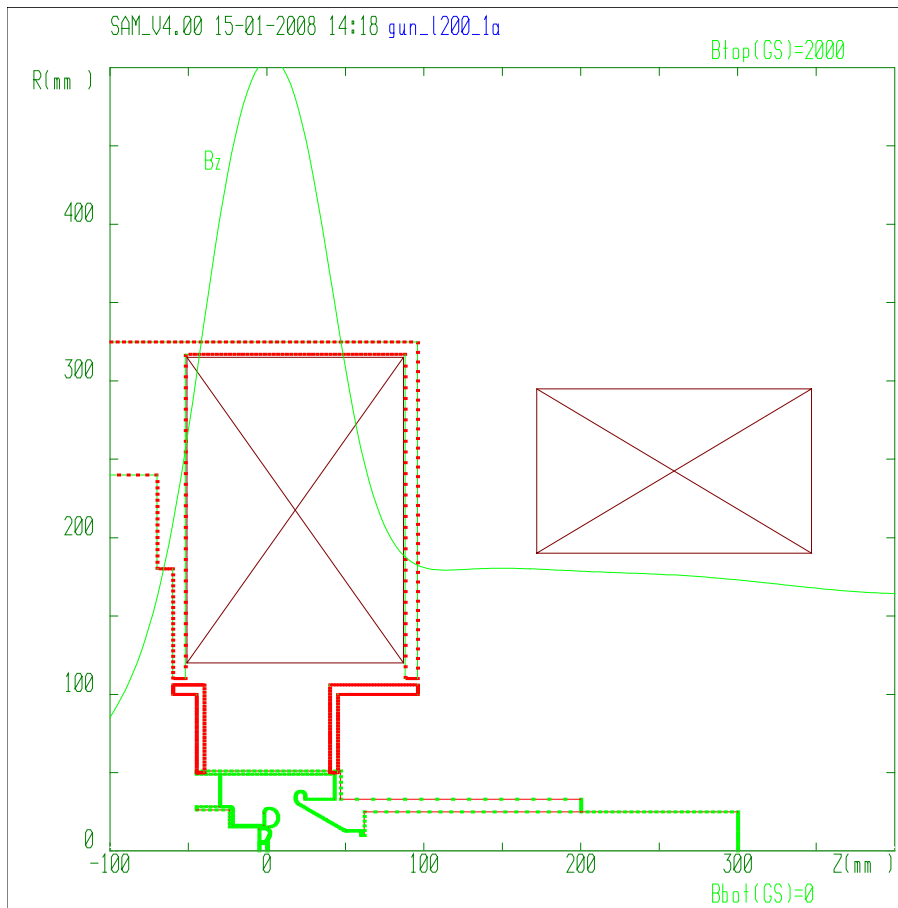


Figure 3-11: Magnetic field on the axis in the gun

3.1.14.3 Magnetic system

Magnetic field at the cathode is created by a dedicated solenoid with a flux return (so-called gun lens) concentrating the field at a narrow region near the cathode to 0.2 T. The emitter surface is placed at the position of the field maximum. The field decreases in the anode region down to the average field in the acceleration tube, 0.07 T. See Figure 3-11. The solenoid placed at the terminal separation box is identical to other separation box solenoids.

When preparing for a bake-out, the gun lens will be lifted up from its nominal position. Also the disk parts of its flux return will be removed.

The total power dissipated by the gun lens is comparable with that of the separation box solenoids. Because the lens doesn't have a direct contact with a separation box, the heat will be removed through a copper insertion in the central plane of the lens (not shown in Figure 3-10).

A pair of dipole correctors mounted around the drift tube (not shown in Figure 3-10) will allow steering the beam in the acceleration tube to check possible aperture limitations.

3.1.14.4 Electric fields

A large insulator allows testing the gun with air insulation up to 40 kV.

At most vacuum surfaces electric fields are below 70 kV/cm in all modes up to $U_a = 50$ kV. The critical place is a 1 mm gap between the control electrode and the cathode, because the potential difference is up to 8 kV to close the gun at $U_a = 50$ kV. Special attention is put into the mechanical design to ensure the concentricity of these electrodes.

To avoid emission from the area of the control electrode with a high electric field, the part of the control electrode closest to the emitter is made out of hafnium.

3.1.14.5 Optics

Simulation of the gun optics is described in section 7.2. A summary of the results is:

- The transition of the magnetic field from 0.2 T at the cathode to 0.07 T is done smoothly enough not to introduce cyclotron oscillations.
- The gun electrodes are optimized to produce minimum transverse electron temperature inside the gun. Excluding the very boundary electrons we obtain a transverse electron temperature of 1.6 eV at the exit of the gun. If the linear part of the transverse velocity is subtracted, the remaining temperature is below 0.1 eV.
- The potential difference between the outer and axial electrons does not result in a significant variation of the total phase advances over the length of the equipotential region. The total phase shift is estimated to be 0.035 ($\approx 2^\circ$).
- Because of the strong magnetic field in the gun region, the electron trajectories stay nearly unchanged at proportional changes of the anode voltage U_a and the control electrode voltage U_{ce} .
- To close the gun at $U_a = 26$ kV, the voltage of -4.5 kV is required at the control electrode.
- A 1 mA pencil beam is obtained at $U_{ce} = -4.0$ kV.

Figure 3-12 shows a simulation with the code UltraSAM [14].

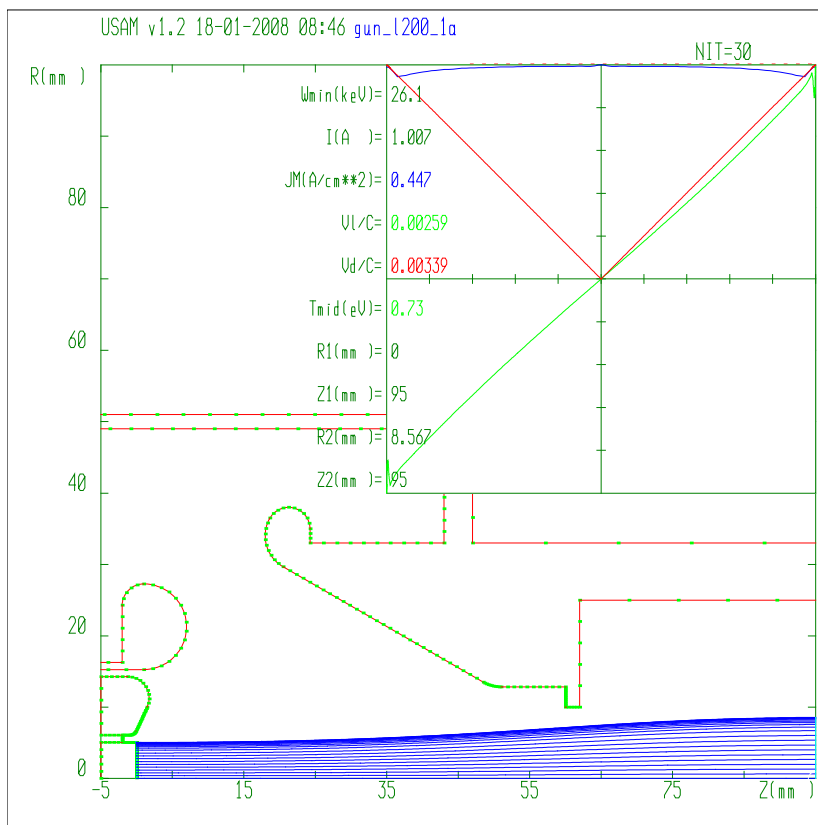


Figure 3-12: Electron trajectories in the gun. The graph in the upper right corner shows current density (blue), transverse velocity in Larmor rotations (green) and transverse drift velocity caused by $E \times B$ or un-uniformity of B (red) as a function of radius in the beam at $z = 95$ mm.

3.1.15 The electron collector

3.1.15.1 Requirements on the collector

The collector should be suitable for the nominal current of 1 A while suppressing effectively the flow of secondary electrons.

The requirement on the current loss needs more detail consideration. The most obvious limitation is the maximum Pelletron current of $\sim 300 \mu\text{A}$.

A really critical limitation is a current loss to tube electrodes. According to the Fermilab experience, any loss above 1 - 3 μA significantly increases frequency of full discharges. A continuous longitudinal magnetic field in the deceleration tube should significantly suppress losses. Because of the axial symmetry, a particle can reach a tube electrode only if at the entrance of the deceleration tube it is separated from the minimum tube radius by less than 2ρ , where ρ is a Larmor radius calculated from the transverse momentum of the particle and the magnetic field in the tube:

$$\rho = \frac{p_{\perp}}{eB}$$

The maximum possible value of ρ is determined by the collector voltage eU_{col} and for the chosen parameters ρ is 3 mm. The value is comparable with the gap between the primary beam boundary and the tube electrodes which is 4 mm.

Simulations show a significant growth of the longitudinal momentum spread in the electron beam toward the end of the beam line [18]. One of the consequences is that electrons in the low-energy tail are reflected from the collector. To minimize the effect, it is useful to avoid a deep potential minimum in the collector.

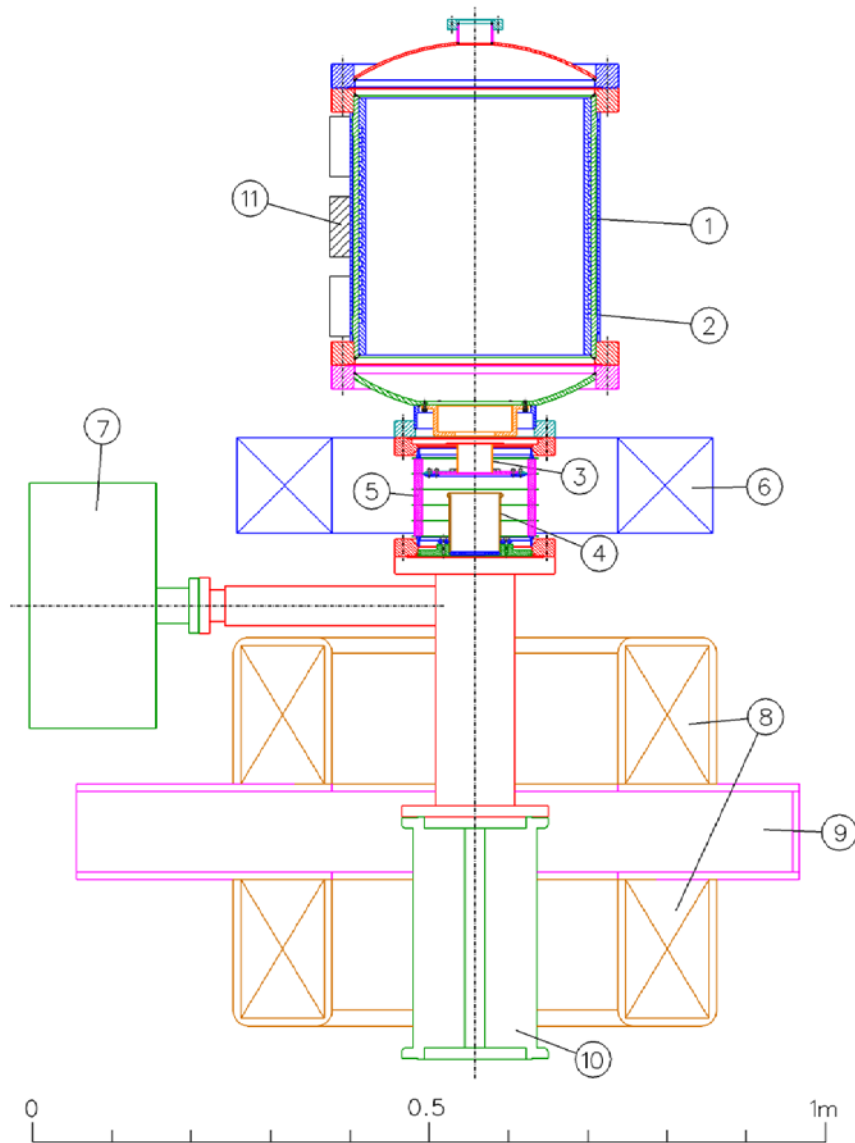


Figure 3-13: Cross section of the collector mounted on top of the decelerating column. 1 = collector cavity, 2 = steel plates 3 = collector control electrode, 4 = anode, 5 = isolator, 6 = collector lens, 7 = ion pump, 8 = HV solenoid, 9 = separation box, 10 = acceleration tube, 11 = permanent magnets

3.1.15.2 Design

The design is based on the Fermilab collector and assumes that the collector size is large enough and the collector perveance is low enough to suppress the secondary electrons by applying a transverse magnetic field to the collector cavity. An electrode near the collector entrance, the collector control electrode, can be used for fine tuning of the primary beam envelope and for suppression of slow secondary electrons in a mode without the transverse magnetic field in the collector. Its operational potential is close to the collector's one.

The main mode of the collector operation is with a transverse magnetic field, when the beam comes to a comparatively compact spot with a typical size of 5 cm. Nevertheless, the collector body has an axial symmetry to avoid fine tuning and dependence on possible external magnetic fields. In addition, an axially symmetric solution seems to be more technological.

Pumping of both the collector and the upper portion of the deceleration tube is provided by an ion pump at the anode (terminal) potential. The main factor that determines pressure near the collector is outgassing of the collector itself, and this coefficient changes by orders of magnitude with time. With this uncertainty in mind, there is not much sense to add a separate pumping in the collector cavity. All vacuum components of the collector are supposed to be baked prior to final assembly to 300°C.

The collector walls are made thick enough to withstand a test pressure of 10 bar. The collector is cooled by water circulating in channels in the copper cylinder.

3.1.15.3 Magnetic system

Magnetic fields in the collector region are formed by the terminal separation box solenoids, the short solenoid near the collector entrance (so-called collector lens), and by permanent magnets attached to steel plates near the collector cavity, see Figure 3-13. Combination of these fields creates field lines in the collector cavity that are bent by nearly 90° from the near-axis region to the collector side surface.

A pair of dipole correctors mounted around the drift tube between the deceleration tube and the collector insulator (not shown in Figure 3-13) allow steering the beam to the collector.

3.1.15.4 Optics and efficiency

The secondary electrons are suppressed by the transverse magnetic field in the collector cavity [20]. The mechanism of suppression can be explained in terms of a drift of adiabatically moving electrons in a bent longitudinal magnetic field. The drift velocity of an electron in a bent longitudinal field B with bending radius R_c is [19]

$$v_d = \frac{\gamma m_e v^2 (1 + \cos^2 \alpha)}{e B R_c} \frac{1}{2}$$

where $\alpha = \arccos \frac{v_{\parallel}}{v}$ is the angle between the momentum of the electron and the magnetic field. The direction of the drift is perpendicular to the plane of bending. If the magnetic field is bent by an angle ϕ , the electrons drift away from the field lines by

$$\Delta = \phi \frac{p_{\parallel}}{e B} \frac{(1 + \cos^2 \alpha)}{2 \cos \alpha}$$

In a simplest model of a 90-degree bend with a nearly constant absolute value of the magnetic field B , the primary beam drifts away from the field lines by

$$\Delta_0 = \frac{\pi p_{\parallel}}{2 e B} \approx \frac{\pi m_e}{2 e B} \sqrt{\frac{2 e U_{col}}{m_e}}$$

where U_{col} is the potential of the collector with respect to the cathode. Secondary electrons move backwards along the same field line, and those elastically scattered shift by $\geq \Delta_0$. If the shift of all secondary electrons is large enough, they are missing the entrance opening of the collector and are captured. The farther from the opening the secondary beam hits the wall, the lower is the chance electrons of the next generations (produced by secondary etc. electrons) would escape the collector.

The mechanism works better for lower magnetic fields, because at a fixed flux in the beam the size of the primary beam at the collector entrance increases as $B^{-\frac{1}{2}}$ but the drift goes as B^{-1} . However, to provide similar conditions for all electrons, the beam diameter needs to be significantly smaller than the bending radius, which, in turn, is approximately equal to the radius of the collector cavity R_{col} . Therefore, the collector size determines applicability of this approach and its efficiency. Numerically the necessary condition can be written for a modest collector perveance [20] as

$$R_{col} > 3\varepsilon_b ,$$

where

$$\varepsilon_b = \frac{e\Phi}{2\pi m_e v_s}$$

is the effective beam emittance determined by the flux in the beam Φ . For the parameters in the cooling section $B_{cs} = 0.2$ T, $R_{cs} = 5$ mm, $U_{col} = 3.5$ kV we obtain $\varepsilon_b = 1.3$ cm and $R_{col} > 4$ cm.

The formula above gives only the lower boundary for the collector diameter.

First, it estimates a suppression of elastically scattered electrons. Slower electrons will drift less on their way toward the collector entrance; the lowest energy is determined by the potential minimum created by the primary beam inside the collector cavity. An axially symmetrical simulation of the collector (i.e. without transverse fields in the cavity) gives $U_{min} \sim 1.2$ kV for $I = 1$ A.

Therefore, the critical secondary particle to be simulated starts from the collector surface with a kinetic energy of $eU_{min} = 1.2$ keV.

Second, the magnetic field is not constant along the bend; generally speaking, the energy changes as well. The drift is an integral over the trajectory

$$\Delta = \int_0^{\varphi_{max}} \frac{p_{\parallel}}{eB} d\varphi$$

where φ is the bending angle. Part of bending occurs in the high-field region with a low drift, while limitations to the ratio of R_{col}/R_{beam} most likely is determined by the region with minimum field.

Third, in practice it is difficult to bend the beam by full 90 degree.

Finally, the beam at the collector entrance should be somewhat smaller than the opening that limits the secondary electron flow.

As a result, simulations show that for the HESR cooler parameters one needs $R_{col} = 13$ cm.

Simulation of the electron optics in the collector is described in section 7.5.

3.1.15.5 Collector cooling

The collector is water cooled. The water channel is a double helix groove on the outside of the copper cylinder allowing a water flow of 10 l/min at a pressure of 5 bar. The terminal water system is located on the electronics deck and has a heat exchanger cooled by the SF6 gas.

3.1.15.6 Testing

The estimations and simulations above predict collector properties with much larger uncertainty than in the case of a gun. It is difficult to take into account 3D effects of the space charge, details of the secondary emission spectra, ion compensation etc. Also, suppression of secondary electrons by a transverse field in the collector has not been tested for so large magnetic fluxes in the beam.

Therefore, the collector needs to be carefully tested at low beam energy with an easy access to the collector body to estimate both current losses and the thermal regime.

An optimum test bench should include two 90-degree bends. The total drift of secondary electrons on their way from the collector toward the gun is then

$$\Delta = 2\pi \frac{p_{\parallel}}{eB} = \lambda_c$$

where λ_c is the cyclotron wavelength. p_{\parallel} is calculated by the electron energy in bends. If the testing is done at the energy determined by the anode voltage ~ 26 kV, passing through bends at 700 G generates the shift of 50 mm. It is significantly more than the diameter of opening in the proposed gun, 20 mm. Therefore, all electrons coming from the collector are lost, and the measurement gives an accurate prediction of losses in the final apparatus (except the IBS contribution).

3.1.16 Energy measurement beam line

The negative ion beam system will provide a negative hydrogen ion beam and appropriate magnetic analysis for precise control of the gun and collector potentials. The system includes a negative direct extraction duoplasmatron, extraction and focusing elements and a permanent magnet velocity selector in the high voltage terminal. The source potential will be the same as the gun potential. The ion source will be vertically oriented over the third acceleration tube. A beam-line valve in the terminal allows ion source servicing without venting the acceleration tube.

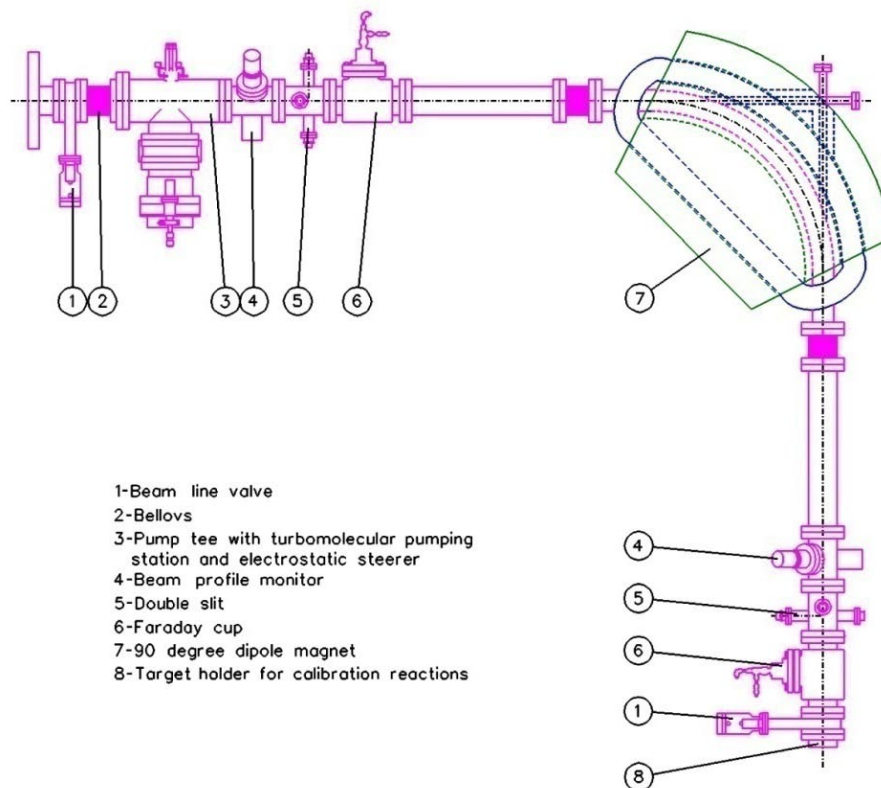


Figure 3-14: Assembly drawing of the energy measurement beam line

An electrostatic quadrupole triplet in the tank base will focus the beam on an object slit for a 90° magnet with a bending radius of 610 mm. The image slit is made of two halves electrically isolated

from each other. The halves serve as beam current pickups and the differential signal is used for the high voltage regulation.

We anticipate that a beam current of about 1-2 μA will be sufficient for tight energy control. The slit signals is processed in the Terminal Potential Stabilizer, model TPS-7, and stabilize the terminal voltage in the DC to about 5Hz region using the corona probe in the high voltage terminal. A second error signal in the 5Hz to 100Hz range can be sent to the terminal via light links to correct the gun, collector and ion source bias voltage.

In order to be able to obtain a voltage stability better than 1×10^{-5} the dimensions of the velocity analyzer need to be stable to the same order. This leads to the demand of a very rigid support for the structure containing the object slit, the magnet and the image slit. The dipole magnet and the slits will be included in an insulated box with stabilization of air temperature to better than $\pm 0.2^\circ \text{C}$. The cooling water for the dipole magnet must have temperature stability better than $\pm 0.2^\circ \text{C}$.

A turbo pump station below the tank is provided, along with beam profile monitors and Faraday cups near both object and image positions. Beam-line valves allow insulation of the entire beam-line from the acceleration tube and the target chamber from the analyzing magnet.

The magnet power supply will be stable to 3 PPM. An NMR magnetometer will be employed to stabilize the magnetic field. The spectrometer is commercially available.

3.2 Interaction Straight

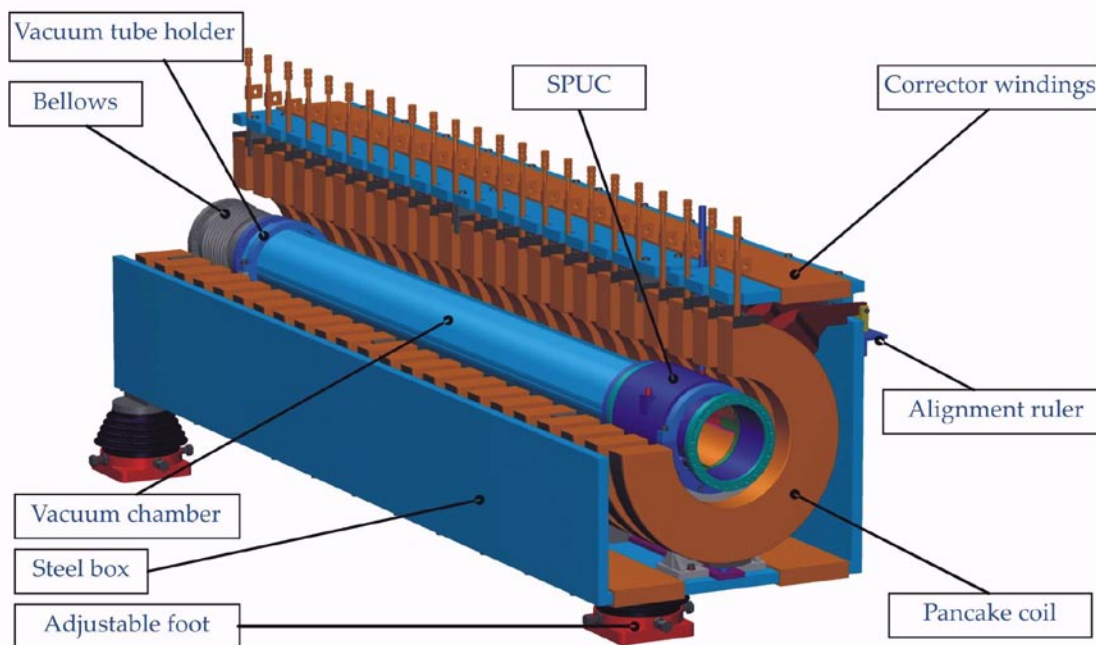


Figure 3-15: Three-meter module on the interaction straight

The interaction straight is made out of 8 three-meter modules shown in Figure 3-15. The magnetic field on the interaction straight needs to be straight within 10^{-5} radians rms. To verify field straightness along the interaction straight the magnetic field measuring system described in section 3.8 will be used.

To align the electron and the antiproton beams, beam-based alignment will be applied. Then the offset of the electron beam relative to the anti-proton beam is measured and corrected for using the dipole corrector windings. This requires pick-up electrodes in each module with a resolution of 10^{-5} m. These electrodes are mounted together with a pair of scrapers in the same unit, see section 3.9.1.1

3.2.1 The Solenoid

3.2.1.1 Pancake coils

The solenoid of each module is made out of short pancake coils [22] mounted in a rigid steel box. The position and angle of these coils can be adjusted individually to a high precision. The solenoid parameters listed in Table 3-3 have been chosen to

- Generate a sufficiently homogenous field. The magnetic field along the interaction straight must be continuous enough, that the straightness of the magnetic field, measured within 5 mm distance from the nominal path of the electron beam must be within 10^{-5} radians rms. This is to ensure that accurate field measurements can be carried out.
- Make room for diagnostics and baking equipment. The SPUC (see paragraph 3.9.1.1 below) has an outer diameter of 273 mm. To this connectors and equipment for baking (bands, insulation and shielding) has to be added.
- Allow assembly, especially to fasten 24 bolts on the Conflat flanges between adjacent subunits. 50 mm separation between solenoids is needed.
- Minimize costs

Table 3-3: Solenoid parameters

Pancake Coil Parameters			Comments:
Inner radius	R	170 mm	Centre to centre distance between two pancake solenoids 12 mm Cu + 1 mm insulation $6 \times \delta + 2 \times 1 \text{ mm insulation}$ $11 \times \delta + 2 \times 1 \text{ mm insulation}$ $6 \times 11 - 3$
Period	L	130 mm	
Wire dimension	δ	13 mm	
Width	D	80 mm	
Height	H	145 mm	
Number of turns	N	63	
Conductor			
Copper cross section	A_{Cu}	116 mm ²	12 mm × 12 mm conductor, water hole
Cooling water hole	d	∅ 6 mm	
Length	λ	96.5 m	$= \pi N(2R + H) + 0.5 \text{ m}$
Weight	M	100 kg	$= 8.93 \times 10^3 \text{ kg/m}^3 \cdot A_{Cu} \lambda$

Power consumption			
Current	J	328 A	$= \frac{BL}{\mu_0 N}$
Power consumption	P	1.8 KW	$= \frac{(0.02 \mu\Omega\text{m}^{-1})\lambda J^2}{A_{Cu}}$
Voltage	U	5.5 V	$= \frac{P}{J}$
Water cooling			
Temperature increase	ΔT	10 K	Maximum allowed
Water flow	Φ	2.6 dm ³ /min	$= \frac{P}{(4.2 \text{ J g}^{-1}\text{K}^{-1})\Delta T}$
Water pressure	P	5 bar	Water flow formula in [17] is used.

Each pancake coil is made out of three-double disks soldered together at the innermost and outermost turns. In total it is wound $N = 63$ turns with a $12 \times 12 \text{ mm}^2$ copper wire, with a 6 mm hole for water cooling.(Figure 3-16).

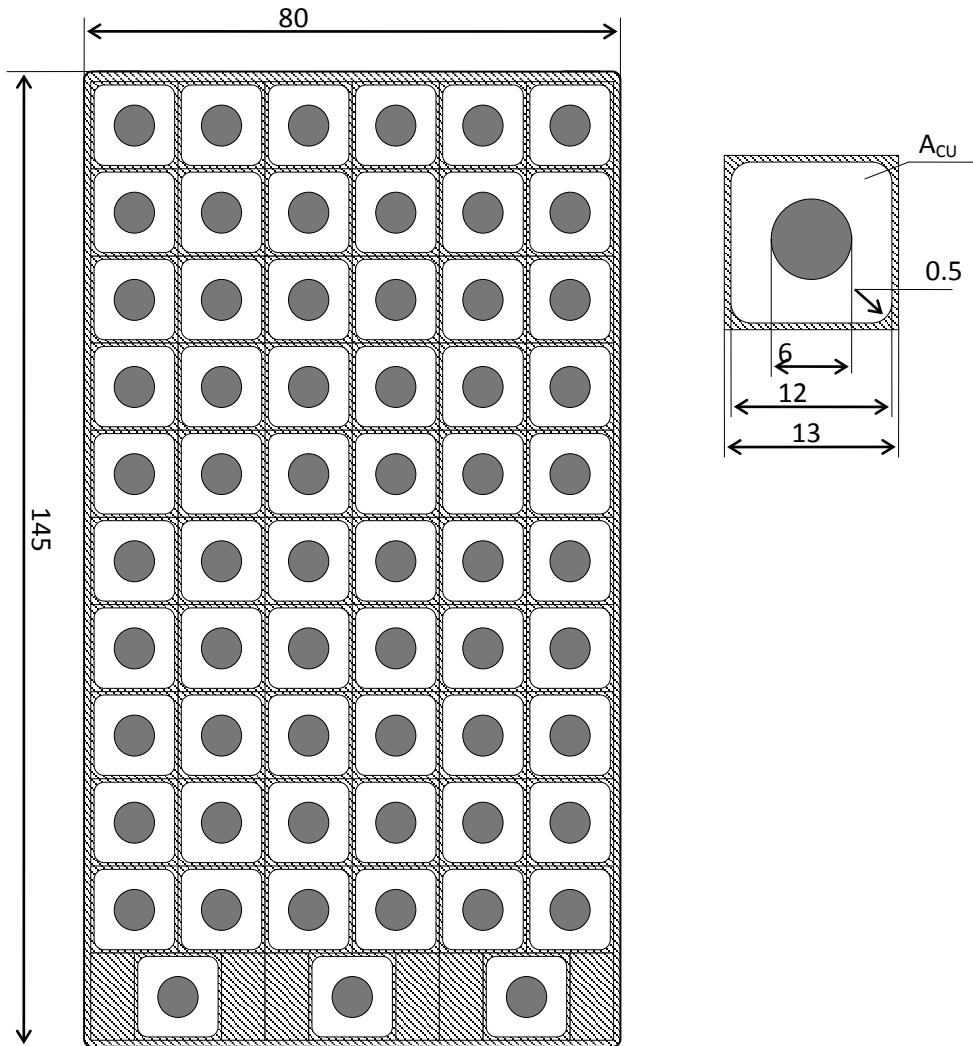


Figure 3-16: The pancake solenoid is made of three double discs wounded 63 turns in total.

3.2.1.2 Dipole correctors of pancake coils

Each pancake coil is equipped with horizontal and vertical dipole correctors that are used together with the magnetic field measuring system to compensate for mechanical deviations of the pancake coils that are larger than 0.1 mrad.

3.2.1.3 Support

Each coil is supported at three locations in the steel box. At the bottom, it rests on a bearing ball. At the sides, it is supported by handlebars, which can be adjusted from the outside (Figure 3-17).

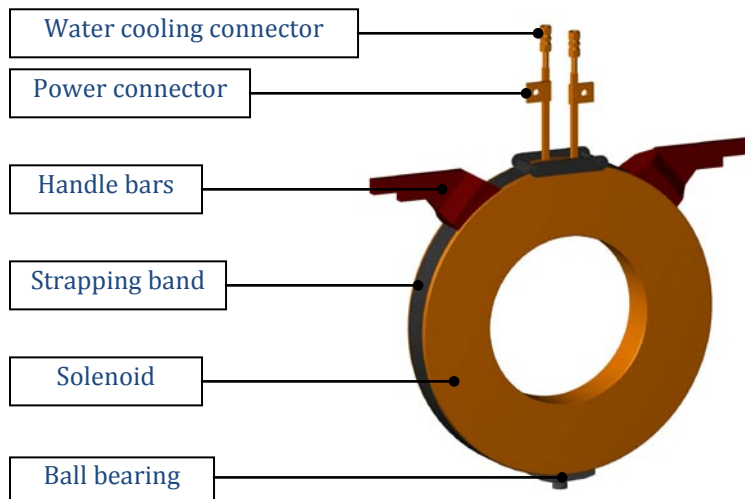


Figure 3-17: Pancake coil

The pancake solenoid is supported at three locations in the iron stand. At the bottom, it rests on a bearing ball. At the sides, it is supported by handlebars, which can be adjusted from the outside.

3.2.2 Vacuum system

To reach the vacuum requirement of 10^{-9} mbar, a bake-out temperature of 150 °C is required. Vacuum pumps will be located at both ends of the interaction and return straights, outside of the solenoid field. With no pumping along the 24-meter interaction straight the nominal inner diameter of the vacuum chamber has to be 200 mm.

The vacuum chamber is made of aluminium in order to be guaranteed to be non-magnetic and also because aluminium can be extruded in a shape suitable for creating ridges which serve as rails for the magnetic-field measurement carriage, see section 3.8 below.

Special Conflat flanges which are made of aluminium and stainless steel brazed together will be used. Another complication is thermal expansion. A two-meter aluminium tube expands 6 mm as the temperature increases by 130 °C. This expansion will be taken care of by the bellows at the end of each subunit, which is designed to compress ± 5 mm.

In each module, the vacuum chamber will be supported at two locations. There are two mechanical arms of the SPUC (see Section 3.9.1.1) used to fold the scrapers in and out. These arms come out between two pancake solenoids and therefore the vacuum chamber is held fixed at this location. The hold is tight to counteract strong vacuum forces. The other support holds the bellows and allows the vacuum chamber to slide longitudinally as the temperature changes.

During bake-out, cooling water will flow in the copper windings to protect the epoxy and to minimize any mechanical shifts. The inclusion of a shielding tube on the inside of the solenoid is considered. This would also protect the baking bands and insulation from being torn off the vacuum chamber during assembly.

3.2.3 The Steel Box

The box that defines a module is made of 30 mm thick plates of low carbon steel and holds 23 pancake solenoids. The box supports the pancake solenoids, the vacuum chamber, the dipole correctors and equipment for mechanical alignment. All these components are positioned relative to the steel box, which therefore must be very rigid. The steel box will also serve as a shield of external

fields (e.g. the earth magnetic field) and protect equipment on the outside from the magnetic field. Its third function is to guide the flux of the corrector windings.

3.2.4 Dipole correctors of modules

The dipole correctors of the solenoid field are designed to produce dipole fields of 5×10^{-4} T in straight sections, with a variation below 10^{-3} across the electron beam.

The dipole correctors are made of four copper windings around the top and bottom of each steel box. These are used to compensate for mechanical shifts of the modules due to floor instabilities etc and are part of the beam based alignment system. The windings are connected diagonally to two power supplies, indexed 1 and 2 in Figure 3-18. With NJ_i ampere-turn per winding, the horizontal and vertical components of the magnetic field at the beam centre can be approximated as

$$B_H = \frac{\mu_0 N}{h} (J_1 + J_2)$$

$$B_V = \frac{\mu_0 N}{h} (J_1 - J_2)$$

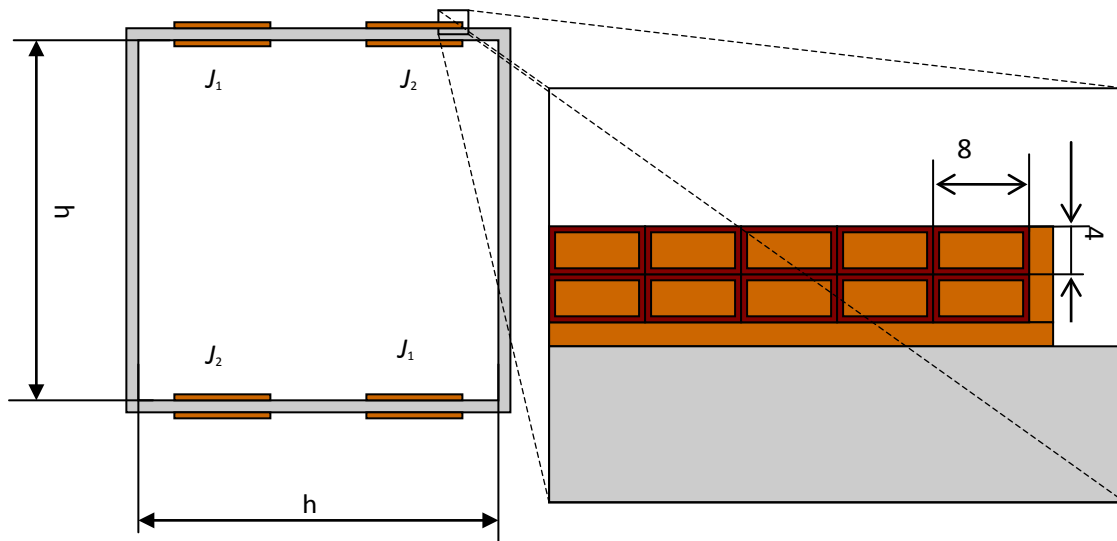


Figure 3-18: The dipole corrector of the solenoid field is made out of four windings around the top and bottom of the steel box.

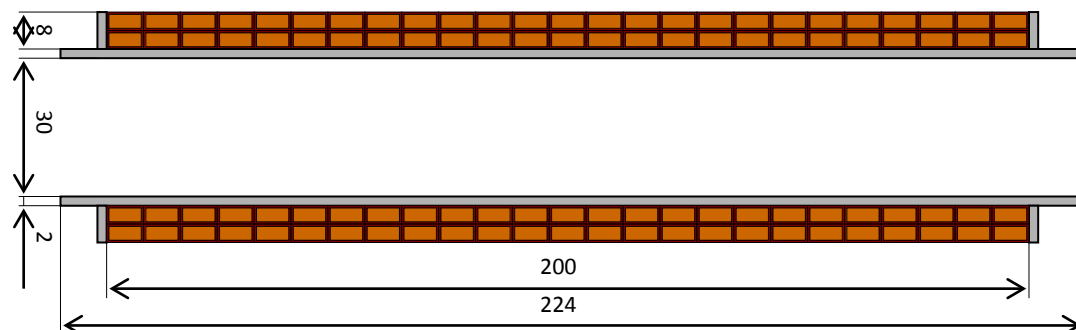


Figure 3-19: The cross section of corrector winding of a straight module.

Figure 3-19 shows the corrector windings for the straight modules. A $3 \times 7 \text{ mm}^2$ conductor ($4 \times 8 \text{ mm}^2$ including insulation) is wound 50 turns around a bobbin of 2 mm thickness. A current of ± 3 ampere in the four windings generates a horizontal or vertical field of ± 0.0005 T. This corresponds to a correction of the longitudinal field direction of $\pm 2.5 \times 10^{-3}$ radians.

Table 3-4: Parameters for each of the four corrector windings in one straight three meter module

Corrector windings of straight units			Comments:
Wire dimension		8 mm × 4 mm	including insulation
Width		200 mm	= 25 × 8 mm
Height		10 mm	= 2 × 4 mm + 2 mm
Number of turns	N	50	= 25 × 2
Conductor			
Copper cross section	A_{CU}	21 mm ²	= 7 mm × 3 mm
Length	λ	299 m	= $2N \cdot 2.99$ m
Weight		56 kg	= $(8.93 \text{ kg dm}^{-3}) \cdot A_{CU}\lambda$
Power consumption			
Design field	B	5×10^{-4} T	
Current	J	3 A	= $\frac{Bh}{\mu_0 2N}$
Power consumption	P	2.6 W	= $\frac{(0.02 \mu\Omega\text{m}^{-1})\lambda J^2}{A_{CU}}$
Voltage	U	1 V	= $\frac{P}{J}$

3.2.5 System to align pancake solenoids in straight modules

The pancake solenoids in the straight modules have to be mechanically adjusted so that the magnetic field in each module has a straightness better than 10^{-5} radians. The magnetic field measurement system described in section 3.8 is intended to be used both for these module adjustments and later for the measurements of the complete cooling straight section.

Based on the measured field errors the corresponding angle for each pancake will be calculated and corrected for. The method was developed by the BINP group and has proved to generate a solenoid field with straightness better than 10^{-5} radians rms in a 3m long electron cooler.

3.2.6 System to align modules mechanically

Each module will be aligned mechanically relative to the HESE to a precision of 10^{-4} radians. This requires optical alignment targets in each end of the modules. Each module will be supported by three stands that are horizontally and vertically adjustable.

3.3 Return straight

On the return straight, the field requirements are less severe than on the interaction straight. The return straight is nearly identical to the interaction straight with the following differences:

- The SPUCs are replaced with ordinary pick-up electrodes (without scrapers)
- One 1.026 m long module with 8 pancake coils has been added at the end of the return straight to compensate for the distance between accelerating and decelerating columns. (See layout in Figure 2-1).

3.4 Horizontal bends

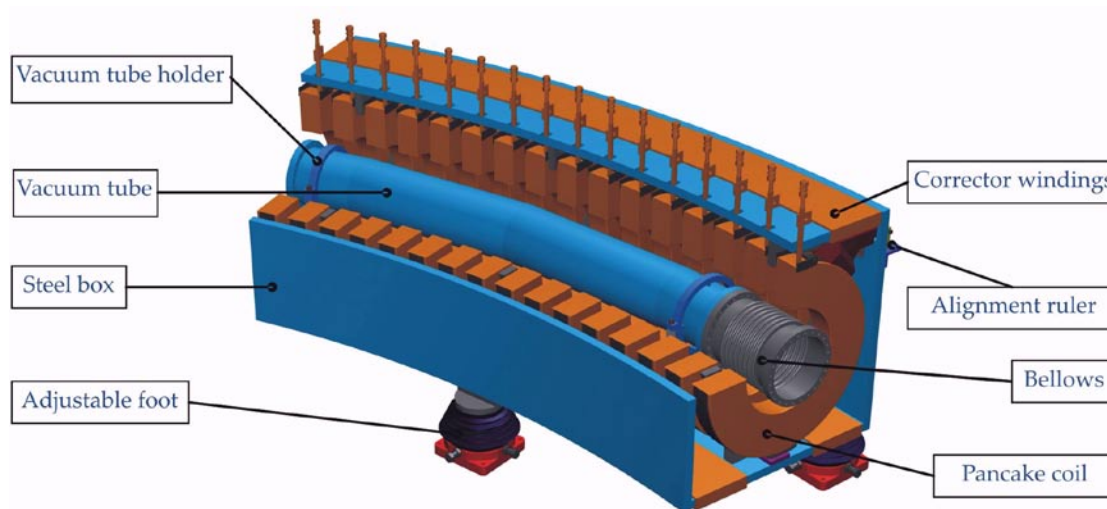


Figure 3-20: Horizontal bend module.

The bent modules are 2 meters, which corresponds to 30 degree bending. Each module holds 16 pancake coils as shown in Figure 3-20.

3.4.1 Dipole magnet of bent modules

Corrector windings of the same length as the bending modules will be used to compensate for the centrifugal drift. These have been designed to generate dipole fields of 7.1×10^{-3} T, corresponding to electron energy of 8 MeV.

The curvature of the solenoid field will be matched to the dipole field by adjusting the angles of individual pancakes. This process, which is supported by simulations and mathematical optimization methods, will be carried out off-line during commissioning of the modules. The accuracy of the matching is limited by the accuracy of field measurements and long term stability of pancake alignment. Therefore, a correction system will be used to detect and quench remaining cyclotron oscillations on the interaction straight, see section 3.9.1 below.

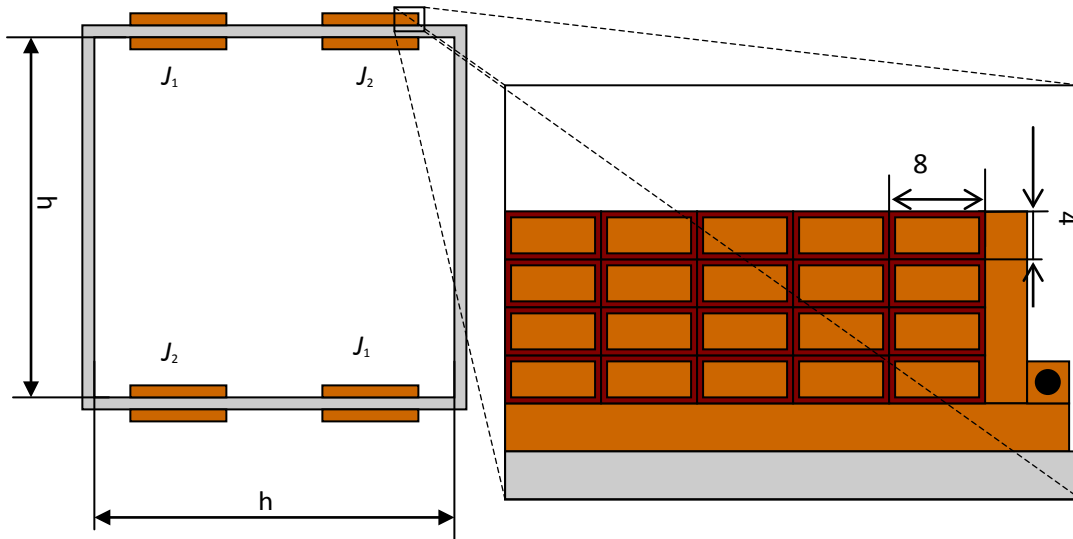
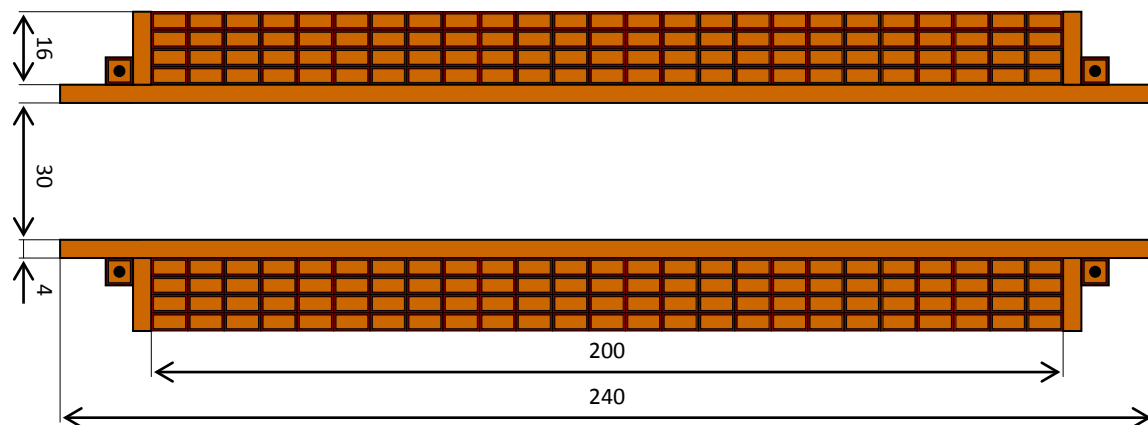


Figure 3-21



3.5 Vertical bends

3.5.1 Support of coils

The mechanical support of the coils in a vertical bend module is more complicated than in the horizontal modules since the gravitational force is not perpendicular to the axis of the coils.

The requirements on the solenoid supports in the vertical bends are

- Possibility to tilt each coil +/- 5 mrad.
- Tilt angle long term stability better than $1 \cdot 10^{-5}$ rad.

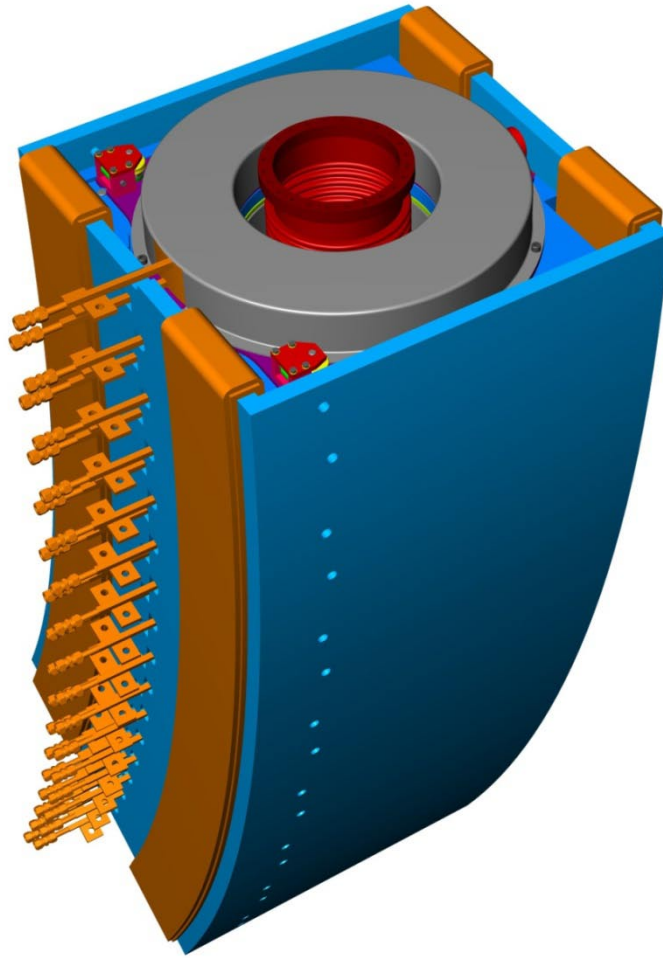


Figure 3-22: A complete vertical bend module

To fulfil the requirements of stability each coil is cast by epoxy firmly into a stainless steel pot consisting of a cover, thickness 3 mm, bolted to a stainless steel base plate, thickness 8 mm. The base plate is mounted on a wedge shaped aluminium support plate by joints in three corners. Two of the joints are adjustable and one joint allows the coil to pivot around a fixed point.

One coil is mounted on each side of the wedge-shaped support plate.

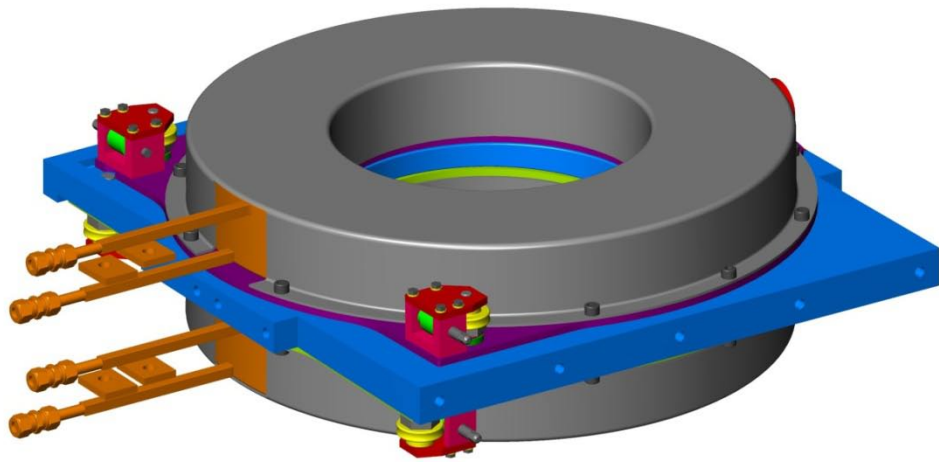


Figure 3-23: Two coils mounted on a wedge-shaped base plate. Each coil has two tilt adjustment mechanisms.

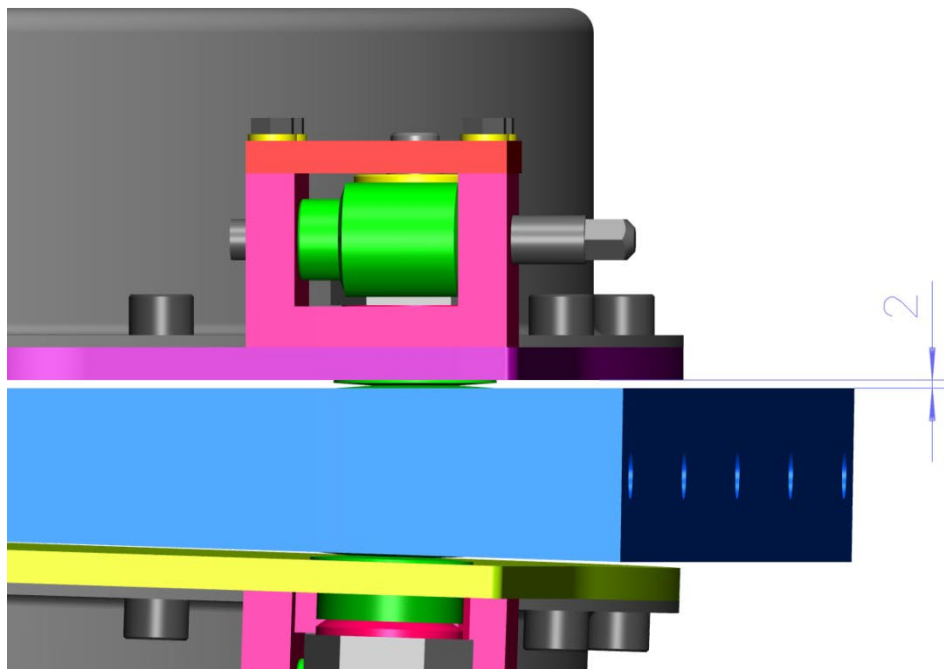


Figure 3-24: Detail of the adjustment mechanism.

The mechanism allows adjustment of one corner by ± 2 mm. Spring washers are used to create a counter force to eliminate play. The adjustment is done through a hole in the iron box.

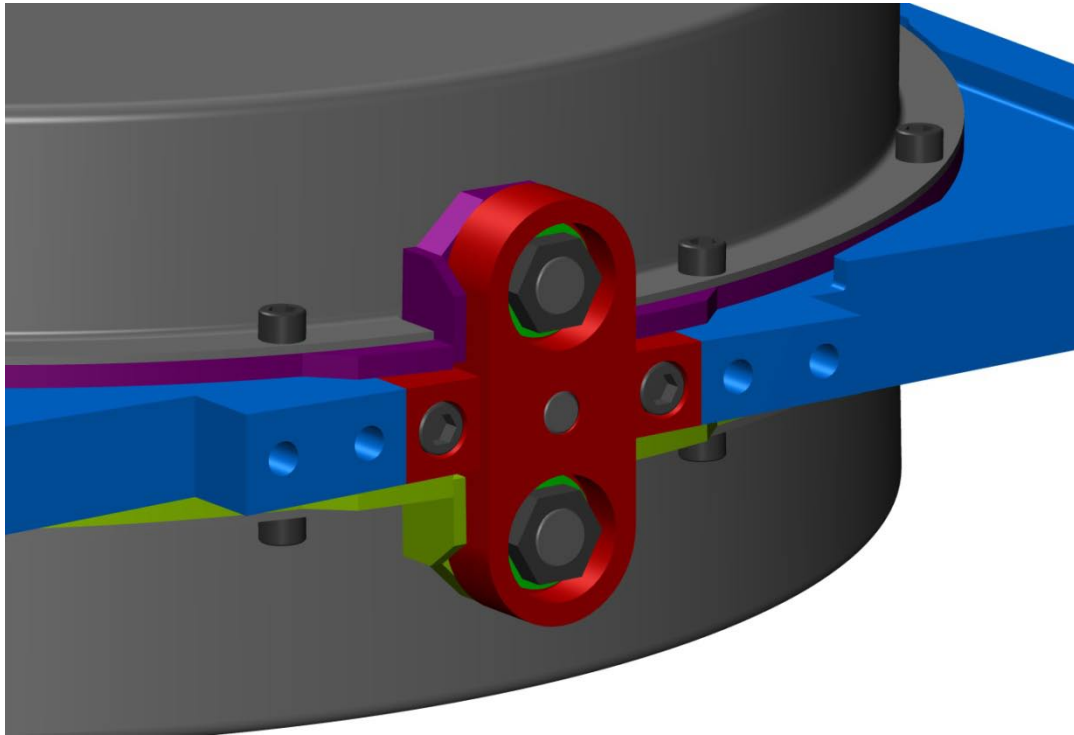


Figure 3-25: Detail of the joint allowing each coil to pivot around a fixed point.

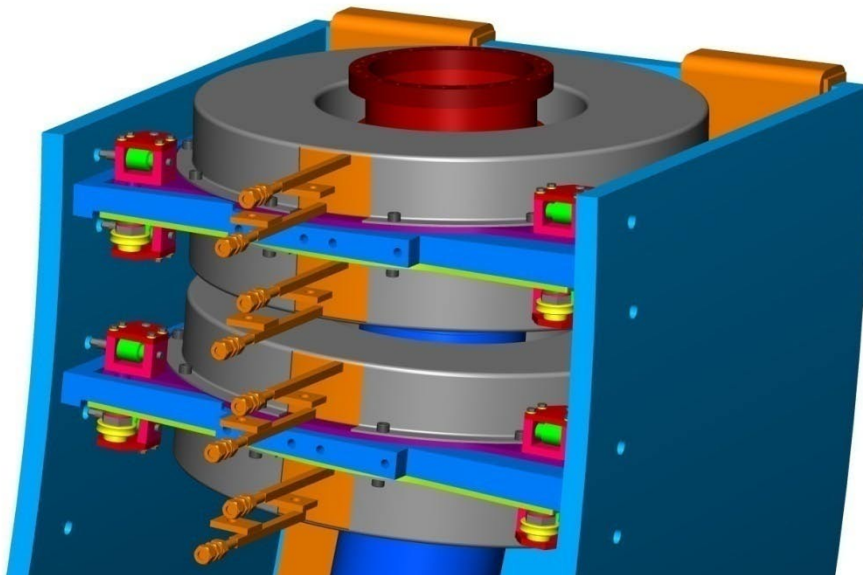


Figure 3-26: The end of a vertical bend with the cover plate removed showing two wedge-shaped support plates with coils attached.

3.5.2 Mounting

The vertical bends will be mounted below the high voltage tank. Lifting capabilities are limited in this area and special beams will be used to slide the bend modules into the correct position.

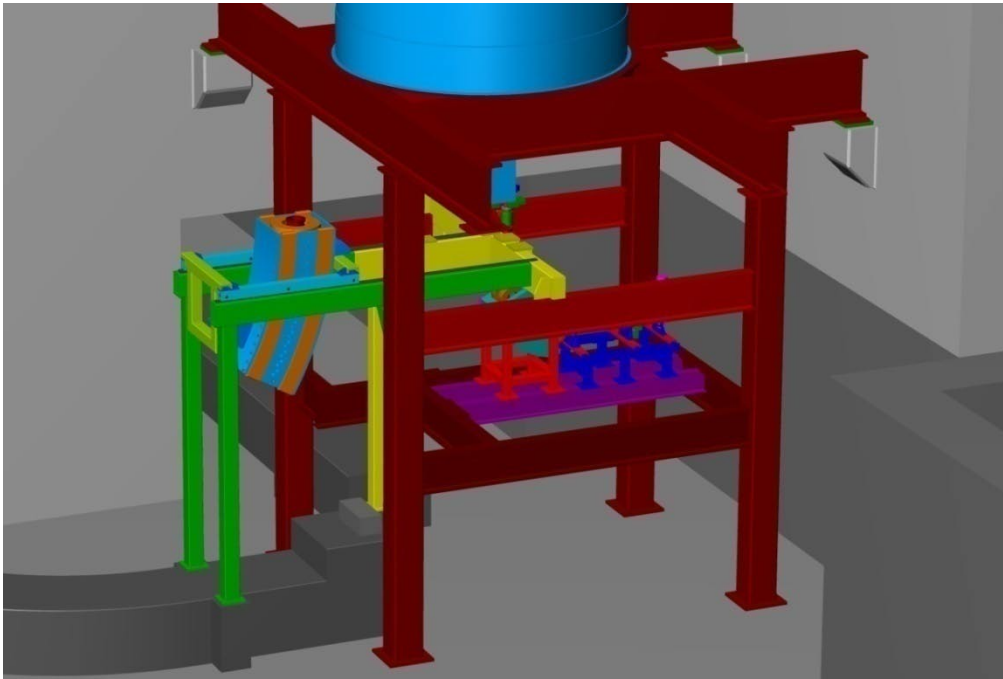


Figure 3-27: Mounting of first vertical bending module below high voltage tank.

3.6 Merging modules

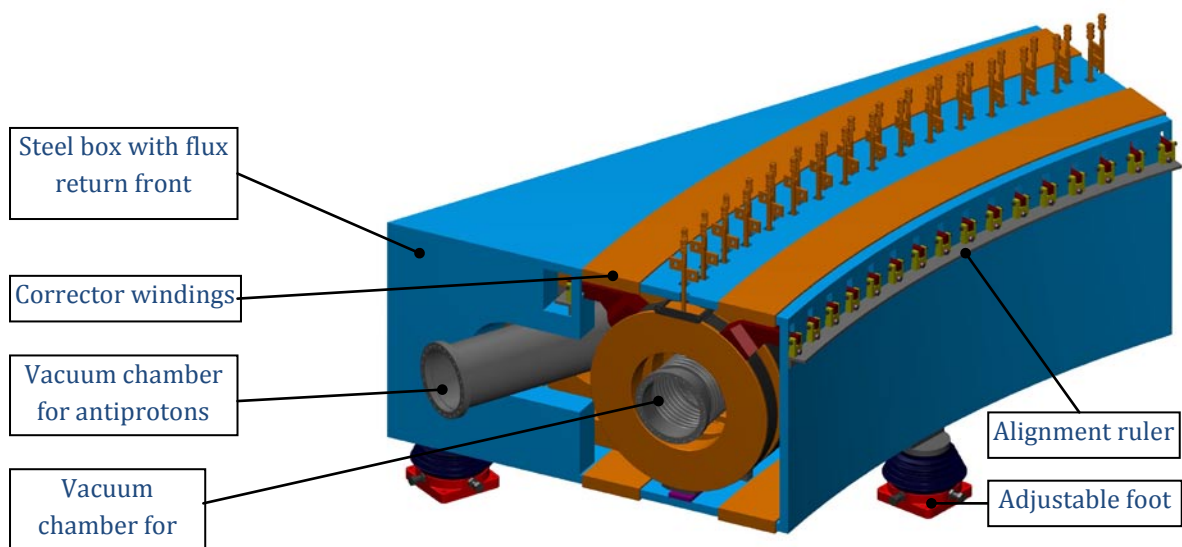


Figure 3-28: Merging module

The solenoids of the merging modules are made out of ordinary and racetrack-shaped pancakes. Five are circular, eight are racetrack-shaped with variable length and three solenoids are circular and racetrack-shaped in combination as shown in Figure 3-29.

In the merging modules the steel boxes guide excess flux, which is due to larger cross section of the racetrack shaped solenoids. To make the solenoidal field uniform along the electron reference path the current in each winding will be set individually. The current in each winding will be determined

not only by the main power supply but also by individual small floating power supplies, which will add or subtract from the main current. The drawback of this method is that around twenty small floating power supplies are required (An alternative method would be to modify the number of windings for each of the solenoids to even out the field). The process to determine the proper current for each pancake is similar to the field matching mentioned 3.4.1., and will be carried out simultaneously with that matching during commissioning of the modules.

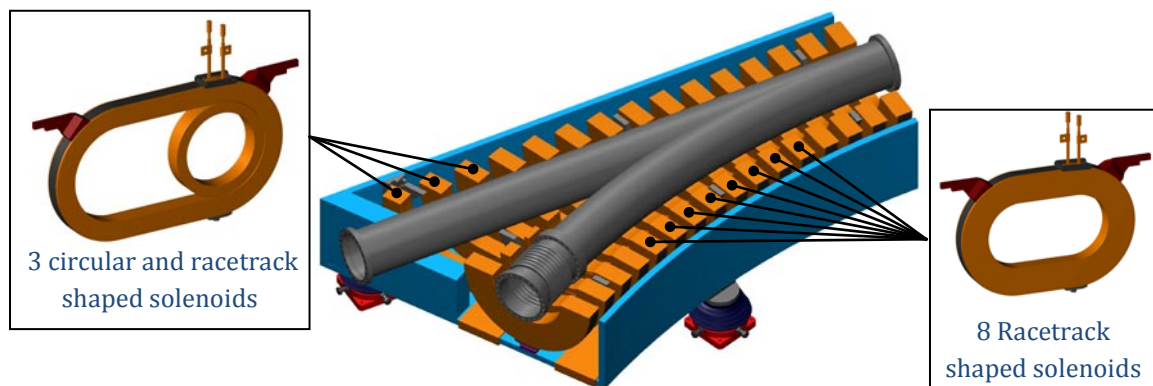


Figure 3-29: Solenoid of merging modules.

3.7 Transition

The transition between 0.07 T and 0.2 T takes place between the acceleration column and the first vertical bend. The transition back to 0.07 T takes place between the last vertical bend and the deceleration column.

The field transition can be made either resonant or adiabatic. We have chosen the adiabatic alternative since the energy of the electrons is variable from 0.45 to 4.5 MeV.

A perfectly adiabatic field transition for 4.5 MeV electrons would require a length of at least 5 m. If the transition is made shorter beam envelope oscillation will be created. However, a perfectly adiabatic transition makes no sense since considerable envelope oscillation has already been created in the accelerating column by the periodic variation of the electric and magnetic fields. The length of the semi-adiabatic field transition section is chosen to be 2 m. To minimize the vertical beam transport length the field transition starts already inside the HV tank.

3.7.1 Magnet flux return

The field transition section is surrounded by an iron yoke. The yoke needs a cross section large enough to carry the difference in magnetic flux between the high and low field side. The flux difference is $\Delta B \cdot A = (0.2 - 0.07)\pi 0.24^2 = 0.024 \text{ Tm}^2$.

A magnetic flux bridge, located below the tank exit, closes the magnetic flux between the cooling and the return beam lines, except the flux in the accelerating and decelerating columns. The iron flux bridge needs a cross-section large enough to carry the flux difference between the high and low field side which is 0.024 Tm^2 . The cross-section of this iron plate is 30 x 800 mm.

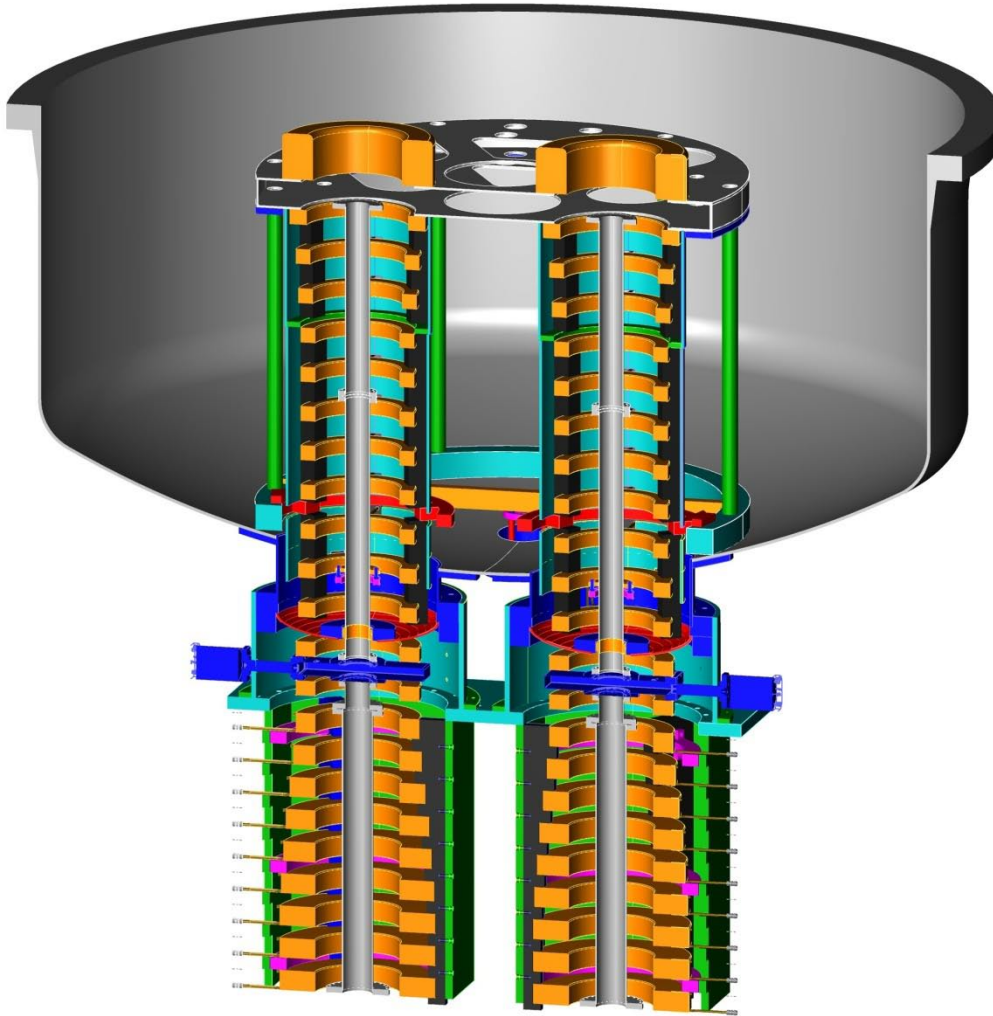


Figure 3-30: Magnetic system in the transition region. A cross section through the accelerating and decelerating beam pipes from the bottom separation box (shown in the upper part of the figure) to the beginning of the vertical bends.

3.7.2 Solenoids

The electron beam must exit the HV tank without excessive beam heating. Therefore a continuous magnetic field must be maintained during the tank exit. The outer radius of the coils in the tank exit is limited by the thick iron ring which supports the HV column to 0.23 m. A solenoid thickness of 0.06 m gives an inner radius of 0.17 m at the tank exit. The centre-to-centre distance between the solenoids is here chosen to be 0.158 m. The space between the last solenoid inside the tank and the first solenoid outside the tank is then ~ 90 mm, which is large enough for a dish shaped flange made of stainless steel. The flange must be un-magnetic in order not to disturb the magnetic field. The tank and the nozzles will however be made of ordinary magnetic steel.

The distance between the coils ~ 90 mm allows the insertion of a vacuum valve below the tank flange. The valve must be un-magnetic in order not to disturb the magnetic field.

The solenoids below the accelerating columns are at ground potential and will be water cooled. The coils are made of hollow copper conductors (10 x 10 mm). A summary of the coil parameters is given in Table 3-5 and Table 3-6.

Table 3-5: Solenoids inside tank below the accelerating column

Sol. no	z distance from cathode	Δz Coil length	R_{inner}	ΔR	NI ampere-turns	P power	Weight
16	4.432 m	0.060 m	0.205 m	0.070 m	9704 At	1.2 kW	59 kg
17	4.590	0.060	0.190	0.060	8847	0.8	37
18	4.748	0.060	0.180	0.060	8847	0.74	36
19	4.906	0.060	0.170	0.060	8847	0.7	34
20	5.064	0.060	0.170	0.060	8847	0.7	34
21	5.222	0.060	0.170	0.060	8847	0.7	34
22	5.380	0.060	0.170	0.060	8847	0.7	34
23	5.538	0.060	0.170	0.060	8847	0.7	34
24	5.696	0.060	0.170	0.060	8990	0.9	36
25	5.854	0.060	0.170	0.070	9133	0.9	37
26	6.012	0.060	0.170	0.070	9704	1.0	44

Table 3-6: Solenoids below tank exit and before first vertical bend

27	6.170 m	0.060 m	0.170 m	0.080 m	10703 At	1.1 kW	44 kg
28	6.328	0.060	0.170	0.080	11559	1.1	44
29	6.458	0.080	0.170	0.080	11844	0.9	55
30	6.588	0.080	0.170	0.090	13128	1.0	60
31	6.718	0.080	0.170	0.0105	14984	1.2	70
32	6.848	0.080	0.170	0.0120	16981	1.4	80
33	6.978	0.080	0.170	0.0130	18836	1.6	90
34	7.108	0.080	0.170	0.0140	20121	1.7	96
35	7.238	0.080	0.170	0.0145	20690	1.8	100
36	7.368	0.080	0.170	0.0145	20690	1.8	100
37	7.498	0.080	0.170	0.0145	20690	1.8	100

3.7.3 Coils for correction of envelope oscillations

In addition to the coils listed in Table 3-5 and Table 3-6 there are 3 coils below the accelerating column to correct for beam envelope oscillations created in the accelerating column. The method to reduce envelope oscillation is to kick the electrons radially by introducing a short bump in the magnetic field with correct amplitude and phase. Any of the solenoids in the tank or in the transition section can be used for elimination of envelope oscillation. However, the kick is most efficient if the characteristic length of the bump is short as compared to the cyclotron wavelength of the electrons. The characteristic length of the bump created by a short solenoid is proportional to the coil radius. Therefore the coil radius shall be as small as possible for efficient reduction of envelope oscillation at low beam energies. For this purpose 3 solenoids with small inner radius are mounted below the accelerating and decelerating columns. Control of envelope oscillation is necessary also in the deceleration column to optimize the collector efficiency. Therefore an identical set of correction coils is included also in the decelerating column.

Table 3-7: Coils for correction of envelope oscillations

Sol. no	z distance from cathode	Δz Coil length	R_{inner}	ΔR	NI ampere-turns	P power	Weight
38	4.432 m	0.060 m	0.130 m	0.060 m	10000 At	1.0 kW	25 kg
39	4.828	0.060	0.130	0.060	10000	1.0	25
40	5.302	0.080	0.130	0.060	10000	1.0	25

Simulation of elimination of beam envelope oscillation is described in section 7.6.

3.7.4 Magnetic field in the transition

The change of the electrons transversal temperature after a change of the longitudinal magnetic field from a low field B_1 to a high field B_2 over a given distance $z_2 - z_1$ depends strongly on the function $B_z(z)$ in the transition region. Simulations have shown that minimum increase of the equivalent transversal electron temperature is obtained if the magnetic field in the transition region is approximately given by

$$B_z(z) = B_1 + \Delta B \sin^2\left(\frac{\pi}{2} \varphi^2\right)$$

where $\varphi = \frac{z-z_1}{z_2-z_1}$ and $\Delta B = B_2 - B_1$.

The field in the transition section is generated by the coils listed in Table 3-5 and Table 3-6. The current in the solenoids have individual power supplies to generate the desired field. By using individual power supplies in the transition region it is also possible to change ration between the magnetic field in the acceleration tubes and the field in the cooler straight section.

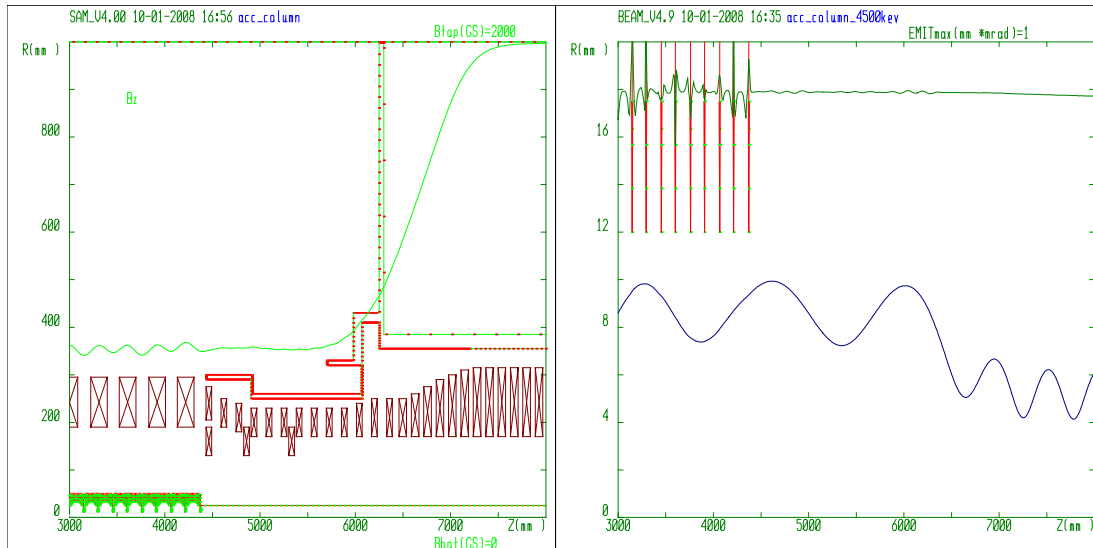


Figure 3-31: Magnetic field on axis (left) and beam envelope (right) in the transition region. z = distance from the cathode. Acceleration ends at $z = 4400$. Field transition takes place at $5200 < z < 7200$. The tank exit takes place at $z = 6100$. The bent solenoid starts at $z = 7500$. The envelope oscillation correction solenoids (the 3 solenoids with smaller radius) all have zero current in this simulation.

Simulation of the electron optics in the transition region is described in more detail in section 7.4.

3.7.5 Alignment

Any non-adiabatic change of the direction of the magnetic field will create dipole oscillations of the electron beam. To keep these oscillations at an acceptable level the angle between the magnetic field lines and the symmetry axis must everywhere be less than 10^{-4} radians. To achieve the desired straightness of the magnetic field the tilt of each coil needs to be adjustable. The straightness of the magnetic field has to be verified by magnetic field measurements before the vacuum tubes are installed.

3.8 Magnetic field measuring system

There will be two different magnetic field measurement systems in the electron cooler, one on the interaction straight section and another in the bending section prior to the interaction straight section. In the high voltage tank and in the transition section measurement of the magnetic field will be made during the assembly of these sections.

3.8.1 Interaction straight

3.8.1.1 Requirements

In section 2.1.3 the requirements on the longitudinal magnetic field in the cooling straight section are described. The most fundamental requirement is that of a field straightness of at least 10^{-5} radians. In order to have reasonable maintenance and service times, this accuracy requirement has to be complemented with a requirement to be able to perform the straightness measurements in the low pressure of the ring vacuum system.

3.8.1.2 Earlier experiences

Relevant experiences of straightness measurements have been obtained at Fermilab [21] and at BINP [22]. However the straightness requirements in Fermilab were only 10^{-4} radians and the measurements were performed in normal air pressure. The measurements at BINP had a

straightness accuracy of better than 10^{-5} radians for a 3 m long solenoid field. Also in this latter case the measurements were made at normal air pressure.

3.8.1.3 *The high resolution straightness measurement system.*

Based on the earlier experiences and the requirements the following measurement system, with principal design shown in Figure 3-32 is suggested:

- A BINP type of compass sensor with angle sensitivity better than 10^{-5} radians (Figure 3-33).
- The sensor mounted in a holder and with a magnet locking mechanism (Figure 3-34).
- Sensor in holder mounted in a trolley (Figure 3-35).
- The trolley is moveable along the vacuum pipe and is guided by ridges in the vacuum pipe. Such pipes can be made by extruding aluminium and with very high straightness. The trolley is capable to bridge gaps in the ridges introduced by beam position measurement and scraper units. This transport system is capable to keep the sensor within ± 2 mm from the nominal path (Figure 3-36).
- The trolley is drawn by chains made of titanium or nonmagnetic stainless steel (Figure 3-36).
- The sensor in its holder can be entered/extracted to/from the vacuum system through a vacuum lock (Figure 3-36).
- The trolley can be parked in a chamber so that it does not disturb the antiproton beam (Figure 3-36).
- A laser beam system for determination of the orientation of the compass sensor. The laser beam is centred on the quadrant detector by means of adjustments of the currents in the dipole correction windings. The current adjustments are proportional to the field direction errors (Figure 3-37).
- Initial laser beam setup is facilitated by means of pinhole orifices and moveable mirror and laser. These units have parking positions outside the antiproton beam path (Figure 3-37).

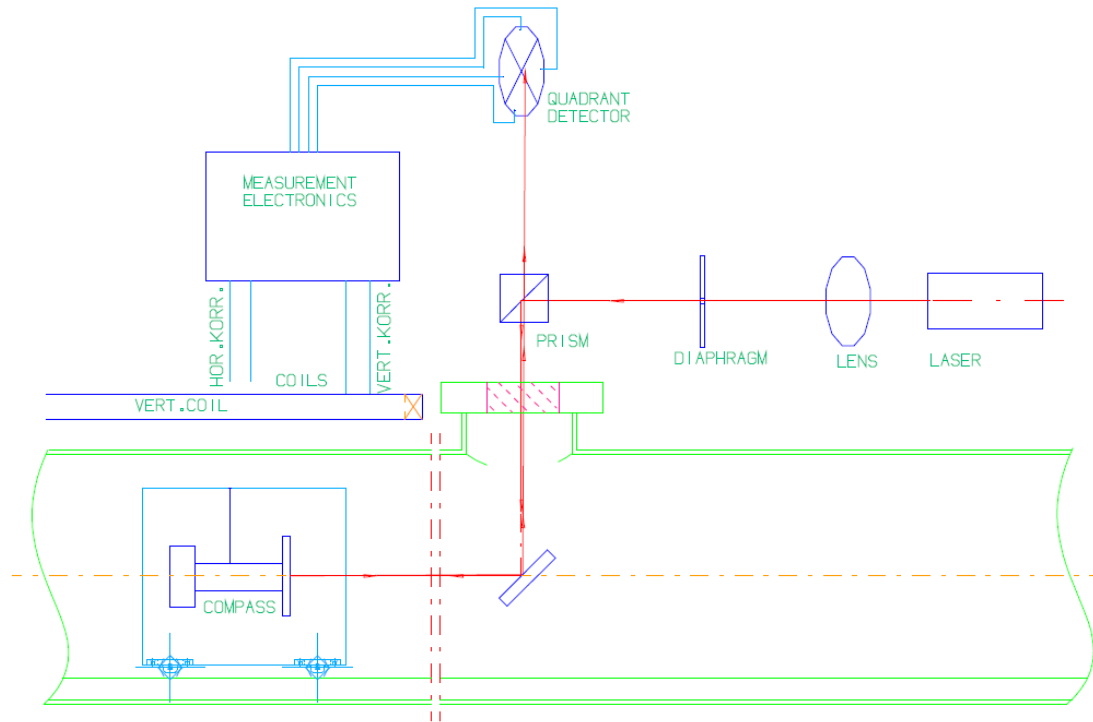


Figure 3-32: Principal design of the magnetic field straightness measurement system. The laser beam reflected in the compass sensor mirror will be kept centered on the quadrant detector by means of adjustments of the currents in the horizontal and vertical correction coils. These adjustments are proportional to the field direction errors.

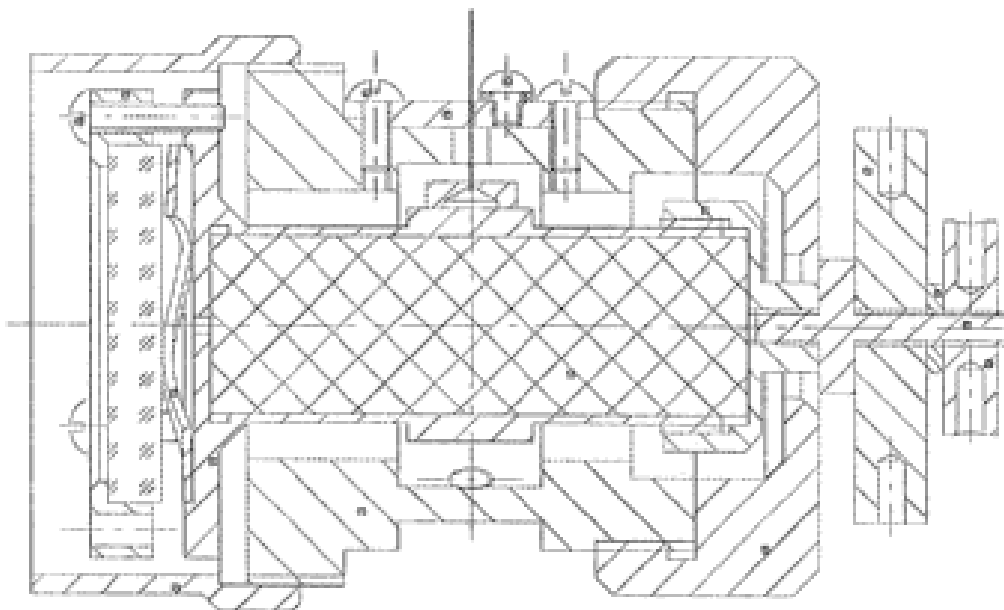


Figure 3-33: Mechanical drawing of the compass sensor in its protecting housing. The central body is the magnet with attached mirror to the left. To the right is a balancing counterweight. The suspending wire is clamped between the central top of the magnet and the housing above.

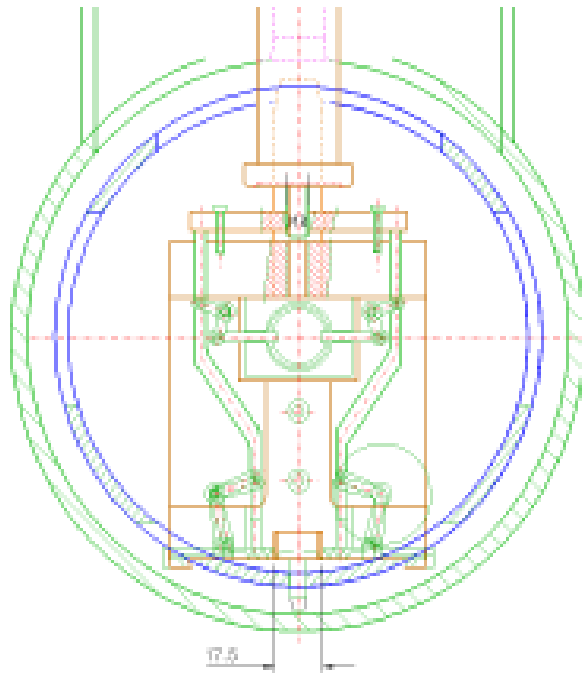


Figure 3-34: The sensor mounted in a holder with a magnet locking mechanism. The sensor and its holder are shown mounted in a trolley (blue in this figure).

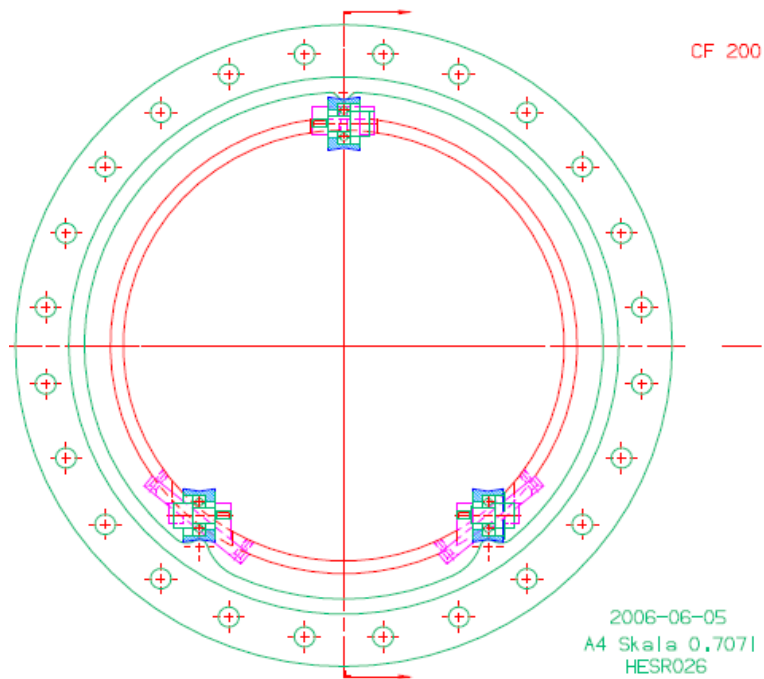


Figure 3-35: The trolley has a cylindrical shape (red in this figure), with wheels that roll on ridges at the inside of the vacuum pipe.

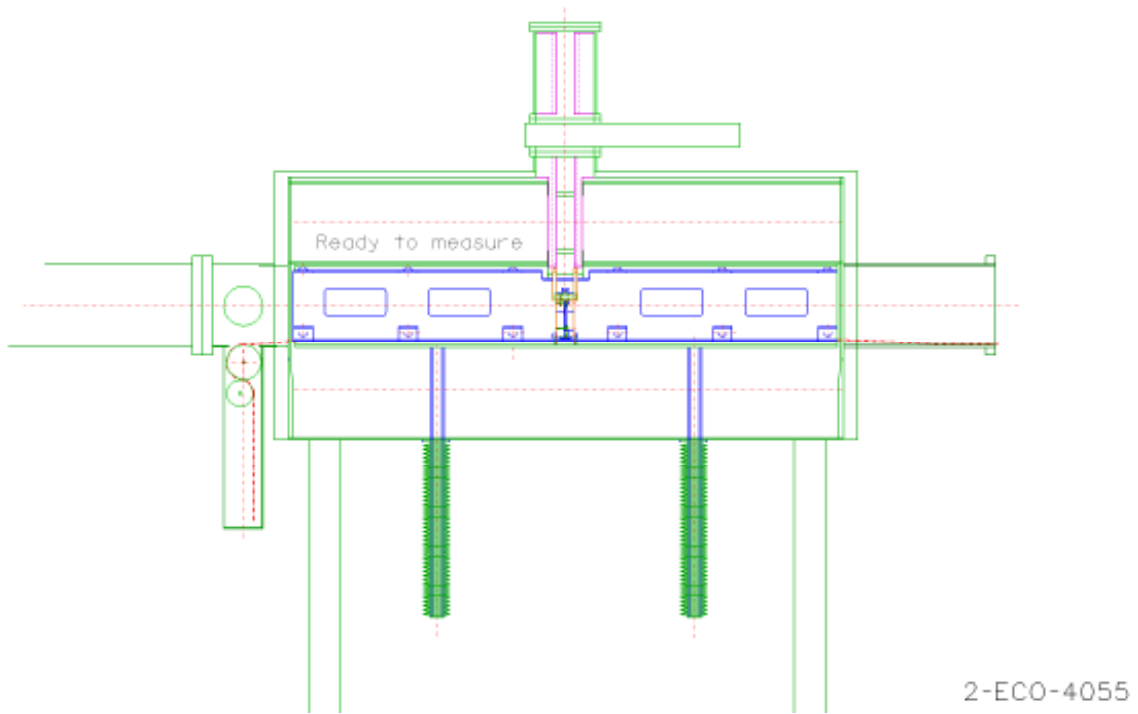


Figure 3-36: To the left is shown a chain drawing mechanism. The trolley (blue in this figure) with the sensor is in a measuring position. During normal operation of HESR it is lowered to the parking chamber below its present position after that the sensor has been extracted through the vacuum lock shown in the top of the figure.

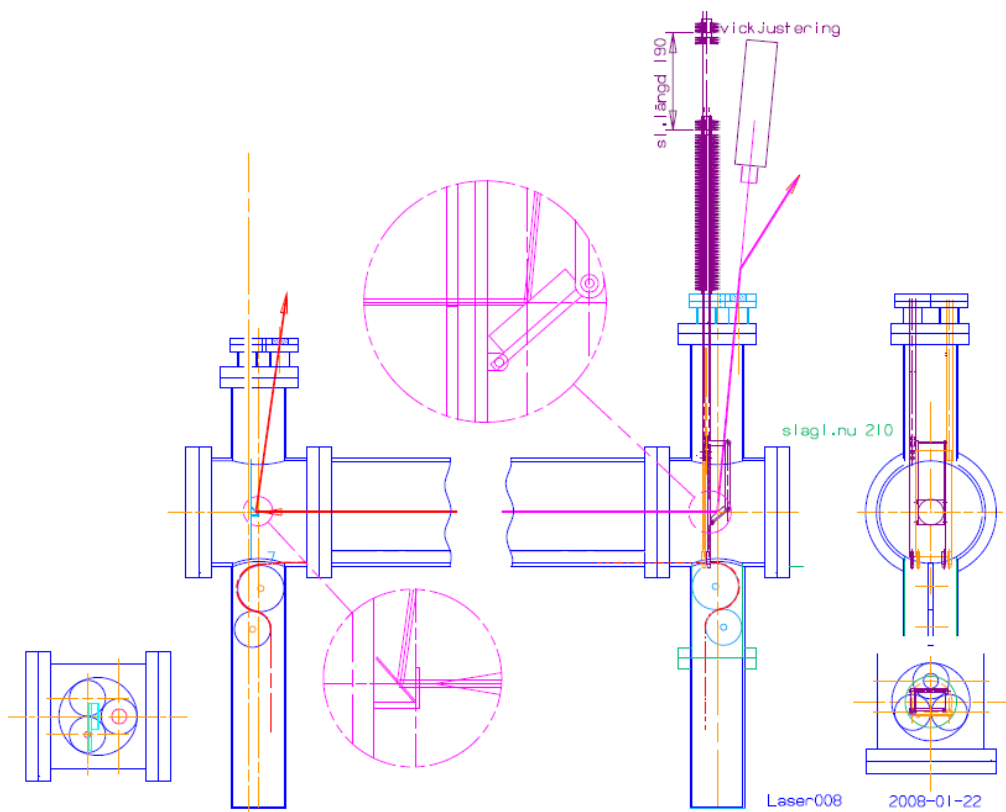


Figure 3-37: Drawing of the orifice and mirror system for initial setup of the laser beam.

3.8.2 Measurement system bends

In the bending section prior to the interaction straight section a system based on Hall-probe on rails will be used. With a Hall probe it is possible to reach a straightness of the magnetic field of 10^{-4} radians.

3.9 Electron beam diagnostics and correction

3.9.1 Electron beam diagnostics

It will be necessary to commission the electron beam diagnostics to establish a recirculating electron beam. At start a pulsed electron beam is used, and it will be necessary to measure its position along the beam transport system. Once recirculation is established, it will be necessary to measure the alignment of the electron beam to the antiproton beam most accurately in order to achieve the required alignment angle with precision corresponding to less than 10^{-5} radians. An even more challenging task will be to measure the envelope oscillation of the electron beam. Also it is necessary to accurately measure the coherent cyclotron motion of the beam.

The following list of different types of electron beam diagnostics elements is anticipated:

- Integrated Beam position monitor and scraper unit. 9 units.
- Beam position monitor. 6 units.
- Beam loss monitors. 20 units.
- Beam profile monitors: OTR, Optical Transition Radiation monitor. 2 units.
- H^0 detector. 1 Unit.

3.9.1.1 Integrated Beam position monitor and scraper

In the electron cooling straight section 9 pairs of beam position monitors, horizontal and vertical, are foreseen. Due to space limitation each position monitor has to be integrated with a scraper. The space limitation is implied by the magnetic field measurement system explained in Section 3.8

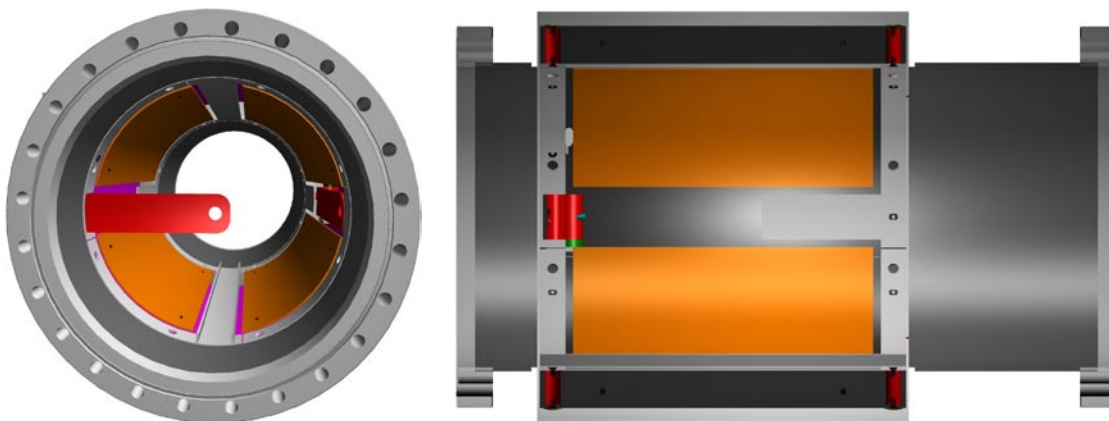


Figure 3-38: Position monitor and Scraper. One scraper (in red) is folded in to the vacuum chamber center.

The position monitor consists of 4 electrodes that together form a cylinder, see Figure 3-38. The radius of the electrode cylinder is 100 mm. The radius of the cylinder behind the electrodes in the position monitors is 125 mm. This cylinder is kept at ground potential. The length of the electrode is 200 mm. The radius of the vacuum chamber at the position monitor is 134 mm. The radius elsewhere of the vacuum chamber is 100 mm.

In between the electrodes there are four plates that are at ground potential, Figure 3-39. Two of these plates are used as scrapers, the two plates positioned to the right and to the left of the vacuum chamber centre. These two plates are possible to fold in towards the centre of the vacuum chamber. At the end of each of these plates there is a small orifice, with a diameter of 14 mm. The electron beam will pass through this orifice. When the scraper plates are folded into the beam centre the unit acts as a scraper, and when the scraper plates are in their parking position, the unit acts as a position monitor. The scraper will mainly be used to measure the envelope oscillation of the electron beam. The position resolution is ± 0.01 mm or better.

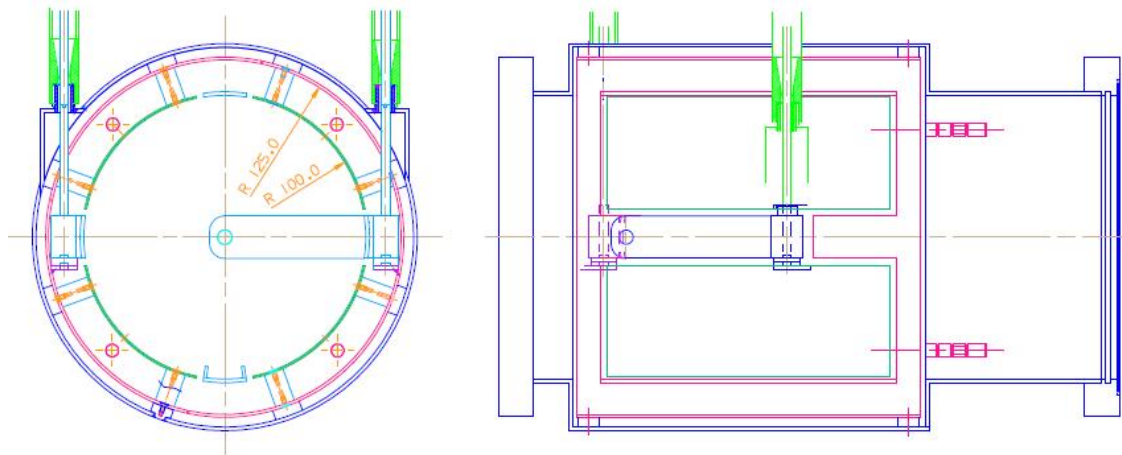


Figure 3-39: Drawing of beam position monitor and scraper

3.9.1.2 *Beam position monitor*

Outside of the cooling straight section there will be beam position monitors that are identical to the above described integrated monitor, except that these do not have any scrapers. There will be four on the return straight section, one at the exit of the high voltage tank and one before the entrance of the high voltage tank. The position resolution is ± 0.01 mm or better.

3.9.1.3 *Beam loss monitor*

The beam loss monitor is a silicon-based photodiode detector used to detect when the electron beam starts to hit the scraper. At high electron energies, above 0.5 MeV, the sensitivity is determined by the background radiation and is expected to be better than 10 nA. At lower energies the sensitivity will be less. The photodiodes will be placed after the scraper outside of the vacuum tubes. The photodiode detector is small enough to be placed inside of the solenoids.

3.9.1.4 *Beam profile monitor*

Optical transition radiation monitors makes use of the radiation emitted when a charged particle beam passes through the interface of two media with different dielectric constants, like vacuum and a metal sheet. The beam images generated this way are transported with the help of mirrors and lenses, and acquired with a CCD-camera. The OTR screens will be used to measure both position and emittance of the beam. The spatial resolution is better than 100 μm .

3.9.1.5 *H⁰ detector*

Downstream of the electron cooler there will be an H⁰-detector placed after the first bending magnet in bending section after the electron cooler. The detector measures the count rate of H⁰

atoms, which are produced during electron cooling of protons. A bending magnet is needed to separate the H^0 beam from the proton beam.

With the help of the H^0 monitor the electron and proton energies are made to match by maximizing the H^0 -rate. Also with the help of the H^0 monitor the position and the angle of the electron beam will be fine tuned. Finally the dipole and envelope oscillations of the electron beam will be reduced even further.

3.9.2 Diagnostics of envelope oscillations

Envelope oscillations will be measured with a set of scrapers, each with a circular orifice, see Figure 3-40, together with a set of beam position monitors and beam loss monitors. After the beam has been centred in the vacuum chamber, with the help of the beam position monitors, one scraper is folded in to the centre of the vacuum chamber. The beam is then also centred in the orifice of that scraper. Then the beam is moved in one direction until the beam loss monitor detects that the beam has hit the edge of the scraper.

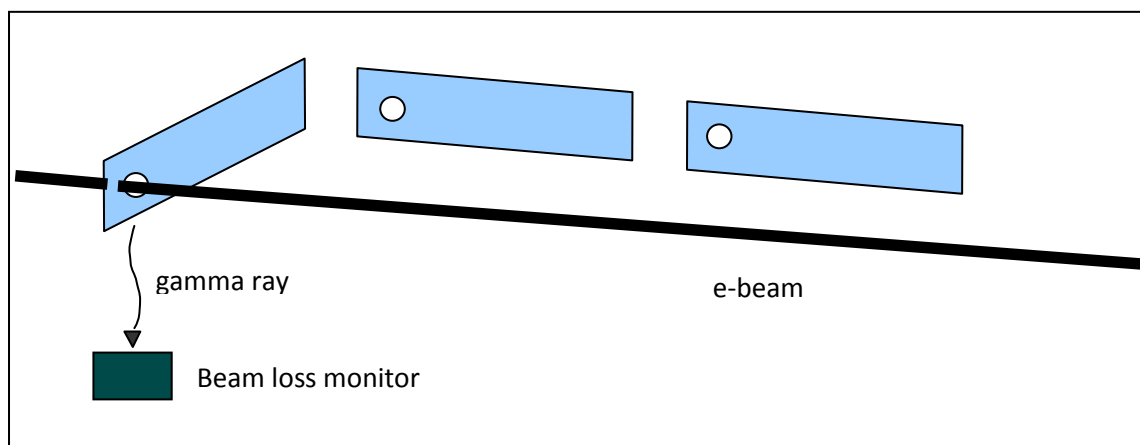


Figure 3-40: Electron beam and scrapers. One scraper is folded into the beam

By repeating the procedure in several directions, up, down, left, right, and in the four diagonal directions, the dimension of the beam at this position can be measured, see Figure 3-41.

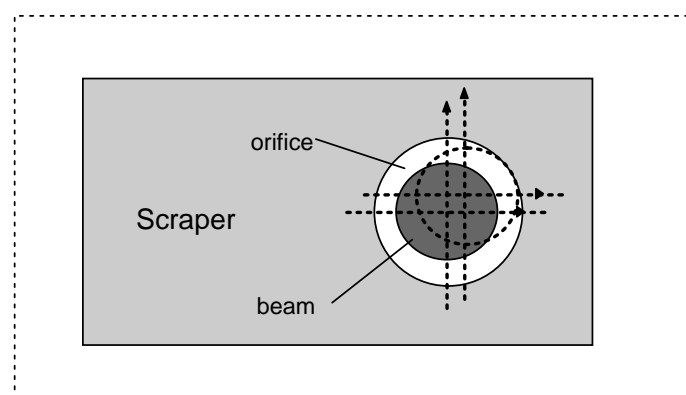


Figure 3-41: Moving the beam diagonally, up and to the right, until the beam hits the edge of the orifice.

By doing the same measurements at several scrapers, and comparing the dimensions of the beam at the different locations, the envelope oscillation of the beam can be calculated.

Once the envelope oscillation has been detected, the field in a correction magnet is changed until the envelope oscillation is minimised. There are also three solenoids with extra small diameter located inside the high-voltage tank that will be used to quench the envelope oscillations.

This method has been used at FNAL and the resolution and reproducibility of the procedure is at the level of 0.05 mm.

3.9.3 System to detect and quench beam dipole oscillations

The coherent dipole oscillation of the electron beam is measured with the beam position monitors on the cooling straight section. The resolution of this measurement of the dipole oscillation is 0.1 mm. The coherent dipole oscillation of the electron beam is reduced by changing the current in the three dipole coils in the first 90 deg bending section. Remaining dipole oscillations will be reduced with four un-adiabatic dipole magnets in the beginning of the cooling straight section.

3.9.4 Beam based alignment

To reach the necessary field quality beam-based alignment will be applied.

After the electrons have been adjusted to within 20 μm on all pick-ups, and envelope oscillations and dipole oscillations have been minimized, anti protons will be put into the ring. Then the anti proton beam's position on the two outermost pick-ups in the cooling straight section is adjusted so that the anti proton beam is centred within 20 μm in these pick-ups. Then the electron beam position is adjusted with the dipole correction coils, so that it coincides with the position of the (anti) proton beam within 20 μm on all pick-ups. This will make the magnetic field straight within 1×10^{-5} and the electron and antiproton beams centred in the solenoid within a fraction of a millimetre.

3.10 Vacuum system

3.10.1 Pumping of acceleration/deceleration tubes

The only type of pump which is feasible to use inside the pressure vessel is the ion pump. In the layout there is one 50 l/s ion pump mounted sideways close to the gun and one close to the collector. Additional 50 l/s ion pumps at the gun and the collector are planned. 30 l/s pumps are placed 2.2 m from the gun and collector, respectively. These pumps have to be of a special reinforced design to withstand the outer pressure in the tank.

The minimum diameter of the acceleration tube holes is 25.4 mm and the conductance has been measured by the manufacturer to be 15 l/s per 610 mm long 1 MV segment. This is well matched with the 30 l/s pumping speed of the intermediate 30 l/s ion pumps. We refer to measurements in the FNAL electron cooler, where the pressure in the ground end of the acceleration beam tube is $3 \cdot 10^{-10}$ mbar without electron beam and $4 \cdot 10^{-10}$ mbar with 0.5 A beam. At the corresponding position on the collector side the pressure is $4 \cdot 10^{-10}$ mbar without electron beam and $1.1 \cdot 10^{-9}$ mbar with 0.5 A beam.

4 How to achieve electron cooling

4.1.1 Commissioning of the electron beam and alignment of the electron and proton and antiproton beams

After the magnetic field has been measured and corrected and the high voltage has been conditioned, the electron and (anti) proton beams will be aligned.

First, the electron beam needs to be transported around the system. This is to begin with done with a pulsed electron beam of modest voltage. The position of this pulsed electron beam is observed with the pick-up electrodes and the electron beam profile monitors. When this beam has been brought all around the system and into the collector, and reasonable collection efficiency has been established, then a continuous electron beam, still with a modest voltage, shall be transported around the system. This is first done with very small electron beam intensity, so that high collector inefficiency is acceptable. Then the electron beam current is increased, and collection efficiency is optimized. Also, the electron beam voltage is increased successively.

The position of the electron beam in the straight sections is adjusted by changing the current in the dipole magnets on the bending sections before the straight section in question. This is done so that the electron beam is well centered in the pick-up electrodes.

If needed the position of the electron beam is also adjusted by use of the dipole correction coils in the straight sections.

Then the coherent cyclotron oscillations are measured with the beam position monitors and then minimized by changing the strength of the dipole fields in the entrance bend. Remaining coherent cyclotron oscillations are minimized further by use of the non-adiabatic dipole correction coils in the beginning of the cooling straight section. After that, the envelope oscillations of the electron beam are measured with all the scrapers on the cooling straight section by moving the electron beam up, right, down, left and in the four diagonal directions about 3 mm in each direction, and by doing this measurement with several slightly different magnetic fields on the cooling straight section. The envelope oscillations are minimized by changing the strength of the dipole fields in the three different 30°-parts of the entrance bend and by changing the strength of the “envelope oscillation correction solenoids” located in the high voltage column. After the (anti) proton beam is put in the ring, its position on the two outermost pick-ups in the cooling straight section is adjusted so that the (anti) proton beam is centered within 1 mm in these pick-ups. Then the electron beam position is adjusted with the dipole correction coils, so that it coincides with the position of the (anti) proton beam within 20 μm on all pick-ups. This will make the magnetic field straight within 1×10^{-5} and the electron and (anti) proton beams centered in the solenoid within a fraction of a millimeter. The electron and proton energies are made to match by maximizing the H^0 -rate. Coherent cyclotron motion in the electron beam is minimized by further adjustments of the dipole fields in the three different 30°-parts of the entrance bend, and by the non-adiabatic dipole correction coils in the beginning of the cooling straight section.

After this alignment procedure the following criteria should be fulfilled:

- The magnetic field on the electron cooling straight section is straight within 1×10^{-5} radians r.m.s.
- The (anti) proton beam is made parallel or accurately tilted with respect to the direction of the straight magnetic field within 2×10^{-6} radians (50 μm over 24 m).

- The coherent oscillation, or cyclotron motion, of the electron beam as a whole is less than what corresponds to a cyclotron radius of 50 μm , which also corresponds to about 10 eV.
- The envelope oscillation of the electron beam is less than what corresponds to a cyclotron radius of 100 μm (35 eV).

5 SERVICES

5.1 Control system

A control system for the pelletron is included in the delivery from the manufacturer. This includes extra channels for users equipment such as HV-solenoids, gun and collector electronics.

The control system for the electron cooler will follow the FAIR standard and will include interface to the main control system.

5.2 Water cooling demands

Pelletron	90 kW	120 l/min,	$\Delta P = 5 \text{ bar}$, $\Delta T = 5 \text{ }^\circ\text{C}$, $T_{\text{in}} = 15 \text{ }^\circ\text{C}$
Cooler hall	1,2 MW	1700 l/min	$\Delta P = 5 \text{ bar}$, $\Delta T = 10 \text{ }^\circ\text{C}$, $T_{\text{in}} = 15 \text{ }^\circ\text{C}$
Power supplies	64 kW	20 l/min,	$\Delta P = 5 \text{ bar}$, $\Delta T = 5 \text{ }^\circ\text{C}$, $T_{\text{in}} = 15 \text{ }^\circ\text{C}$
Analyzing magnet	1 kW	5 l/min	

5.3 Electricity

	Input	power	fuse	
Pelletron	3 x 380 V	90 kVA		
SF6 system	3 x 380 V	30 kVA		
Power supply room	3 x 480 V	1,2 MVA	3 x 630 A	3 groups
	3 x 480 V		3 x 16 A	2 groups
	3 x 220 V		3 x 10 A	8 groups

5.4 Temperature stabilization

The requirements on temperature stabilization are

	Temperature	Power to air
Pelletron tower	20 $^\circ\text{C}$ +/- 1 $^\circ\text{C}$	40 kW
Cooler hall	20 $^\circ\text{C}$ +/- 1 $^\circ\text{C}$	30 kW
Analyzing magnet	20 $^\circ\text{C}$ +/- 0.2 $^\circ\text{C}$	
Power supply room	20 $^\circ\text{C}$ +/- 2 $^\circ\text{C}$	30 kW

5.5 Compressed air

Compressed air is needed at the following locations:

Pelletron 5 bar 10 l/min

Pump stations 5 bar 10 l/min

5.6 Radiation protection

The walls of the pelletron tower shall be made of concrete up to at least the level of the high voltage terminal. The maximum radiation from the pelletron is calculated from a loss current of 20 μ A at 8 MeV.

5.7 Safety system SF6

A SF6 safety system is needed to protect personnel and vacuum systems in the case of a leak between the accelerator tank and the vacuum system. The SF6 safety system should include

- Bursting discs to protect the vacuum system from overpressure
- Fast closing valves
- Forced ventilation in critical areas, such as below pelletron, 1000 l/s
- Personal oxygen meters with alarm

Design of the SF6 safety system is not included in this study.

5.8 Building

The building required for the electron cooler includes a cooler hall, a pelletron tower and a hall for power supplies and control. The proposed building is designed for a 8 MeV high voltage tank.

5.8.1 Requirements on the cooler hall:

- 4 m space is needed between the cooler magnets and the walls.
- Possibility to lift down magnets modules with a weight of 6 tons.
- Stability of floor under cooler magnets must meet the requirements of magnetic field straightness.
- Roof height at least 4 m
- Free space is needed in the bends between the center of curvature and the magnets (no pillars).

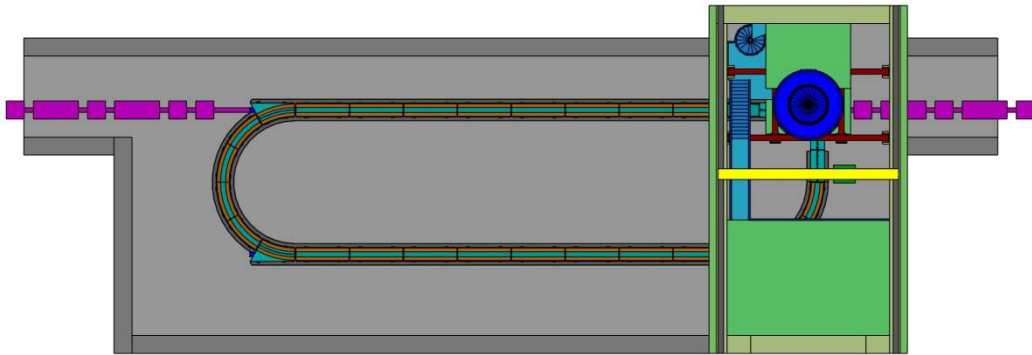


Figure 5-1: Building. View from above.

5.8.2 Requirements on the pelletron tower:

- The tower must have 9 x 12.5 m inside cross section for a 8 MeV high voltage tank. The extra 3.5 m in one direction is needed to lift and store the upper tank access door and to lift the components of the pelletron into the tank.
- Walls with radiation protection are needed up to the level of the high voltage terminal.
- A roof crane with a minimum capacity of 3 tons is needed to assemble the pelletron inside the tank. Minimum height of crane = 2 m above the upper tank flange, which corresponds to 22 m above floor level in the case of an 8 MeV tank.
- The roof has to be removed during installation of the tank. If possible, also one of the walls shall be removable (an opening of 6 m is needed to move in the tank)

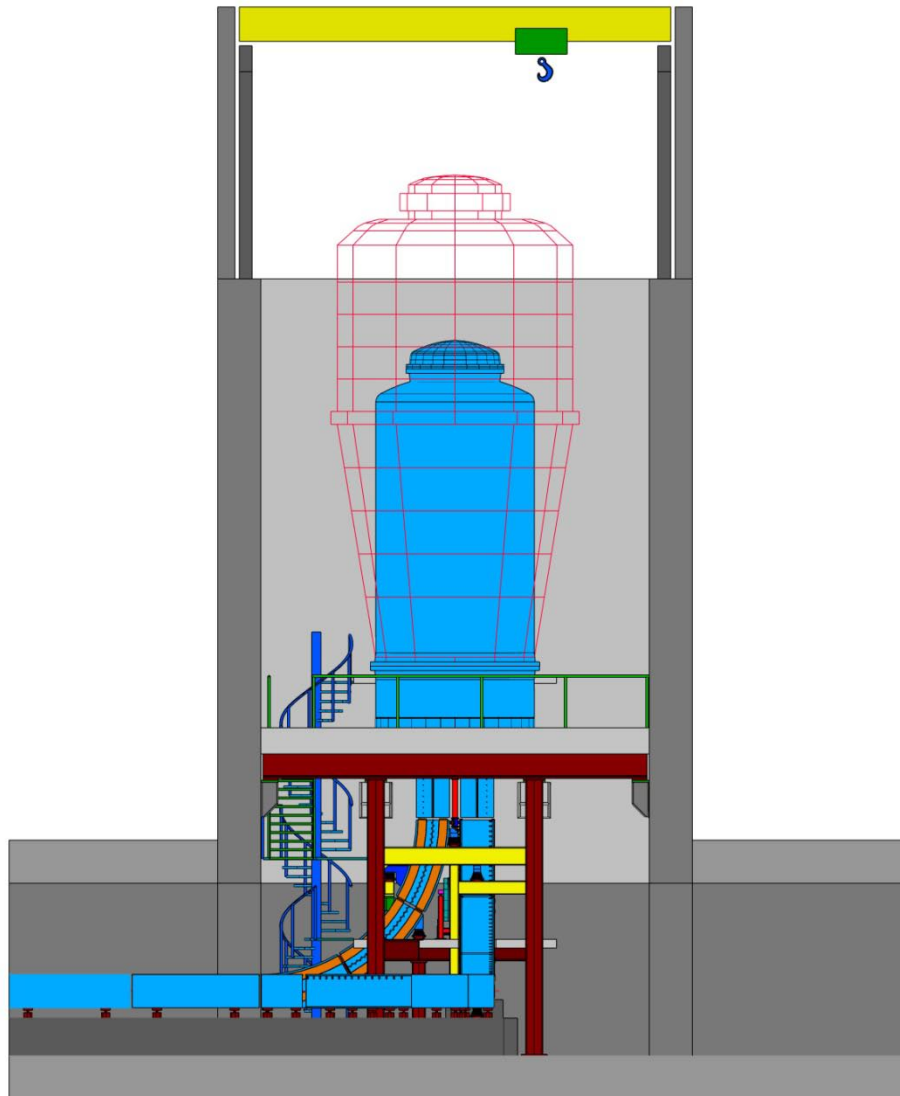


Figure 5-2 Pelletron tower, sideview.

5.8.3 Concrete sockets

The support of the cooler magnets must be stable enough to meet the requirement of magnetic field straightness. We have considered the use of a rigid concrete socket above floor level under the magnets. Another alternative is to make the reinforcement under floor level and to use steel supports under the magnet modules.

5.8.4 Tank support

The proposed tank support is made of steel beams. The floor under the support must stand a total weight of 185 tons.

high voltage tank including pelletron	130 tons
vertical magnets	30 tons
support	25 tons

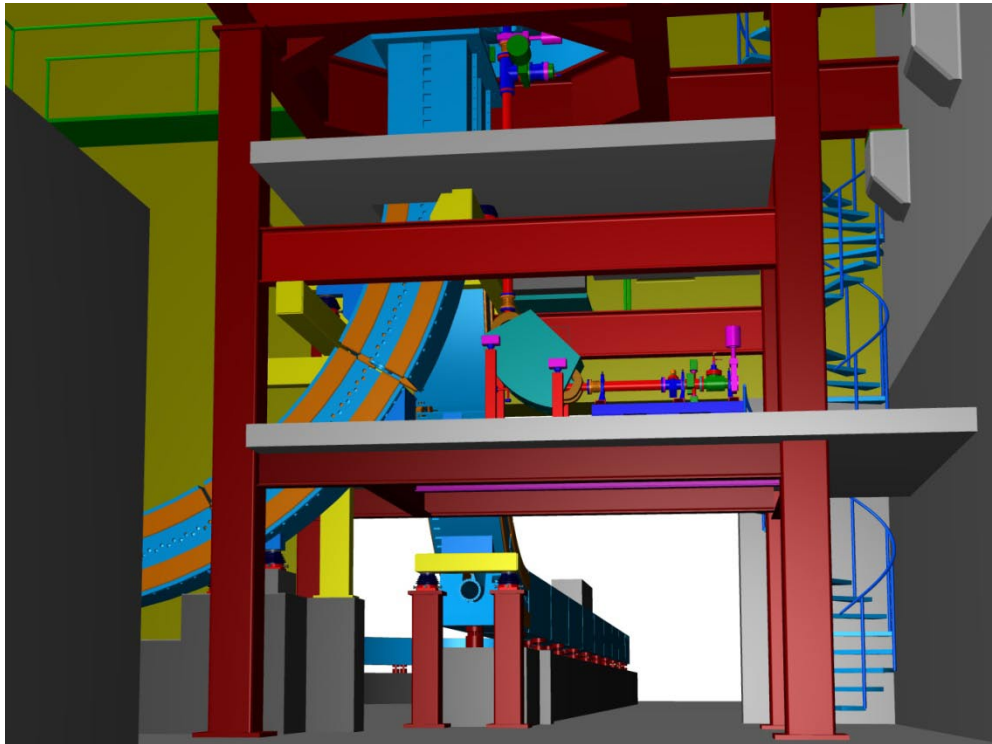


Figure 5-3: Tank support

5.8.5 Space for SF6 handling equipment

The SF6 recirculation system consists of a heat exchanger to cool the SF6 gas, a blower and a gas purification filter. It will be mounted in the pelletron tower close to the pelletron.

An additional gas handling plant is needed to evacuate air from the tank, fill the tank with SF6 gas, evacuate SF6 gas from the accelerator tank and transfer the gas to a separate storage tank. The gas handling plant for a 95 m³ accelerator tank (4.5 MeV) has the size:

- Dimensions of gas handling plant: length 3 m, width 2 m, height 2 m
- Storage tank: 2500 l /50 bar, length 3.5 m, width 1.3 m, height 1.3 m

5.8.6 Power supplies room

Power supplies will be placed in separate room close to the cooler hall. The total space needed for the power supplies is 100 m². A list of the electronics racks and power supplies is shown in Table 5-1.

Table 5-1: Power supplies sizes and services

Rack	Equipment	l [m]	Size		Input		Power to water [kW]	Power to air [kW]
			d [m]	h [m]	Electricity U [V]	Fuse [A]		
1	PS solenoids straight section	2.4	1.6	2	3 x 480	630	20	7
2	PS solenoids return section	2.4	1.6	2	3 x 480	630	20	7
3	PS solenoids bend	2.4	1.6	2	3 x 480	630	20	7

4	PS transition above flux bridge	0.6	0.6	2	3 x 480	16	2	1
5	PS transition above flux bridge	0.6	0.6	2	3 x 480	16	2	1
6	PS merging additional	1.2	0.6	2	3 x 220	10		2
7	PS straight corrector windings	0.6	0.6	2	3 x 220	10		0.1
7	PS oscillation correction	0.6	0.6	2	3 x 220	10		1
8	PS bend dipole correction	1.2	0.6	2	3 x 220	10		0.7
9	Diagnostics	1.2	0.6	2	3 x 220	10		0.5
10	Vacuum pumps	1.2	0.6	2	3 x 220	10		0.5
11	Control system	1.2	0.6	2	3 x 220	10		0.5
12	Control desk	2	1	1	3 x 220	10		0.5
	Total	17.6					64	28.8

6 PROTOTYPE TESTS

6.1 Magnetic field measuring system

6.1.1 The prototype test setup

In section 3.8 it is described that we have chosen to use a measurement equipment for the measurements of the straightness of the magnetic field in the cooling straight section based on a sensor principally consisting of a compass rod suspended in a wire. The direction of the rod is measured by observing a collimated laser beam being reflected in a mirror attached to the compass rod.

It was decided to evaluate this measurement principle with a prototype sensor. A sensor with a NdFeB magnet rod was ordered from BINP according to the drawings in Figure 6-1.



Figure 6-2: Sensor in holder



Figure 6-3: Trolley for the sensor

Vacuum pipes, with guiding ridges for the trolley, were made by an extrusion technique, see Figure 6-4.

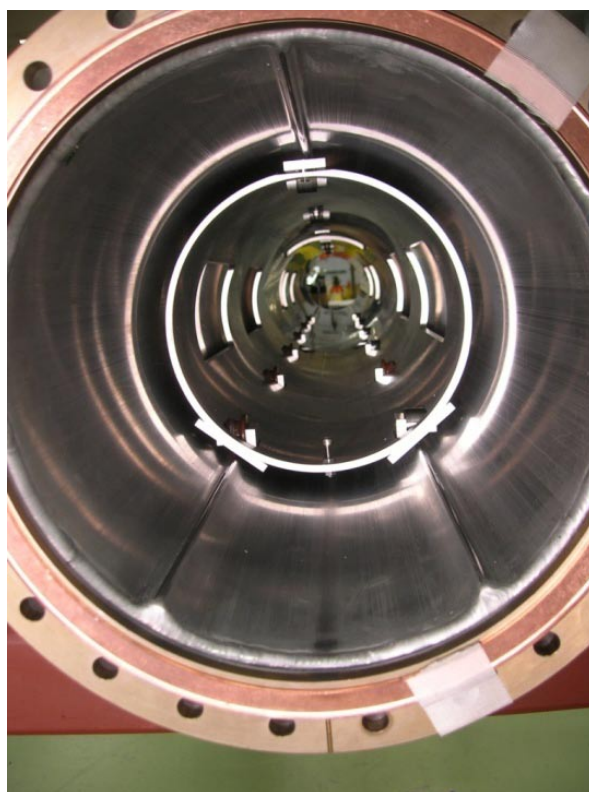


Figure 6-4: End view of vacuum pipe with guiding ridges for the trolley

A laser beam system with a quadrant detector was bought from Thorlabs Inc., see Figure 6-5.



Figure 6-5: Adjustment of the laser system

The position resolution of this detector is better than $4\ \mu\text{m}$. A spare solenoid was used to generate a 0.2 T field, see Figure 6-6. Additional coils were mounted in the solenoid in order to generate transverse horizontal and vertical field modifications.



Figure 6-6: To the right in the figure, a setup for test of the sensor sensitivity. To the left and in the middle in the figure a setup for test of trolley movements. The trolley should be capable to bridge gaps in the ridges introduced by beam position measurement and scraper units. The trolley is drawn by a chain

The suspending wire was damaged in the transport from Novosibirsk to Uppsala. The broken wire was replaced by a 50 μm Tungsten wire. New adjustments of the torsion of the wire and of the mechanical balance had to be done. These adjustments were conveniently done in a Helmholtz coil system, see Figure 6-7, which could reduce disturbing magnetic fields to below the 10^{-8} T level.



Figure 6-7: Helmholtz coil system

For the tests the sensor was placed in the center of the solenoid. At a distance of 5.8 m the laser beam system was mounted on an optical bench. The complete test setup was placed on the floor of the former CELSIUS ring, a very ridged concrete floor.

The laser beam was collimated and focused to a parallel beam with a circular cross-section. The diameter of the beam was 5 mm just before the detector. A lens in front of the detector reduced the beam diameter on the detector about a factor of 2. A test was also made of the ability of the laser system to focus the beam on longer distances. At a distance of 27 m the beam could be focused to a diameter of about 8 mm.

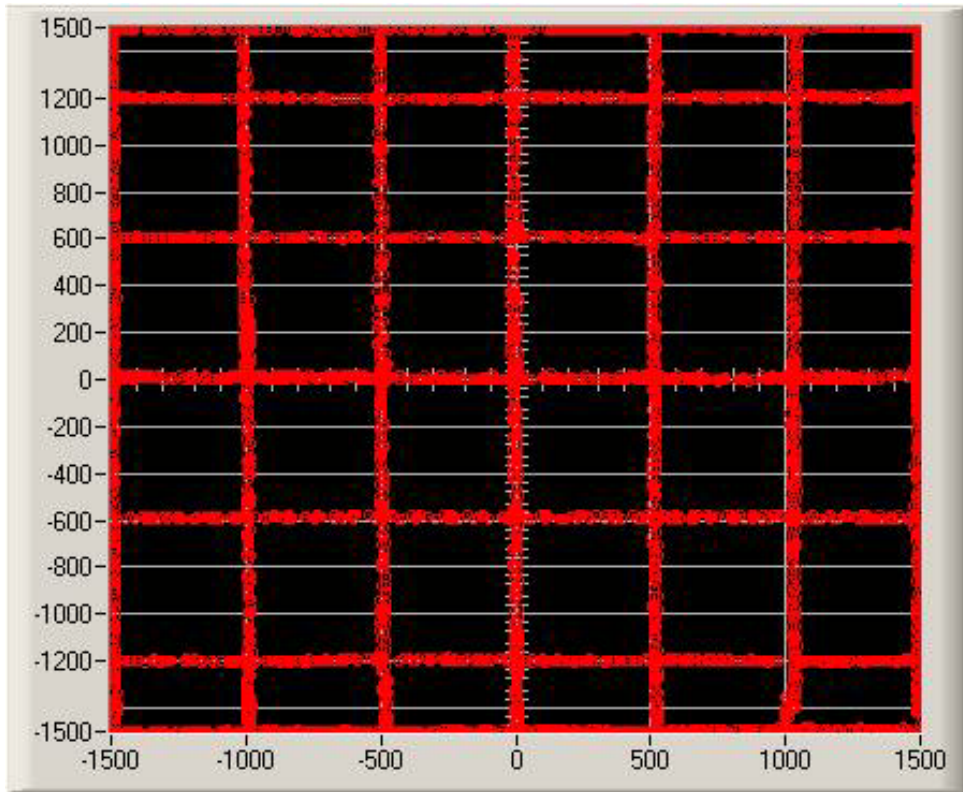


Figure 6-8: Stored position information in the Thorlabs system from a test of the quadrant detector (The laser beam was moved linearly across the detector in orthogonal directions).

The beam positioning system from Thorlabs displayed position information on a computer screen, see Figure 6-8.

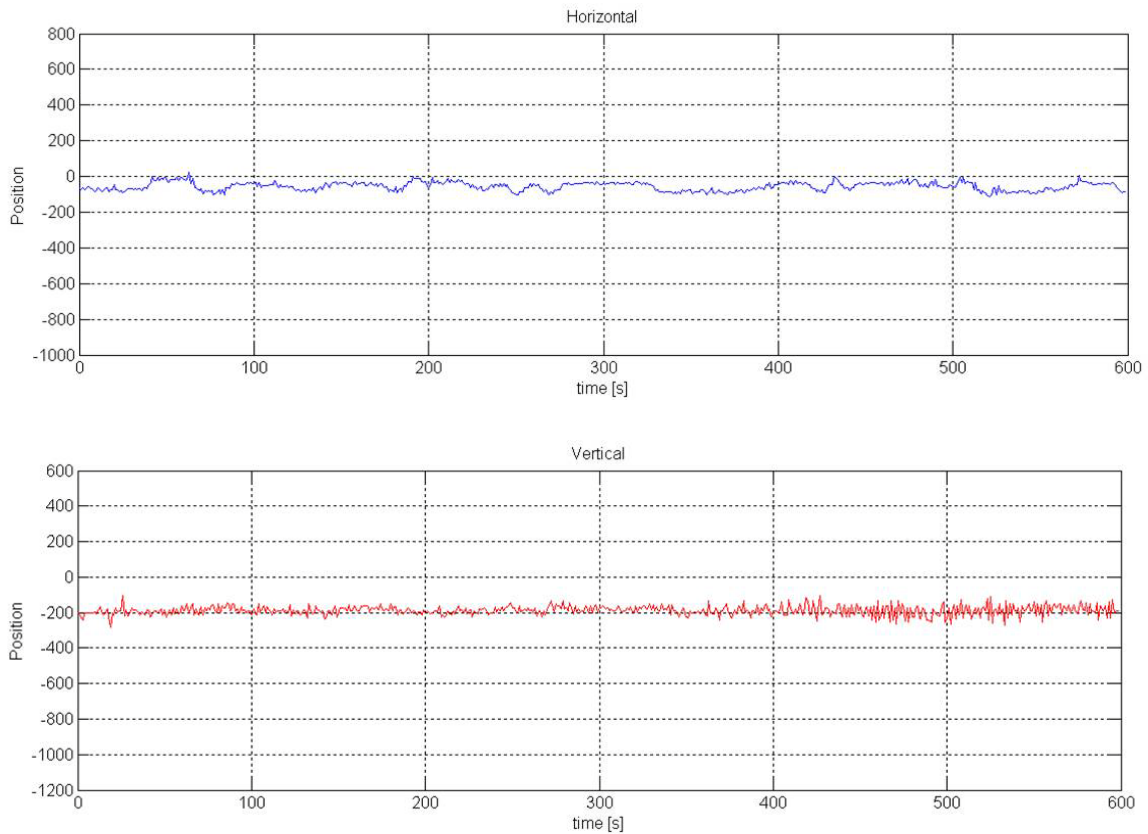


Figure 6-9: Typical recording of laser beam position variations on the quadrant detector with a sampling rate of 1Hz.

It could also record position values with a maximum sampling rate of 1 Hz. A typical recording is shown in Figure 6-9. The variations seen in this recording are mainly due to disturbances in the external “geomagnetic field”.

6.1.2 Determination of the sensitivity of the measurement system

The sensitivity of the measurement system was determined by recording of beam positions, in scale units of the Thorlabs system, as a function of current in the additional coils in the solenoid. The solenoid field was 0.2 T. The result is:

- Horizontal plane: 0.13 ± 0.02 scale units/mA
- Vertical plane: 0.13 ± 0.02 scale units/mA

The additional coils are designed to generate a field B given by:

- $B = 6.10^{-6}$ T/A

Thus the sensitivity is: 4 scale units/ μ radian.

The required sensitivity is 10^{-5} radians which corresponds to 40 scale units. Thus the sensitivity requirement is fulfilled.

6.1.3 Noise of the measurement system

It is also needed that the sensitivity requirement of 40 scale units is observable in the noise of the measurement system. In the test system there are noise sources as listed below:

1. Variations in the external “geomagnetic” field, to a large extent generated by neighbouring vehicle traffic.
2. Vibrations in the floor and the solenoid, mainly generated by direct mechanical coupling between the power supply and the solenoid and by turbulence in the cooling water for the solenoid.
3. The lighting of the test area gave a background signal in the detector with strong 50 and 100 Hz components.
4. Turbulence in the air which the laser beam passed.
5. Noise in the generation and detection of the laser beam.

RMS values of the noise in the recordings of the type shown in Figure 6-10 were calculated. The result is 20 ± 5 scale units, thus showing that variations on the order of 10^{-5} radiana are well observable above the noise in our test setup. Moreover, most of the noise from sources of types 1 to 4 ought to be strongly reduced in HESR. A recording with a mechanically locked sensor rod gave an RMS noise value of 10 ± 1 in scale units. This shows that the main noise source in the test was due to external field variations.

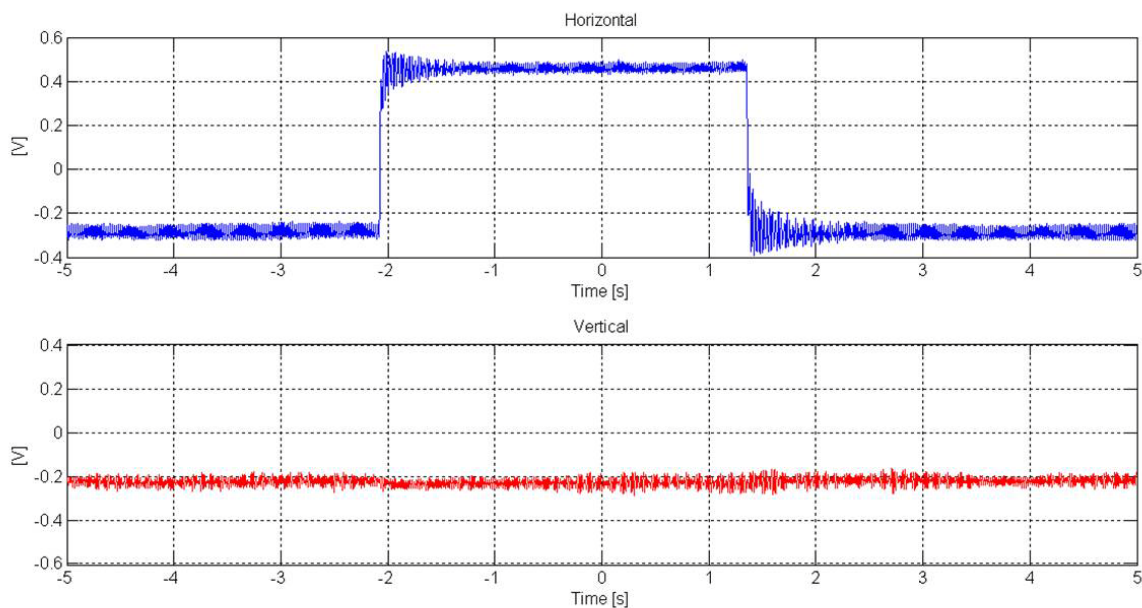


Figure 6-10: Recording of position detector signals during a stepwise change of the transverse magnetic field at the sensor. The recording was made with an oscilloscope.

The Thorlabs recording system limited the recording rate to 1 Hz. Since faster varying noise sources were known we made a direct connection of the detector signals to an oscilloscope. Thereby we could record fast varying detector signals in the oscilloscope. For example by stepwise changes of the current in an additional coil, oscillations of the sensor were excited, see Figure 6-11.

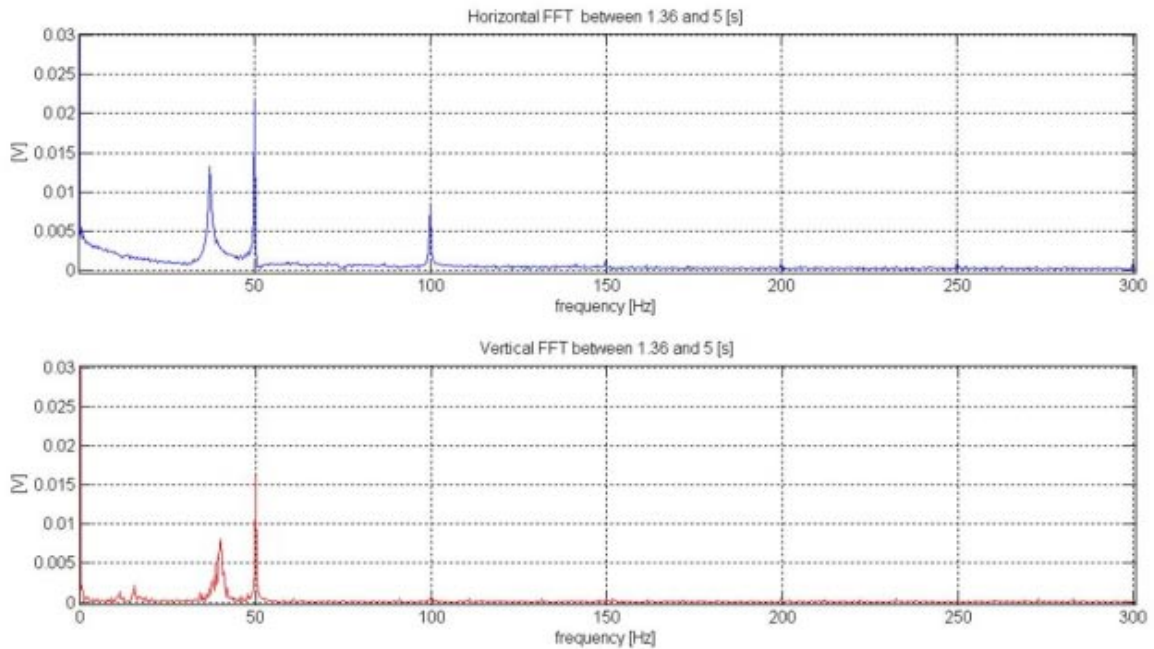


Figure 6-11: FFT of the recording shown in Figure 6-9 for the time interval 1.36 to 5 s.

These oscillations probably are eigenmodes of vibrations of the suspended magnet system. The frequency analysis in Figure 6-11 shows background signals with frequencies of 50 and 100 Hz and an oscillation with a frequency of about 38 Hz.

A similar recording is shown in Figure 6-12 and Figure 6-13. In this case a strong oscillation started just before time = 0 by a person stamping in the ridged concrete floor a few meters away from the sensor. The frequency analysis again shows peaks at about 38 Hz indicating that the same eigenmode vibrations are excited. By knocking on the vacuum pipe in which the sensor is placed oscillations were excited in the 11 – 17 Hz interval, apparently eigenmode vibrations in the vacuum pipe coupling to the sensor. These observations of excitations of vibrations show the demand of an extremely rigid construction of the cooling section and of the offline measurement setup for the cooling section subunits. Figure 6-12 also shows that the vibrational eigenmodes are damped with a half-time less than 0.1 s.

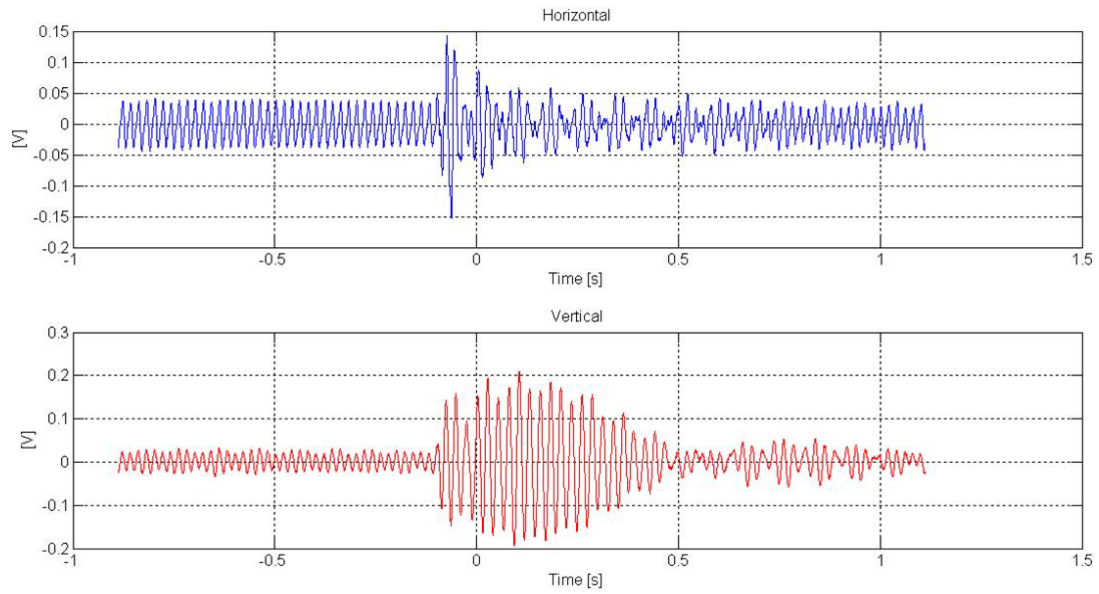


Figure 6-12: Recording of position detector signals during a stamp in the floor

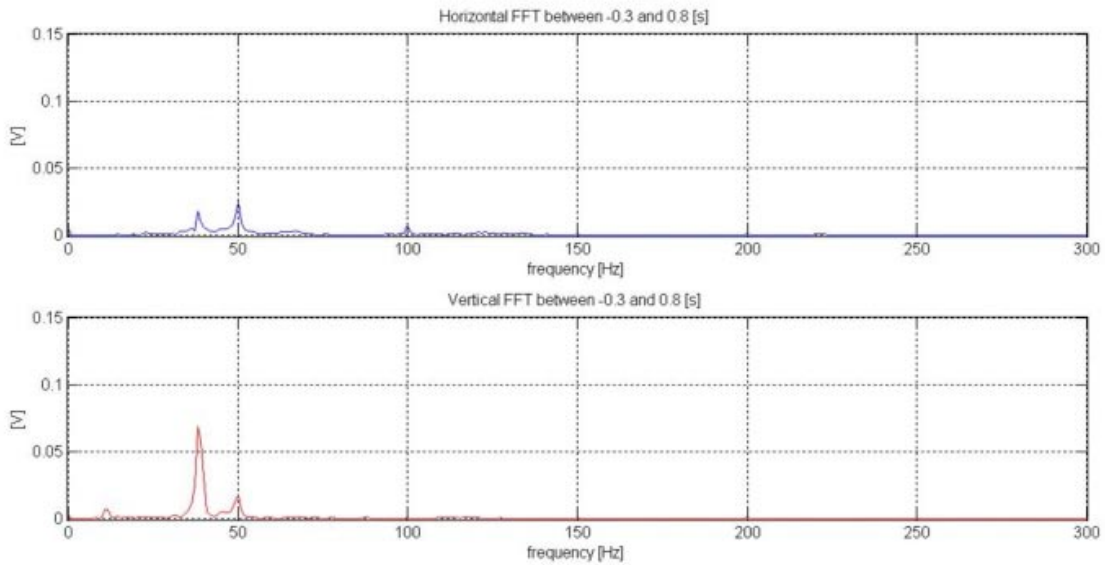


Figure 6-13: FFT of the signal shown in Figure 6-12 for the time interval -0.3 to 0.8 s.

6.1.4 Sensor transport tests

The sensor for the measurement of the magnetic field straightness in the cooling section is intended to be mounted on a trolley which should be moveable along this section. The trolley movement is guided by ridges on the inside of the vacuum pipe. However the ridges are not continuous since gaps are needed for bellows and beam position monitors. The trolley is designed to be able to bridge the gaps.

In order to find out restrictions on misalignments between different parts of the ridges tests were made in the following way. Two vacuum pipes were mounted along each other with a gap of the

worst-case length. We could make transverse and rotational misalignments. Table 6-1 shows the results.

Table 6-1

Misalignment direction	Size (mm)	Judgment
Horizontal	1	OK
Horizontal	2	Acceptable
Vertical	1	OK
Vertical	2	Not possible
Rotation (periphery movement)	1	Acceptable
Rotation (periphery movement)	2	Not possible

The results show that the demands on the mounting alignments are acceptable. However improvements in the design of the ridges and the trolley are recommended.

6.2 Beam dimension measurement prototype tests

6.2.1 Motivation and test setup

A critical task in the diagnostic system is to measure the electron beam dimension. By measuring the beam dimension at several points along the beam line it is possible to calculate the electron beam envelope oscillation. The resolution of the beam envelope oscillation measurements, expressed as the oscillation of the mean diameter of the electron beam, needs to be better than 100 μm .

For this reason it was decided to do test measurements of the beam dimension using the former CELSIUS cooler.

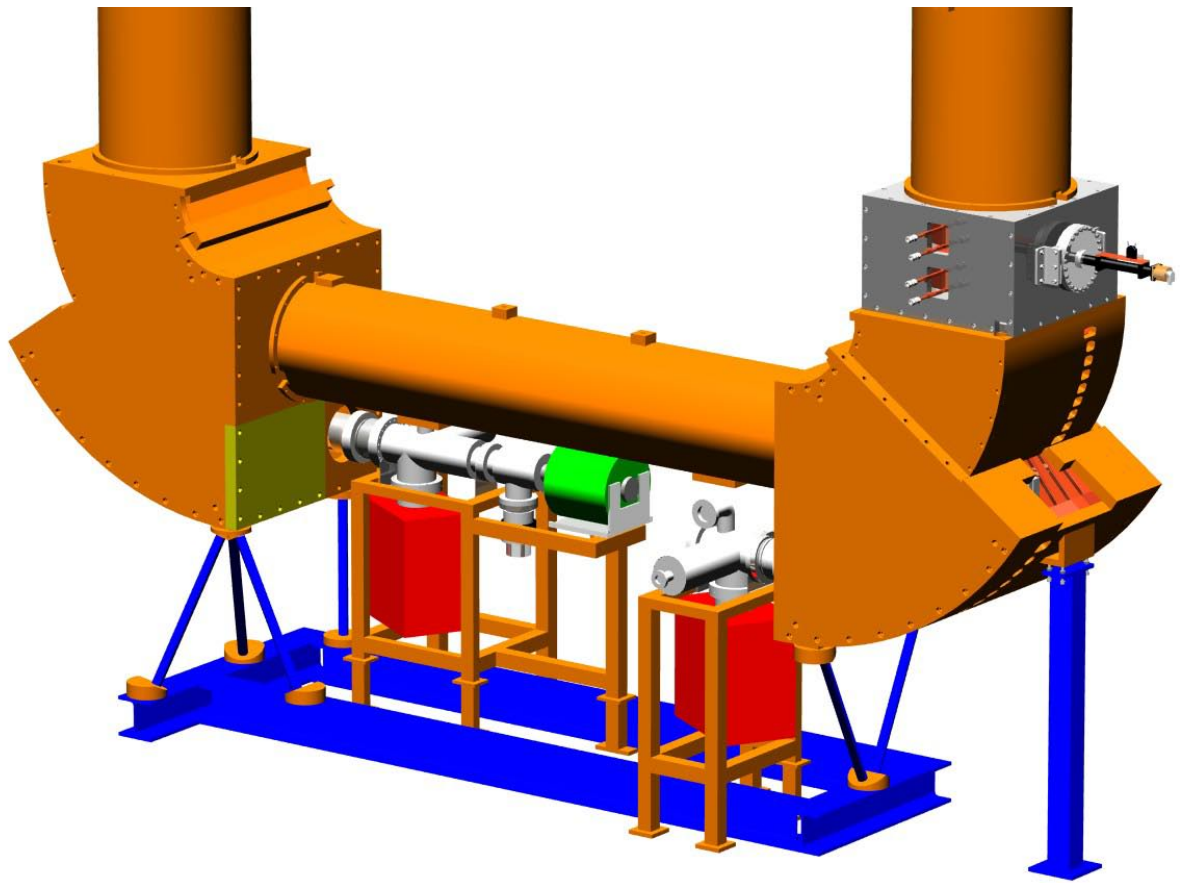


Figure 6-14 The CELSIUS cooler with a new unit added. The new unit, in white, is to the right and contains two solenoids and a scraper.

To be able to do this the CELSIUS cooler was slightly modified. A specially designed scraper and two extra solenoids were added to the cooler, see Figure 6-14 and Figure 6-15. These units were inserted slightly before the collector.

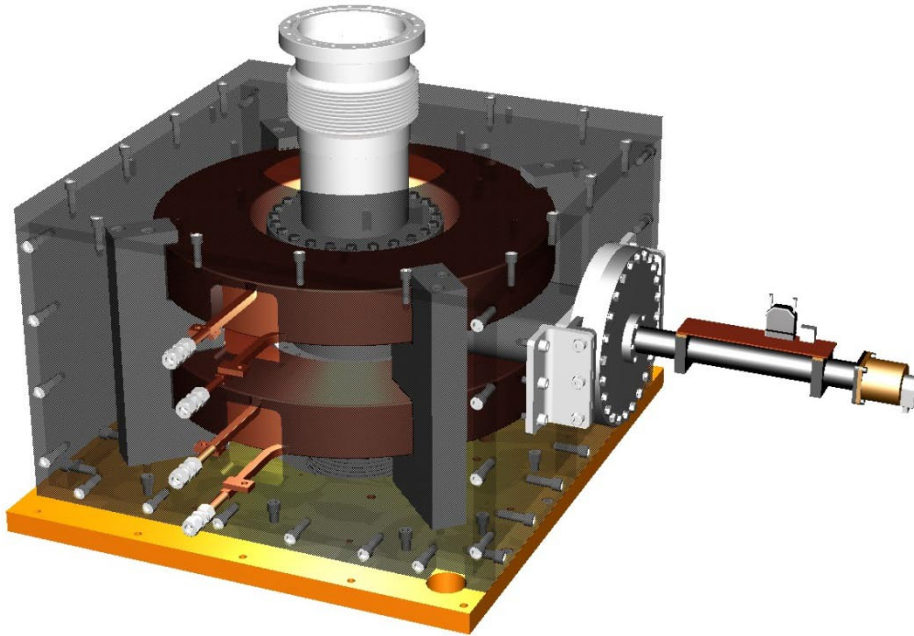


Figure 6-15: The new unit, with two solenoids and a scraper.

The longitudinal magnetic field in the cooler is fixed and is 0.1 T, except at the position of the scraper where it is variable. By changing the current in the two extra solenoids the dimension of the electron beam is changed at the position of the scraper. The scraper has a circular orifice with a diameter of 30 mm, see Figure 6-16. The diameter of the electron beam is 20 mm.

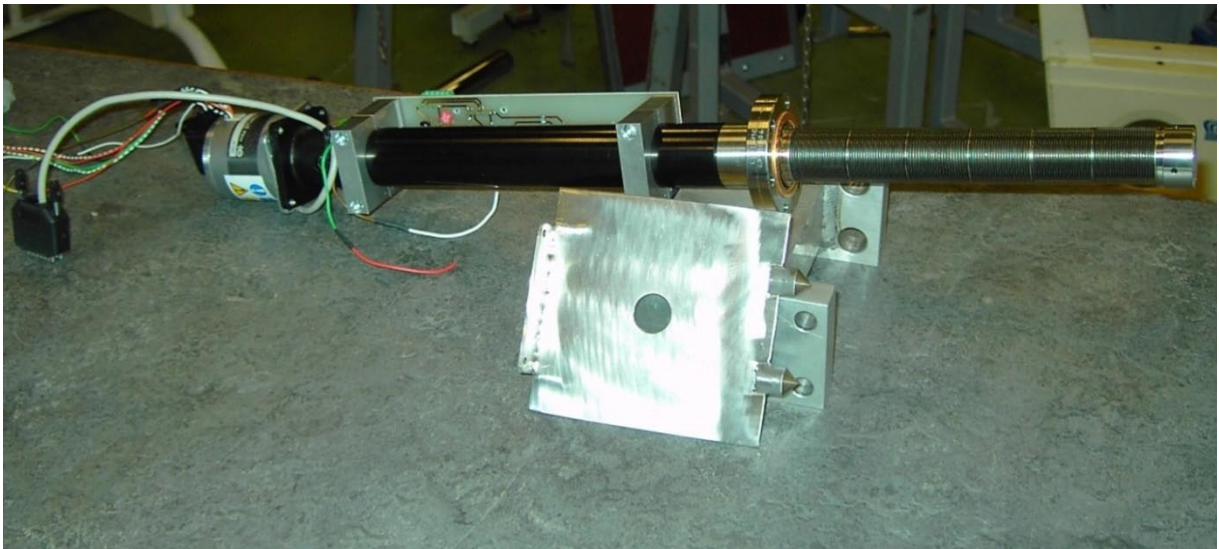


Figure 6-16: The scraper and the scraper arm. The scraper orifice has a diameter of 30 mm. The nominal electron beam diameter is 20mm.

To measure the dimension of the electron beam, the scraper is moved in to the centre of the vacuum tube so that the electron beam is centred in the orifice of the scraper. Then the beam is moved in one direction until a beam loss monitor detects that the beam has hit the edge of the scraper, as shown in Figure 6-17. By repeating the procedure in several directions, up, down, left, right, and in the four diagonal directions, the dimension of the beam is measured.

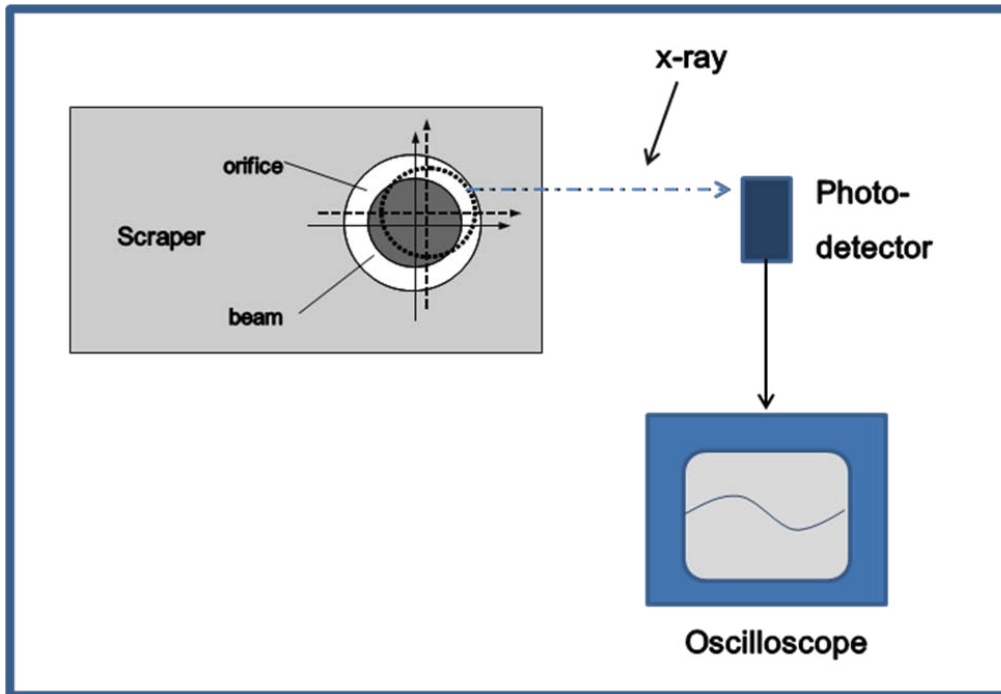


Figure 6-17: Beam size measurements with a scraper and a photo detector.

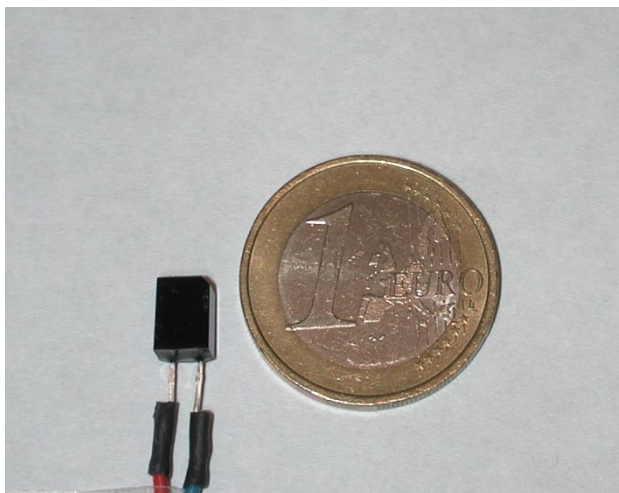


Figure 6-18: The beam loss monitor. A silicon based photodiode detector. Placed outside of a vacuum window but inside of the solenoids.

6.2.2 Measurements

The beam dimension was measured with three different currents in the extra solenoids, 200 ampere, 225 ampere and 250 ampere. The measurements were made with an electron beam of 10 mA and with an energy of 35 kV. Figure 6-19 shows a plot of how far it is possible to move the electron beam, in different directions, before it starts to hit the scraper. Figure 6-20 shows the beam dimensions calculated from the measurements in Figure 6-19.

Table 6-2: Result of beam dimension measurement.

Current in the solenoids	Magnetic field (long)	Diameter of the electron beam
200 A	0.0767 T	22.12 mm
225 A	0.0857 T	20.94 mm
250 A	0.0946 T	19.70 mm

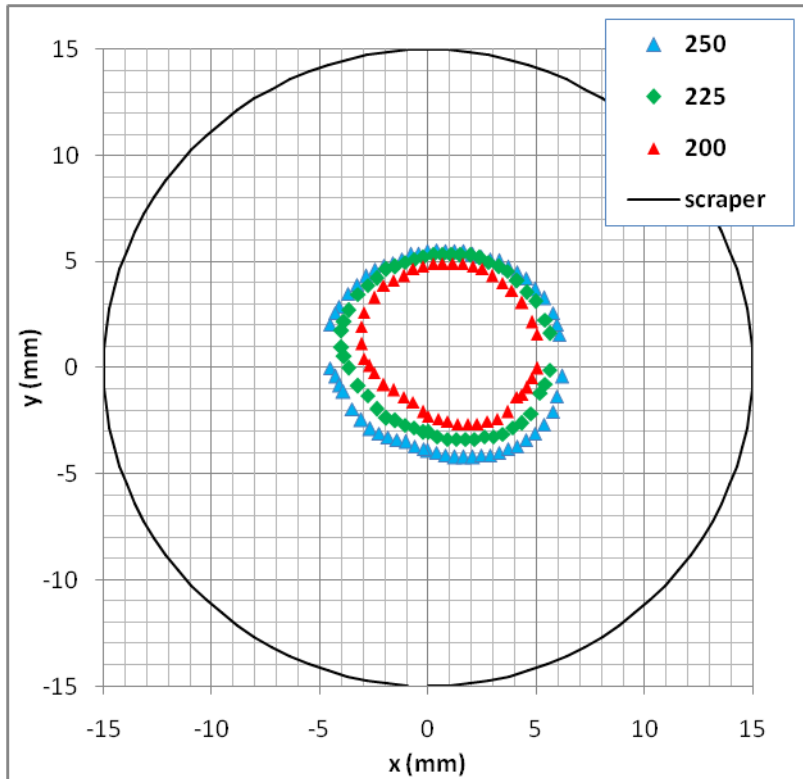


Figure 6-19: The circles shows how far it is possible to move the electron beam in different directions, before it starts to hit the scraper. Blue circle with 250 A in the solenoid with gives a magnetic field of 0.0946 T. Green circle with 225 A in the solenoid with gives a magnetic field of 0.0857 T. And the red circle with 200 A in the solenoid with gives a magnetic field of 0.0767 T. The black circle shows the size of the scraper orifice, which is 30 mm diameter.

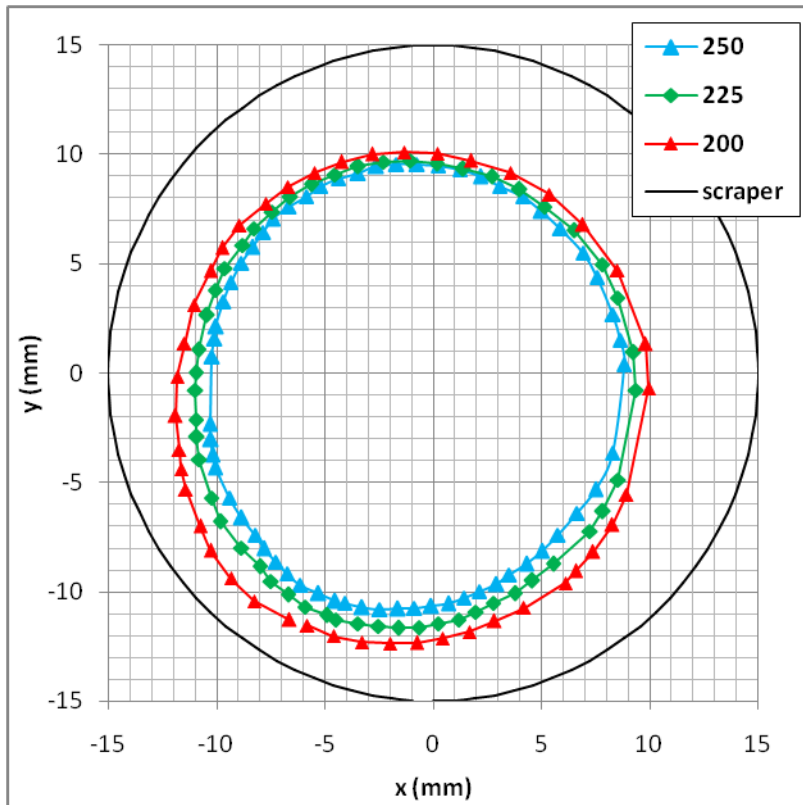


Figure 6-20: Calculated beam diameters from the three different measurements. Blue circle $D=19.70$ mm. Green circle $D=20.94$ mm. And red circle $D=22.12$ mm. The black circle is the scraper orifice with a diameter of 30 mm.

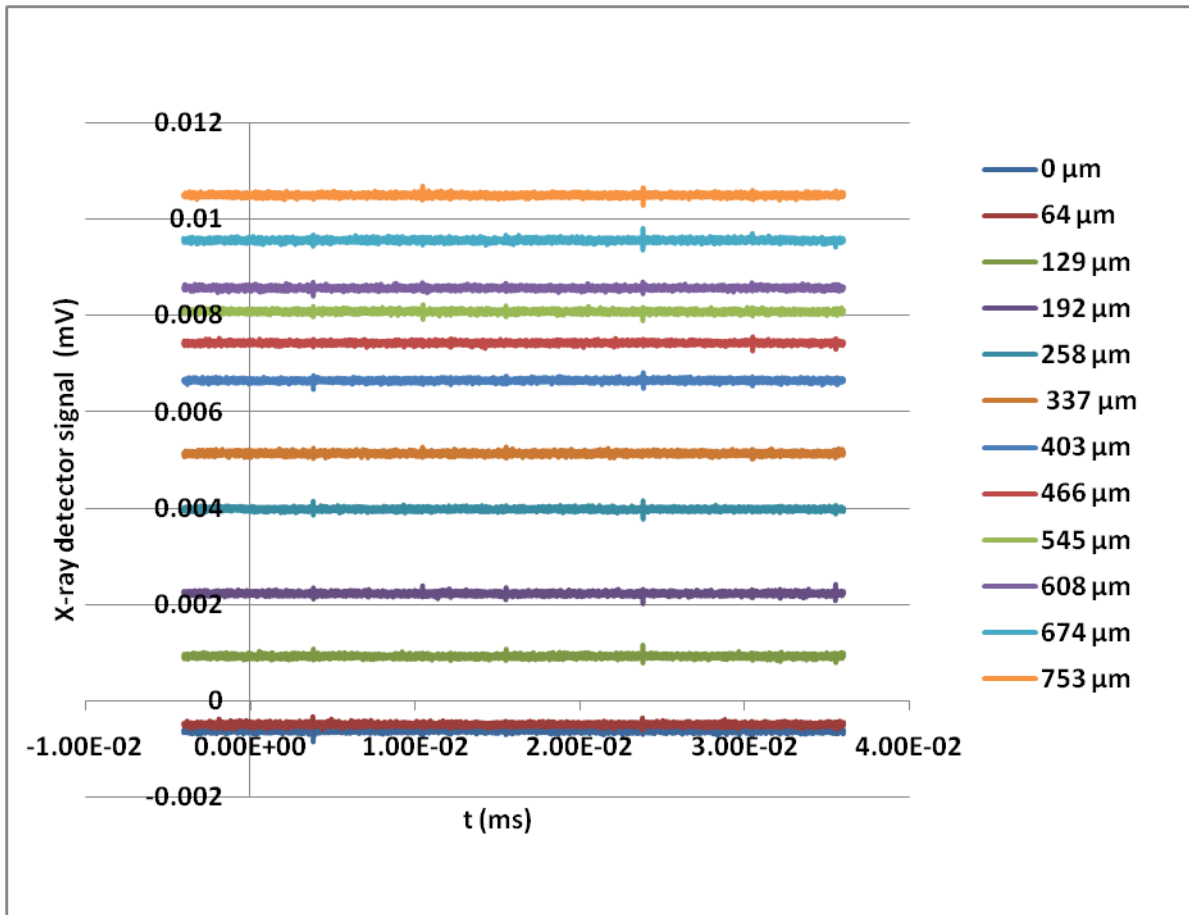


Figure 6-21: Moving the beam with small steps over the edge of the scraper orifice. At the lower blue trace the beam has not yet started to hit the edge of the scraper orifice.

6.2.3 Resolution

By moving the electron beam in small steps over the edge of the scraper orifice, the resolution of the measurements of the mean diameter of the electron beam is found to be better than 100 μm . The result is seen in Figure 6-21.

6.2.4 Conclusion

At 35 kV of electron energy with an electron beam of 10 mA it is possible to measure the mean electron beam diameter with a resolution of better than 100 μm .

At higher energies and with higher currents the resolution will increase considerably. The reason for this is that the sensitivity of the photo detector will increase as the number of photons will increase with higher energies and higher currents.

6.3 High voltage regulation tests

6.3.1 Motivation

A Pelletron is proposed as the electron accelerator of the HESR electron cooler. One of the basic requirements on such a Pelletron is that its accelerating voltage is stable to better than 1 part in 10^5 . Published reports on Pelletron stabilities just come close to this requirement, e.g. reference 1. Since this is a requirement that has to be fulfilled it was considered important to study accelerating voltage stabilities in a Pelletron with operating voltages in the same range as the HESR electron cooler Pelletron, 0.5 – 8 MV.

At the Tandem Laboratory of the Uppsala University there is such a Pelletron, operating in a tandem accelerator configuration. The Tandem Laboratory kindly made it possible for us to study the stability of the terminal voltage of their Pelletron at some occasions during the time 2006-01 -- 2006-10. To some extent this was motivated by their observation of bad voltage stability in some operating modes.

6.3.2 Measurement systems

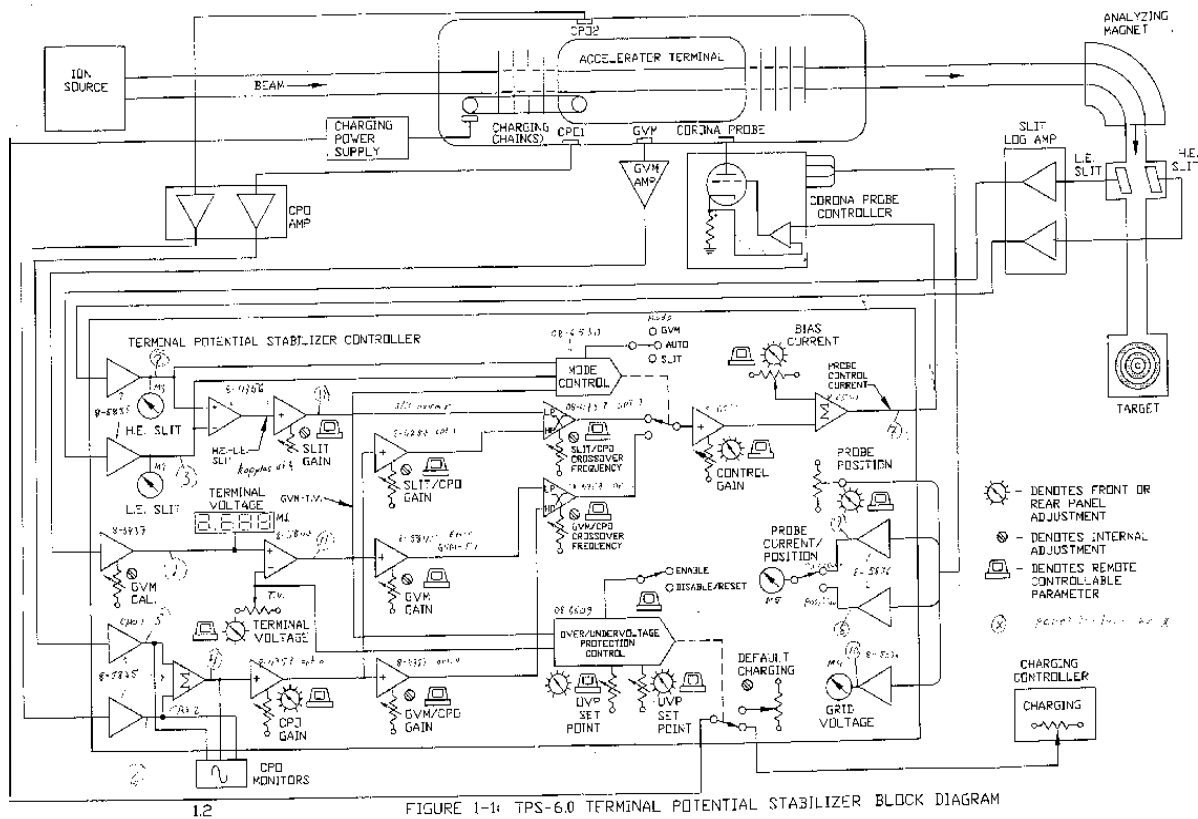
At the Pelletron of the Tandem Laboratory there are three measurement systems by means of which the terminal voltage or its variation can be observed. Namely, a generating voltmeter in the Pelletron tank wall, two capacitive pickups also in the tank wall and placed on opposite sides of the high voltage terminal and an energy analysing magnet bending the extracted ion beam 90° and equipped with entrance and exit slits. The slit halves are isolated in order to facilitate individual measurements of the currents to/from them.

The signals from the three measurement systems are fed to a terminal potential stabilizer control unit as shown in Figure 6-22. The slit signals thereby pass a logarithmic amplifier. Most of the measurements were made with the control unit in a closed loop but sometimes we managed to do some measurements with an open loop.

Measurements of the signals in the control unit were made mainly by a 2-channel oscilloscope, Tektronix TDS 3032, and by a 4-channel ADC-card connected to a PC. The sampling speed of the ADC-card was 8 kHz and the lower limit of its bandwidth was 2 Hz. The oscilloscope could record 10k samples with a bandwidth of 0 to more than 1 MHz. The ADC-PC system was just memory limited by its hard disk capacity.

The ADC-card also had an analogue output channel which could be programmed from the PC. This facility was used to add stimuli into the control unit in order to observe the systems response. A frequency sweep or a step function was used.

Recorded measurements were handled in the TSL computer system and typically we made high quality drawings of the time series and their FFT into the frequency domain.



1.2 FIGURE 1-1: TPS-6.0 TERMINAL POTENTIAL STABILIZER BLOCK DIAGRAM

Figure 6-22: Block diagram showing NEC's design of the terminal potential stabilizer for the Pelletron of the Tandem Laboratory in Uppsala University, Sweden.

Most of the experimental time during the spring was devoted to learning of the Pelletron operation and its signal system and to construction of adapters to the measuring and storing instruments. We also looked for malfunctions in the electronic circuits for the measurements, especially in the logarithmic amplifiers. No errors of this kind were found. Still we, on the desire of the Tandem Laboratory, constructed a logarithmic amplifier with improved current range.

6.3.3 Measurement results

Typical recordings of signals from a slit after the energy analyzing magnet (HE) and from a capacitive pickup (CPO1) are shown in Figure 6-23 and Figure 6-24.

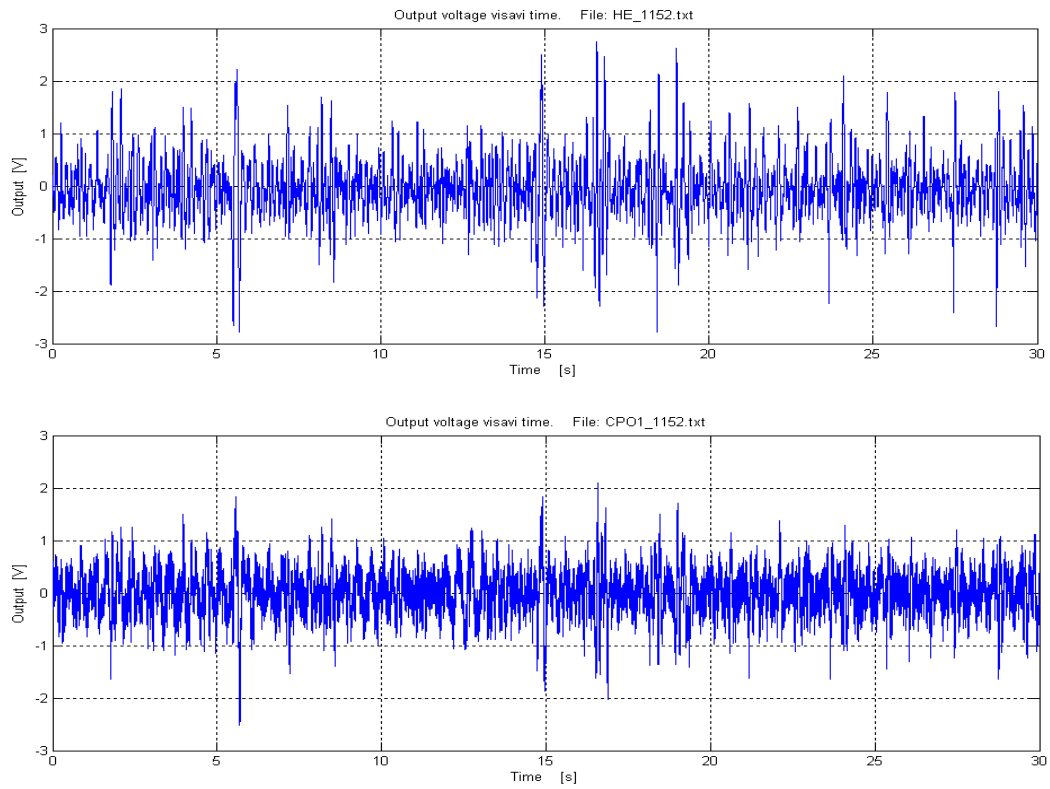


Figure 6-23: Typical time variations of signals from the slit after the energy analyzing magnet (HE) and from a capacitive pickup (CPO1) when the Pelletron is in slit regulation mode.

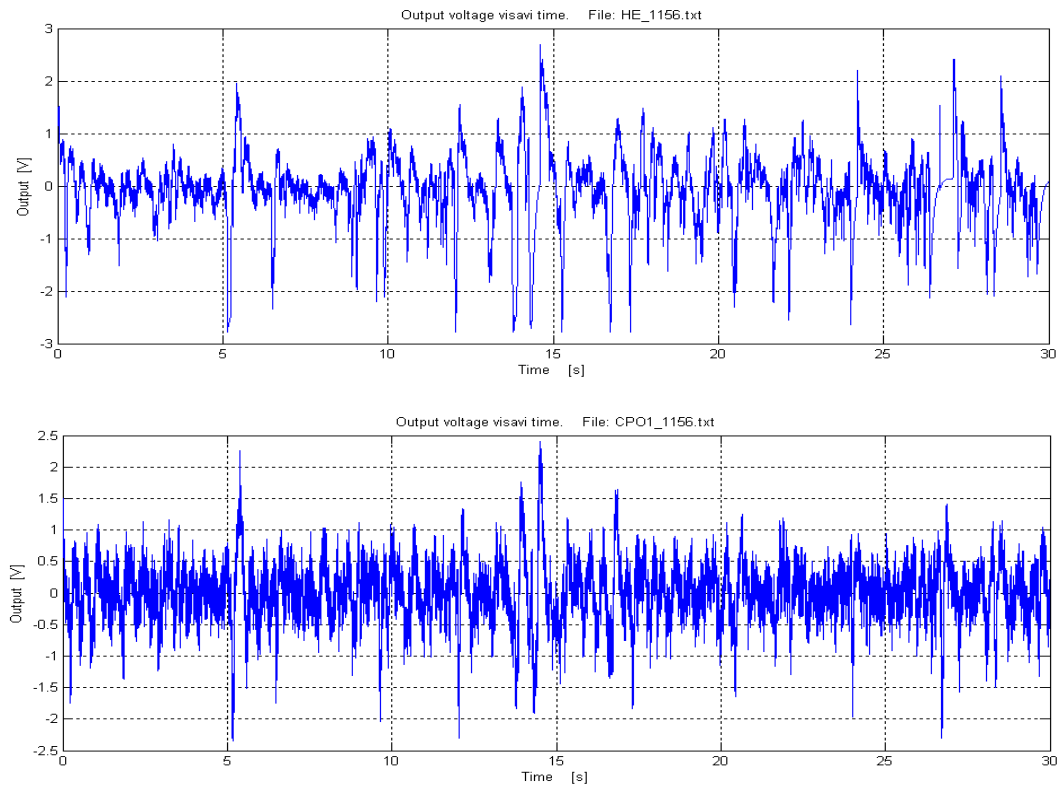


Figure 6-24: Typical time variations of signals from the slit after the energy analyzing magnet (HE) and from a capacitive pickup (CPO1) when the Pelletron is in GVM regulation mode.

The recordings shown in Figure 6-23 were done with the Pelletron running in slit regulation mode. The summing of the slit and the capacitive pickup signals had a cross-over frequency of about 1 Hz. The recordings shown in Figure 6-24 were done with the regulation system in open loop (unregulated) mode. This Pelletron also has a regulation mode in which signals from the generating voltmeter (GVM) are used instead of those from the slits after the energy analyzing magnet (LE,HE). The regulation modes are called slit, GVM and unregulated modes.

The capacitive pickup signals are calibrated in terminal voltage. In order to compare the different regulation modes, rms values of the variations of the capacitive pickup signals of 5 recordings in each of the regulation modes and with ion beam currents from 5 to 450 nA, were calculated. The results are:

Slit mode	185 V
GVM mode	200 V
Unregulated mode	240 V

This indicates that the slit regulation mode is working best. For a single recording with a medium ion beam current of 50 nA and slit regulation mode we obtained 165 V rms at a terminal voltage of 3.47 MV.

Thus $\Delta V/V = 5 \cdot 10^{-5}$.

6.3.4 Frequency spectra of the measurements

Frequency spectra of the recordings were obtained by FFT. Typical results are shown in and. They are based on the same recordings as the signals shown in Figure 6-23 and Figure 6-24. Expansions of the 0 – 10 Hz regions are shown in Figure 6-27 and Figure 6-28.

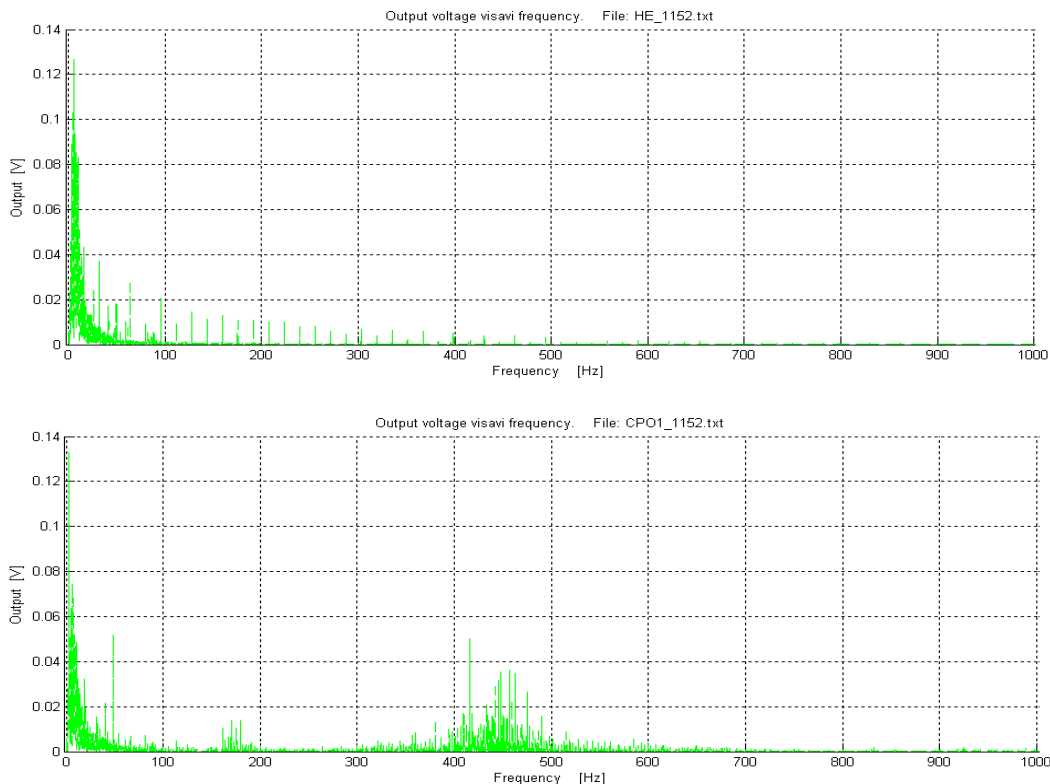


Figure 6-25: Typical frequency spectra of the HE and CPO1 signals with the Pelletron in slit regulation mode.

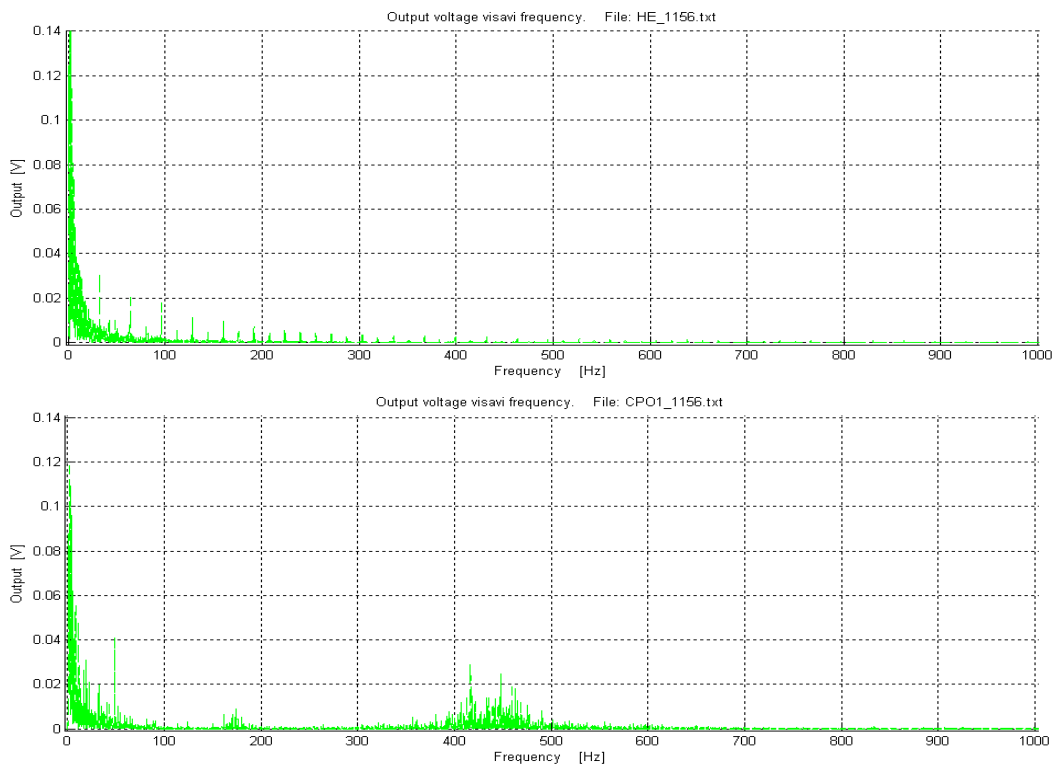


Figure 6-26: Typical frequency spectra of the HE and CPO1 signals with the Pelletron in GVM regulation mode.

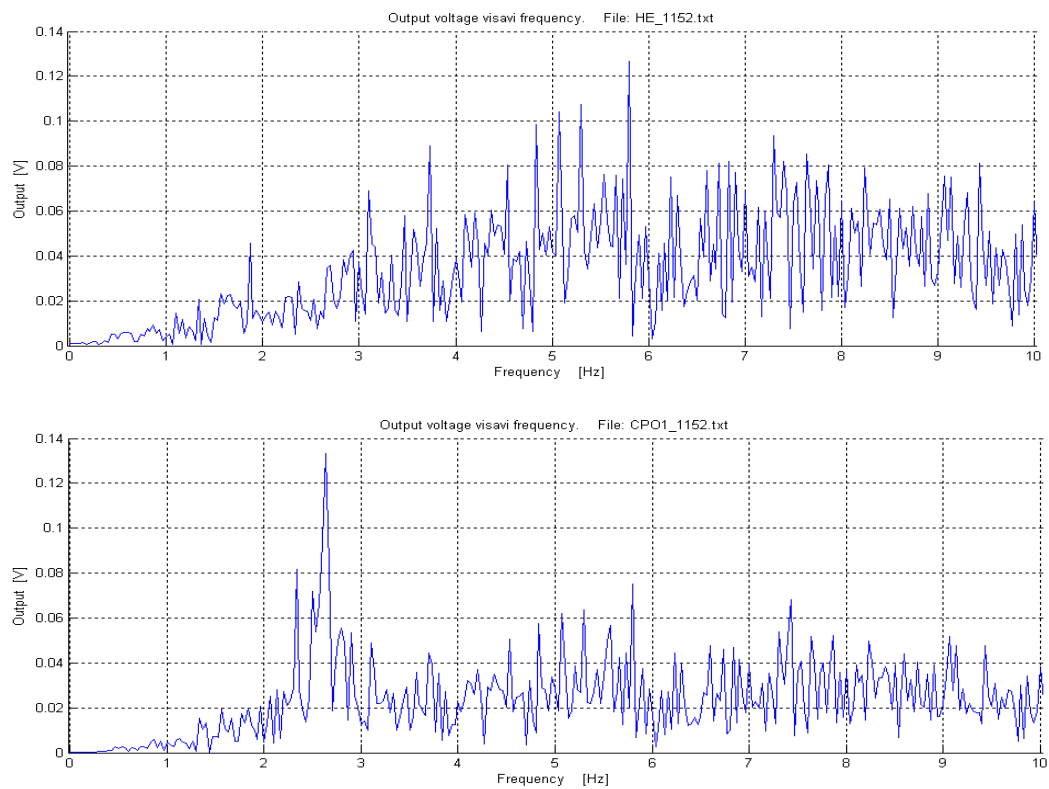


Figure 6-27: Expansion of the 0 – 10 Hz region of the spectra shown in Figure 6-25.

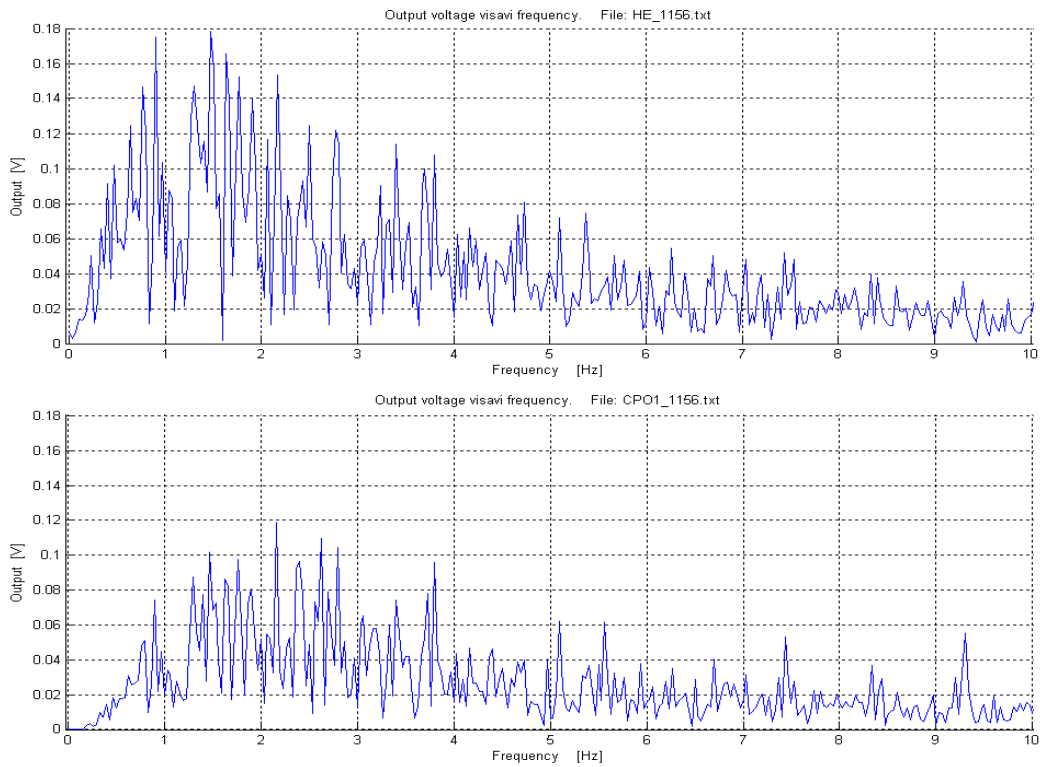


Figure 6-28: Expansion of the 0 – 10 Hz region of the spectra shown in Figure 6-26.

One observes three frequency bands, centred at ≈ 5 Hz, ≈ 180 Hz and ≈ 450 Hz in the capacitive pickup signals. While the slit signals mainly appear in the low frequency band. The signals in the 180 and 450 Hz bands are of low importance since the bandwidth of the full regulation system is ≤ 10 Hz. This can be deduced from the spectra shown in Figure 6-29 and

Figure 6-30. These spectra are from recordings with the regulation system opened before the corona probe amplifier and with a swept frequency signal fed into this amplifier. The frequency was swept from 0 to 3.6 kHz while a slit signal (SLD) and a signal returned to the opening in the regulation loop (CPCC1) were recorded.

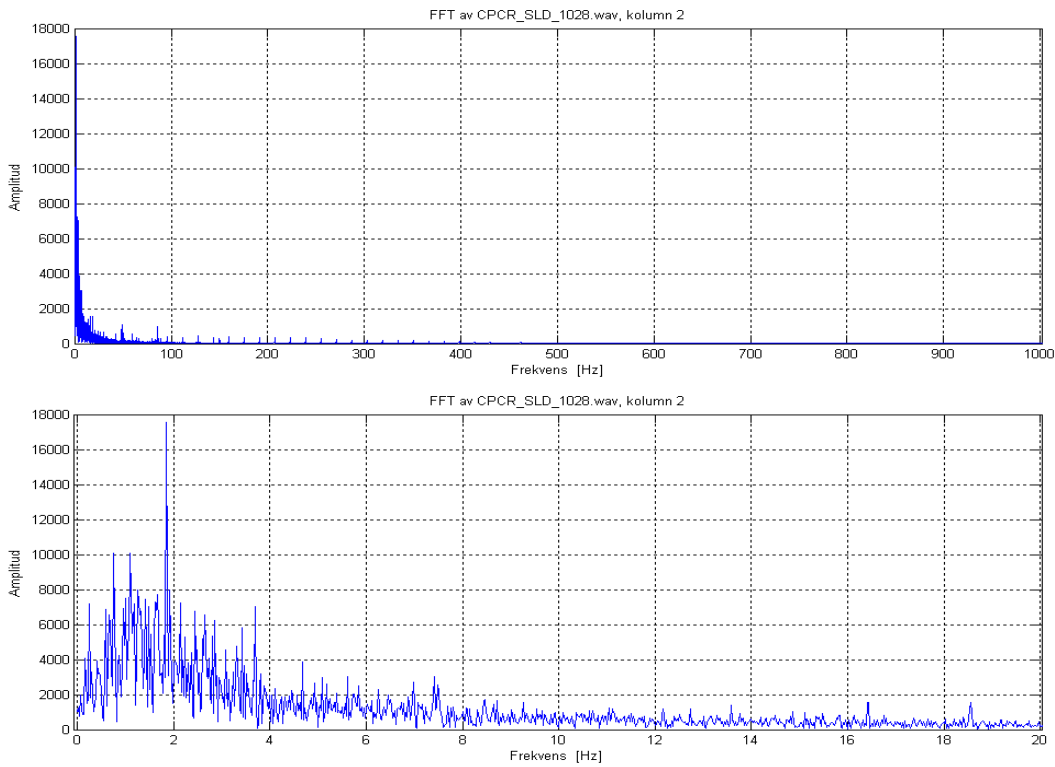


Figure 6-29: Spectra of a signal from the slit after the energy analyzing magnet, when the regulation system was opened before the corona probe amplifier and a swept frequency signal was fed into this amplifier. The frequency was swept from 0 to 3.6 kHz in 30 seconds. Upper diagram: Frequency interval 0 – 1 kHz. Lower diagram: Frequency interval 0 – 20 Hz.

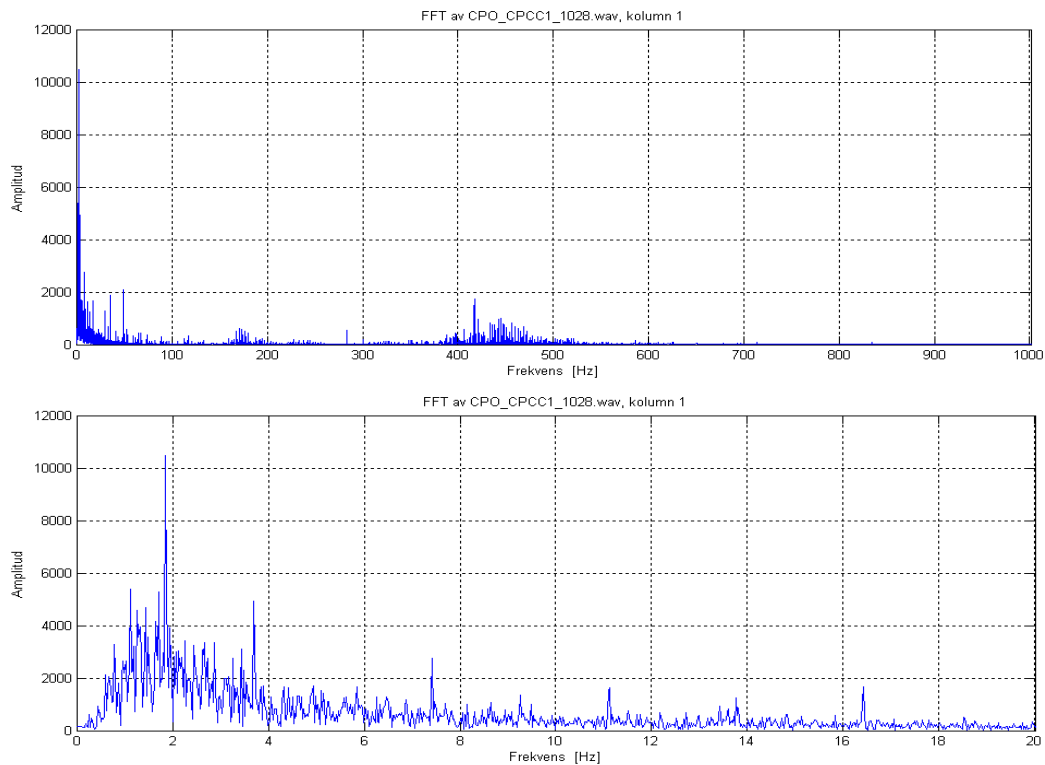


Figure 6-30: Spectra of a signal returned to the corona probe amplifier, when the regulation system was opened before the corona probe amplifier and a swept frequency signal was fed into this amplifier. The frequency was swept from 0 to 3.6 kHz in 30 seconds. Upper diagram: Frequency interval 0 – 1 kHz. Lower diagram: Frequency interval 0 – 20 Hz.

The 450 Hz band is most likely generated by vibrations of the high voltage terminal driven by the repetition of chain links which has the frequency of about 420 Hz. The origin of the 180 Hz band is unknown.

One should also notice the extremely high peak at about 1.9 Hz in these spectra. The charging chain revolution frequency is about 1.8 Hz and most probably these peaks are generated by vibrations of the terminal with this frequency.

The variations of the signals from the slithalves in front of the energy analyzing magnet are mainly caused by transverse motions of the ion beam. These beam motions can in their turn be caused by vibrations of e.g. the accelerating column or parts in the beam transport system. In figure 10 are shown spectra of the left and right slits. In these and the following figures there are also indications in the lower diagram showing the phase of this signal relative to that in the upper diagram at the same frequency. Blue cross: $-45^\circ \leq \text{phase} \leq 45^\circ$, red diamond: $135^\circ \leq \text{phase} \leq -135^\circ$ and red circle: other phases. One observes that all the main peaks are about 180° out of phase between the two halves. This is in accordance with the hypothesis of a vibrating beam.

There can be several reasons for vibrations of the ion beam. The accelerating column have intrinsic vibrational modes, the cover of the terminal deform in various modes and the following list gives sources for driven terminal motions:

Chain pellet rotation	1.8 Hz
Transverse chain vibrations	4 Hz
Rotation of chain driving motor	16 Hz
Rotation of generator driving motor	48 Hz
Link repetition	420 Hz

Frequency components corresponding to the frequencies in this list are seen in the spectra of the signals from the slit before the analyzing magnet. There are also unidentified signals.

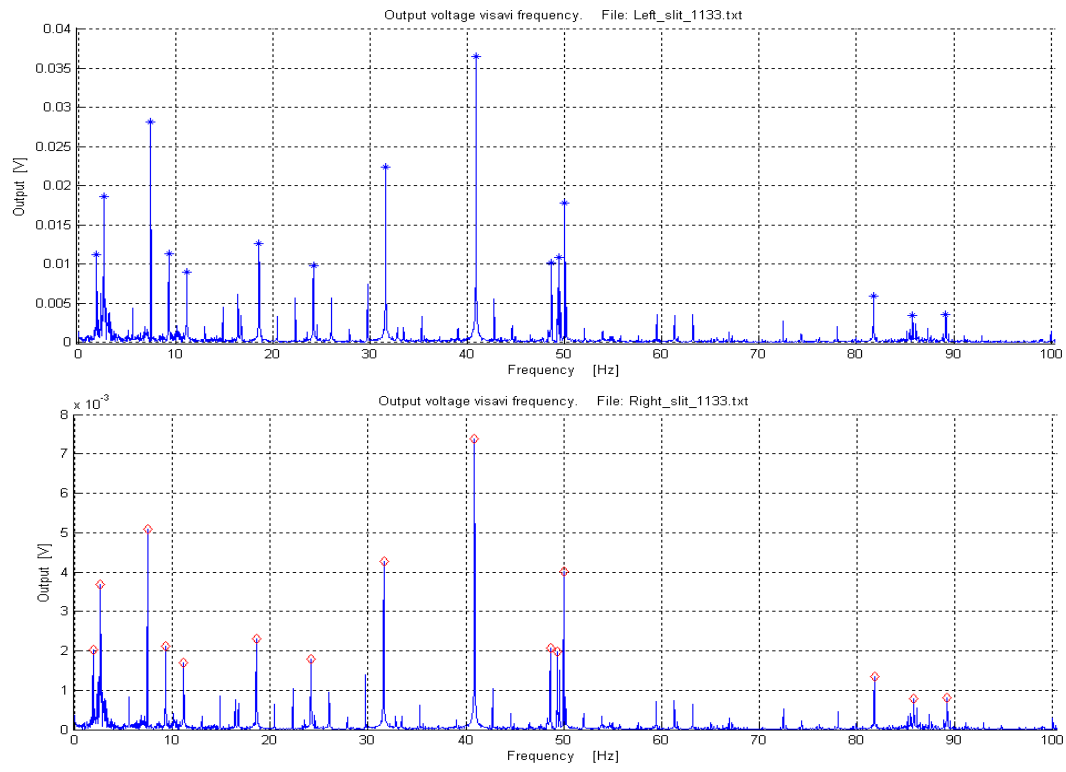


Figure 6-31: Spectra and phase indications of signals from the left and right slit halves in the slit before the energy analyzing magnet.

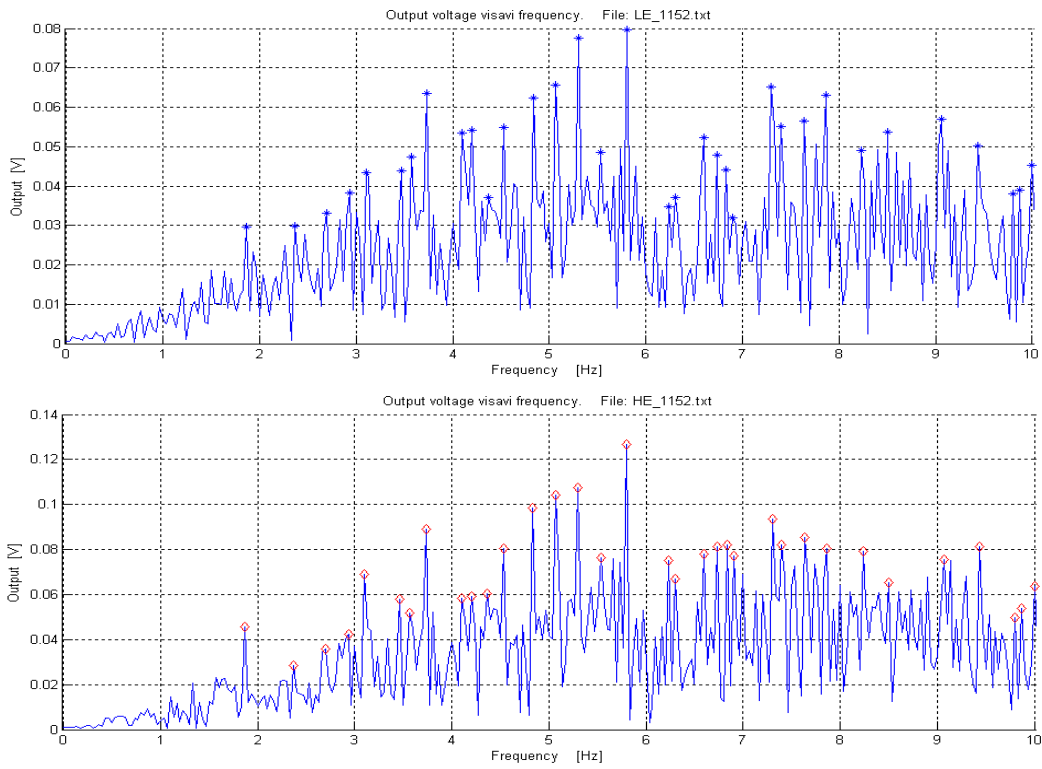


Figure 6-32: Spectra and phase indications of the signals LE and HE from the slit after the energy analyzing magnet and with the Pelletron in slit regulation mode.

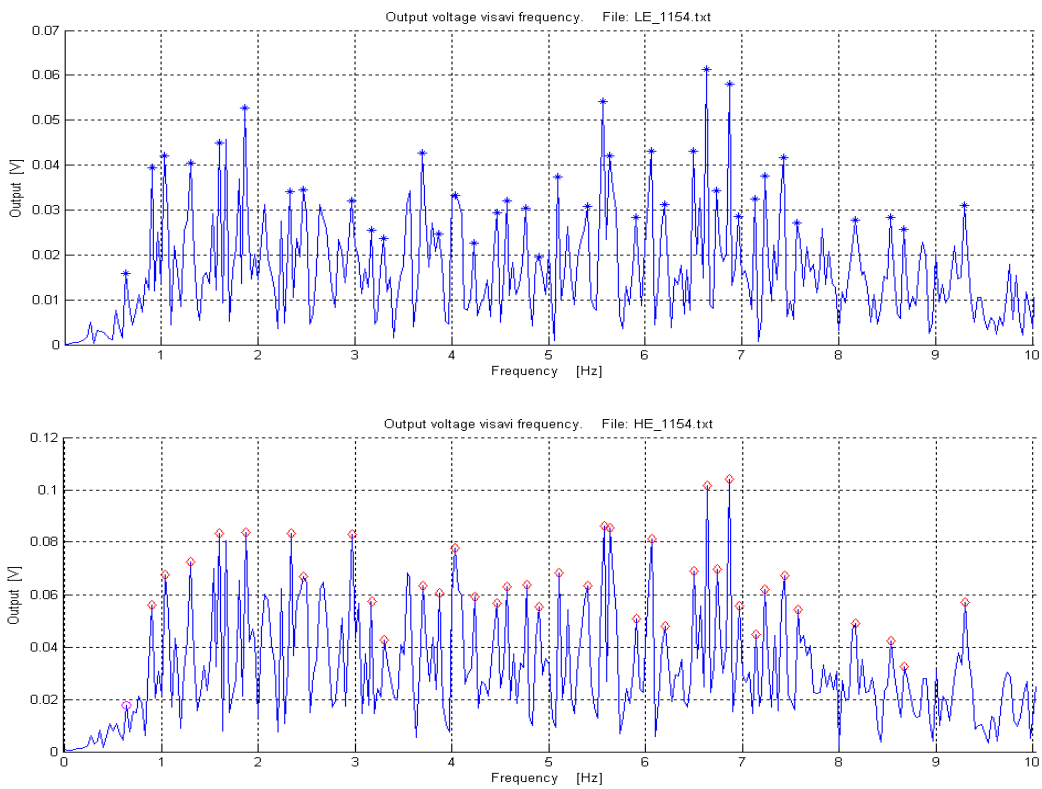


Figure 6-33: Spectra and phase indications of the signals LE and HE from the slit after the energy analyzing magnet and with the Pelletron in GVM regulation mode.

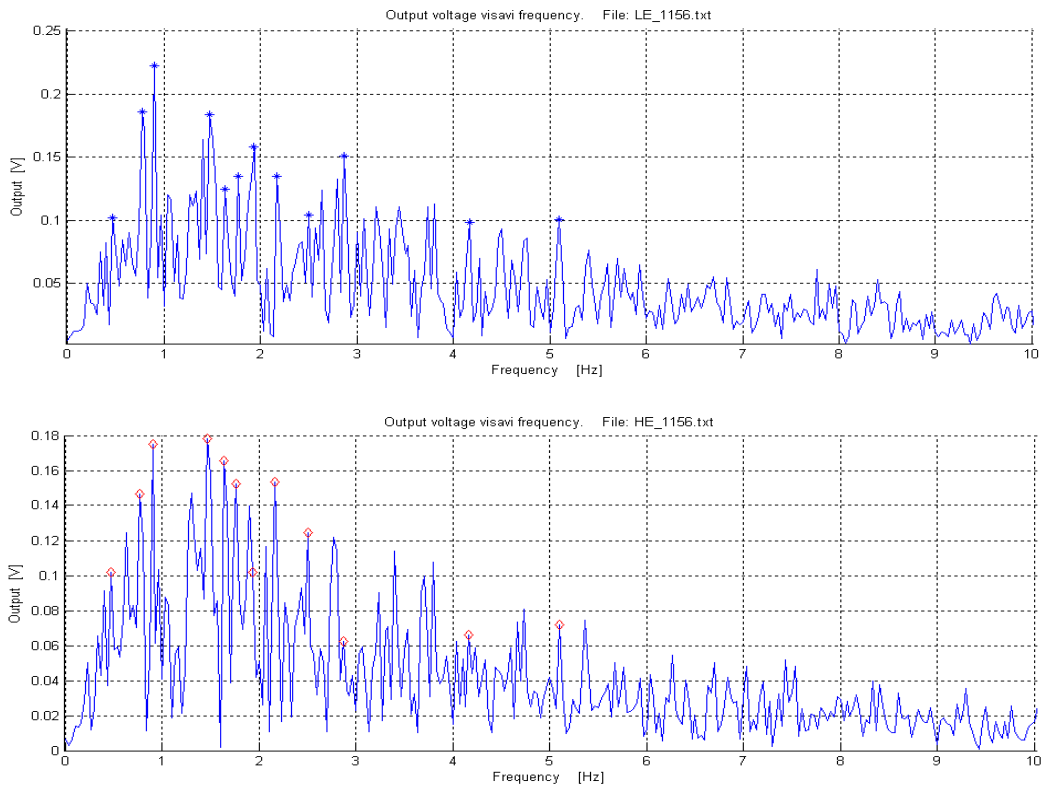


Figure 6-34: Spectra and phase indications of the signals LE and HE from the slit after the energy analyzing magnet and with the Pelletron in unregulated mode.

The signals from the high energy (HE) and low energy (LE) slit halves of the slit after the energy analyzing magnet show variations in the ion beam energy. Figure 6-32, Figure 6-33 and Figure 6-34 show frequency spectra of LE and HE signals obtained with the Pelletron in slit, GVM and unregulated modes respectively. The spectra are limited to 0 – 10 Hz since the bandwidth of the regulation system is less than 10 Hz.

For all the intense peaks in these figures the phase differences are close to 180° indicating that they are due to energy (terminal voltage) variations. If only LE and HE signals were used in the regulation system it ought to be possible to increase the counteracting feedback. However, the regulation system always makes use of the CPO signals. In Figure 6-35, Figure 6-36 and Figure 6-37 the CPO signal spectra corresponding to the signals in Figure 6-32, Figure 6-33 and Figure 6-34 respectively, are shown.

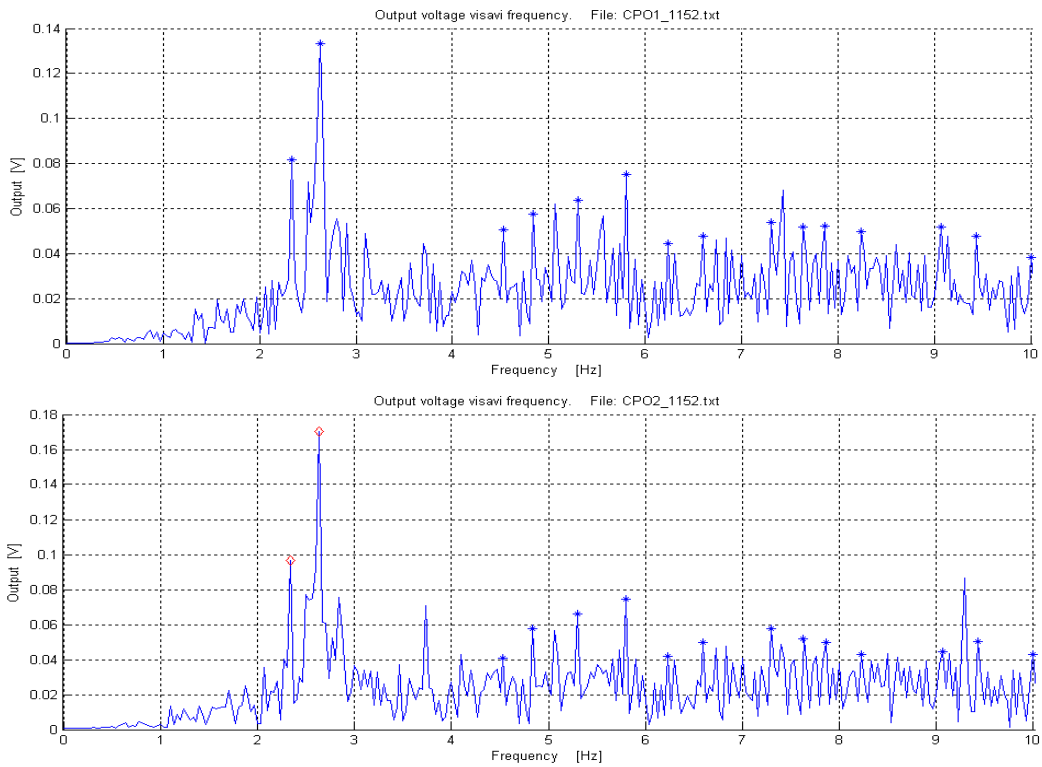


Figure 6-35: Spectra and phase indications of the two capacitive pickup signals CPO1 and CPO2 and with the Pelletron in slit regulation mode.

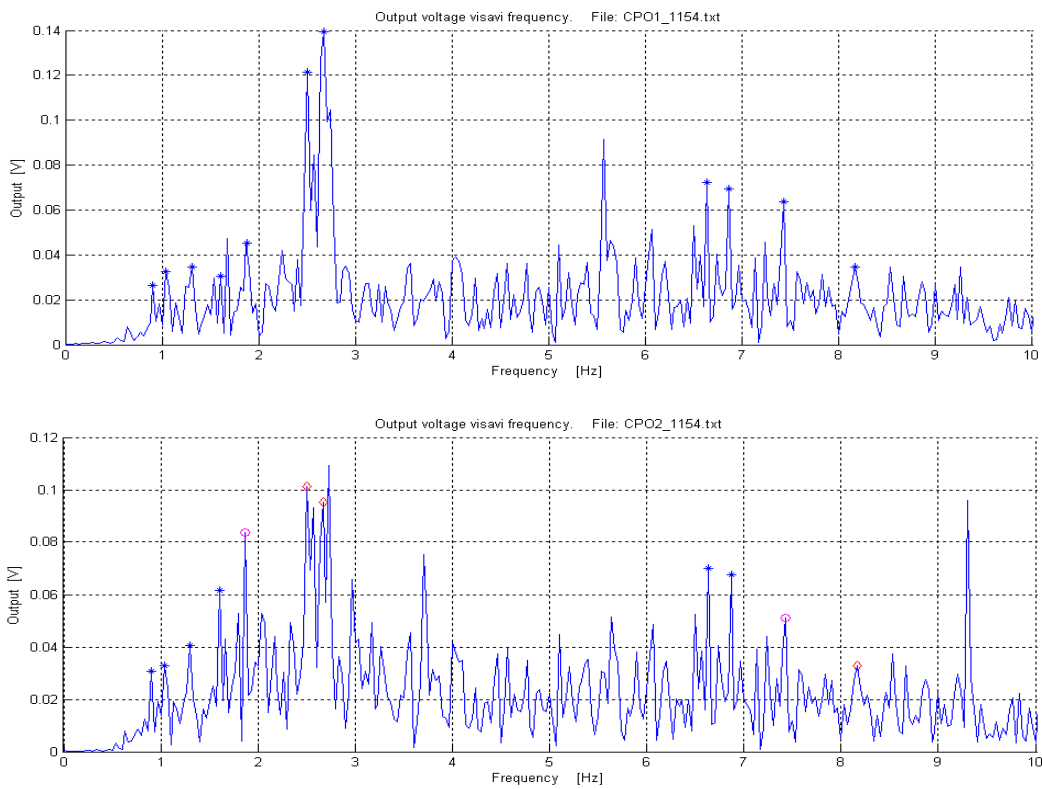


Figure 6-36: Spectra and phase indications of the two capacitive pickup signals CPO1 and CPO2 and with the Pelletron in GVM regulation mode.

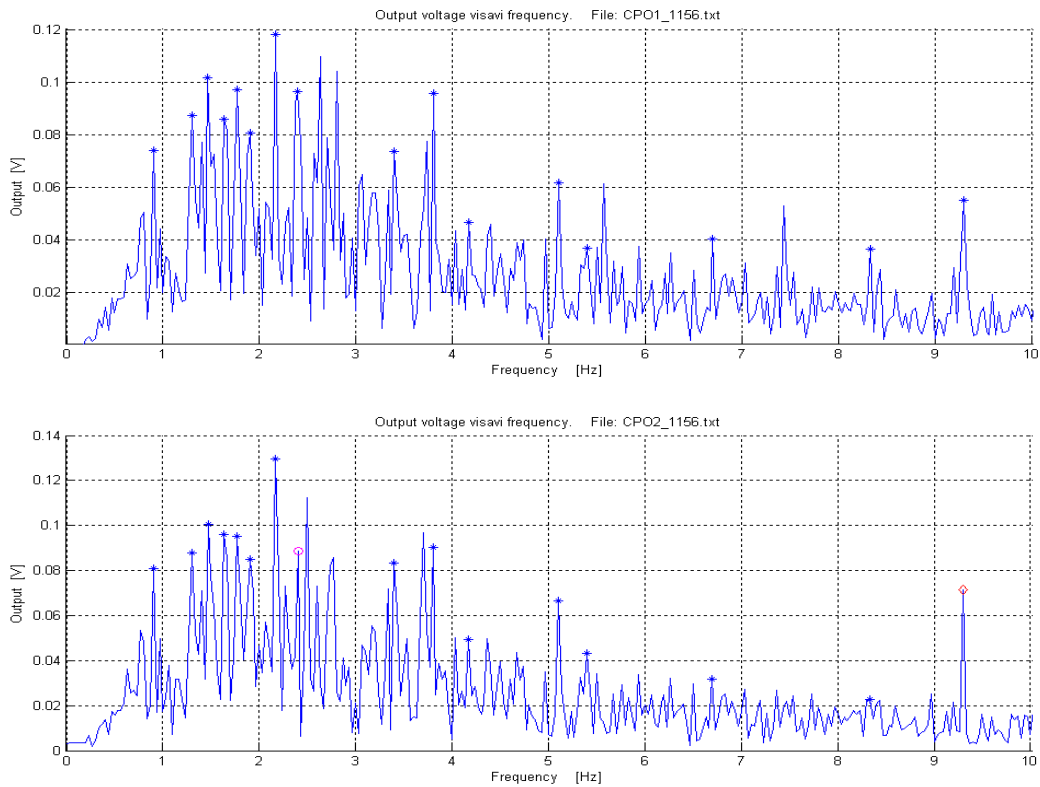


Figure 6-37: Spectra and phase indications of the two capacitive pickup signals CPO1 and CPO2 and with the Pelletron in unregulated mode.

In the spectra from the regulating modes (Figure 6-35 and Figure 6-36) one observes intense peaks between 2 and 3 Hz. The phase between CPO1 and CPO2 for these peaks is about 180° . When the CPO1 and the CPO2 signals are summed they cancel each other and the regulation system loses its ability to counteract these signals. This limits the regulation ability of the regulation system. We have not had the opportunity to localize the origin of these signals.

6.3.5 Conclusions for the HESR Pelletron

The Tandem Laboratory is only close to fulfil the requirements for the HESR, improvements have to be done.

Firstly it is apparent that vibrations deteriorate the stability. Therefore the Pelletron should be constructed so that vibrations are strongly reduced.

The regulation system should not make use of sensors that are highly sensitive to vibrations (CPO and GVM) in high stability regulation mode.

The bandwidth of the regulation system can be increased.

The intensity of the beam for the voltage regulation must be stabilized in order to avoid common mode errors.

6.4 High-voltage solenoid

The electron beam will be transported in a continuous longitudinal magnetic field in the accelerating columns. The magnetic field is generated by so-called HV-solenoids mounted above and below the separation boxes.

A prototype of a HV-solenoid was manufactured and tested. The purpose of the test was to verify the model of solenoid cooling.

6.4.1 The solenoid



Figure 6-38: Cross section of a HV-solenoid.

The solenoid has two concentric windings separated by an aluminum ring. The purpose of the ring is to transport heat generated in the windings to the aluminium base which is in thermal contact with the separation box. The coil is surrounded by an aluminum cover.

Table 6-2: Coil parameters

Conductor		3 x 7	mm	conditions
Conductor area	$A_{\text{conductor}}$	$2.1 \cdot 10^{-5}$	m^2	
Insulation thickness	δ	0.1	mm	See 6.4.7
No of layers		16 + 14		
No of turns/layer		23		
No of turns	N	690		
Coil resistance	R	1.0	Ω	$T_{\text{coil}} = 52 \text{ }^\circ\text{C}$
Current	I	25	A	
Voltage	U	25	V	$T_{\text{coil}} = 52 \text{ }^\circ\text{C}$
power	P	633	W	$T_{\text{coil}} = 52 \text{ }^\circ\text{C}$

A current of 25 A will in the acceleration column of HESR generate a magnetic field of

$$B = \frac{\mu_0 NI}{L_{cc}} = 0,071 \text{ T}$$

Where $L_{cc} = 0.305 \text{ m}$ is the center to center distance between the solenoids in the accelerating column.

6.4.2 Test set-up

The solenoid was mounted on a test “separation box” and was tightened by 9 M6 screws at $R = 249 \text{ mm}$ (see Figure 6-40 and Figure 6-41).

The surface flatness of the separation box was $< 0.1 \text{ mm}$.

6.4.3 Transient average coil temperature

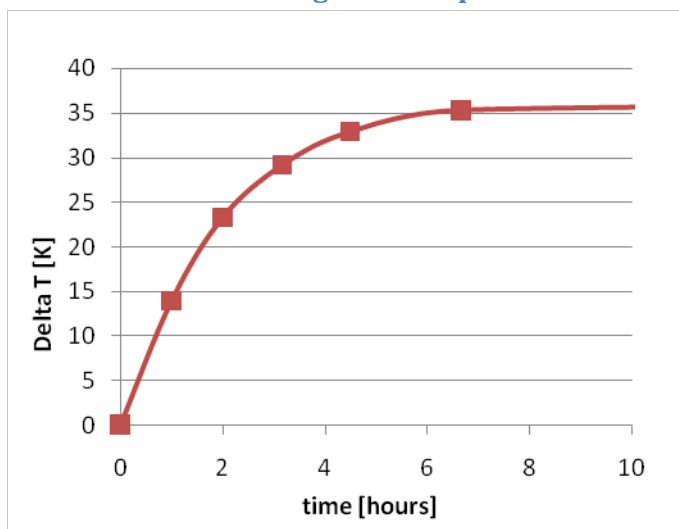


Figure 6-39: Average coil temperature rise with current 25 A (P=625 W after 8 hours).

The average coil temperature rise was calculated from the resistance variation as

$$\Delta T = \frac{\frac{R}{R_0} - 1}{\alpha}$$

where

R_0 is the initial resistance.

$\alpha = 0.00393$ is the temperature coefficient of copper

6.4.4 Azimuthal surface temperature variation

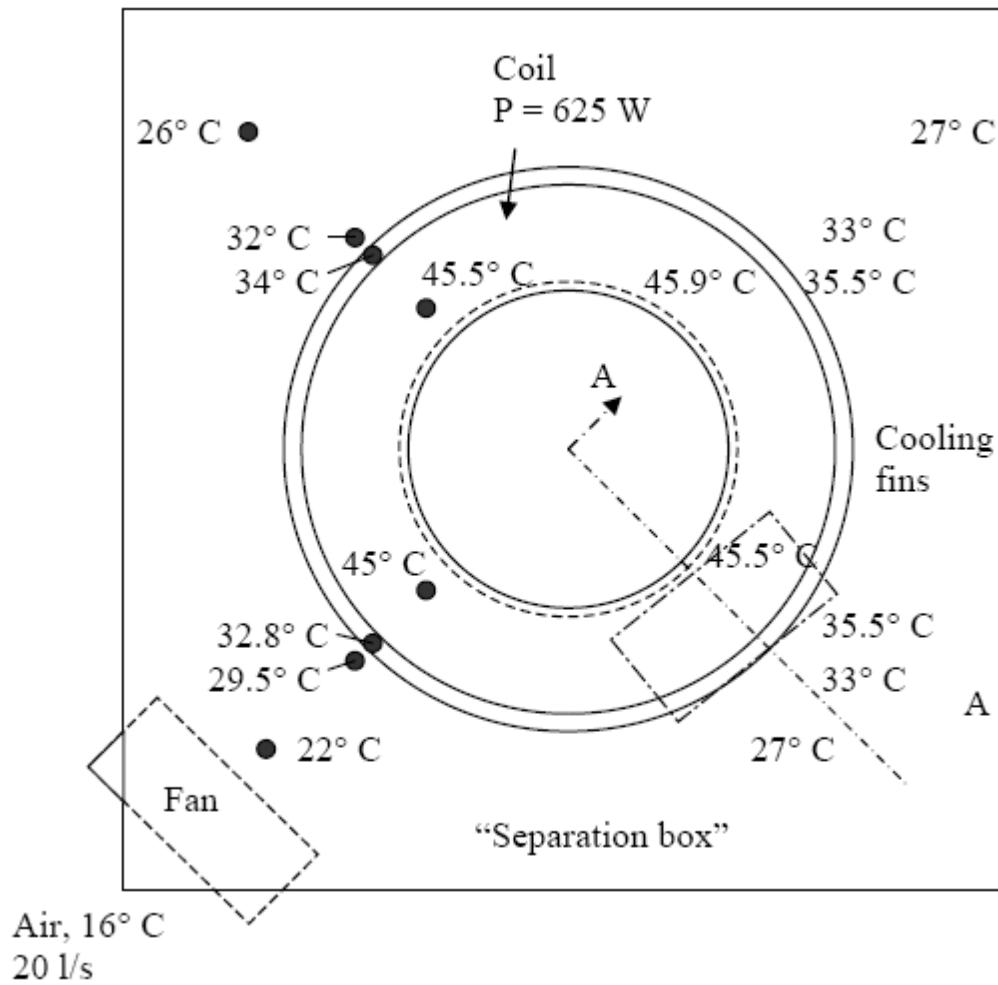


Figure 6-40: The HV-solenoid mounted on the test separation box. View from above. Steady state surface temperatures (24 hours after power on). (With silicon grease between the aluminum coil cover and the separation box. Without cooling fins)

The separation box was cooled by a tangential fan blowing air (16°C , 20 liters/s) between the two aluminum plates. The arrangement gives an unsymmetrical cooling of the solenoid as can be seen in Figure 6-40. The temperature was measured by a surface temperature probe (Fluke 80T-150U).

6.4.5 Steady state surface temperatures (after 24 hours)

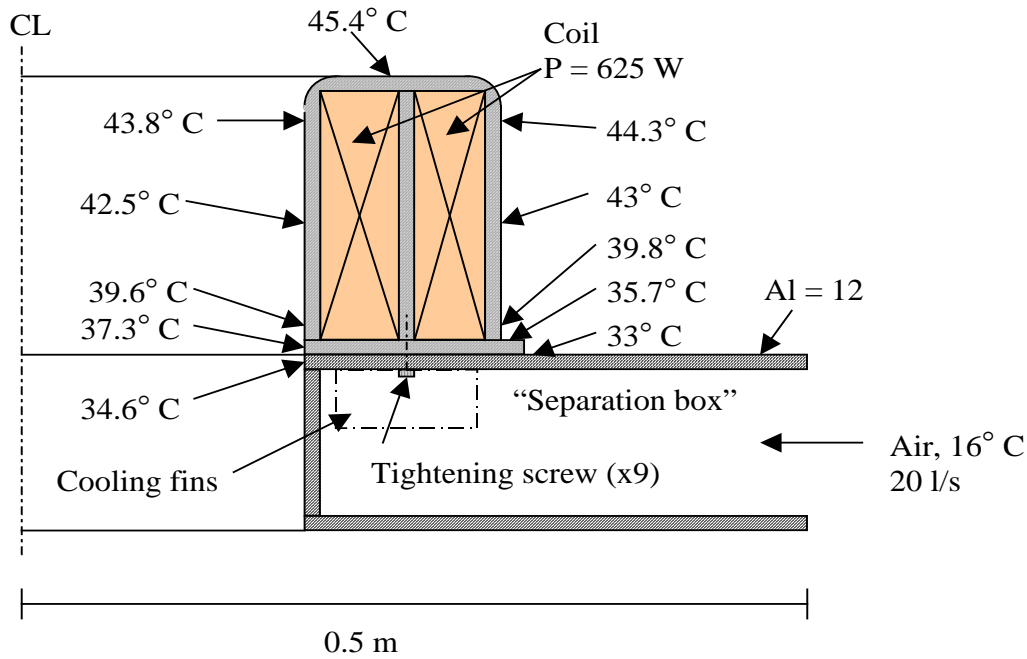


Figure 6-41: Steady state surface temperatures measured along line A-A in fig 2. (With silicon grease between the aluminum coil cover and the separation box. Without cooling fins)

6.4.6 Simulation of coil temperature

Simulations with Comsol Multiphysics predict a steady state temperature distribution in a cross section of the coil as shown in figure 4

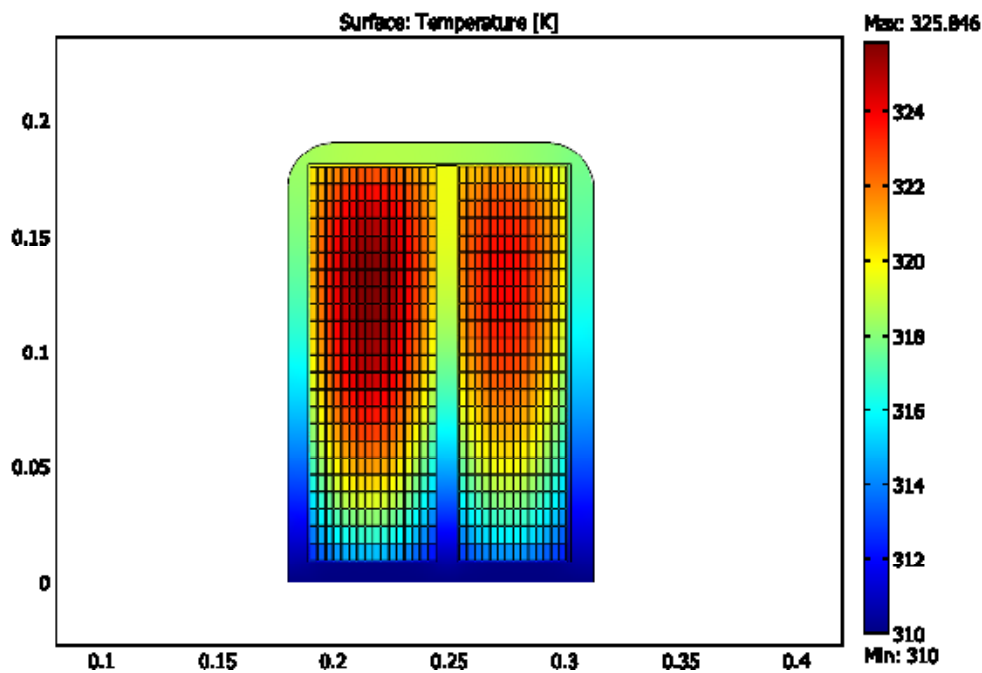


Figure 6-42: Temperature distribution in a cross section of the coil as calculated by Comsol Multiphysics. The temperature of the bottom surface is fixed at 310 K ($=37^\circ \text{C}$). The other surfaces are isolated.

The measured surface temperature is in good agreement with the simulations.

6.4.7 The conductors

The copper conductors have 3 x 7 mm cross section and have two layers of insulation. The inner layer (base layer) consists of THEIC-modified polyester (imid) and the cover layer consists of polyamidimid. The space between the conductors is filled with epoxy.

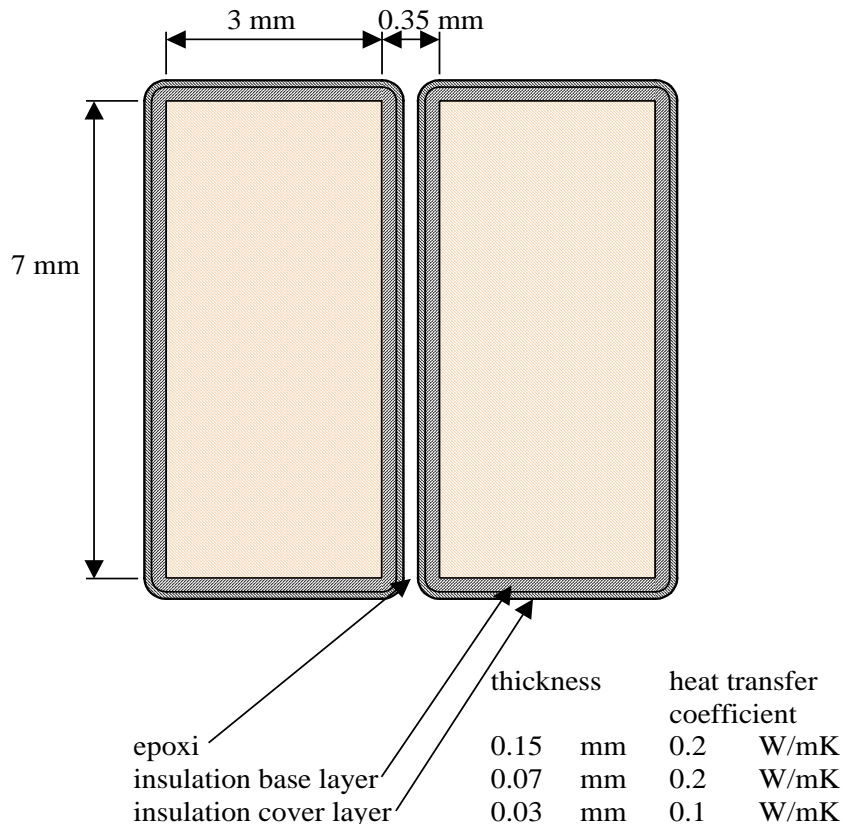


Figure 6-43: Cross section of two conductors in the coil

The thickness of the layers is estimated from measurements and from data sheets of the conductors.

6.4.8 Steady state coil temperature

The resistance measurements show that the steady state average coil temperature is

$$T_{start} + T_{increase} = 16 + 36.1 = 52.1^{\circ} \text{ C.}$$

The simulations with Comsol Multiphysics (see Figure 6-42) predict a maximum steady state temperature in the coil of 52.8° C if the contact surface is assumed to have a constant temperature = 37° C.

6.4.9 Thermal contact resistance

The thermal contact resistance between the aluminum coil cover and the separation box can be decreased by applying silicon grease between the aluminum surfaces. The temperature drop

between the coil cover bottom plate and the separation box plate was measured. One measurement was done without silicone grease and one with a thin layer of silicon grease on the surfaces. The temperature drop was measured at 4 azimuthal positions on the outside of the coil (see Figure 6-40) and at one position on the inside (see Figure 6-41)

	Without silicon grease	With silicon grease
Average temperature drop	5° C	2.1° C

6.4.10 Cooling fins

The heat transfer to air (or SF6) can be increased by increasing the area of heat transfer. Cooling fins were mounted on the aluminum plate inside the separation box, see Figure 6-40 and Figure 6-41, with the fins parallel to the air flow. The average temperature rise was measured 24 hours after power on with and without the cooling fins

	Without cooling fins	With cooling fins
Average temperature rise	36.1° C	33.6° C

6.4.11 Conclusions

The temperature inside the coil must not exceed 70° C to avoid softening of the epoxy. The test has shown that it is possible to run the coil with nominal current in air without exceeding 70° C in the coil. Cooling with SF6 at 6 bar is more efficient and therefore the coil temperature will be lower during normal operation in the Pelletron tank assuming the same gas flow and gas temperature.

Possible ways to decrease the coil temperature are

- decrease the thermal contact resistance between the coil and the separation box.
- apply silicone grease or indium foil
- increase the contact pressure (more tightening screws)
- increase the area of heat transfer
- cooling fins inside the separation box
- increase flow of cooling gas
- decrease temperature of cooling gas

7 SIMULATIONS

7.1 Simulation codes

For simulation of electron cooling the code BETACOOOL has been used.

For simulation of 2-dimensional beam optics with space charge the codes SAM, UltraSAM [14] and BEAM [15] developed at BINP have been used.

- SAM is a code for simulation of electro-static and magneto-static axially symmetric problems using the Boundary Element Method.

- UltraSAM is a code for calculation of electron guns using curved meshes for description of space charge.
- BEAM is a code for simulation of high perveance beam dynamics in long systems.

For simulation of 3-dimensional beam optics without space charge the 3-D codes MAG3D developed at BINP and TOSCA from Vectorfields have been used.

- MAG3D is code for 3-D electro-static and magneto-static calculations using the Boundary Elements Method.
- TOSCA is a code for 3-D magneto-static calculations.

Simulation with SAM, UltraSAM, BEAM and MAG3D was done in cooperation with A. Ivanov and M. Tiunov from BINP.

Simulation with TOSCA was done in cooperation with H. Danared from Manne Siegbahn Laboratory.

Simulation with Betacool was done in cooperation with A. Sidorin from JINR.

7.2 Electron gun

Angles between the electrons momentum and the magnetic field are created by un-adiabatic changes of electric or magnetic fields. Electron angles can be completely compensated downstream by a kick in the longitudinal magnetic field if:

- the electrons move in the same phase
- the electron angles increase linearly with radius

In contrast to the Fermilab-gun, electrons make a large number of Larmor rotations at the energy of $e \cdot U_a$ before reaching an acceleration field. At this comparatively low energy, it has to be verified that the potential difference between the outer and axial electrons does not result in a significant variation of the total phase advances over the length of the equipotential region.

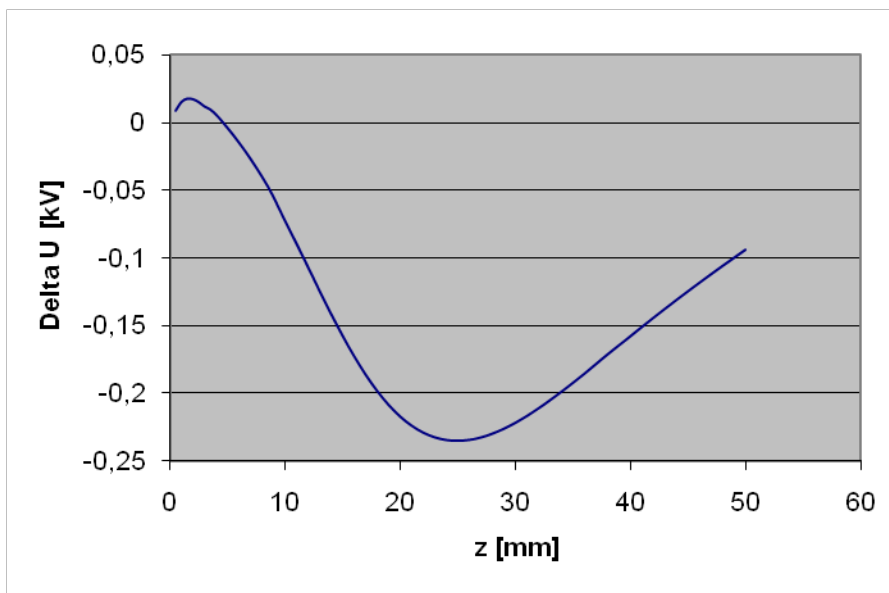


Figure 7-1: Potential difference between outer and axial electrons in the beam. $\Delta U = U_{R=4,8 \text{ mm}} - U_{R=0}$

Figure 7-1 shows that the potential difference between outer and inner electrons in the beam is less than 0.25 kV.

Estimation for the total phase shift

$$\Delta\varphi = \frac{l}{\lambda_c} \frac{\Delta U}{2U} \sim 0.035 (= 2^\circ)$$

where

$l = 0.36$ m is the drift distance from the gun anode to the accelerating tube

$\lambda_c = 0.05$ m is the cyclotron wavelength of 26 keV electrons at $B = 0.07$ T

$\Delta U = 0.25$ kV is the potential difference between the outer and axial electrons

$U = 26$ kV is the potential in the drift region

We conclude that the phase shift is acceptable.

There are two sources of electron angles in the gun region:

- E_r in the gun
- The transition from 0.2 T at the cathode to 0.07 T.

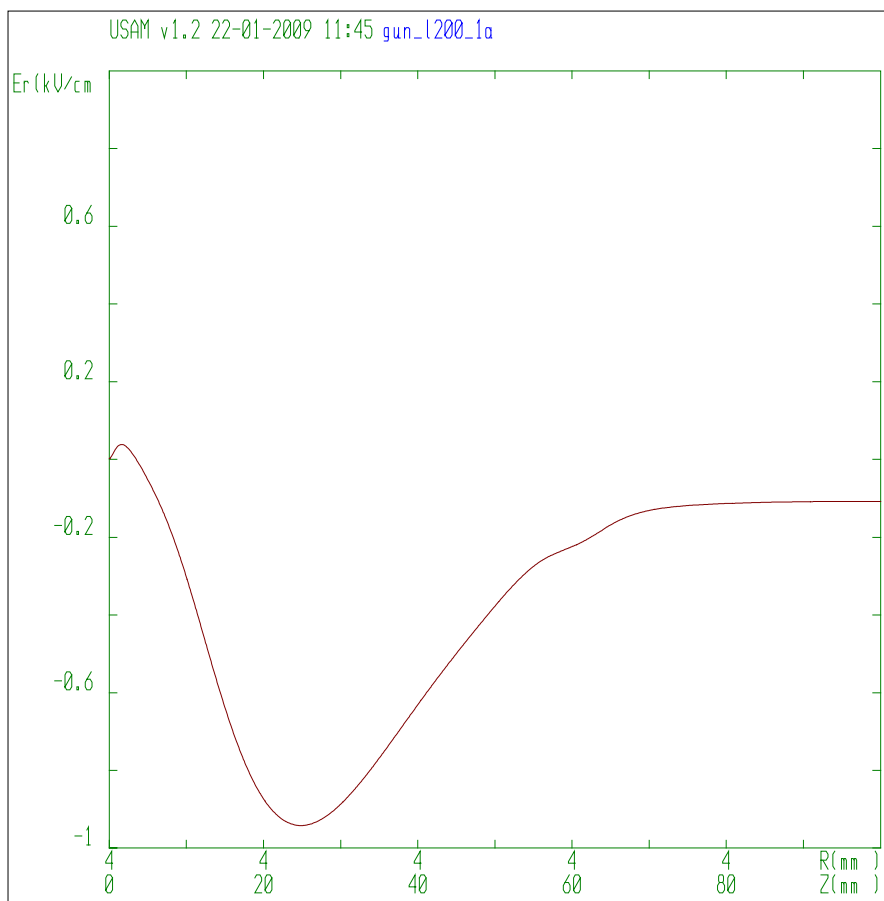


Figure 7-2: Transverse electric field at radius 4 mm

The gun electrodes are optimized to produce minimum transverse temperature inside the gun. The Larmor wavelength calculated for $U_a = 26$ kV and $B = 0.2$ T is 17 mm. The value is lower than the width of the transverse electric field distribution, and, therefore, the electrons move adiabatically. Optimization in the adiabatic case means decreasing the peak value of the transverse field and increasing the width of its distribution while keeping the perveance reasonably high.

The transition in magnetic field is done smoothly enough to not introduce cyclotron oscillations.

The result is shown in Figure 7-3

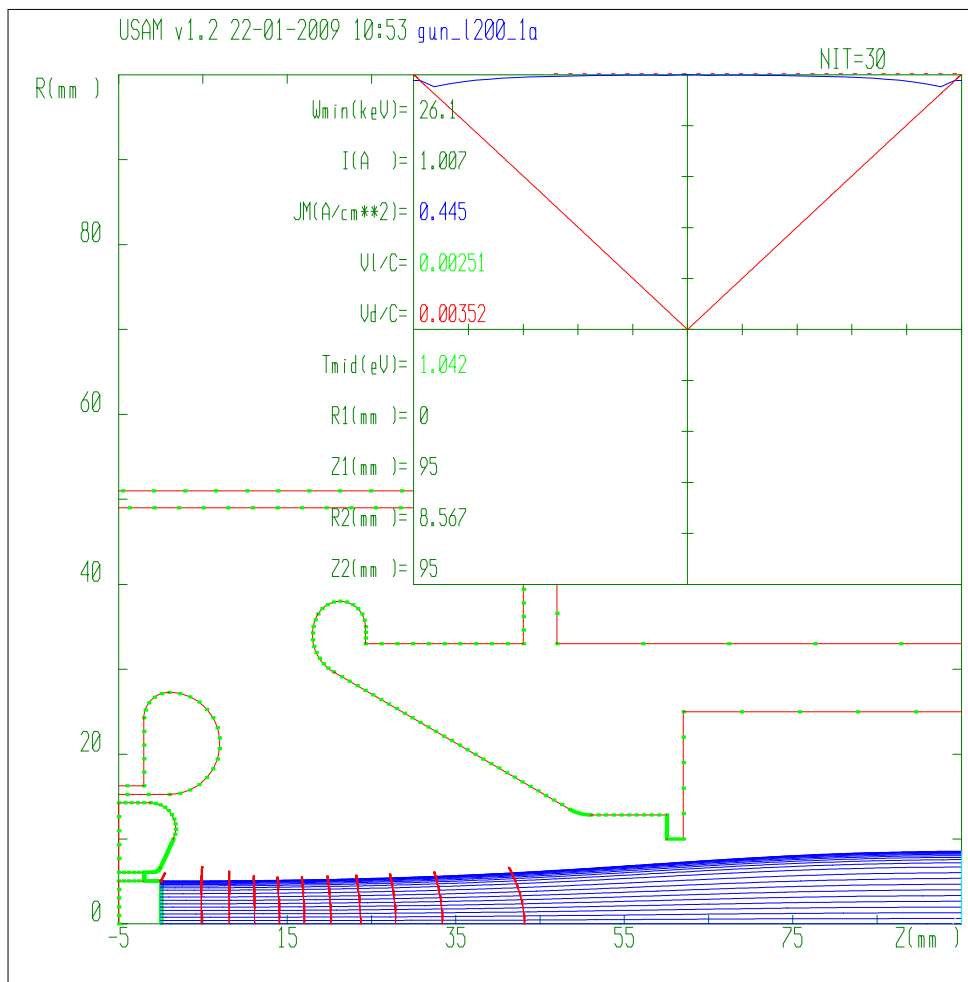


Figure 7-3: Electron trajectories in the gun. The graph shows current density (blue), transverse velocity in Larmor rotations (green) and transverse drift velocity caused by $E \times B$ or un-uniformity of B (red) as a function of radius in the beam at $z = 95$ mm. $U_a = 26$ kV, $U_{ce} = -0.38$ kV, $I = 1$ A. Equipotential lines, $\Delta U = 2.5$ kV

The equivalent transverse electron temperature in the beam can be found by calculating the transverse velocity V_l of the electrons in the Larmor rotations. The program UltraSAM [14] gives V_l/c as function of radius in the beam at a test surface. Excluding the very boundary electrons we obtain $V_l/c = 0.0025$ at $R = 8.5$ mm which gives a transverse electron temperature of 1.6 eV at the exit of the gun. If the linear part of the transverse velocity is subtracted, the remaining temperature is below 0.1 eV.

Because of the strong magnetic field in the gun region, the electron trajectories stay nearly unchanged at proportional variations of the anode voltage U_a and the control electrode voltage U_{ce} . As a result, the gun perveance is determined with a good precision by the ratio of U_a/U_{ce} . Therefore electron trajectories in the gun are not changed if the gun voltage is increased to 50 kV and the control electrode voltage is scaled to -0.72 kV. This gives $I = 2.6$ A.

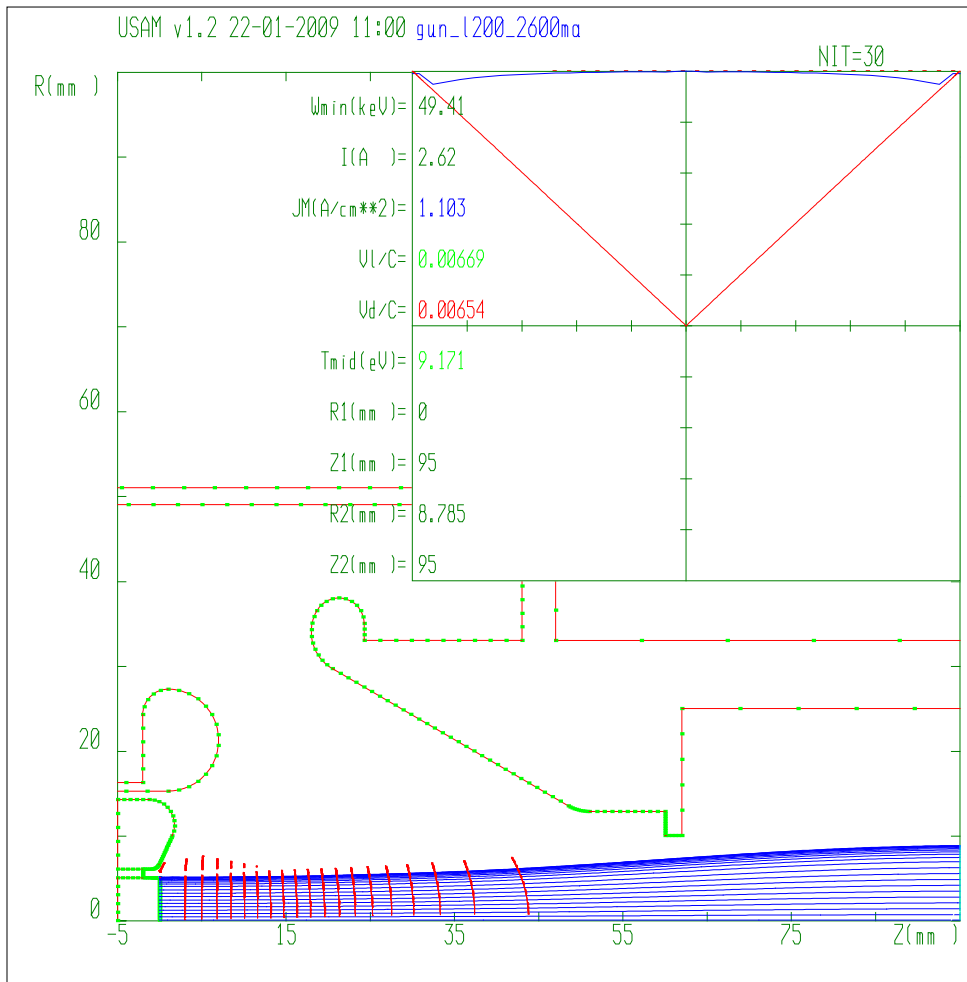


Figure 7-4 Electron trajectories in the gun. $U_a = 50$ kV, $U_{ce} = -0.72$ kV, $I = 2.6$ A. Equipotential lines, $\Delta U = 2.5$ kV.

Note that in shown simulations, the boundary trajectories have characteristics different from the main portion of the beam. The behaviour of trajectories from the cathode edge depends on its sharpness. Here the edge curvature radius was assumed to be 0.1 mm. For estimation of the electron angles, we will ignore the boundary electrons and take as a measure of the maximum electron angles the corresponding value for the outermost trajectory on the flat part of the emitter.

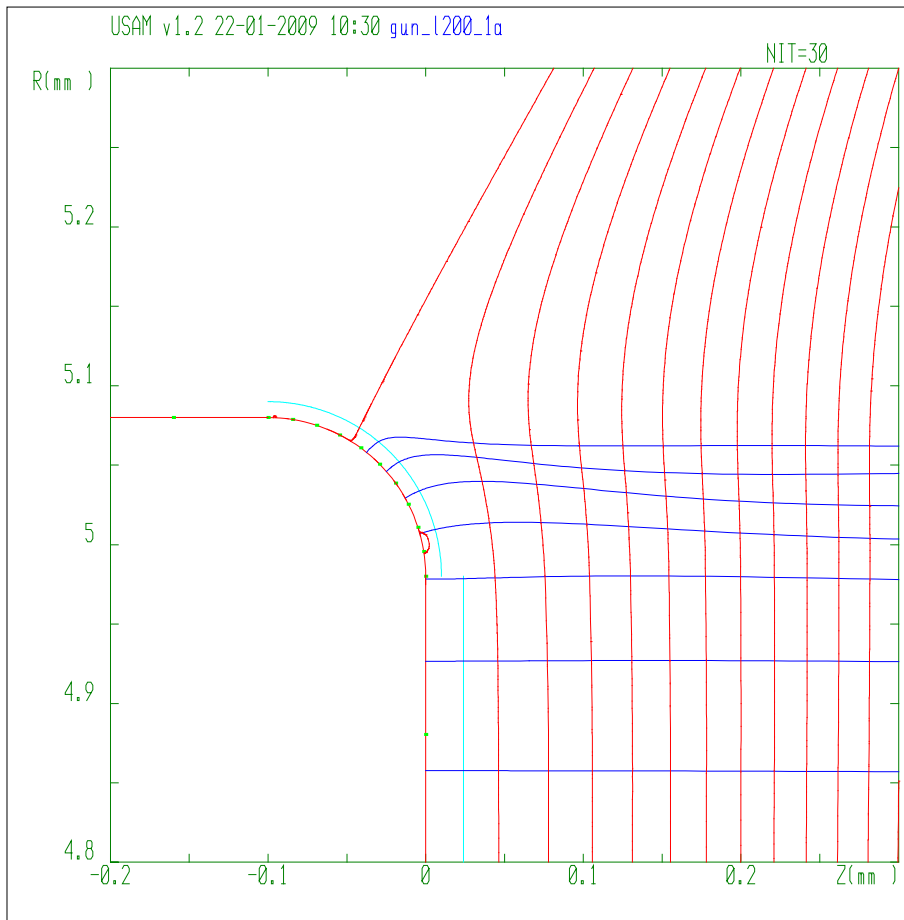


Figure 7-5: Electron trajectories near the cathode edge and equipotential lines starting from $U = 0$ V, $\Delta U = 5$ V.

The increasing density of trajectories close to the cathode edge does not indicate that the current density is increasing, it just a result of decreasing the mesh size towards the edge.

To close the gun at $U_a = 26$ kV, the voltage of -4.5 kV is required at the control electrode. At $U_{ce} = -4.0$ kV a 1 mA pencil beam is obtained.

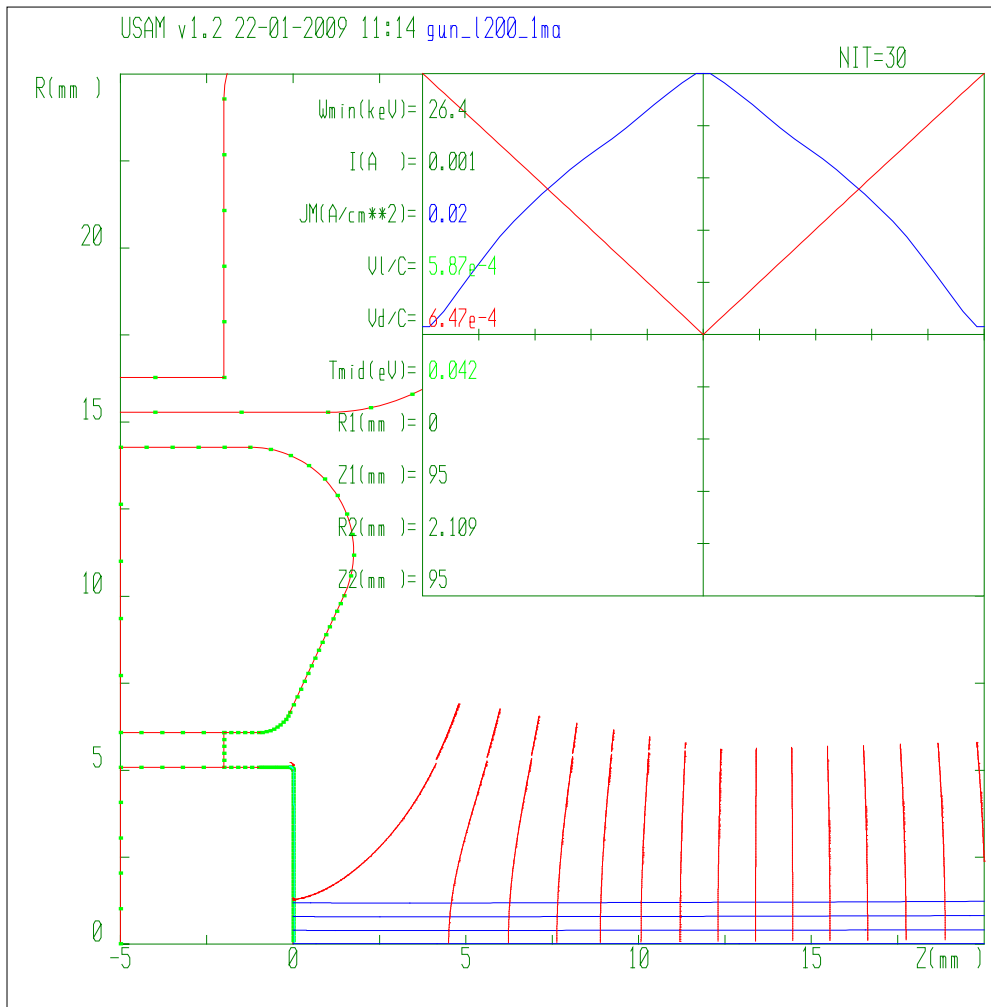


Figure 7-6: Pencil beam 1 mA. Trajectories and equipotential lines starting from $U = 0$, $\Delta U = 1$ kV

7.3 Acceleration column

As already mentioned, the electron beam will be transported in a continuous longitudinal magnetic field in the accelerating columns. The spacing of the focusing solenoids in the high voltage column will affect the electron beam size, which has to pass through the one-inch aperture of the standard NEC accelerating tubes. One has to make sure that the periodic variations of the magnetic and electrical fields do not cause excessive beating of the beam envelope since this would significantly decrease the space between the beam envelope and the tube aperture. Under no circumstances may any part of the halo of the beam hit the accelerating tubes since this would cause a high voltage breakdown. We estimate that an electron beam with diameter 17 mm can be safely transported through the accelerating column, which has an aperture of 25.4 mm.

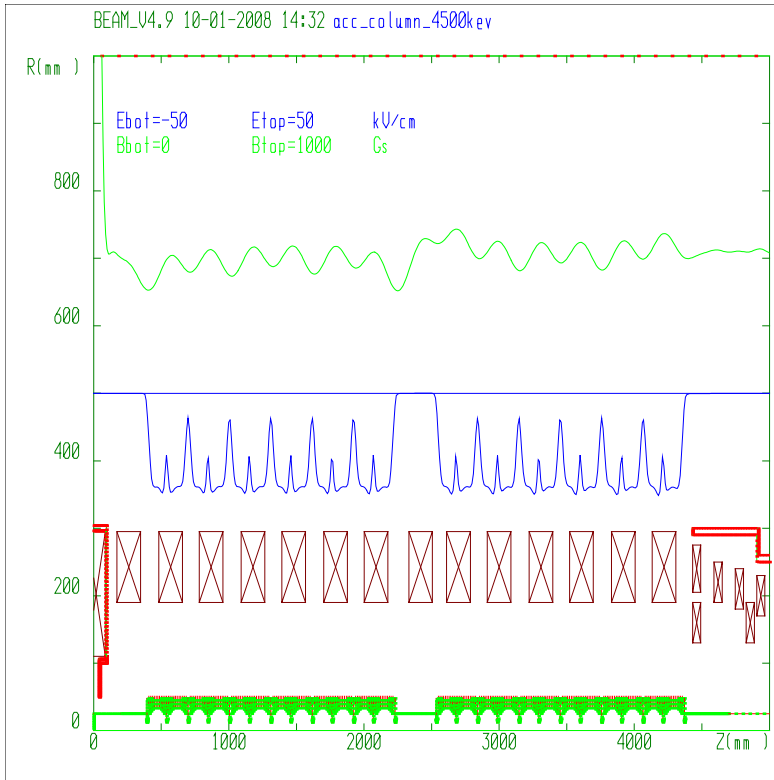


Figure 7-7: Magnetic and electric fields in the acceleration column. The vertical scale is 0 to 1000 gauss for the magnetic field and -50 to +50 kV/cm for the electrical field. Also shown are electrodes (red) and coils (brown).

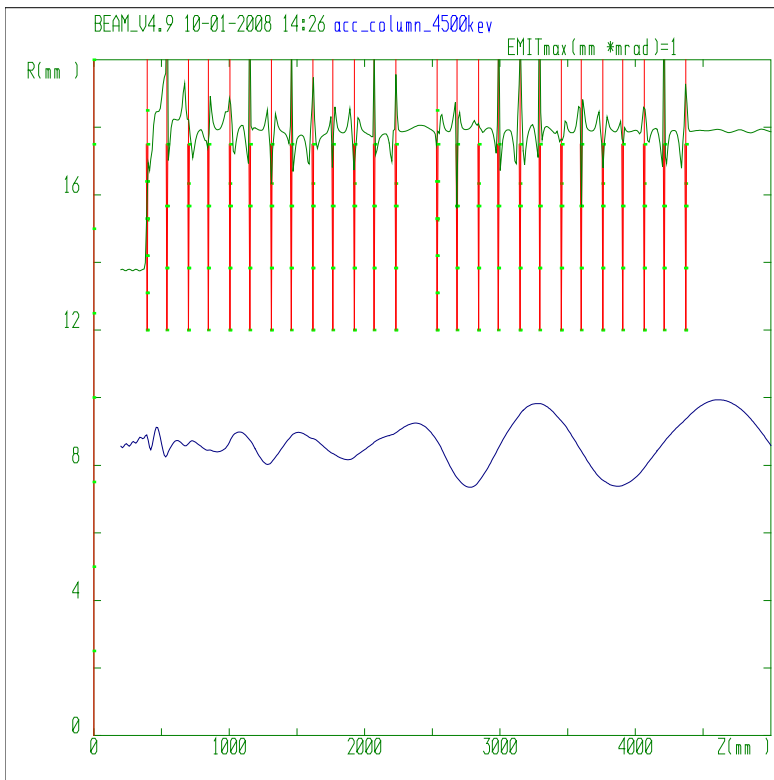


Figure 7-8: Beam envelope in the acceleration column during acceleration to 4.5 MeV.

Figure 7-7 shows the geometry of the solenoids (brown) and electrodes (red) and the resulting magnetic (green) and electric (blue) fields. The solenoids are spaced ≈ 0.305 m centre-to-centre except in so-called dead section where one of the solenoids is shifted 20 mm downstream to allow space for ion pumping.

Figure 7-8 shows the beam envelope (blue) and emittance (green) of a 1 A electron beam during acceleration to 4.5 MeV. Initial beam parameters were obtained from simulations of the electron gun (beam radius 8.5 mm and electron energy 26.4 keV). The beam is influenced by the radial component of the electric field close to the apertures of the acceleration tubes and by the periodic variation of the magnetic field. We observe that the amplitude of the beam envelope oscillations is everywhere less than ± 1.5 mm in radius so the beam stays well inside the available radial aperture of 12.7 mm.

Simulations show that the amplitude of oscillation is smaller at lower energies, as expected since the electric field is then lower.

The simulation shown above was done with the magnetic field as homogenous as possible. It is however possible to reduce the envelope oscillation by introducing a short bump in the magnetic field. A short bump in the magnetic field kicks the beam radially. If the radial kick is applied with correct phase and amplitude the envelope oscillation is cancelled. For this purpose three short solenoids with small radius are installed below the acceleration tube. By tuning one or two of the correction solenoids and observing the beam with the diagnostics in the cooling straight section the remaining envelope oscillation can be reduced to an acceptable level.

7.4 Transition

The change of the electrons transversal temperature after a change of the longitudinal magnetic field from a low field B_1 to a high field B_2 over a given distance $z_2 - z_1$ depends strongly on the function $B_z(z)$ in the transition region. Simulations have shown that minimum increase of the equivalent transversal electron temperature is obtained if the magnetic field in the transition region is approximately given by

$$B_z(z) = B_1 + \Delta B \sin^2\left(\frac{\pi}{2}\varphi^2\right)$$

where $\varphi = (z - z_1)/(z_2 - z_1)$ and $\Delta B = B_2 - B_1$.

The field in the transition section is generated by the coils listed in Table 3-5 and Table 3-6. The current in the solenoids have individual power supplies to generate the desired field. By using individual power supplies in the transition region it is also possible to change ration between the magnetic field in the acceleration tubes and the field in the cooler straight section.

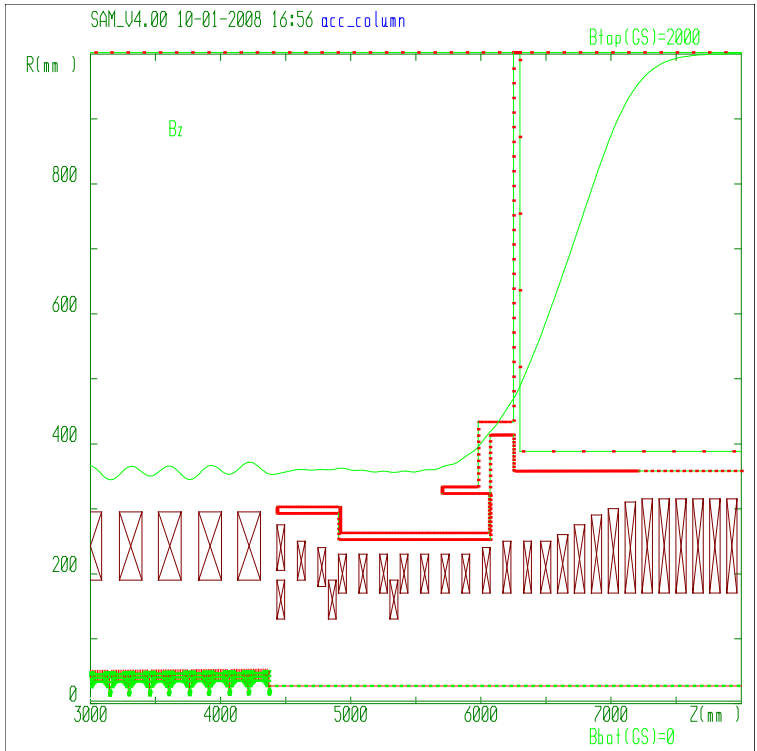


Figure 7-9: Magnetic field on axis in the transition region. z = distance from the cathode. Acceleration ends at $z = 4400$. Field transition takes place at $5200 < z < 7200$. The tank exit takes place at $z = 6100$. The bent solenoid starts at $z = 7500$.

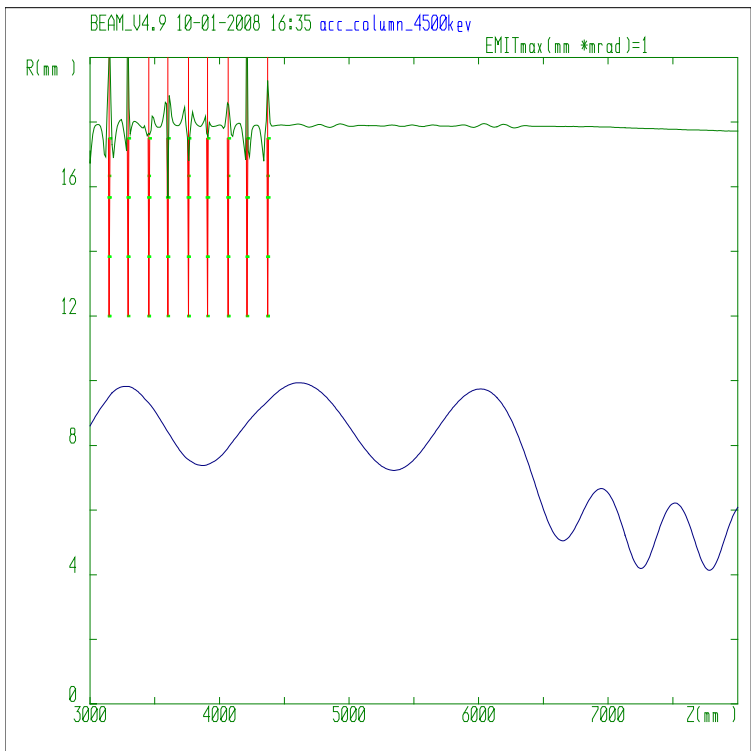


Figure 7-10: Beam envelope in the transition region for 4.5 MeV electrons. The envelope oscillation correction solenoids (the 3 solenoids with smaller radius in Figure 7-9) all have zero current in this simulation.

7.5 Collector

The secondary electrons are suppressed by the transverse magnetic field in the collector cavity [20]. The mechanism of suppression can be explained in terms of a drift of adiabatically moving electrons in a bent longitudinal magnetic field.

The direction of the drift is perpendicular to the plane of bending. If the magnetic field is bent by an angle ϕ , the electrons drift away from the field lines by

$$\Delta = \phi \frac{p_{\parallel}}{eB} \frac{(1 + \cos^2 \alpha)}{2 \cos \alpha} = \phi \frac{p_{\parallel}}{eB} f(\alpha)$$

$f(\alpha)$ is always ≥ 1 .

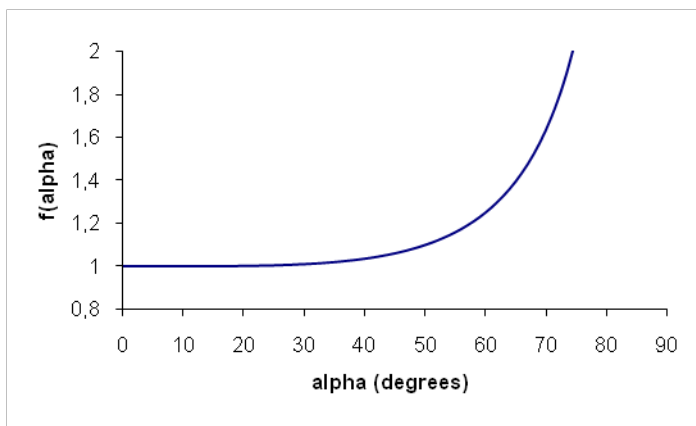


Figure 7-11. $f(\alpha)$ as a function of the pitch angle α

In a simplest model of a 90-degree bend with a nearly constant absolute value of the magnetic field B , the primary beam drifts away from the field lines by

$$\Delta_0 = \frac{\pi p_{\parallel}}{2 eB} \approx \frac{\pi m_e}{2 eB} \sqrt{\frac{2eU_{col}}{m_e}}$$

where U_{col} is the potential of the collector with respect to the cathode. Secondary electrons move backwards along the same field line, and those elastically scattered shift by $\geq \Delta_0$. If the shift of all secondary electrons is large enough, they are missing the entrance opening of the collector and are captured. The farther from the opening the secondary beam hits the wall, the lower is the chance electrons of the next generations (produced of secondary etc. electrons) would escape the collector.

7.5.1 Axially symmetric simulation

An axially symmetric simulation of the collector (i.e. without transverse fields in the cavity) including the effects of space charge gives the potential in the centre of the beam. The difference between the collector potential and the potential minimum in the beam defines the critical energy of a secondary electron to escape from the cavity. An axially symmetrical simulation of the collector gives

$$U_{min} = 3.5 - 2.33 \sim 1.2 \text{ kV for } I = 1 \text{ A.}$$

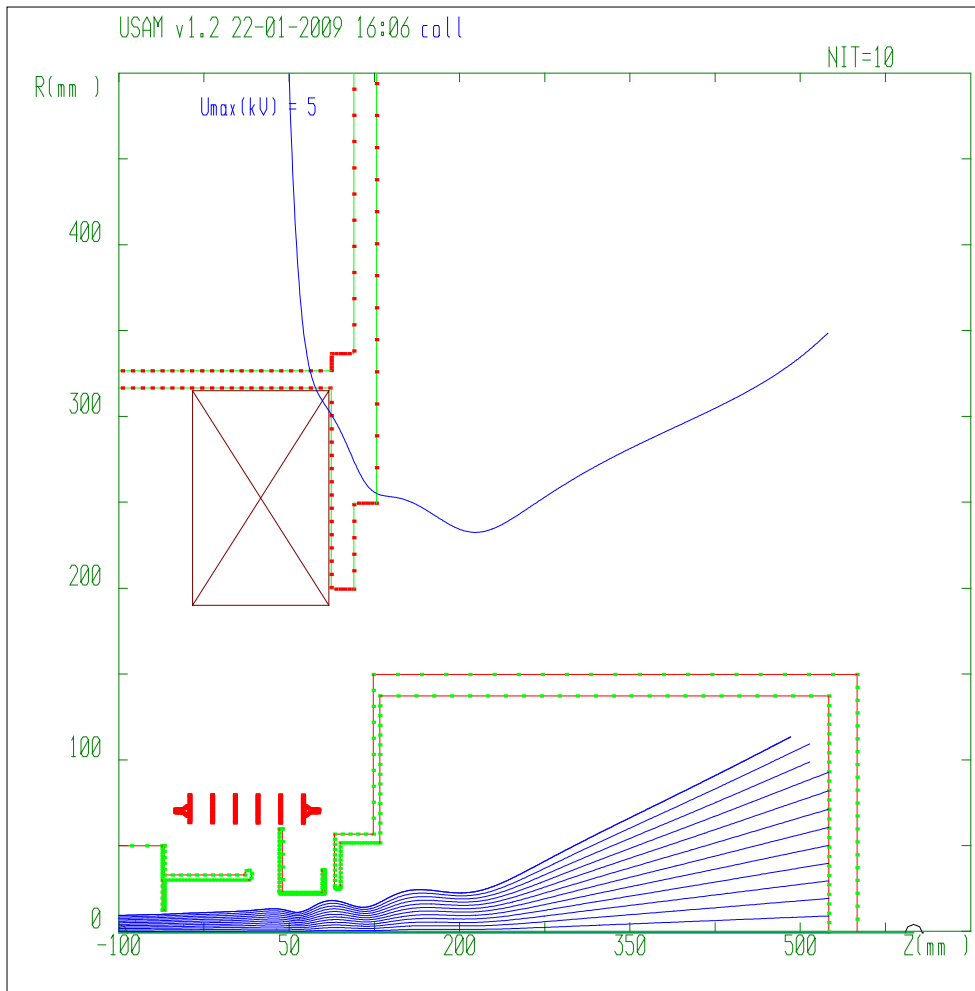


Figure 7-12: axially symmetrical simulation. $U_{\text{anode}} = 26.4 \text{ kV}$, $U_{\text{coll}} = 3.5 \text{ kV}$, $U_{\text{sup}} = 3.5 \text{ kV}$ gives $U_{\text{min}} \sim 1.2 \text{ kV}$

Therefore, the critical secondary particle to be simulated starts from the collector surface with a kinetic energy of $eU_{\text{min}} = 1.2 \text{ keV}$.

7.5.2 Three dimensional simulation

Magnetic fields in the collector region are formed by the terminal separation box solenoids, the short solenoid near the collector entrance (so-called collector lens), and by permanent magnets attached to steel plates near the collector cavity. Combination of these fields creates field lines in the collector cavity that are bent by nearly 90° from the near-axis region to the collector side surface.

Figure 7-13 shows a 3-dimensional simulation of the collector. The view is from the side. Magnetic force lines are shown in green colour. The trajectories of the primary electrons are shown in purple colour. The beam spot size is $\approx 8 \text{ cm}$.

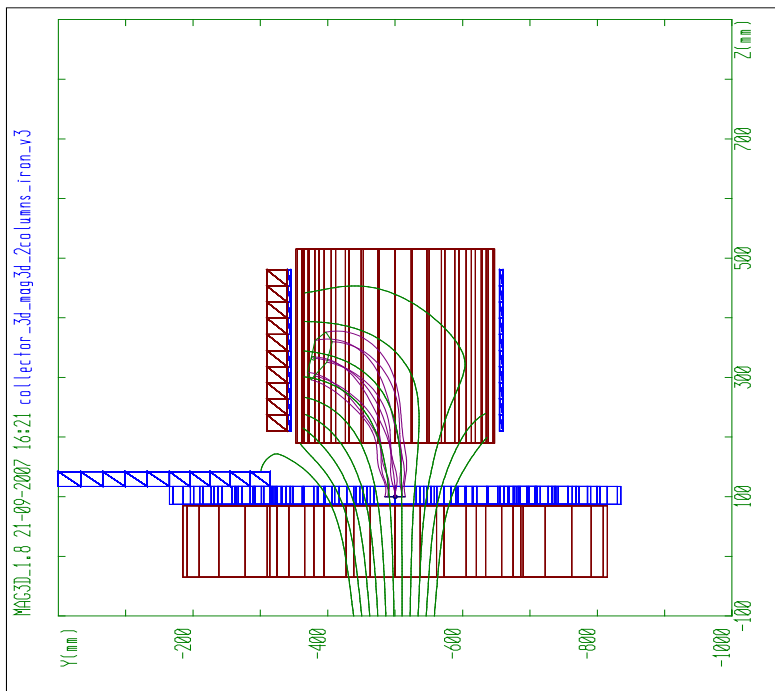


Figure 7-13: 3-D simulation of the collector. Magnetic force lines (green) and trajectories of primary electrons (purple)

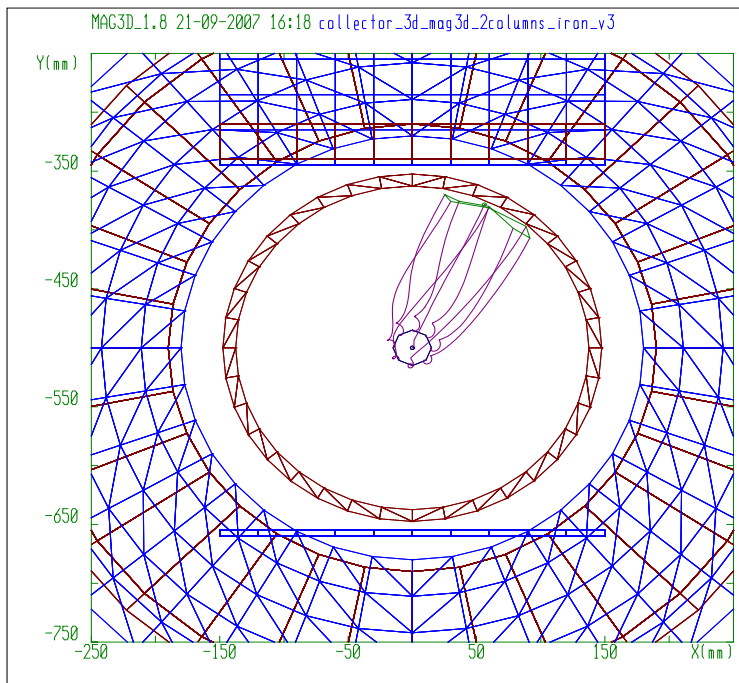


Figure 7-14: 3-D simulation of trajectories of primary electrons in the collector cavity. View from above. The direction of the transverse magnetic field is "up".

A view from above shows the drift of the primary electrons. The direction of the drift is to the right in Figure 7-14. Secondary electrons will drift in the same direction and cannot escape from the collector.

7.6 Envelope oscillations

As shown in Figure 7-8 considerable envelope oscillation is created in the acceleration column by the un-adiabatic variations of electric and magnetic fields. The method to reduce envelope oscillation is to kick the electrons radially by introducing a short bump in the magnetic field with correct amplitude and phase. Any of the solenoids in the tank or in the transition section can be used for elimination of envelope oscillation. However, the kick is most efficient if the characteristic length of the bump is short as compared to the cyclotron wavelength of the electrons. Therefore the coil radius shall be as small as possible for efficient reduction of envelope oscillation at low beam energies. In practice it is difficult to adjust the phase of the bump. It is easier to use two bumps at fixed phases but with adjustable amplitudes.

For this purpose 3 solenoids with small inner radius are mounted below the accelerating and decelerating columns. Control of envelope oscillation is necessary also in the deceleration column to optimize the collector efficiency. Therefore an identical set of correction coils is included also in the decelerating column.

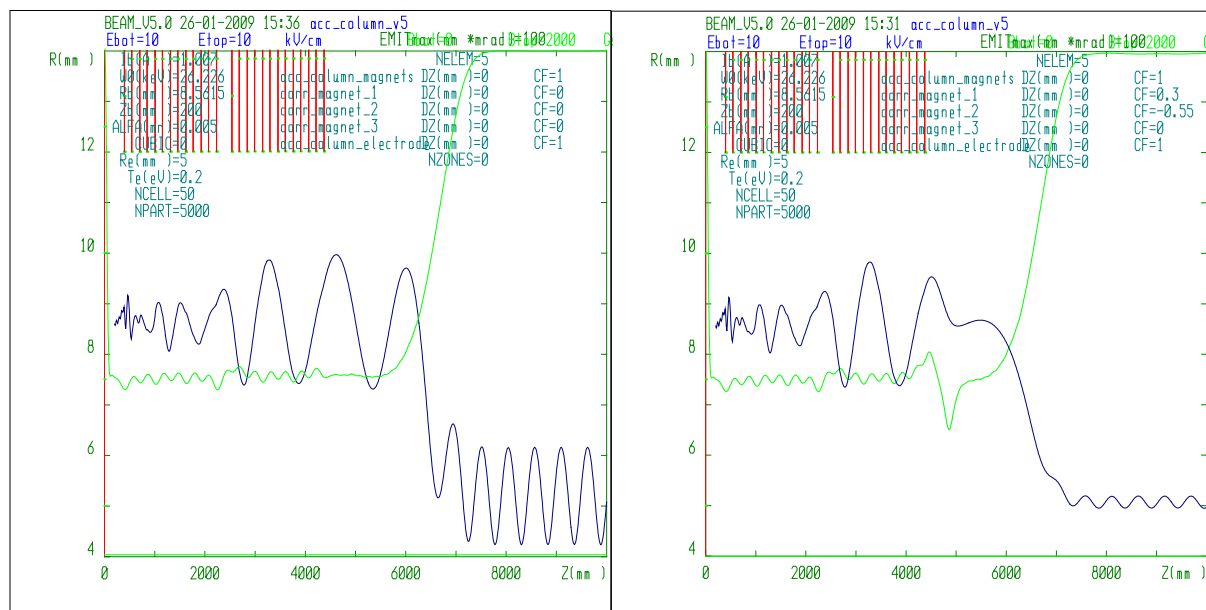


Figure 7-15: Magnetic field (green) and beam envelope (blue) during acceleration and transition. With zero current in the correction coils (left) and with current in two of the correction coils (right)

Figure 7-15 shows the effect of the envelope oscillation correction coils. In the left figure two bumps in the magnetic field have been introduced after acceleration. Coil no 1 at $z = 4460$ has +3000 Ampere-turns and coil no 2 at $z = 4860$ has -5500 Ampere-turns.

7.7 Magnetic flux return

The magnetic flux between the two columns is closed by an iron flux bridge. The flux bridge consists of two iron rings and an iron plate connecting the two rings. Only a minor part of the flux in the decelerating column is entering the collector through a hole in the iron ring. This flux is necessary to create the longitudinal component of the magnetic field in the collector.

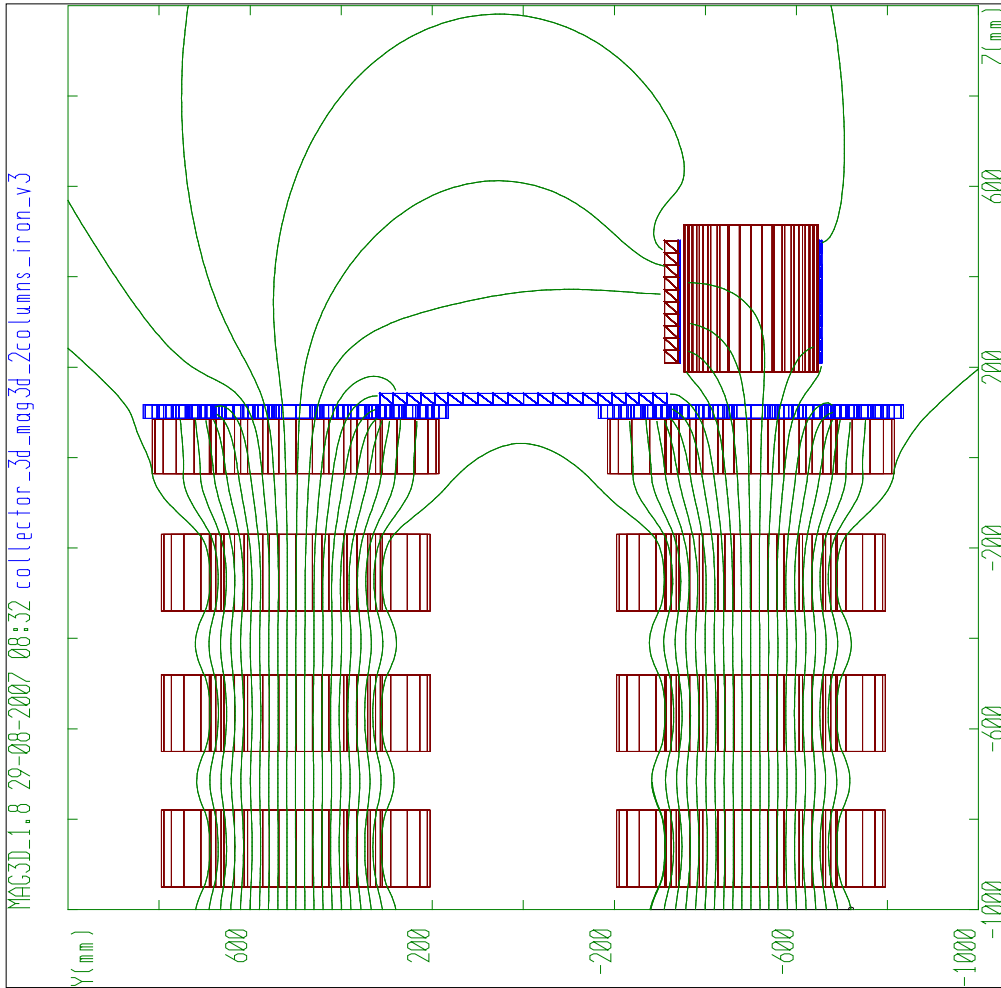


Figure 7-16: Magnetic flux return between the acceleration and deceleration columns

7.8 The solenoid field

7.8.1 The magnetic field of a pancake coil

In Figure 7-17 a schematic drawing of a pancake coil is shown. The vector potential is given by the volume integral

$$\mathbf{A}(\mathbf{x}) = \frac{\mu_0}{4\pi} \int d^3\mathbf{x}' \frac{\mathbf{j}(\mathbf{x}')}{|\mathbf{x}' - \mathbf{x}|}$$

where $\mathbf{j}(\mathbf{x}')$ is the current density. In spherical coordinates (r, φ, z) the location \mathbf{x}' of the source current is related to the point of observation $\mathbf{x} = z\hat{z} + r\hat{r}$ as:

$$\mathbf{x}' = z'\hat{z} + r' \cos(\varphi' - \varphi) \hat{r} + r' \sin(\varphi' - \varphi) \hat{\varphi}$$

Then, with $D\Delta R$ as the cross section of the coil (Figure 7-17) and NI as the total current, the current density is given by

$$\mathbf{j}(\mathbf{x}') = \frac{NI}{\Delta RD} (-\sin(\varphi' - \varphi) \hat{r} + \cos(\varphi' - \varphi) \hat{\varphi})$$

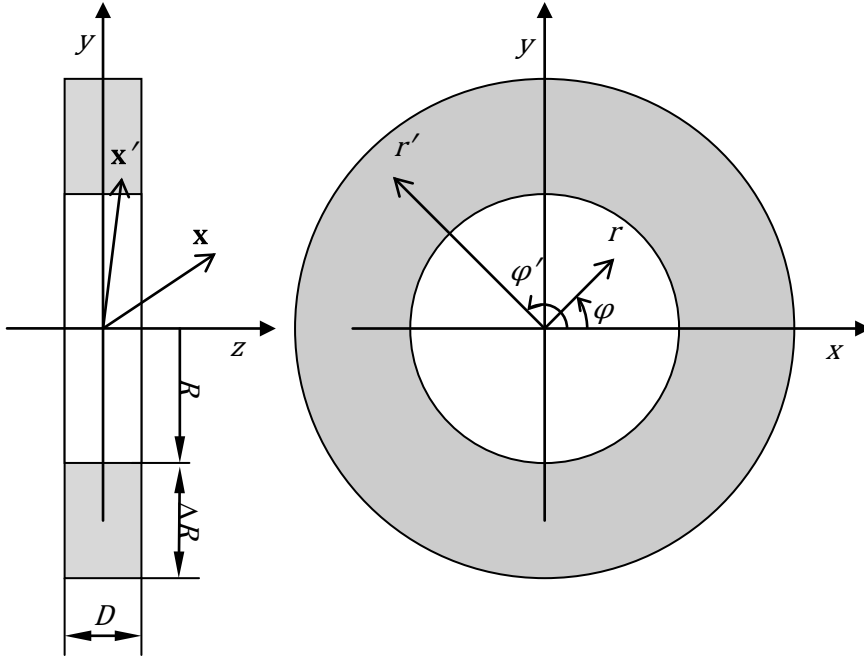


Figure 7-17: Geometry and coordinates of the pancake coil.

The radial component of the vector potential vanishes during integration while the azimuth component is given by an elliptical integral:

$$A_{\varphi}(\mathbf{x}) = \frac{\mu_0 N I}{4\pi} \int_{-D/2}^{D/2} \frac{dz'}{D} \int_R^{R+\Delta R} \frac{r' dr'}{\Delta R} \int_0^{2\pi} \frac{d\varphi' \cos \varphi'}{\sqrt{(z' - z)^2 + r^2 + r'^2 - 2rr' \cos \varphi'}}$$

The beam is small compared to the inner radius of the pancake coil, i.e. $r \ll r'$. Therefore the above expression can be approximated to the first order in r/R as:

$$A_{\varphi}(\mathbf{x}) = \frac{\mu_0 N I r}{4} \int_{-D/2}^{D/2} \frac{dz'}{D} \int_R^{R+\Delta R} \frac{dr'}{\Delta R} \frac{r'^2}{((z' - z)^2 + r'^2)^{3/2}}$$

The magnetic field is given by the curl of the vector potential. Since it is proportional to r the magnetic can be written as

$$\mathbf{B}(\mathbf{x}) = B_z(z) \hat{z} - \frac{r}{2} \frac{\partial B_z(z)}{\partial z} \hat{r}$$

Equation 7.8-1

where the longitudinal component is given by:

$$B_z(z) = \frac{\mu_0 N I}{2} \int_{-D/2}^{D/2} \frac{dz'}{D} \int_R^{R+\Delta R} \frac{dr'}{\Delta R} \frac{r'^2}{((z' - z)^2 + r'^2)^{3/2}}$$

Equation 7.8-2

The integration over the cross section can in principle be carried out analytically as:

$$B_z(z) = \frac{\mu_0 NI}{2D\Delta R} \left\{ \left(z + \frac{D}{2} \right) \ln \left(\frac{R + \Delta R + \sqrt{(R + \Delta R)^2 + \left(z + \frac{D}{2} \right)^2}}{R + \sqrt{R^2 + \left(z + \frac{D}{2} \right)^2}} \right) - \left(z - \frac{D}{2} \right) \ln \left(\frac{R + \Delta R + \sqrt{(R + \Delta R)^2 + \left(z - \frac{D}{2} \right)^2}}{R + \sqrt{R^2 + \left(z - \frac{D}{2} \right)^2}} \right) \right\}$$

Equation 7.8-3

In Figure 7-18 the longitudinal field (Equation 7.8-3) is plotted as a function of the longitudinal coordinate z with the parameters listed in Table 7.8-1.

Table 7.8-1: Parameters of the pancake solenoid

Number of turns:	N	63
Current	I	328 A
Width	D	80 mm
Inner radius	R	170 mm
Height	ΔR	145 mm
Centre to centre distance	L	130 mm
Beam radius	r_0	5 mm

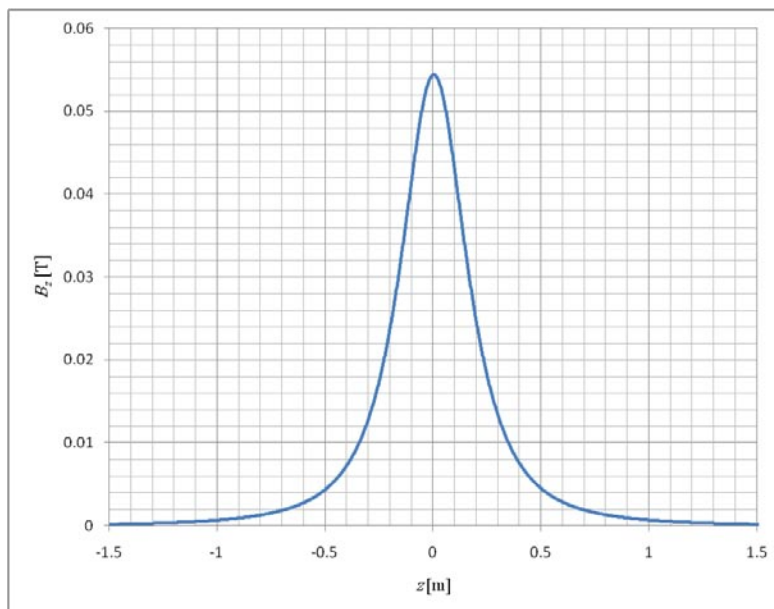


Figure 7-18: The magnetic field of one pancake coil (Equation 7.8-3) vs. the longitudinal coordinate with parameters according to Table 7.8-1.

7.8.2 The solenoid field of a pancake-coil array

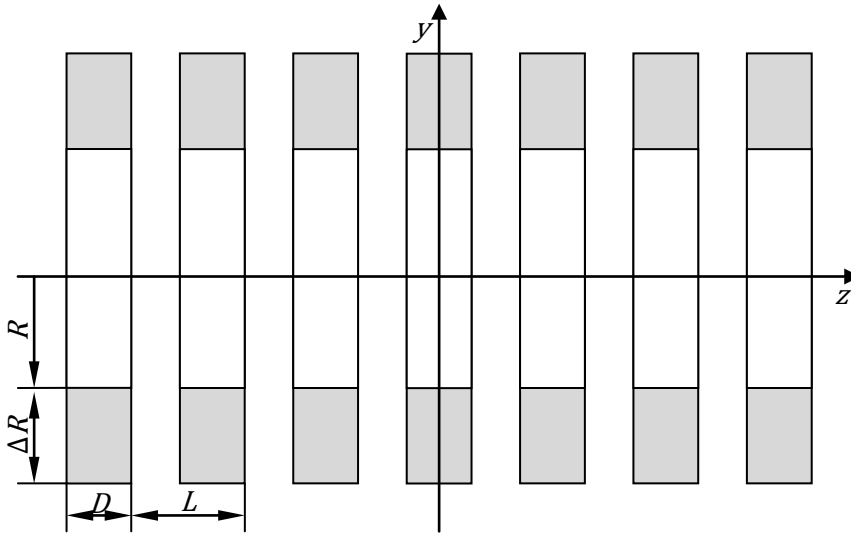


Figure 7-19: The solenoid is made out of an array of pancake coils.

With an infinite number of pancake coils that are equally separated from each other as shown in Figure 7-19, the solenoid field is given by a superposition of Equation 7.8-2:

$$B_s(z) = \sum_{n=-\infty}^{\infty} B_z(z - nL)$$

where L is the center to center distance between pancake coils (Figure 7-19). Since $B_s(z)$ is an even and a periodic function it can be Fourier transformed according to:

$$B_s(z) = B_0 + \sum_{n=1}^{\infty} b_n \cos \frac{2\pi n z}{L}$$

Equation 7.8-4

where the average solenoid field is given as the number of Ampere turns per unit length:

$$B_0 = \frac{\mu_0 NI}{L}$$

Equation 7.8-5

With $NI = 63 \times 328$ A and $L = 130$ mm (Table 7.8-1) the average solenoid field is 0.2 T. The Fourier coefficients are given by

$$b_n = \frac{2}{L} \int_{-\infty}^{\infty} dz B_z(z) \cos \frac{2\pi n z}{L}$$

By inserting Equation 7.8-2 into the above expression and carrying out the integration over z and z' gives:

$$b_n = \frac{2B_0 L}{\pi n D} \sin \left(\frac{\pi n D}{L} \right) \int_R^{R+\Delta R} \frac{dr'}{\Delta R} \frac{2\pi n r'}{L} K_1 \left(\frac{2\pi n r'}{L} \right)$$

Equation 7.8-6

where

$$K_1(x) = \frac{1}{x} \int_0^{\infty} dt \frac{\cos xt}{(t^2 + 1)^{3/2}}$$

is a modified Bessel function of first order. For large arguments, i.e. for $2\pi R/L \gg 1$, the following asymptotic expansion can be used:

$$xK_1(x) \approx \sqrt{\frac{\pi x}{2}} e^{-x} \left\{ 1 + \frac{3}{8x} - \frac{15}{2(8x)^2} + \dots \right\}$$

Then its primitive function can be obtained by partial integration as:

$$\int dx xK_1(x) \approx -\sqrt{\frac{\pi x}{2}} e^{-x} \left\{ 1 + \frac{7}{8x} - \frac{71}{2(8x)^2} + \dots \right\}$$

This function decays exponentially with x and thus only the first order term contributes to the magnetic field. Further, in the case $2\pi\Delta R/L \geq 2$ the upper integration limit in Equation 7.8-6 can be set to infinity. Hence:

$$b_1 \approx \frac{B_0\sqrt{LR}}{\Delta R} \frac{L \sin\left(\frac{\pi D}{L}\right)}{\pi D} e^{-\frac{2\pi R}{L}} \left\{ 1 + \frac{7}{8} \left(\frac{L}{2\pi R}\right) - \frac{71}{128} \left(\frac{L}{2\pi R}\right)^2 + \dots \right\}$$

To the first order approximation the longitudinal force component (Equation 7.8-4) is given by

$$B_s(z) \approx B_0 + \frac{B_0\sqrt{LR}}{\Delta R} \frac{\sin\left(\frac{\pi D}{L}\right)}{\frac{\pi D}{L}} e^{-\frac{2\pi R}{L}} \left\{ 1 + \frac{7}{8} \left(\frac{L}{2\pi R}\right) \right\} \cos\left(\frac{2\pi z}{L}\right)$$

Equation 7.8-7

Then the radial component (Equation 7.8-1) becomes [3]

$$B_r(z, r) \approx \frac{B_0\sqrt{LR}}{\Delta R D} \sin\left(\frac{\pi D}{L}\right) e^{-\frac{2\pi R}{L}} \left\{ 1 + \frac{7}{8} \left(\frac{L}{2\pi R}\right) \right\} \sin\left(\frac{2\pi z}{L}\right) r$$

Equation 7.8-8

These components are plotted in Figure 7-20 and Figure 7-21 with the parameters given by Table 7.8-1.

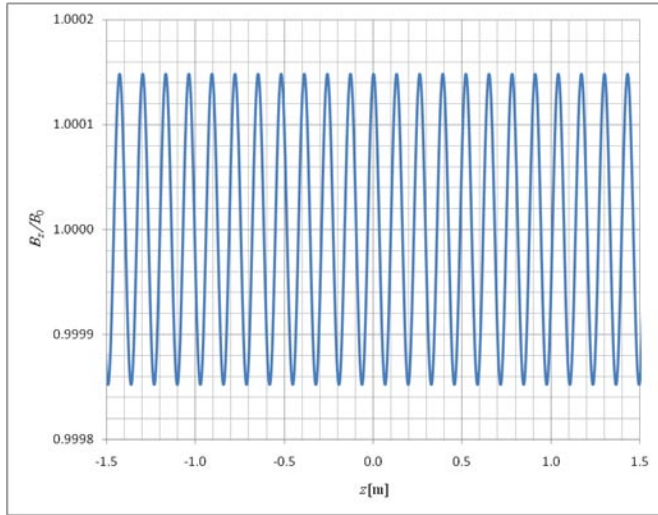


Figure 7-20: The longitudinal component of the solenoid field (Equation 7.8-7) with solenoid parameters from Table 7.8-1.

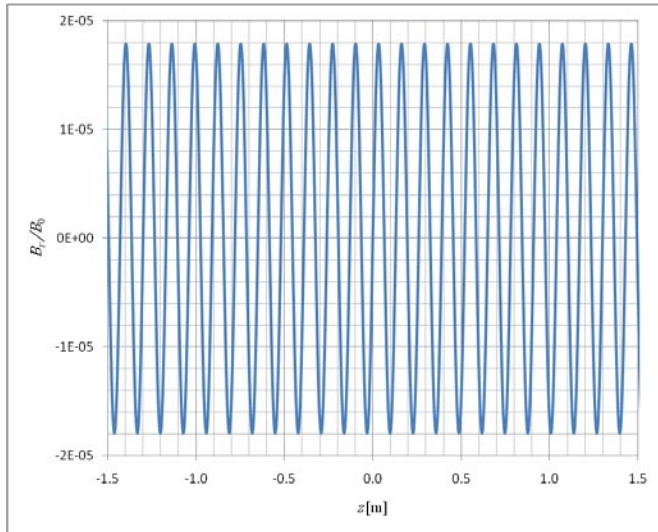


Figure 7-21: The radial component of the solenoid field (Equation 7.8-8) with $r = 5$ mm and solenoid parameters from Table 7.8-1.

7.8.3 The uniformity of the solenoid field

Averaging B_r^2 over the longitudinal coordinate and electron beam cross section,

$$\langle B_r^2 \rangle = \frac{1}{L\pi r_0^2} \int_0^L dz \int_0^{r_0} dr \int_0^{2\pi} r d\varphi B_r^2(z, r)$$

the rms angular divergence $\theta_{\text{rms}} = \sqrt{\langle B_r^2 \rangle / 2B_s^2}$ of the electron beam, per degree of freedom becomes

$$\theta_{\text{rms}} = \frac{r_0 \sqrt{LR}}{2\sqrt{2}D\Delta R} \sin\left(\frac{\pi D}{L}\right) \left\{ 1 + \frac{7}{8} \left(\frac{L}{2\pi R} \right) \right\} e^{-\frac{2\pi R}{L}}$$

Equation 7.8-9

With the solenoid parameters of Table 7.8-1 this rms variation is 0.63×10^{-5} radians, which is within specification. Equation 7.8-9 puts an upper limit on the period L relative to the inner circumference $2\pi R$.

To disentangle errors caused by variation of the field strength from errors introduced by misaligned coils, both the direction and the absolute value of the magnetic field will be measured. The resolution probe must thus be better than the rms variation

$$\frac{\Delta B_s}{B_s} = \frac{L\sqrt{LR}}{\pi\sqrt{2}D\Delta R} \sin\left(\frac{\pi D}{L}\right) e^{-\frac{2\pi R}{L}}$$

which is approximately 10 times larger than θ_{rms} .

7.8.4 Distortion due to longitudinal displacement

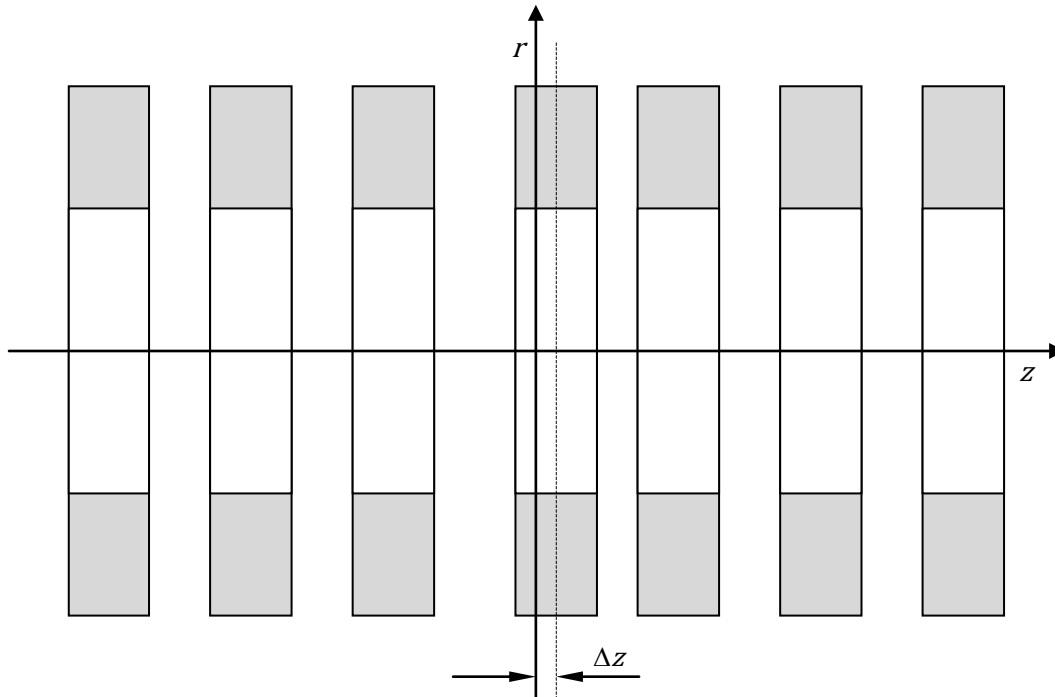


Figure 7-22: One pancake coil is displaced a distance Δz in the longitudinal direction.

Assume that one pancake coil is displaced a distance Δz as shown in Figure 7-22. Then the solenoid field will be altered by

$$\Delta B_z(z) = B_z(z - \Delta z) - B_z(z)$$

where $B_z(z)$ is the contribution from a single coil (Equation 7.8-3) and z is the longitudinal distance from it. Assume that the shift is small. Then, with Equation 7.8-1 the longitudinal and radial field corrections to Equation 7.8-8 become

$$\Delta B_z(z) \approx -\frac{dB_z(z)}{dz} \Delta z$$

$$\Delta B_r(z, r) \approx \frac{d^2 B_z(z)}{dz^2} \frac{r \Delta z}{2}$$

Equation 7.8-10

These distortions are shown in Figure 7-23 and Figure 7-24 with $\Delta z = 0.1$ mm and $r = 5$ mm.

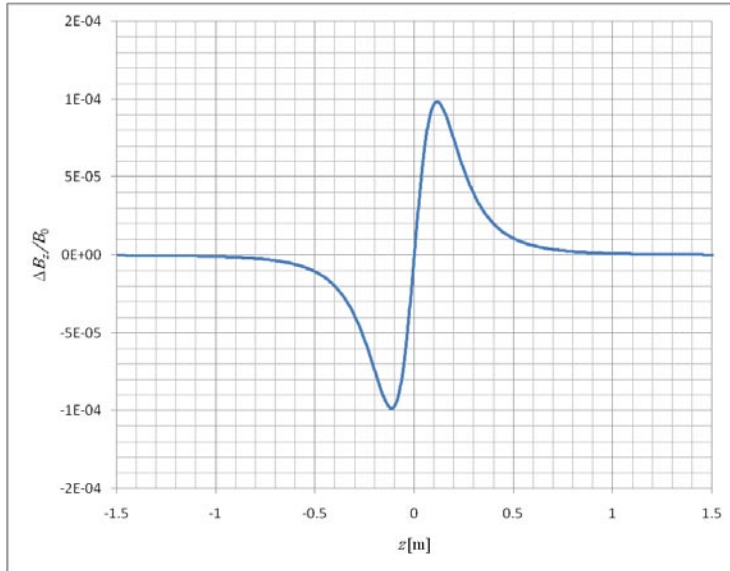


Figure 7-23: The distortion of the longitudinal field component (Equation 7.8-10) due to a 0.1 mm displacement of one pancake coil as a function of the longitudinal coordinate z .

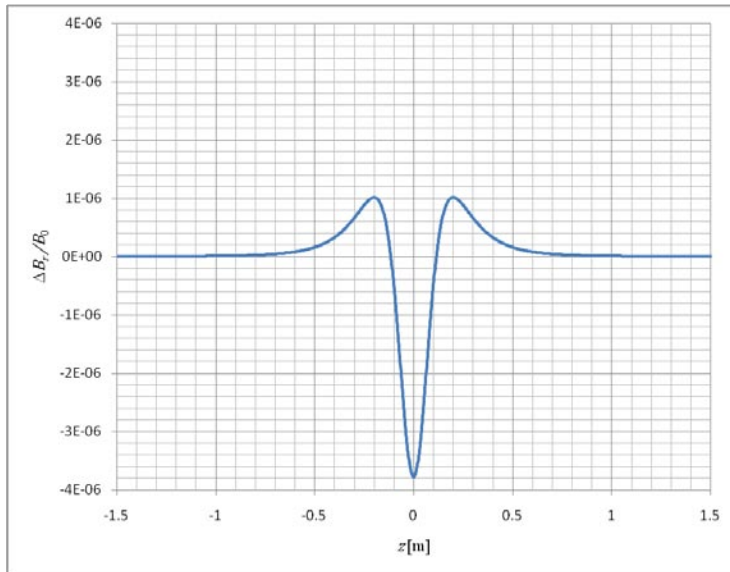


Figure 7-24: The distortion of the radial field component (Equation 7.8-10) at $r = 5$ mm due to a 0.1 mm displacement of one pancake coil plotted as a function of the longitudinal coordinate.

7.8.4.1 Superposition of errors

To obtain the total error of the transverse field caused by the longitudinal displacement of solenoids a superposition over a large number M of pancake coils is carried out:

$$\Delta B_r(z) = \frac{r_0}{4} \sum_{n=-M/2}^{M/2-1} \frac{d^2 B_z(z - nL)}{dz^2} \Delta z_n$$

Equation 7.8-11

where r in Equation 7.8-10 has been replaced with the average radius $r_0/2$. Then, in order to calculate the transverse rms error (per degree of freedom in the transverse plane) it remains to average $|\Delta B_r|^2$ over the longitudinal coordinate:

$$\langle |\Delta B_r|^2 \rangle = \frac{1}{ML} \int_{-ML/2}^{ML/2} dz |\Delta B_r(z)|^2$$

Equation 7.8-12

With the following definition of the Fourier transformation and its inverse

$$\tilde{f}(k) = \int_{-\infty}^{\infty} dz f(z) e^{ikz}$$

Equation 7.8-13

$$f(z) = \frac{1}{2\pi} \int_{-\infty}^{\infty} dk \tilde{f}(k) e^{-ikz}$$

Equation 7.8-14

the Fourier transformation of Equation 7.8-11 becomes:

$$\Delta \tilde{B}_r(k) = -k^2 \tilde{B}_z(k) \frac{r_0}{4} \sum_{n=-M/2}^{M/2-1} \Delta z_n e^{iknL}$$

The relation between the Fourier transformation of $B_z(z)$ in Equation 7.8-2 and the Fourier coefficient b_n given by Equation 7.8-6 can be identified as

$$b_n = \frac{2}{L} \tilde{B}_z\left(\frac{2\pi n}{L}\right)$$

which gives:

$$\tilde{B}_z(k) = \frac{2\mu_0 NI}{kD\Delta R} \sin\left(\frac{kD}{2}\right) \int_R^{R+\Delta R} dr' kr' K_1(kr')$$

Equation 7.8-15

Assuming that the errors are uncorrelated,

$$\frac{1}{M} \sum_{n=-M/2}^{M/2-1} \sum_{m=-M/2}^{M/2-1} \Delta z_n \Delta z_m e^{ik(n-m)L} = \frac{1}{M} \sum_{n=-M/2}^{M/2-1} |\Delta z_n|^2$$

then the Parseval's formula,

$$\int_{-\infty}^{\infty} dz |f(z)|^2 = \frac{1}{2\pi} \int_{-\infty}^{\infty} dk |\tilde{f}(k)|^2$$

Equation 7.8-16

implies that the average radial component Equation 7.8-12 is related to the r.m.s. displacement as

$$\langle |\Delta B_r|^2 \rangle = \langle |\Delta z_n|^2 \rangle \frac{1}{2\pi L} \int_{-\infty}^{\infty} dk \left| \frac{r_0 k^2 \tilde{B}_z(k)}{4} \right|^2$$

Hence, the angular divergence of the solenoid field is given by

$$\theta_{\text{rms}} = \alpha \Delta z_{\text{rms}}$$

where

$$\alpha = \sqrt{\frac{1}{2\pi L} \int_{-\infty}^{\infty} dk \left| \frac{r_0 k^2 \tilde{B}_z(k)}{4B_0} \right|^2}$$

For the parameters given in Table 7.8-1, $\alpha = 0.018$ rad/m which implies that $\Delta z_{\text{rms}} = 5 \times 10^{-4}$ m results in an angular divergence equal to $\theta_{\text{rms}} = 9.1 \times 10^{-6}$ radians.

7.8.4.2 Correction

The field errors caused by longitudinal displacement of pancake coils can be corrected provided that the absolute value of the field errors ΔB_s can be accurately measured and that the solenoids are adjustable. This requires some modifications to the present design (section 3.2.1). To resolve Δz_n the method of inverse convolution is used. It is a standard technique used in for example optics.

The longitudinal field perturbation is obtained as a superposition of errors from a large number of pancake solenoids

$$\Delta B_s(z) = \sum_{n=-\infty}^{\infty} -\frac{dB_z(z-nL)}{dz} \Delta z_n$$

Equation 7.8-17

The Fourier transform (Equation 7.8-13) is given by

$$\Delta \tilde{B}_s(k) = ik \tilde{B}_z(k) \sum_{n=-\infty}^{\infty} \Delta z_n e^{iknL}$$

This implies that the ratio $\Delta \tilde{B}_s(k)$ to $ik \tilde{B}_z(k)$ is periodic in k with period $2\pi/L$. Therefore, the errors can be resolved as

$$\Delta z_n = \frac{L}{2\pi} \int_{-\pi/L}^{\pi/L} dk \frac{\Delta \tilde{B}_s(k)}{ik \tilde{B}_z(k)} e^{-iknL}$$

Equation 7.8-18

except for a constant average shift corresponding to $k = 0$, which cannot be determined. By defining a function $f(z)$ as

$$f(z) = \frac{1}{2\pi} \int_{-\pi/L}^{\pi/L} dk \frac{L}{ik \tilde{B}_z(k)} e^{-ikz}$$

Equation 7.8-18 can be expressed as a convolution between $f(z)$ and the measured field errors:

$$\Delta z_n = \int_{-\infty}^{\infty} dz f(z) \Delta B_s(nL - z)$$

Hence, measuring the field errors $\Delta B_s(z)$ along the interaction straight and carrying out the above intergration with $f(z)$ as a known function, the longitudinal displacements can be determined and corrected for.

Equation 7.8-19

7.8.5 Distortions due to deflection of pancake coils

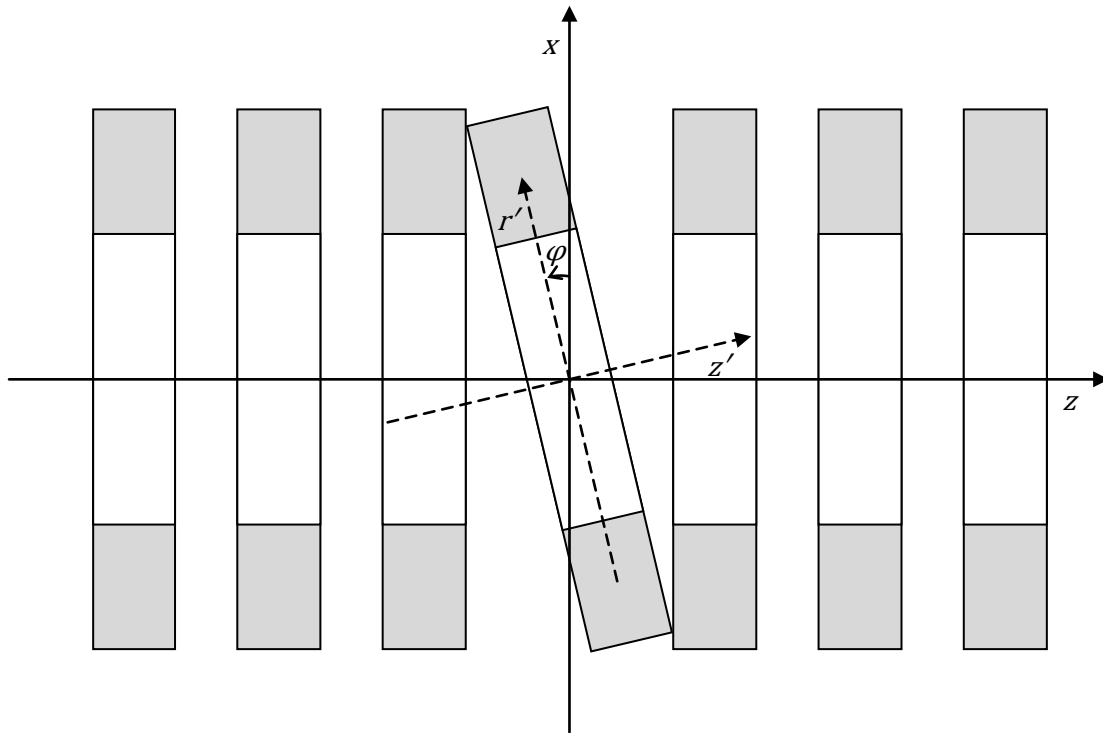


Figure 7-25: Tilt of one pancake coil

A coil which is deflected an angle φ as shown in Figure 7-25 causes a deflection of the solenoid field. The magnetic field along the z -axis created by deflected pancake coil is given by

$$\mathbf{B}(\mathbf{x}) = B_z(z')\hat{z}' - \frac{r'}{2} \frac{\partial B_z(z')}{\partial z'} \hat{r}'$$

where $\mathbf{x} = z\hat{z}$ and

$$z' = z \cos \varphi$$

$$r' = -z \sin \varphi$$

are the coordinates relative to the deflected coil (Figure 7-25) The relation between the unit vectors of the two systems reads

$$\hat{z}' = \hat{z} \cos \varphi + \hat{x} \sin \varphi$$

$$\hat{r}' = -\hat{z} \sin \varphi + \hat{x} \cos \varphi$$

To the first order in φ the transverse component of the magnetic field becomes:

$$\Delta B_x(z) = \left(B_z(z) + \frac{z}{2} \frac{\partial B_z(z)}{\partial z} \right) \varphi$$

Equation 7.8-20

This deflection is shown in Figure 7-26 for $\varphi = 10^{-4}$ radians

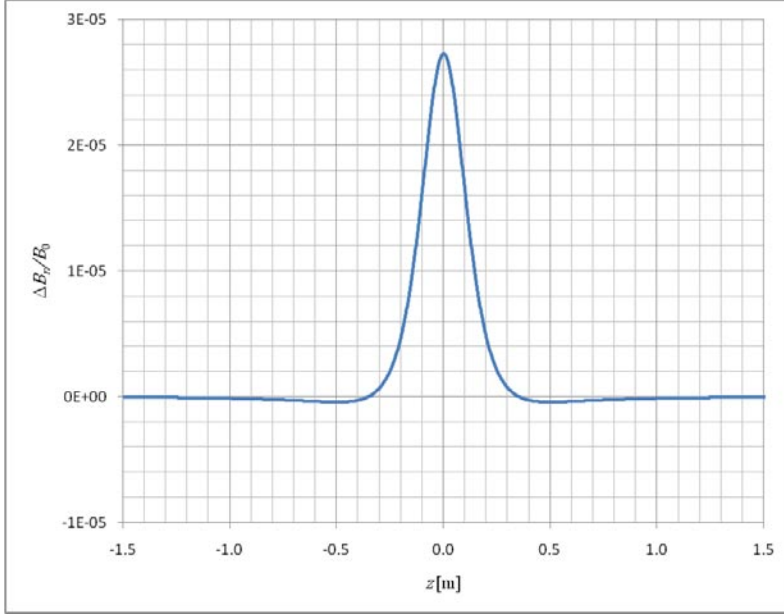


Figure 7-26: The transverse field (Equation 7.8-20) along the symmetry axis caused by a 10^{-4} radian deflection of one pancake coil.

Using the same method as in section 7.8.4.1 the total field component with contributions from a large number of pancake coils

$$B_x(z) = \sum_{n=-M/2}^{M/2-1} \left(B_z(z - nL) + \frac{z - nL}{2} \frac{\partial B_z(z - nL)}{\partial z} \right) \varphi_n$$

can be Fourier transformed as

$$\tilde{B}_x(k) = \frac{1}{2} \left(\tilde{B}_z(k) - k \frac{d\tilde{B}_z(k)}{dk} \right) \sum_{n=-M/2}^{M/2-1} \varphi_n e^{iknL}$$

Assuming that the errors φ_n are uncorrelated and using the Parseval formula (Equation 7.8-16) the variance

$$\langle |B_x|^2 \rangle = \frac{1}{ML} \int_{-M/2}^{M/2} dz |B_x(z)|^2$$

can be calculated as

$$\langle |B_x|^2 \rangle = \frac{\langle |\varphi|^2 \rangle}{2\pi L} \int_{-\infty}^{\infty} dk \left| \frac{1}{2} \left(\tilde{B}_z(k) - k \frac{d\tilde{B}_z(k)}{dk} \right) \right|^2$$

Hence, the rms angle $\theta_{rms} = \sqrt{\langle |B_x|^2 \rangle / B_0^2}$ of the solenoid field is related to the angular rms error of the pancake coils as

$$\theta_{rms} = \beta \varphi_{rms}$$

where

$$\beta = \sqrt{\frac{1}{2\pi L} \int_{-\infty}^{\infty} dk \left| \frac{1}{2B_0} \left(\tilde{B}_z(k) - k \frac{d\tilde{B}_z(k)}{dk} \right) \right|^2}$$

Calculation of the scaling factor with solenoid parameters of Table 7.8-1 gives $\beta = 0.32$. This implies that the angle of the pancake coils needs to have an rms value smaller than 3×10^{-5} radians to meet the requirement for the straightness of the solenoid field.

By measuring the direction of the magnetic field along the symmetry axis, the errors can be determined and corrected by deflecting the pancake coils. Using the same method as in 7.8.4.2, the inverse convolution of the field errors can be obtained as

$$\varphi_n = \int_{-\infty}^{\infty} dz g(z) B_x(nL - z)$$

Equation 7.8-21

where

$$g(z) = \frac{1}{2\pi} \int_{-\pi/L}^{\pi/L} dk \frac{2Le^{-ikz}}{\tilde{B}_z(k) - k \frac{d\tilde{B}_z(k)}{dk}}$$

7.8.6 Distortion due to transverse displacement

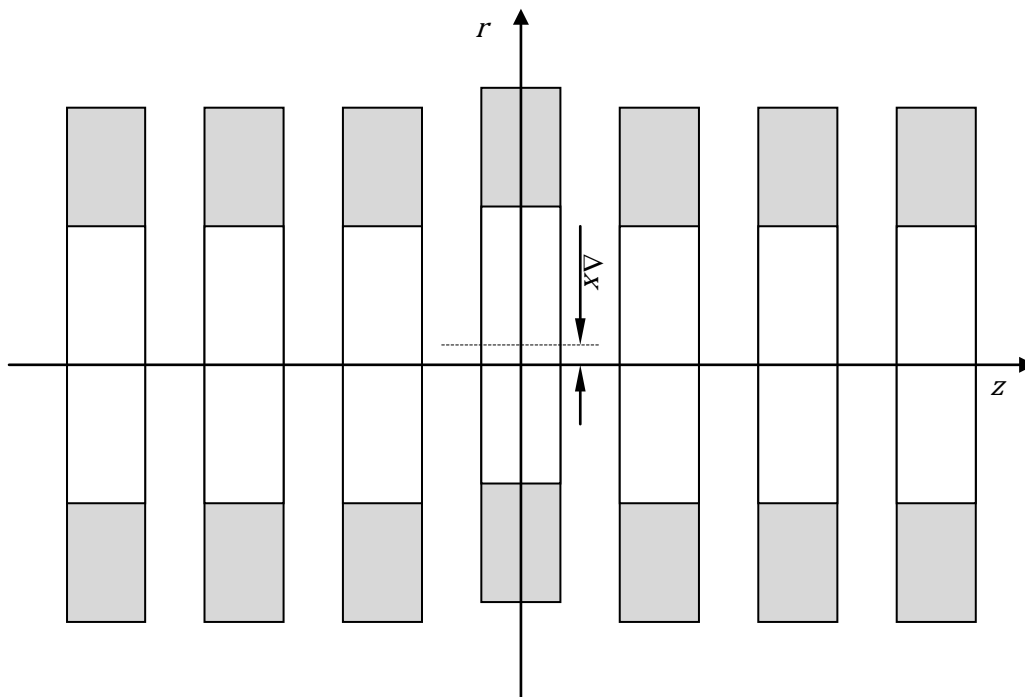


Figure 7-27: Transverse displacement Δr of one pancake coil

The solenoid field in Equation 7.8-8 is valid if the coils are uniformly distributed along and centered about the symmetry axis. Assume that one pancake coil is off center a distance Δx as shown in Figure 7-22. Then the total solenoid field will be altered by

$$\Delta \mathbf{B}(\mathbf{x}) = \mathbf{B}(\mathbf{x} - \Delta \mathbf{x}) - \mathbf{B}(\mathbf{x})$$

where \mathbf{B} is the contribution from one pancake coil. Insertion of $\Delta\mathbf{x} = \Delta r \hat{x}$ into the above equation together with Equation 7.8-1 shows that the transverse displacement of the pancake coil results in a field component in the same direction:

$$B_x(z) = \frac{1}{2} \frac{\partial B_z(z)}{\partial z} \Delta r$$

Equation 7.8-22

This transverse field is shown in Figure 7-28 for $\Delta r = 0.1$ mm with solenoid parameters given by Table 7.8-1.

Using the same method as in sections 7.8.4.1 and 7.8.5 the rms angle of the magnetic field can be related to the rms displacement of the pancake coils as

$$\theta_{rms} = \gamma \Delta r_{rms}$$

where

$$\gamma = \sqrt{\frac{1}{2\pi L} \int_{-\infty}^{\infty} dk \left| \frac{k \tilde{B}_z(k)}{2B_0} \right|^2}$$

is equal to 0.8 radians per meter (Table 7.8-1). Therefore, to achieve a straightness of the magnetic field of the level of 10^{-5} radians along the interaction straight the coils needs to be correctly positioned to a 0.01 mm precision!

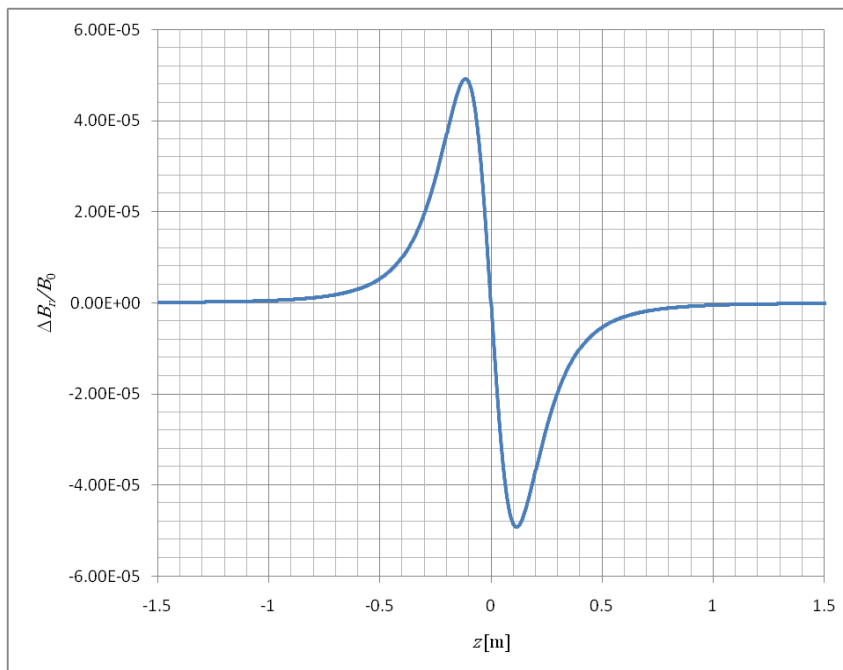


Figure 7-28: The transverse distortion of the solenoid field due to a 0.1 mm transverse displacement of one pancake coil.

The question is how much of the distortion that can be corrected for by deflecting pancake coils, which is the planned method for correction of field errors. The angles φ_n are obtained by inserting $B_x(z)$ calculated from Equation 7.8-22 into Equation 7.8-21. The field after correction is shown in

Figure 7-29. It shows that a large part of the perturbation caused by a transverse displacement of a coil indeed can be corrected by deflecting pancake coils, but not entirely.

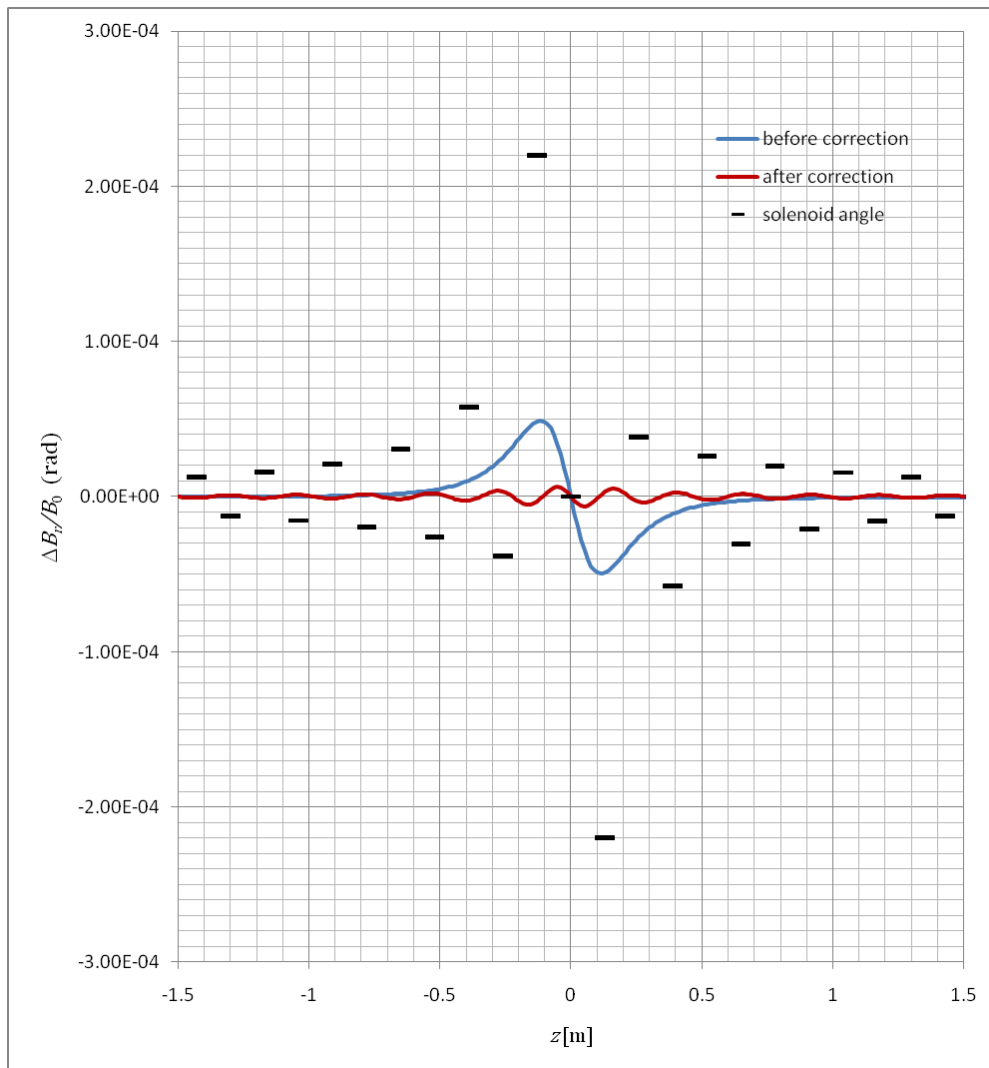


Figure 7-29: The field error caused by a 0.1 mm transverse displacement of one pancake coil (blue). The field error after correction (red) by adjusting the angles of pancake coils (black).

To calculate both the transverse displacement of coil centre and angles based on data from magnetic field measurements is rather complicated to carry but necessary. The transverse component of the magnetic field in this case is given by

$$B_x(z) = \sum_{n=-M/2}^{M/2-1} a(z - nL)\varphi_n + b(z - nL)\Delta r_n$$

where the contribution from angular errors

$$a(z) = B_z(z) + \frac{z}{2} \frac{\partial B_z(z)}{\partial z}$$

Equation 7.8-23

is an even function while the contribution from displacement of the centre

$$b(z) = \frac{1}{2} \frac{\partial B_z(z)}{\partial z}$$

Equation 7.8-24

is odd.

The Fourier transform of the magnet field then becomes

$$\tilde{B}_x(k) = \tilde{a}(k) \sum_{n=-\infty}^{\infty} \varphi_n e^{iknL} + \tilde{b}(k) \sum_{n=-\infty}^{\infty} \Delta r_n e^{iknL}$$

The periodicity in k implies:

$$\tilde{B}_x\left(k + \frac{2\pi}{L}\right) = \tilde{a}\left(k + \frac{2\pi}{L}\right) \sum_{n=-\infty}^{\infty} \varphi_n e^{iknL} + \tilde{b}\left(k + \frac{2\pi}{L}\right) \sum_{n=-\infty}^{\infty} \Delta r_n e^{iknL}$$

In this way an equation system is obtained which can be solved as:

$$\begin{cases} \sum_{n=-\infty}^{\infty} \varphi_n e^{iknL} = \frac{\tilde{B}_x(k)\tilde{b}\left(k + \frac{2\pi}{L}\right) - \tilde{B}_x\left(k + \frac{2\pi}{L}\right)\tilde{b}(k)}{\tilde{a}(k)\tilde{b}\left(k + \frac{2\pi}{L}\right) - \tilde{a}\left(k + \frac{2\pi}{L}\right)\tilde{b}(k)} \\ \sum_{n=-\infty}^{\infty} \Delta r_n e^{iknL} = \frac{-\tilde{B}_x(k)\tilde{a}\left(k + \frac{2\pi}{L}\right) + \tilde{B}_x\left(k + \frac{2\pi}{L}\right)\tilde{a}(k)}{\tilde{a}(k)\tilde{b}\left(k + \frac{2\pi}{L}\right) - \tilde{a}\left(k + \frac{2\pi}{L}\right)\tilde{b}(k)} \end{cases}$$

The inverse discrete Fourier transform then gives:

$$\begin{cases} \varphi_n = \frac{L}{2\pi} \int_{-2\pi/L}^0 dk e^{-iknL} \frac{\tilde{B}_x(k)\tilde{b}\left(k + \frac{2\pi}{L}\right) - \tilde{B}_x\left(k + \frac{2\pi}{L}\right)\tilde{b}(k)}{\tilde{a}(k)\tilde{b}\left(k + \frac{2\pi}{L}\right) - \tilde{a}\left(k + \frac{2\pi}{L}\right)\tilde{b}(k)} \\ \Delta r_n = \frac{L}{2\pi} \int_{-2\pi/L}^0 dk e^{-iknL} \frac{-\tilde{B}_x(k)\tilde{a}\left(k + \frac{2\pi}{L}\right) + \tilde{B}_x\left(k + \frac{2\pi}{L}\right)\tilde{a}(k)}{\tilde{a}(k)\tilde{b}\left(k + \frac{2\pi}{L}\right) - \tilde{a}\left(k + \frac{2\pi}{L}\right)\tilde{b}(k)} \end{cases}$$

With

$$\tilde{B}_x(k) = \int_{-\infty}^{\infty} dz B_x(z) e^{ikz}$$

one has

$$\begin{cases} \varphi_n = \int_{-\infty}^{\infty} dz B_x(z) \frac{L}{2\pi} \int_{-2\pi/L}^0 dk \frac{e^{ik(z-nL)}\tilde{b}\left(k + \frac{2\pi}{L}\right) - e^{i\left(k + \frac{2\pi}{L}\right)(z-nL)}\tilde{b}(k)}{\tilde{a}(k)\tilde{b}\left(k + \frac{2\pi}{L}\right) - \tilde{a}\left(k + \frac{2\pi}{L}\right)\tilde{b}(k)} \\ \Delta r_n = \int_{-\infty}^{\infty} dz B_x(z) \frac{L}{2\pi} \int_{-2\pi/L}^0 dk \frac{-e^{ik(z-nL)}\tilde{a}\left(k + \frac{2\pi}{L}\right) + e^{i\left(k + \frac{2\pi}{L}\right)(z-nL)}\tilde{a}(k)}{\tilde{a}(k)\tilde{b}\left(k + \frac{2\pi}{L}\right) - \tilde{a}\left(k + \frac{2\pi}{L}\right)\tilde{b}(k)} \end{cases}$$

Finally, the angles and the centre displacements can be written as

$$\begin{cases} \varphi_n = \int_{-\infty}^{\infty} dz B_x(z) g_\varphi(nL - z) \\ \Delta r_n = \int_{-\infty}^{\infty} dz B_x(z) g_{\Delta r}(nL - z) \end{cases}$$

Equation 7.8-25

where

$$\begin{cases} g_\varphi(z) = \frac{L}{2\pi} \int_{-\pi/L}^{\pi/L} dk \frac{\tilde{b}\left(k + \frac{\pi}{L}\right) e^{-i(k-\pi/L)z} - \tilde{b}\left(k - \frac{\pi}{L}\right) e^{-i(k+\pi/L)z}}{\tilde{a}\left(k - \frac{\pi}{L}\right) \tilde{b}\left(k + \frac{\pi}{L}\right) - \tilde{a}\left(k + \frac{\pi}{L}\right) \tilde{b}\left(k - \frac{\pi}{L}\right)} \\ g_{\Delta r}(z) = \frac{L}{2\pi} \int_{-\pi/L}^0 dk \frac{-\tilde{a}\left(k + \frac{\pi}{L}\right) e^{-i(k-\pi/L)z} + \tilde{a}\left(k - \frac{\pi}{L}\right) e^{-i(k+\pi/L)z}}{\tilde{a}\left(k - \frac{\pi}{L}\right) \tilde{b}\left(k + \frac{\pi}{L}\right) - \tilde{a}\left(k + \frac{\pi}{L}\right) \tilde{b}\left(k - \frac{\pi}{L}\right)} \end{cases}$$

Equation 7.8-26

With these two functions calculated, the errors caused by deflection and displacement can be distinguished from each other, provided that the field is measured along the interaction straight with at least two points per pancake coil. The method has numerically been verified by applying it on the field error caused by transverse displacement (Equation 7.8-22) and deflection (Equation 7.8-20) at the time, however further numerical investigations are needed.

The straightness of the magnetic field along the interaction straight is crucial for fast electron cooling. Therefore, other possibilities for correcting the field should be investigated. One solution is to make the pancake coils mechanically adjustable in the transverse directions. After that, the transverse positions have been correction, no other mechanical adjustments shall be carried out. Otherwise the risk to move the coil centre is obvious. Instead, compensation for longitudinal displacement and angular error is made possible with correction windings inside of the pancake. These are described in section 7.8.7 below.

To avoid extensive modifications of the design (section 3.2.1), the suggestion is that the innermost layer of copper conductor of the pancake coils should be replaced by these corrector windings.

The disadvantage with this solution is that a large number of corrector windings and corresponding power supplies has to be added. It could also be necessary to lower the solenoid field strength by 5-10 percent, since one out of eleven layers of copper is taken out. On the other hand, it is advantageous that the correction of the magnetic field can be made electromagnetically. Further, with a 13 mm larger inner radius of the solenoids the field will be almost twice as homogenous, which can be obtained from Equation 7.8-9.

7.8.7 Solenoid correctors

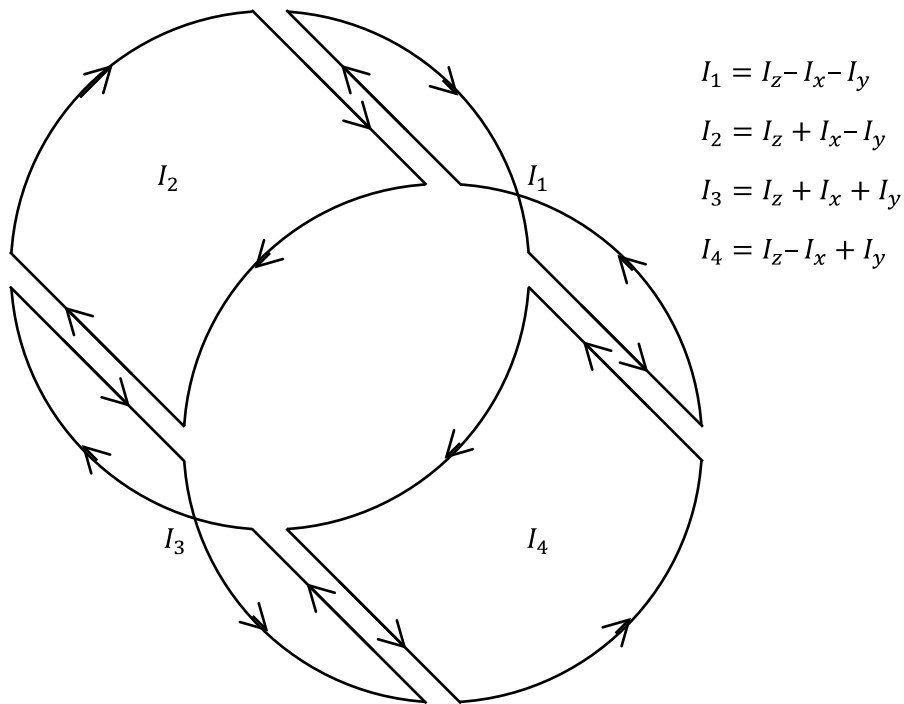


Figure 7-30: Principle of the solenoid corrector. Horizontal, vertical as well as longitudinal correction fields can be created with the four windings dependent on the direction of the current. Here the longitudinal configuration is shown.

In case all the pancake coil would be equipped with corrector windings as shown in Figure 7-30 above, then correcting fields could be created in arbitrary directions by combing the currents of the windings. Using Biot-Savarts formula the longitudinal and transverse field components can be derived as:

$$B_z(z) = \frac{\mu_0 I_z}{2} \left(\frac{R^2}{\left(\left(z + \frac{D}{2} \right)^2 + R^2 \right)^{3/2}} - \frac{R^2}{\left(\left(z - \frac{D}{2} \right)^2 + R^2 \right)^{3/2}} \right)$$

Equation 7.8-27

$$B_x(z) = \frac{\mu_0 I_x}{\pi R} \left(\frac{\left(z + \frac{D}{2} \right) \left(\left(z + \frac{D}{2} \right)^2 + 2R^2 \right)}{\left(\left(z + \frac{D}{2} \right)^2 + R^2 \right)^{3/2}} - \frac{\left(z - \frac{D}{2} \right) \left(\left(z - \frac{D}{2} \right)^2 + 2R^2 \right)}{\left(\left(z - \frac{D}{2} \right)^2 + R^2 \right)^{3/2}} \right)$$

Equation 7.8-28

where I_x and I_z are the currents configured according to Figure 7-30. R is the radius and D is the length of the corrector, which are determined by the parameters of the pancake coils (Table 7.8-1) With. The correcting fields are shown in Figure 7-31 for $I_x = I_z = 1$ A.

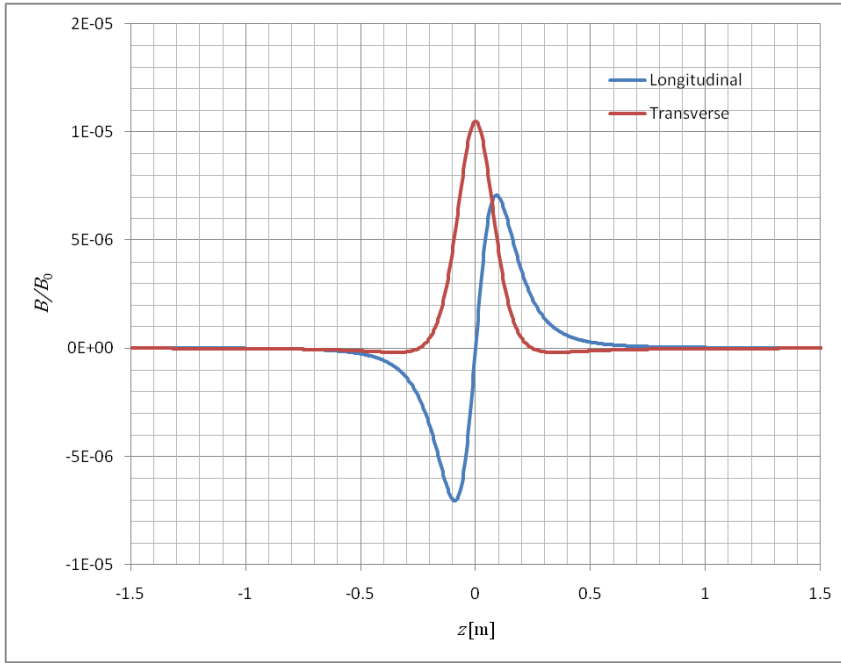


Figure 7-31: The longitudinal (blue) and transverse (red) field components generated by the solenoid corrector with $I_z = I_x = 1$ ampere.

Assume that the field errors are due to superposition of incorrectly adjusted currents I_{tn} in the solenoid correctors where t denotes x , y or z , depending which component that is measured. The field components is then given by a superposition

$$\Delta B_t(z) = \sum_{n=-\infty}^{\infty} \frac{B_t(z - nL)}{I_t} I_{tn}$$

where $B_t(z)$ is given by Equation 7.8-27 or Equation 7.8-28. Using the same method as in section 7.8.4.2 the currents can be deduced as an inverse convolution

$$I_{tn} = \int_{-\infty}^{\infty} dz f_t(z) \Delta B_t(nL - z)$$

Equation 7.8-29

where

$$f_t(z) = \frac{1}{2\pi} \int_{-\pi/L}^{\pi/L} dk \frac{I_t L}{\tilde{B}_t(k)} e^{-ikz}$$

Figure 7-32 and Figure 7-33 show the field errors of a pancake coil displaced 1 mm longitudinally and deflected by 1 mrad before and after correction. From these figures it can be concluded that 1 mrad angular error can be corrected with the use of solenoid correctors. In the longitudinal dimension the limitation of the correction is limited to the amount of power that can be applied to the corrector windings, which is of the order of 100 A.

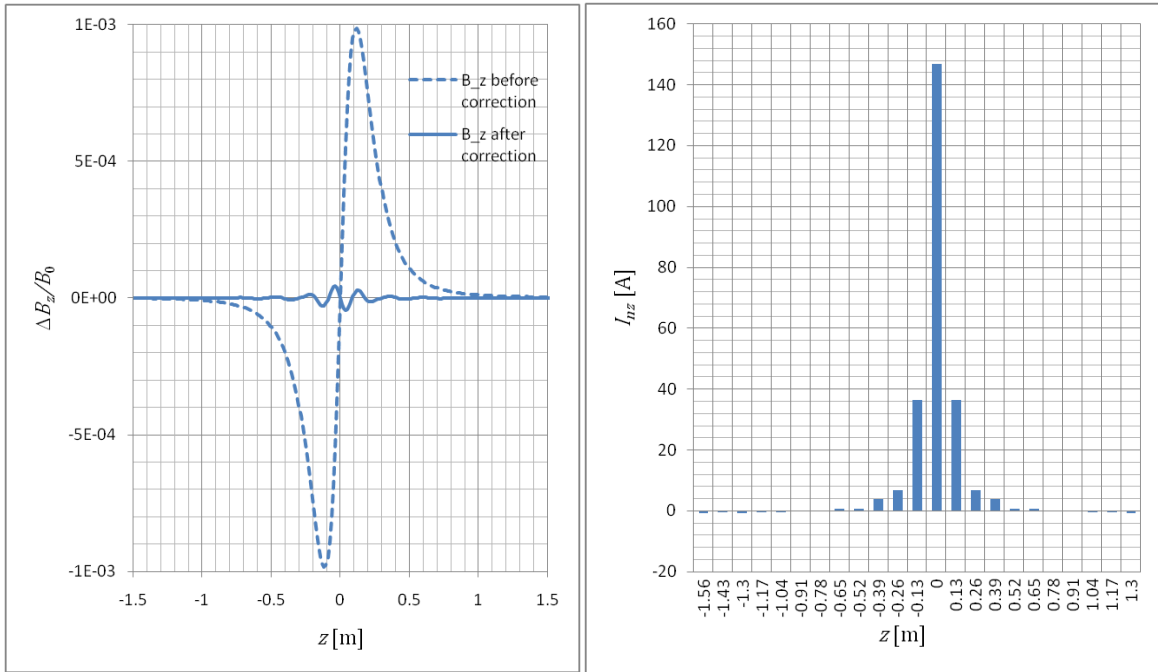


Figure 7-32: Left: The longitudinal field error created by a 1 mm longitudinal displacement of the pancake coil (Equation 7.8-10) before (dashed) and after (solid) correction with the solenoid corrector. Right: The corrector current I_{zn} calculated with Equation 7.8-29.

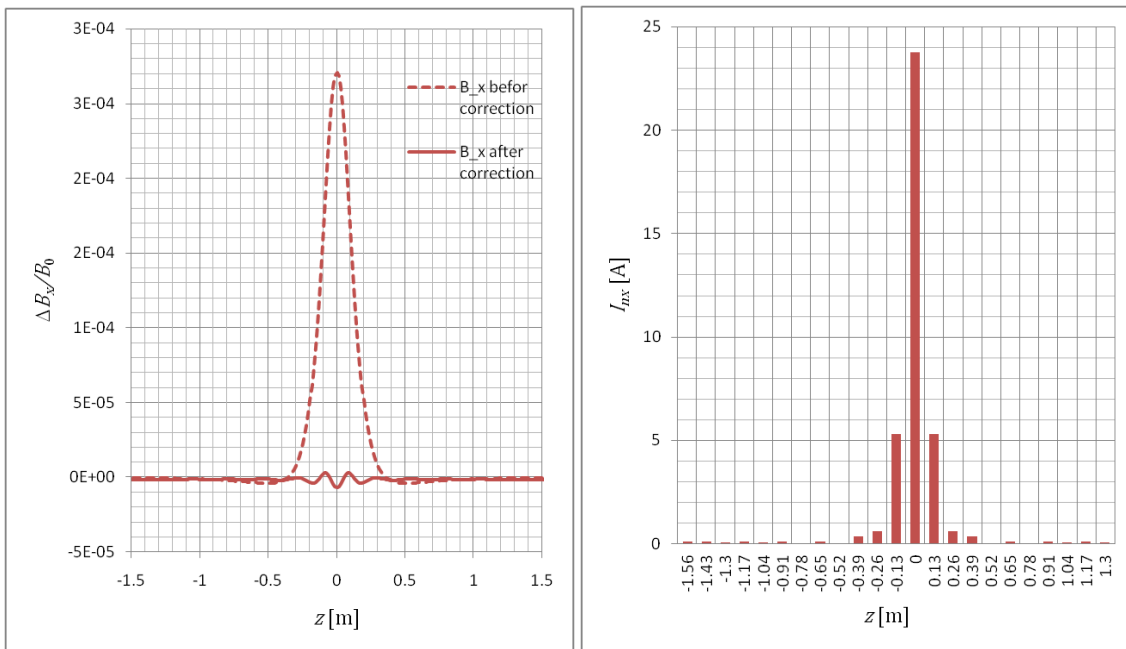


Figure 7-33: Left: The transverse field error caused by a 1 mrad angle of a pancake coil before (dashed) and after (solid) correction with the solenoid correctors. Right: The corrector current I_{xn} calculated with Equation 7.8-29.

7.9 Field errors and dipole oscillations

The requirements on the solenoid field along the interaction straight are very demanding due to the strong influence of transverse field errors on the cooling force, especially at high energies. The requirements in all other parts of the electron beam transport system are lower, however magnetic field errors do create envelope and dipole oscillations, which effectively contributes to the electron beam temperature.

The reference path in the electron beam transport system is determined by the dipole field $B_t(s)$ created by the windings of the steel boxes. In absence of the solenoid field, the electrons would follow this path. This dipole field is uniform across the beam region, i.e. it is independent of the transverse coordinates. The unit vector \hat{s} directed along the reference path as shown in Figure 7-34 is determined by

$$\frac{d\hat{s}}{ds} = -\frac{eB_t(s)}{P} \hat{s} \times \hat{t}$$

where $P = m_e \beta \gamma c$ is the momentum of the electron and \hat{t} is the unit vector of the dipole field. With $\hat{r} = \hat{s} \times \hat{t}$ the following derivatives of the unit vectors are given by

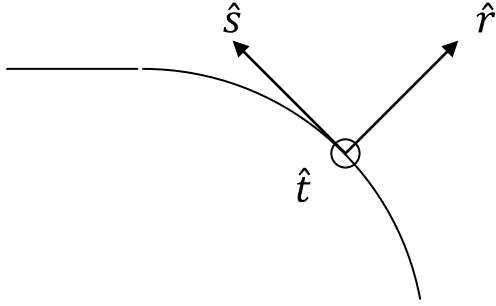


Figure 7-34: Definition of coordinate system along the reference path.

The solenoid field B_s is ideally aligned with the design path. Any transverse deviations $\Delta \mathbf{B}_\perp(s)$ of the solenoid field inevitable lead to coherent oscillations of the electron beam. With the velocity of an electron given by $\mathbf{v} = \beta c \hat{s} + \mathbf{v}_\perp$ the relation between solenoid field and transverse velocity can be derived as:

$$\hat{s} \times \dot{\mathbf{v}}_\perp + \frac{eB_s(s)}{m_e \gamma} \mathbf{v}_\perp = -\frac{e\Delta \mathbf{B}_\perp(s)}{m_e \gamma} \beta c$$

Assuming that the longitudinal velocity is a constant, time can be substituted with the longitudinal coordinate $s = \beta c t$. Then, from the solution to this first order differential equation the absolute value of the transverse velocity can be deduce as the well known expression

$$v_\perp = \beta c \left| \int_{-\infty}^s ds' \left(\hat{s}' \times \frac{e\Delta \mathbf{B}_\perp(s')}{P} \cos \phi(s') + \frac{e\Delta \mathbf{B}_\perp(s')}{P} \sin \phi(s') \right) \right|$$

where the phase $\phi(s)$ is given by

$$\phi(s) = \int_{-\infty}^s ds' \frac{eB_s(s')}{P}$$

Hence, the cyclotron radius $\rho = (v_\perp m_e \gamma) / (eB_s)$ of the oscillation is given by

$$\rho(s) = \frac{1}{B_s(s)} \left| \int_{-\infty}^s ds' (\hat{s}' \times \Delta \mathbf{B}_\perp(s') \cos \phi(s') + \Delta \mathbf{B}_\perp(s') \sin \phi(s')) \right|$$

One way to take into account for the coherent oscillation in the theory of electron cooling, is to interpreted this transverse velocity as a contribution to electron beam temperature. The electron

cooling force depends logarithmically on the rms cyclotron radius. In the electron cooling calculations presented in section 7.11.4 it is assumed that this parameter is smaller than 0.1 mm, corresponding to an electron beam temperature of 1 eV.

There is another reason for reducing the dipole oscillations further. The most challenging task for the HESR electron cooler is to reduce the momentum spread of the antiproton beam so that it can be used for Charmonium spectroscopy. This will be carried out for antiproton momentum of 8.9 GeV/c. Another important task for the HESR electron cooler is to provide absolute calibration of the antiproton energy so that the precision as well as the resolution of scanned resonance can be determined. To calibrate the antiproton beam energy with high accuracy by measuring revolution frequencies is very difficult because the exact beam path is not known. An alternative is to use the spectrometer in the H^- beam line described in 3.1.16. In this case it is necessary to ensure that no significant amount energy is transferred from the longitudinal motion into transverse oscillations.

Since the total energy is preserved, the loss in longitudinal momentum is related to the gain in transverse velocity through the well known relation

$$\frac{\Delta P}{P} = -\frac{\gamma^2 v_{\perp}^2}{2(\beta c)^2}$$

Therefore, the precision in the experiment is limited by the radius of the dipole oscillations as

$$\frac{\Delta P}{P} = -\frac{1}{2} \left(\frac{e B_s \rho}{m_e \beta c} \right)^2$$

With $\rho = 50 \mu\text{m}$, $B_s = 0.2$ and $\beta \approx 1$ the relative momentum loss can be obtained as

$$\frac{\Delta P}{P} = 1.7 \times 10^{-5}$$

which is below the resolution of the spectrometer.

In the case damping of dipole oscillations is limited by the ability to measure the amplitude, one possible solution would be to lower the solenoid field strength. Another solution is to optimize the electron beam transport system using the Schottky pick-up as a diagnostic tool.

7.9.1.1 Field matching

The alignment of the solenoid field to the dipole field is particularly challenging in the merging sections, where the vacuum chamber of the antiproton beam intersects with the solenoid. In the layout of the pancake solenoids together with the dipole windings are shown. In merging modules part of the magnetic flux is returned in the steel boxes. Therefore, to calculate the magnetic field the simulation program Tosca from Vector Fields was used. The angles of the pancake solenoids are iteratively adjusted until solenoid field follows the path determined by the corrector windings. This process is time consuming and to reduce the number of iterations the method of inverse convolution (section 7.8.4.2) is used. However, the transverse field caused by deflecting one race-track shaped pancake is not known and further it varies along the longitudinal coordinate. Therefore the field error is assumed to have a shape of a Cauchy distribution function:

$$B_x(z) = \frac{b}{\pi(a^2 + z^2)}$$

where a and b are constants. This function is well suited for inverse convolution methods because it has long tails. With this method the simulations converge after approximately five iterations.

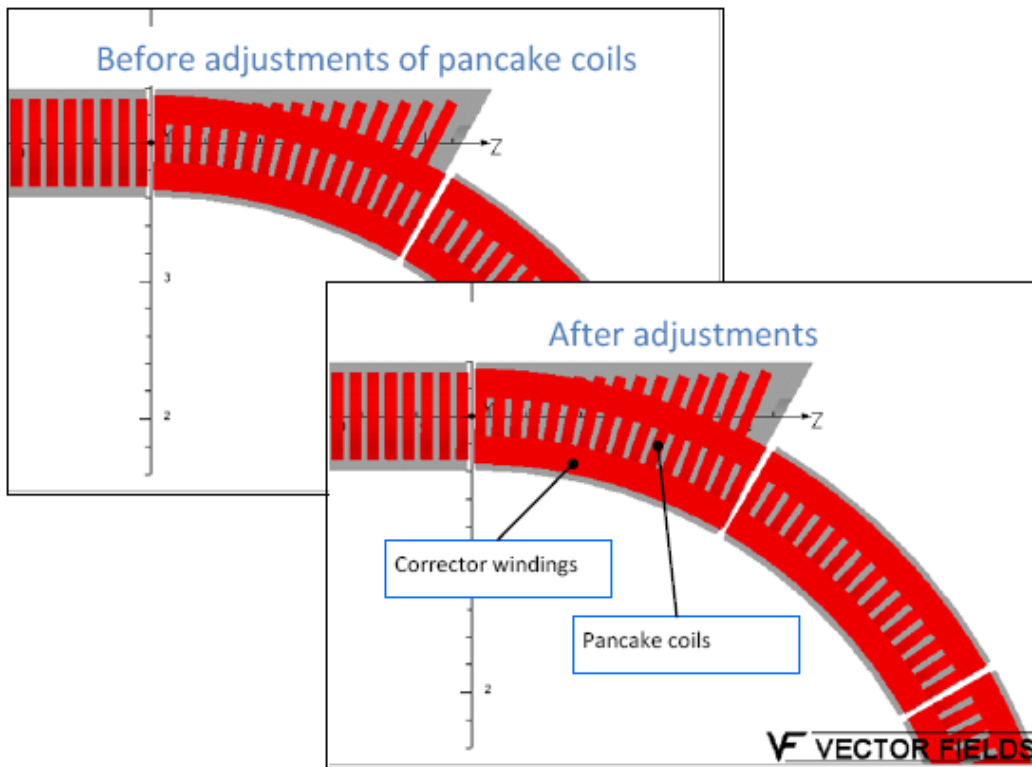


Figure 7-35: Layout of pancake coils and corrector windings in the merging section. The angles of the pancake coils are adjusted so that the solenoid field becomes parallel with the path determined by the corrector windings

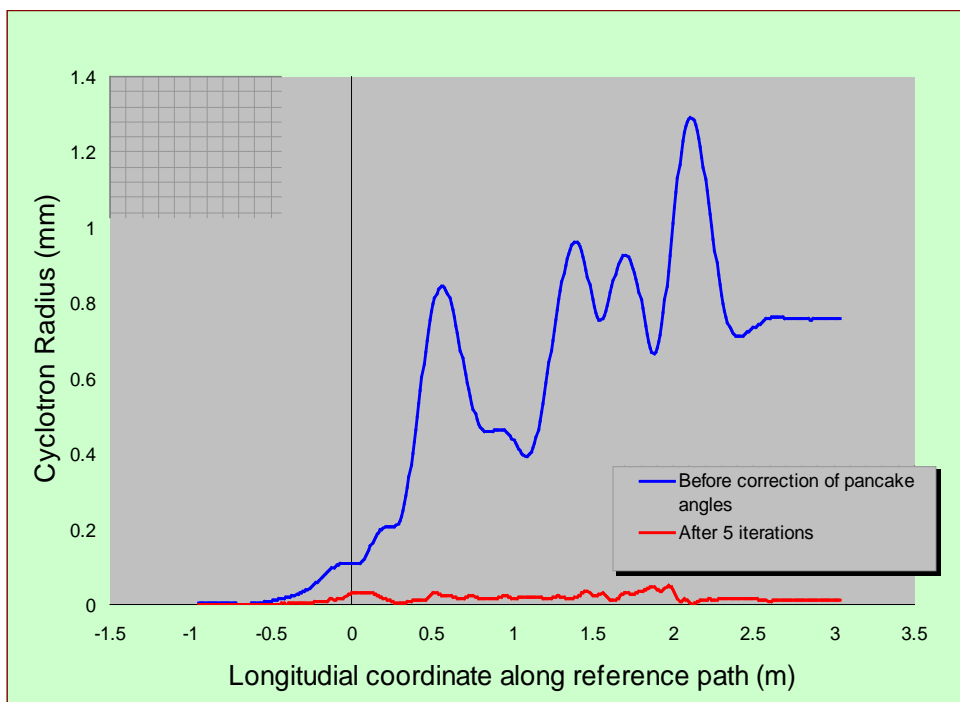


Figure 7-36: The cyclotron radius of the dipole oscillations before (blue) and after (red) five iterations of calculations and adjustments of the pancake coil angles. Tracking of the electrons starts on the interaction straight where the longitudinal coordinate is negative. $z = 0$ corresponds to the entrance of the merging module, which is 2 meter long.

Because of the varying dimensions of the pancake solenoids in merging modules, the current to the pancake solenoids needs to be corrected in order to keep the solenoid field strength constant along the beam path. Otherwise the envelop of the beam will start oscillating. These oscillations cannot be corrected for because in difference to the geometry in transition and acceleration columns (sections 7.3 and 7.4), the geometry in merging modules is not cylindrical.

The calculations of these corrections are carried out simultaneously with the calculations of correcting angles to reduce the number of iterations further. The results are shown the Figure 7-37.

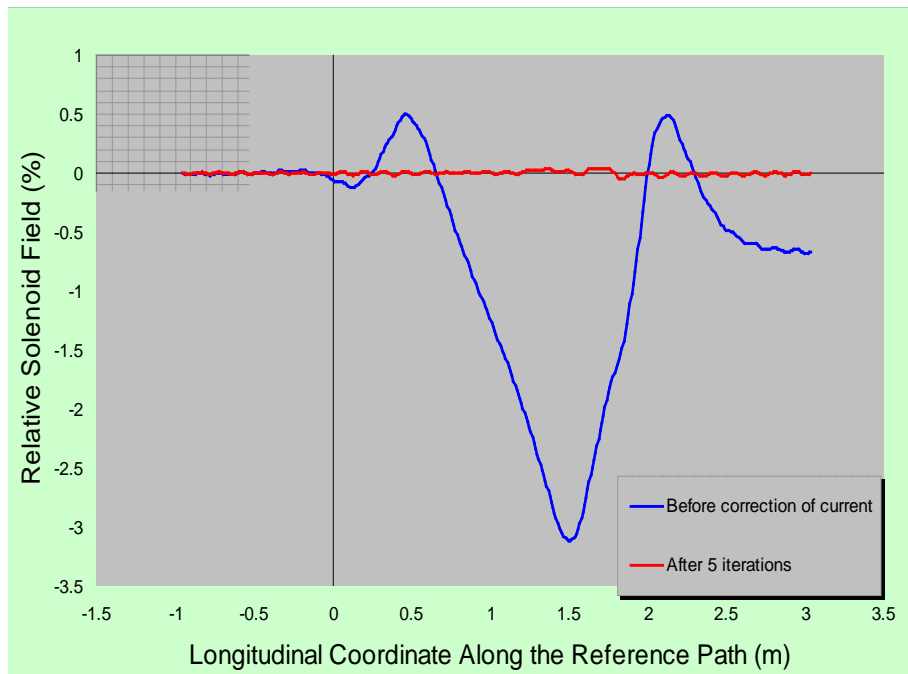


Figure 7-37: The solenoid field strength in the merging sections before and after corrections of the currents of the individual pancake coils (right).

7.9.2 Damping of dipole oscillations.

During beam transport through acceleration columns, transition region, bends and merging, dipole oscillations are created in regions where the field matching is not at an optimum. Four dipole correctors, which are designed according to the principle in Figure 7-30, will be used to damp these oscillations. The correctors are attached to the vacuum chamber and are placed in sequence along the first meter on the interaction straight section. The radius R of the dipole correctors is 12 cm and the length D is 13 cm, which is approximately a quarter of the cyclotron wave length

$$\lambda = \frac{2\pi P}{eB_s}$$

at the the highest energy 4.5 MeV. (There is plenty of space left for another set of correctors to be used after the energy upgrade). The correctors will be designed to operate with a maximum current of 100 A.

The transverse field generated by the corrector is given by equation Equation 7.8-28. In Figure 7-38 the transverse field component is shown with $I_x = 100$ A in the two first correctors and with $I_x = -100$ A in the other two. This field generates a dipole oscillation with an amplitude of 1 mm. The conclusion is that these four dipole correctors can be used to quench oscillations of 1 mm once the phase and the amplitude are known.

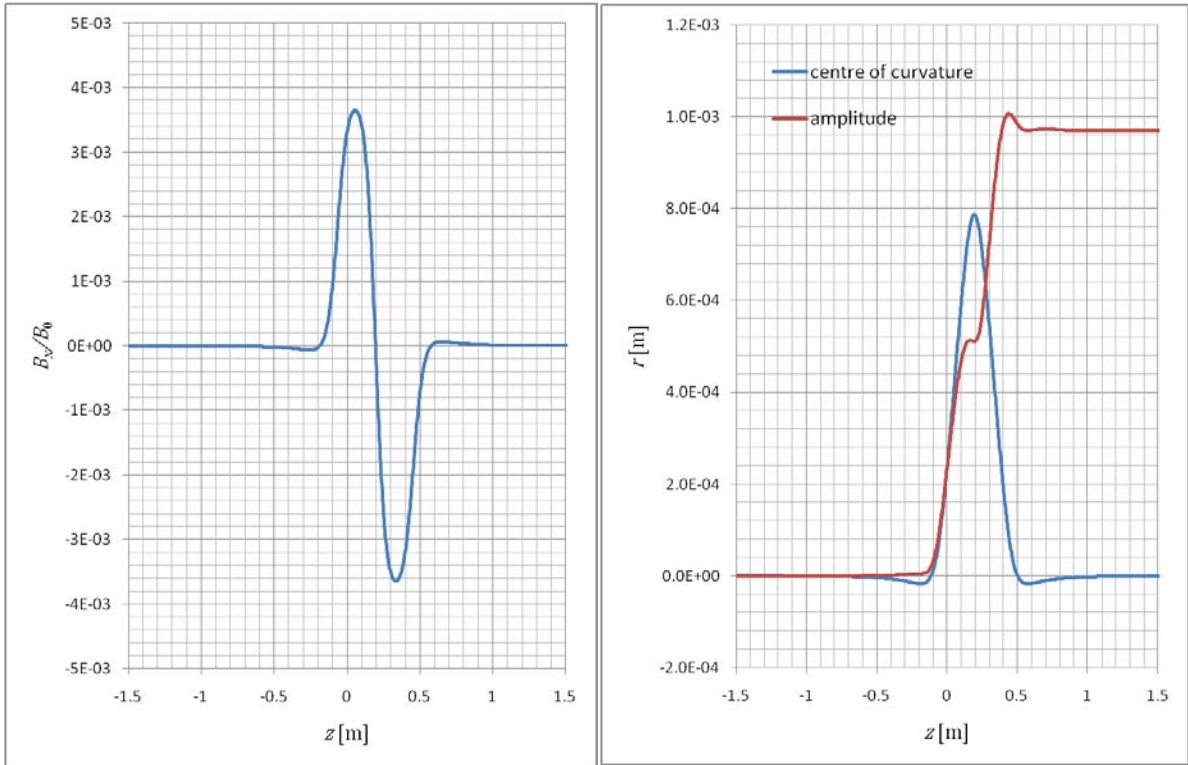


Figure 7-38: Left: The transverse field generated by four dipole corrector placed with total length $4 \times 0.13 = 0.52$ m with $I_x = 100$ A in the two first ones and $I_x = -100$ A in the two second ones. Right: The amplitude of the created dipole oscillation (red) and corresponding displacement of centre of curvature (blue).

7.10 Vacuum and neutralization

The requirement on vacuum on the cooling straight section is determined from the concern regarding the rotation of the electron beam, not by the lifetime of the antiproton beam. This is because the HESR is intended for use with thick internal targets. Therefore, the vacuum on the cooling straight section will have a negligible effect on the antiproton beam. The beam pipe is 200 mm inner diameter, and we assume two rather big pumps in each end of the straight section.

7.10.1 Neutralisation

In order to estimate how much neutralisation we accept, we calculate the rotation of the electron beam due to trapped ions in the electron beam. The rotation of the electron beam is given by (in the moving frame): see e.g. [6666]

$$v_{az}(r) = \frac{I_e(f\gamma^2 - 1)r}{2\pi\epsilon_0\beta\gamma c a^2 B}$$

where f is the neutralisation factor and a is the electron beam radius. If we accept $v_{az}(a) \leq 10^{-5}\beta\gamma c$ (which corresponds to the r.m.s. non-straightness of the magnetic field lines), then we get for 4.5 MeV, $I_e = 1$ A and $a = 5$ mm

$$f \leq \left(\frac{10^{-5}\beta^2\gamma^2 c^2 2\pi\epsilon_0 a B}{I_e} + 1 \right) = 0.06$$

Thus, we accept up to 6 % neutralisation of the electron beam.

7.10.2 Expected vacuum level

We assume big pumps on the outside of the merging module on both sides of the cooling straight section as well as outside of the return straight sections. The distance between pumps is set to 30 m.

We assume that we have a total outgassing rate $q = 1 \times 10^{-12} \text{ mbar}\ell/\text{cm}^2/\text{s}$ [46] after bakeout to 150 °C. This is assumed to consist of H₂ (75 %), CH₄ (14 %), and CO (11 %) [47], thus:

$$\text{H}_2 \quad q = 7.5 \times 10^{-13} \text{ mbar}\ell/\text{cm}^2/\text{s}$$

$$\text{CH}_4 \quad q = 1.4 \times 10^{-13} \text{ mbar}\ell/\text{cm}^2/\text{s}$$

$$\text{CO} \quad q = 1.1 \times 10^{-13} \text{ mbar}\ell/\text{cm}^2/\text{s}$$

The average pressure for each gas will be given by [48]:

$$P_{\text{ave}} = Aq \left(\frac{L^2}{6w} + \frac{L}{S} \right)$$

where $A = 2\pi R = 2\pi \times 10 \times 100 \text{ cm}^2/\text{m} = 6300 \text{ cm}^2/\text{m}$ is the surface area per meter of beam pipe. $L = 30 \text{ m}$ is the distance between the pumps. The specific molecular conductance $w[\text{m}^4/\text{s}] = 305 r^3 \sqrt{T/M}$, where T is the temperature in K and M is the mass number of the gas to be pumped [48]. Thus, $w = 3700, 1300, 1000 \text{ }\ell/\text{s}/\text{m}$ for H₂, CH₄, and CO respectively, and the calculated average pressures become:

$$5.5 \times 10^{-10} \text{ mbar for H}_2 (n_g = 1.5 \times 10^7 \text{ cm}^{-3})$$

$$1.3 \times 10^{-10} \text{ mbar for CO } (n_g = 3.5 \times 10^6 \text{ cm}^{-3})$$

$$2.0 \times 10^{-10} \text{ mbar for CH}_4 (n_g = 5.3 \times 10^6 \text{ cm}^{-3})$$

7.10.3 Neutralisation with clearing electrodes

The ionisation cross sections are [49]

$$2 \times 10^{-23} \text{ m}^2 \text{ for H}_2$$

$$9 \times 10^{-23} \text{ m}^2 \text{ for CO}$$

$$11 \times 10^{-23} \text{ m}^2 \text{ for CH}_4$$

The calculated neutralisation times,

$$\tau_n = \frac{1}{\sigma_i n_g \beta c}$$

(i.e. the time to reach full neutralisation of the electron beam), are 11 s for H₂, 11 s also for CO, and 6 s for CH₄.

The ion escape times are estimated as

$$\tau_{\text{escape}} = L \times \sqrt{\frac{M_i}{4kT}}$$

or 0.013 s, 0.050 s, and 0.038 s for H₂, CO, and CH₄ respectively. The resulting neutralisation factors from H₂, CO, and CH₄ are then

$$f \approx \left(\frac{\tau_{\text{escape}}}{\tau_n}\right)_{\text{H}_2} + \left(\frac{\tau_{\text{escape}}}{\tau_n}\right)_{\text{CO}} + \left(\frac{\tau_{\text{escape}}}{\tau_n}\right)_{\text{CH}_4} = \frac{0.013}{11} + \frac{0.050}{11} + \frac{0.038}{6} = 1.2 \%$$

7.10.4 Conclusion

Sufficiently small neutralisation will be achieved with clearing electrodes only in the toroids. These might be designed as described in [50].

7.11 Simulation of electron cooling

Charmonium spectroscopy is one of the main items in the experimental program of PANDA (and FAIR). Accurate determination of masses and widths depends on the absolute energy calibration of the antiproton beam and the beam energy spread.

7.11.1 Target interaction

PANDA requires a hydrogen pellet target with effective thickness of 4×10^{15} hydrogen atoms per cm^2 and $10^{10} - 10^{11}$ antiprotons circulating in HESR to achieve luminosities ranging from 2×10^{31} to $2 \times 10^{32} \text{ cm}^{-2}\text{s}^{-1}$. The goal of the experiments is to combine this with a relative momentum resolution of $10^{-5} - 10^{-4}$.

The pellet target consists of a stream of frozen droplets of hydrogen with the properties shown in Figure 7-39.

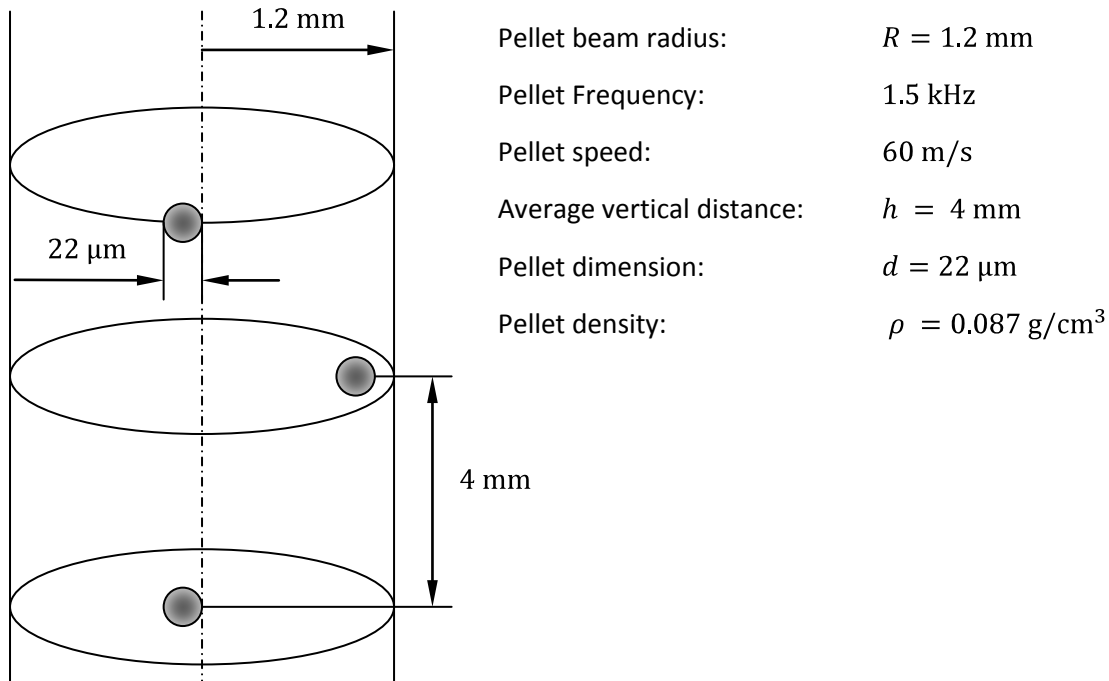


Figure 7-39: Properties of the hydrogen pellet target

The ratio between the maximum instantaneous luminosity \hat{L} (when the antiproton beam hits a pellet head-on) to the average luminosity $\langle L \rangle$ (for an antiproton beam of small emittance, which travels through the cylindrical pellet stream along a diameter) is

$$\frac{\hat{L}}{\langle L \rangle} = \frac{hR}{4\sigma^2}$$

where the pellet stream has a constant density of pellets inside radius R , the average vertical separation between the pellets is h and the antiproton beam is of rms size σ in both planes. With $\hat{L}/\langle L \rangle \leq 5$ then we find $\sigma \geq 0.5$ mm. Thus, the rms antiproton beam size at the target should not be smaller than 0.5 mm. We avoid that the antiproton beam spot size at the hydrogen pellet target becomes too small by a suitable choice of the beta-values at the internal target and electron cooler and by controlling the beam emittance will by adjusting the angle between the electron and antiproton beams. The method is based on a phenomenon known as the monochromatic instability [51] and is illustrated in Figure 7-40.

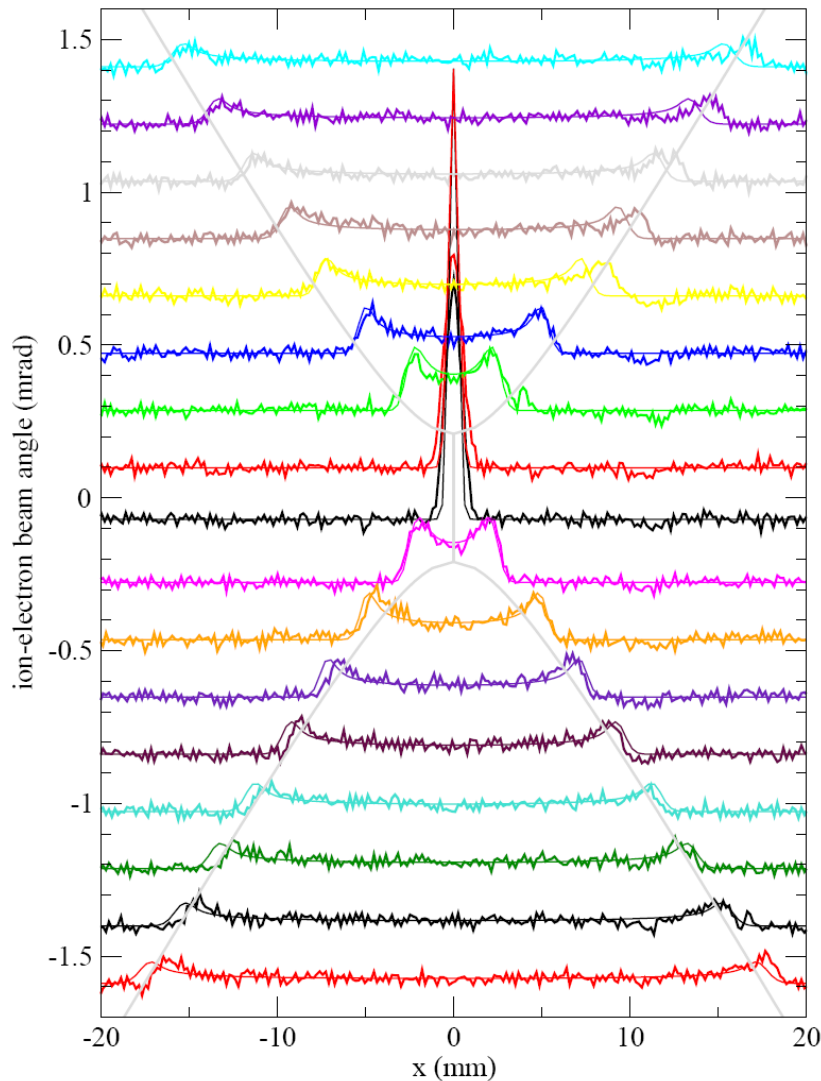


Figure 7-40: Horizontal beam profiles of an $^{40}\text{Ar}^{18+}$ beam accelerated to 200 MeV/u in CELSIUS. In this water fall graph the profiles are separated from each other proportionally to the angle between the ion and electron beams. The graph illustrates how the emittance can be controlled by adjustment of the electron beam angle. For a given beam angle the ions are cooled towards the same betatron amplitude. This amplitude increases with the angle.

7.11.2 Beta-value at the internal target

In order to avoid that the beam becomes too small at the pellet target, there is a preference for choosing a suitable, not too small beta-value at the target. On the other hand, a large beta-value at the target gives a large cross section for large angle single-scattering. Taking this into account and

allowing the single-scattering cross section to be less than 10 % of the hadronic cross section we choose beta-values of 2 m at 1.5 GeV/c and 3.8 GeV/c, 4 m at 8.9 GeV/c and 8 m at 15 GeV/c.

7.11.3 Beta-value at the cooling section

Large beta-values at the cooling section will speed up the cooling-down process and increase the longitudinal cooling force. On the other hand, if the beta values are too large, a significant fraction of the antiprotons will be outside of the electron beam in the beginning of the cooling process. With horizontal and vertical beta values at the cooler chosen as

$$\beta_x = \beta_y = \frac{\beta\gamma}{\beta_0\gamma_0} \times 50 \text{ m}$$

where β and γ are the relativistic parameters and β_0 and γ_0 are those parameters at 3 GeV, more than 90 % of the antiprotons will be inside of the electron beam with radius 5 mm in the beginning of the cooling process, i.e. with

$$\varepsilon_{\text{rms}} = \frac{\beta_0\gamma_0}{\beta\gamma} \times 0.1 \text{ mm mrad}$$

7.11.4 Calculations with BETACOOOL

To simulate electron cooling a large number of input parameters need to be set. The most important of these are listed in Table 7.11-1. The momentum spread Δp is defined as the spread enclosing 68 % of the antiprotons, which for a Gaussian distribution function corresponds to the rms value.

Table 7.11-1: Input parameters to BETACOOOL simulations

Electron energy:	4.5 MeV
Relative high voltage drift and ripple:	2×10^{-5}
Electron current:	1 A
Electron beam radius:	5 mm
Solenoid field strength:	0.2 T
Magnetic field straighness:	10–5 rad
Electron beam temperature:	1 eV
Effective cooling length:	22 m
Target:	
Model for energy loss:	Urban
Pellet beam radius:	1.2 mm
Pellet Frequency:	1.5 kHz
Pellet speed:	60 m/s
Average vertical distance:	4 mm
Pellet dimension (cubic): ($(18 \mu\text{m})^3 = \pi (22 \mu\text{m})^3 / 6$)	18 μm
Pellet density:	0.087 g/cm ³

Electron cooling model:	Parkhomchuk
Model for IBS:	Martini with numerical integration
Lattice:	hesr-new2.tfs (1HESR NC, gtr=6.29, D=0, B.Lorentz Run: 18/12/07)
Horizontal and vertical beta functions at the electron cooler:	80 m
Horizontal and vertical beta functions at the target:	8 m
Vertical angle between electron and antiproton beam:	0.5mm/22m = 23 μ rad
Horizontal angle between electron and antiproton beam:	0.3 mm/22 m = 14 μ rad
Number of antiprotons:	10^{10}
Initial emittances:	0.04 π mm mrad enclosing 39 % of particles
Initial relative momentum:	10^{-4} enclosing 68 % of particles
Barrier bucket:	Amplitude: 0.4 kV, RF duration: 0.1, Gap duration: 0.7
Losses:	
Single scattering:	Interaction events cross section 0.055 barn.
Transverse acceptance:	1.25×10^{-5} m rad
Longitudinal acceptance:	0.002

The first simulation, which is shown in Figure 7-41, was carried out with the hydrogen target off. Then the beam is heated by intra-beam scattering, which results in a relative momentum spread, of 0.6×10^{-5} . The transverse profiles show similarities with the ones measured at CELSIUS (Figure 7-40.) and is due to an angle between the electron and antiproton beam. The vertical profile is intentionally wider than the horizontal in order optimize the target overlap. To be noted is also that the beam cross section, which is rectangular due to large horizontal and vertical betatron oscillations, is wider than the 0.5 mm, which was required in section 7.11.1.

In the second simulation (Figure 7-42) the hydrogen pellet target was switched on after 30 seconds. This simulation shows that it is possible to achieve a momentum resolution of 10^{-5} with a luminosity of $2 \times 10^{31} \text{ cm}^{-2} \text{ s}^{-1}$ and a good target overlap.

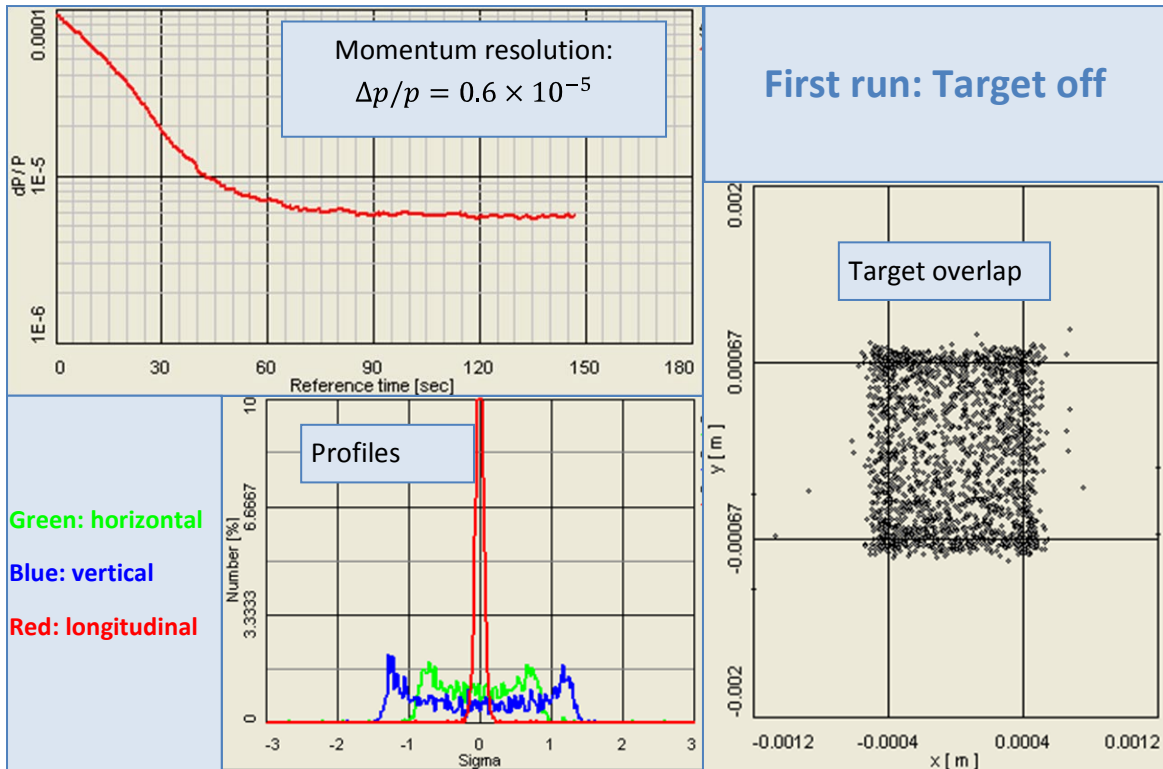


Figure 7-41: First run of BETACOOOL simulation with parameters from Table 7.11-1, with the target switched off. The upper graph shows the momentum resolution. The beam profiles, which the x-axis scaled to the initial rms values, show similarities with the profile measurements in CELSIUS (Figure 7-40). The beam has a rectangular cross section due to large horizontal and vertical betatron oscillations.

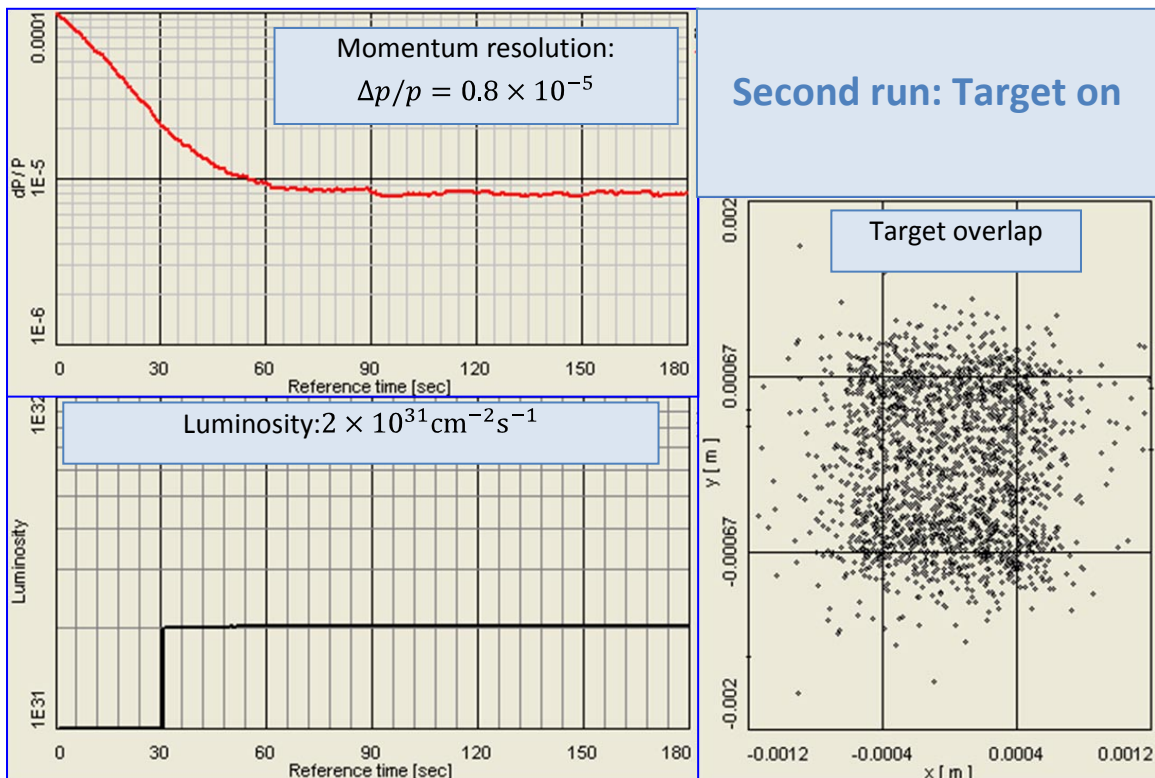


Figure 7-42: BETACOOOL simulation with parameters from Table 7.11-1. The hydrogen pellet target is switched on after 30 seconds.

8 DISCUSSION

8.1 Generation of high voltage

There exist two commercially available accelerator systems for generation of high voltage and acceleration and deceleration of electrons, which have been considered for the construction of the HESR electron cooler. These are the Pelletron available from National Electrostatics Corporation (NEC) [2] and the Dynamitron available from High Voltage Engineering Europe (HVEE) [52].

A Dynamitron uses capacitive coupling to the individual stages of the accelerating/decelerating columns for the generation of the high voltage. This technique is difficult to adapt to the requirement of a longitudinal magnetic field in the accelerating/decelerating columns and is not modular.

A special requirement on the HESR electron cooler high-voltage charging system is that it has to operate with a continuous magnetic field of 0.07 T along the electron beam in the accelerating and decelerating columns. This field has to be directed either along or opposite to the velocity of the electrons. If the accelerating and decelerating columns are positioned side-by-side in the high voltage tank as at FNAL then the field has to have opposite directions in the two columns. This implies that the magnetic field has to be created with solenoids placed at different levels of high voltage.

However, Dynamitron accelerators for Accelerator Mass Spectroscopy have demonstrated a high voltage stability of $\leq 10^{-5}$, which meets the requirements for HESR.

The Pelletron is a well-tested electrostatic accelerator, which has been built for voltages as high as 25 MV. It uses chain transport of charge to the high voltage terminal. The charging current is limited to about 150 μA /chain. At FNAL a Pelletron has been used for electron cooling at 4.3 MV, although without a longitudinal magnetic field and only with a required stability and ripple of 1000 V.

Furthermore, it seems reasonable that the high voltage stability needed in HESR can be reached by introduction of a variable accelerating stage in the electron gun, which is controlled by the high voltage regulation system.

A Pelletron is constructed in a modular way, which facilitates future increase of the high voltage to at least 8 MV.

The positive experience from the FNAL electron cooler, the adaptability of the basic construction to the inclusion of a longitudinal magnetic field, the excellent vacuum properties, and the modular construction facilitating a future upgrade to 8 MV leads to the choice of a Pelletron system for the HESR electron cooler.

8.2 Magnet system

8.2.1 Magnetic field strength

Busch's theorem implies that the magnetic flux, which is contained in the electron beam remains constant during the beam transport from the cathode to the collector. There is a technological upper limit to this flux determined by the magnetic field in the accelerating column and by the aperture of the accelerating tubes. The magnetic field in the accelerating column is limited by the power that can be transmitted to the high voltage terminal using rotating shafts, and there is a limit to the

power that can be cooled away by the insulating SF₆ gas. The accelerating tubes from National Electrostatic Corporation have an aperture diameter of 1 inch. Therefore, it is necessary to trade off electron beam diameter in the cooling section against the magnetic field in the cooling section.

We conclude that the electron beam diameter in the acceleration sections shall be 17 mm in order to have a sufficient margin to a 25 mm aperture, and that the magnetic field in the accelerating section can be up to 0.07 T. Thus, the magnetic flux, which is contained in the electron beam in the cooling section, is going to be $0.07 \times \pi \times 0.085^2 \text{ Tm}^2$.

In [3] it is shown that magnetization of the electron beam at the highest momentum of 15 GeV/c requires a magnetic field strength in the interaction region of 0.2 T at least. As a safety margin, a magnetic field strength of 0.5 T was chosen in the final report.

On the other hand, a lower value of the magnetic field in the drift tube allows a larger diameter of the electron beam. This reduces the effect of resonances induced by the non-linear tune shift caused by the electron beam onto the antiproton beam. We therefore choose a magnetic field strength of 0.2 T in the cooling section. The electron beam radius in the cooling section then becomes $r_0 = 5 \text{ mm}$.

8.2.2 Conventional solenoid

The design presented in this report is based on conventional rather than superconducting magnets. There are two main reasons for this:

- Given this relatively low value of the longitudinal magnetic field, it is reasonable to choose a room temperature solenoid rather than to go for a superconducting design as was proposed by BINP originally [3].
- The desired field quality has been proven for conventional magnets at BINP in Novosibirsk.

8.2.3 The pancake coils

There are two major concerns with the solenoid. First of all, there is only 50 mm space between the pancake coils, which could make the assembly difficult, especially to fasten the bolts on the CONFLATE flanges between modules. Placing the coils further apart is not to recommend. Then the inner radius must be increased by the same amount due to the exponential growth of the modulation. An increase of the radius would require more copper and power consumption. Instead of increasing the radius we would prefer special tools to fasten the bolts.

The second issue is investment cost and power consumption. By moving the solenoids closer together the radius of the solenoids could be made smaller without worsen the modulation. This is not an easy task and would inevitably lead to a design with instrumentation gaps.

In addition to the problem with assembly, access between pancake solenoids is needed for mechanical support of the vacuum chamber and for mechanical arms of the SPUC.

Transversely there is even a worse restriction, namely the outer diameter of the SPUC that is 273 mm. To this connectors and equipment for baking (bands, isolation and shielding) has to be added. The SPUC can only be made smaller if the nominal inner diameter of the vacuum chambers along the cooling section is reduced by the same amount. Otherwise the resolution of the pick-up electrodes, which depends on capacity, will be affected.

To make the inner diameter of the vacuum chamber smaller is also difficult. Among others, the magnetic measurement system must be redesigned and there might be problems with impedances. Perhaps it would be possible to reduce the nominal inner diameter to 150 mm, at the most. Then it would be necessary to introduce vacuum pumps in each three-meter unit, which would require instrumentation gaps between pancake solenoids.

9 References

- [1] Electron cooling at Fermi National Accelerator Laboratory, <http://www-ecool.fnal.gov>.
- [2] National Electrostatics Corporation, <http://www.pelletron.com>.
- [3] Electron cooling for HESR, Technical Feasibility of Fast Electron Cooling of Antiproton Beams in the Energy Range 0.8 to 14.5 GeV, Budker Institute of Nuclear Physics, Novosibirsk, January 4, 2003

Electron cooling for HESR, Second Progress Report (Technical Feasibility of Fast Electron Cooling of Antiproton Beams in the Energy Range 0.8 to 14.5 GeV), Budker Institute of Nuclear Physics, Novosibirsk, 2003

O. Bazhenov et al., Electron Cooling for HESR, Final Report (Technical Feasibility of Fast Electron Cooling of Antiproton Beams in the energy range 0.8 to 14.5 GeV), Budker Institute of Nuclear Physics, Novosibirsk, 2003.
- [4] FAIR Baseline Technical Report, Darmstadt 2006. <http://www.gsi.de/fair/reports/btr.htm>
- [5] A. Denig, Private communication.
- [6] M. Reiser, Theory and Design of Charged Particle Beams, Wiley series in beam physics and accelerator technology, John Wiley & Sons, 1994
- [7] A. Sidorin, private communication, October 2005.
- [8] J. Leibfritz *et al.*, "Status of the Fermilab Electron Cooling Project", Proceedings EPAC 2002, p.1094.
- [9] A. Shemyakin et al., Proceedings of COOL05 Workshop, Galena, IL, 2005.
- [10] S. Nagaitsev et al. Proceedings of COOL05 Workshop, Galena, IL, 2005.
- [11] A. Shemyakin, Private Communication.
- [12] M. E. Veis *et. al.*, Electron beam with energy 1 MeV in recuperation regime, Proceedings of EPAC 1988.
- [13] Electron Gun and Collector for the Fermilab High Energy Electron Cooling. By A. Sharapa, A. Shemyakin, and S. Nagaitsev, Nucl.Instr.and Meth. A417(1998) 177-181
- [14] A.V. Ivanov, M.A. Tiunov. ULTRASAM - 2D Code for Simulation of Electron Guns with Ultra High Precision. Proceedings of ECAP 2002, Paris, France, 2002, p.1634-1636^
- [15] M.A. Tiunov. BEAM - 2D-code package for simulation of high perveance beam dynamics in long systems. Proceedings of SCHEF'99, Dubna, Russia, 1999, p.202-208
- [16] Precise Measurements of a Magnetic Field at the Solenoids for Low Energy Coolers, Beam Cooling and Related Topics, International Workshop on Beam Cooling and Related Topic – COOL05 edited by S.Nagaitsev and R. J. Pasquinelli
- [17] C. Bovet, R. Gouiran, I. Gumowski, K.H Reich, CERN/MPS/Int. DL/70/4
- [18] M. Bryzgunov (BINP). Simulations of IBS effects in the HESR electron cooler. TSL note, unpublished.

- [19] http://theory.physics.helsinki.fi/~plasma/luennot05/summary_0502.pdf
- [20] Efficiency of the Fermilab Electron Cooler's collector. L.R. Prost, A. Shemyakin. FERMILAB-CONF-05-117-AD, May 2005. 3pp. Published in Knoxville 2005, Particle Accelerator Conference 2387
- [21] V. Tupikov, G. Kazakevich, T. K. Kroc, S. Nagaitzev, L. Prost, A. Shemyakin, L. W. Schmidt, M. Sutherland, A. Werner, FERMILAB-CONF-05-397-AD.
- [22] V. N. Bocharov, A. V. Bublei, S. G. Konstantinov, V. M. Panasyuk and V. V. Parkhomchuk, Instruments and Experimental Techniques, Vol. 48, No 6, 2005.
- [23] V. I. Ptitsin and Y. M. Shatunov, Helical Spin Rotators and Snakes, Proc. Third Workshop on Siberian Snakes and Rotators (A. Luccio and T. Roser, Eds.) Upton, NY, Sept. 12-13, 1994, Brookhaven National Laboratory Report BNL-52453.
- [24] A. Lehrach et al., Polarized beams in the high-energy storage ring of the future GSI project, Proc. of the 16th International Spin Physics Symposium SPIN 2004, Trieste, World Scientific, 742 (2005), ISBN 981-25-6315-6.
- [25] R. E. Ruland (SLAC), "Setting reference targets", in Proc. CAS – CERN Accelerator School: Measurement and Alignment of Accelerator and Detector Magnets, Anacapri, Italy, 1997
- [26] I. Pschorn, H. Paluszek (Metronom GmbH), "Implementation and first results of the survey and alignment of accelerator facilities at GSI using the TASA system", in Proc. IWAA1997 – 5th Int. workshop on accelerator alignment, Argonne, USA, 1997
- [27] W. Scandale (CERN), "From tolerance to alignment", in Proc. 2001 LHC days, Villars-sur-Ollon, Switzerland, 2001
- [28] I. Pschorn (Metronom GmbH), "Combined techniques for network measurements at accelerator facilities", in Proc. IWAA1999 – 6th Int. workshop on accelerator alignment, Grenoble, France, 1999
- [29] S. Leinen (Institute of Physical Geodesy, Darmstadt University of Technology), private communication
- [30] C. Zhang, K. Fukami, S. Matsui (JASRI/SPring-8), "From the HLS measurement for ground movement at the SPring-8", in Proc. IWAA2004 – 8th Int. workshop on accelerator alignment, Geneva, Switzerland, 2004
- [31] I. Pschorn (GSI), A. Marbs (i3mainz), "A high-precision survey and alignment system in inaccessible, high-radiation areas of FAIR: Fundamental ideas", in Proc. IWAA2004 – 8th Int. workshop on accelerator alignment, Geneva, Switzerland, 2004
- [32] A. Marbs, F. Boochs (i3mainz), I. Pschorn (GSI), "A photogrammetric alignment approach at high-radiation areas of FAIR", in: Proc. IWAA2006, SLAC, Stanford, Sep. 2006
- [33] A. Marbs (i3mainz), Final report on the research project of RALF (EU FP6 funded), August 2005 - unpublished
- [34] A. Bersani et al, NIMA 586 (2008) 392-408
- [35] R. Parodi, private communication, 26.03.2008

- [36] http://www.zeus.desy.de/bluebook/ch03/section2_4_4.html#SECTION004400000000000000
- [37] R. Parodi, private communication, 27.03.2008
- [38] T.G. O'Connor et al., IEEE Trans. Appl. Superconductivity, 9, 2 (1999)
- [39] Air Liquide Helial ML, data from www.dta.airliquide.com
- [40] Wessington Cryogenics, http://www.wessingtoncryogenics.co.uk/ch_series.htm
- [41] <https://documents.triumf.ca/docushare/dsweb/Get/Document-12014/TRI-DN-07-32.pdf>
- [42] http://hepwww.rl.ac.uk/accel/mice/CMPB/050728/MICE_Refrigerator_001.pdf
- [43] M. Kauschke, GSI, private communication, 04.03.2008
- [44] S. An et al, Chinese Physics C (HEP&NP), Vol 32, No1, p. 60, 2008
- [45] S. An et al, Chinese Physics C (HEP&NP), Vol 32, No2, p. 139, 2008
- [46] J.R. Chen, K. Narushima, H. Ishimaru, J. Vac. Sci. Technol. A3 (1985) 2188
- [47] E. Hedlund, private communication 2005
- [48] L. Westerberg, CERN 99-05, 255
- [49] F.F. Rieke, W. Prepejchal, Phys. Rev. A6 (1972) 1507
- [50] M. Sedláček et al., "CELSIUS Electron Cooler Design", unpublished, 1993
- [51] Y. S. Derbenev and A. N. Skrinsky, The Kinetics of Electron Cooling of Beams in Heavy Particle Storage Rings, Part. Acc. 1977, 8, pp. 1-20 [Preprint INP No.255 (1968)]
- [52] High Voltage Engineering Europe, <http://www.highvolteng.com>.